UNIVERSIDAD COMPLUTENSE DE MADRID

FACULTAD DE CIENCIAS FÍSICAS
Departamento de Astrofísica y Ciencias de la Atmósfera

TESIS DOCTORAL

Distribución de metales en discos galácticos con espectroscopía de campo integral

Distribution of metals within galactic disks using integral field spectroscopy

MEMORIA PARA OPTAR AL GRADO DE DOCTOR

PRESENTADA POR

Raffaella Anna Marino

Directores

Armando Gil de Paz
Sebastián F. Sánchez Sánchez
Francisco Sánchez Moreno

Madrid, 2016

UNIVERSIDAD
COMPLUTENSE
MADRID

campus de Excelencia
MONCLOA Madrid

DISTRIBUTION OF METALS WITHIN GALACTIC DISKS USING INTEGRAL FIELD SPECTROSCOPY

Raffaella Anna Marino

DISTRIBUTION OF METALS WITHIN GALACTIC DISKS USING INTEGRAL FIELD SPECTROSCOPY

Universidad Complutense de Madrid

Madrid 2015

UNIVERSIDAD COMPLUTENSE DE MADRID

FACULTAD DE CIENCIAS FÍSICAS
DEPARTAMENTO DE ASTROFÍSICA Y CIENCIAS DE LA ATMÓSFERA

Distribución de metales en discos galácticos con Espectroscopía de Campo Integral

Distribution of Metals within Galactic Disks using Integral Field Spectroscopy

Dirigida por:

Prof. Armando Gil de Paz	Dr. Sebastián F. Sánchez Sánchez	Prof. Francisco Sánchez Moreno
Profesor Contratado	*Investigador Titular*	*Profesor Titular*
UCM	UNAM	UPM

Memoria presentada por
Dña. Raffaella Anna Marino
para aspirar al grado de
Doctor en Astrofísica
Madrid, June 2015

(Page left blank intentionally)

“ *Se comprendere é impossibile, conoscere é necessario* ”

Primo Levi, *Se questo é un uomo*

“ *Todo pasa y todo queda,*
pero lo nuestro es pasar,
pasar haciendo caminos,
caminos sobre el mar [...]
Caminante, son tus huellas
el camino y nada más;
Caminante, no hay camino,
se hace camino al andar.
Al andar se hace el camino,
y al volver la vista atrás
se ve la senda que nunca
se ha de volver a pisar.
Caminante no hay camino
sino estelas en la mar ”

Antonio Machado, *Caminante no hay camino*

“ *If you’ve found an answer to all your questions,*
it signifies your questions were wrong ”

Oscar Wilde, *The Soul of Man under Socialism*

Cover image credits:
Francisco Rodríguez Fotografía.

A mis familias: la italiana,
la española
y la perruna.

Resumen

Una de las preguntas sin resolver más fundamentales que los astrónomos se han planteado desde hace tiempo es cómo el Universo se originó y cómo las estructuras formadas en aquel entonces se convirtieron en las galaxias que observamos hoy en día. Esta misma motivación se ha aplicado a las diferentes áreas de investigación de la Astronomía Extragaláctica como en el caso de la presente Tesis donde voy a describir mi interés personal en comprender cual es la función y el contenido de informaciones de uno de los ingredientes básicos del medio interestelar (ISM en inglés) de la galaxias espirales: las regiones H II.

Con el fin de arrojar alguna luz sobre los mecanismos que gobiernan la evolución química de las galaxias (y de las regiones H II dentro de ellas) esta Tesis Doctoral se centra en el análisis bidimensional de las abundancias químicas de las regiones H II extragalácticas, estudiando con la más alta resolución posible no sólo la metalicidad global (y también la extinción como medida de esta y de la geometría del polvo) de las galaxias, sino también la variación de estas propiedades entre los diferentes tipos de galaxias. Por otro lado también analizaremos las conocidas discrepancias a la hora de medir la abundancia de oxígeno a partir de diferentes fases del ISM comparando las diferencias entre éstas y la abundancia de la estrellas con especial atención a las zonas más externas de los discos donde el papel relativo de los procesos interno y externo (tanto los seculares como los procesos de mayor velocidad) deberían ser más fáciles de desentrañar. Estas regiones de gas ionizado representan laboratorios perfectos para derivar las abundancias químicas en el Universo Local, ya que representan una herramienta poderosa para la comprensión de las propiedades físicas y la evolución química del ISM en las galaxias. En particular, en esta Tesis voy a utilizar los datos de Espectroscopía de Campo Integral (IFS en inglés) que pertenecen al proyecto CALIFA (*Calar Alto Legacy Integral Field Area Survey*) para, por un lado probar, confirmar y ampliar los resultados anteriores sobre los gradientes de metalicidad de los discos espirales, mientras que por el otro, con este conjunto de datos sin precedentes voy a costreñir las predicciones procedentes de los modelos teóricos y además gracias a nuestros datos podré comprobar los métodos de líneas intensas, un diagnóstico muy utilizados para medir metalicidades. También voy a describir el trabajo realizado dentro de las colaboraciones CALIFA y MEGARA (*Multi-Espectrógrafo en GTC de Alta Resolución para la Astronomía*, el IFU y MOS óptico diseñado para el Gran Telescopio de CANARIAS de 10.4m) como por ejemplo la clasificación morfológica de la muestra madre de CALIFA o las fases más técnicas de la reducción de datos y de los procedimientos de control de calidad en los que estuve profundamente involucrada.

El primer resultado científico de esta Tesis Doctoral ha sido el exhaustivo estudio piloto del cubo de datos de la galaxia espiral cercana NGC 5668 (Marino et al. 2012). A partir de la combinación de los datos de IFS con las imágenes pancromáticas de banda ancha se obtuvieron los perfiles radiales de brillo superficial y de color que se han comparado con modelos evolutivos químico-espectrofotométricos. Hemos investigado a fondo las propiedades de las regiones H II de NGC 5668 y el resultado principal que encontramos es el descubrimiento de un barra en su etapa de formación que está produciendo un aplanamiento inusual en el gradiente de metalicidad del gas. Este resultado sugiere que no todas las galaxias siguen las predicciones del crecimiento suave que se contempla en el escenario *inside-out* para la formación de discos galácticos. El segundo resultado presentado en esta Tesis es la actualización de dos de las calibraciones empíricas más utilizada por la comunidad científica para calcular el contenido de oxígeno basándonos en la recopilación más completa de datos que incluye nuevas medidas de temperatura electrónica en los espectros de CALIFA como otras medidas directa (T_e-based) de la literatura. Este reciente estudio se basa en un conjunto sin precedentes ($\sim$4000) de regiones H II y nos permite derivar la calibración más exacta para las galaxias cercanas hasta la fecha, tanto para el indicador O3N2 como para N2, en términos estadísticos y de más amplia calidad y cobertura del espacio de parámetros (Marino et al. 2013). Por último, he presentado recientemente mi tercer artículo como primer autora, en el que he llevado a cabo un análisis combinado de los gradientes de metalicidad obtenidos a partir de los datos de CALIFA (y basándome en las herramientas y las calibraciones que se han presentado en Marino et al. 2012, 2013), con los perfiles de brillo superficiál y los perfiles de color de la muestra Sloan Digital Sky Survey (SDSS). Nuestro análisis ha confirmado la presencia de perfiles de color con forma de *U* en las partes exteriores de la gran mayoría de las galaxias espirales de CALIFA y que hay un aplanamiento en muchos de los gradientes de metalicidad de gas ionizado para los mismos intervalos radiales. Este resultado se basa en la precisión proporcionada por las nuevas calibraciones y las técnicas de análisis desarrolladas durante toda la Tesis, especialmente durante el análisis experimental de la galaxia NGC 5668.

La metodología, el análisis y los resultados que se presentan en esta Tesis demuestran la fuerza y la urgencia de utilizar datos IFS combinados con imágenes en multiples longitudes de onda para (I) mejorar nuestra comprensión sobre la naturaleza de las propiedades físicas y químicas de la diferentes fases del gas dentro de las galaxias espirales; (II) para derivar la distribución bidimensional del contenido en metales de una galaxia con la mejor resolución espectral y espacial; (III) para estudiar la historia de su enriquecimiento químico y su evolución; (IV) para comprobar la validez de algunas relaciones conocida para los discos espirales, como por ejemplo, las calibraciones empíricas de metalicidad o (V) finalmente para acotar con nuestros resultados observaciones las predicciones teóricas del escenario *inside-out*.

Summary

One of the oldest question of astronomers is to understand how the Universe began and how the structures formed in it evolved into the galaxies we observe today. This motivation is applied at different areas of Extragalactic Astronomy research as in the case of this Thesis where I will describe my personal interest on understanding which is the role and the information content of one of the basic ingredients of the interstellar medium (ISM) of spiral galaxies: H II regions.

In order to shed more light on the mechanisms that regulate the chemical evolution of galaxies (and of H II regions within them) this Ph.D. Thesis is focused on the spatiallly resolved analysis of the chemical abundances of the extragalactic H II regions studying not only the global metallicity (and also extinction as a measure of this and of dust geometry) of galaxies but also the variation across galaxies and the abundance discrepancies among different phases of the ISM and between these and the abundance of the stars paying special attention to the outer edges of the disks where the relative roles of internal and external (both secular and fast) processes should be easier to disentangle. These ionized-gas regions represent perfect laboratories for deriving chemical abundances in the local Universe. Indeed, H II regions are powerful tools for understanding the physical properties and chemical evolution of the ISM in galaxies. In particular, in this dissertation I will use the Integral Field Spectroscopy (IFS) data from the ongoing CALIFA (*Calar Alto Legacy Integral Field Area*) survey to test, confirm and extend previous results on metallicity gradients, while at the same time with this unprecedented dataset, I will be able to better constrain the predictions coming from the theoretical models or to check and strengthen the diagnostic methods and observational calibrations used to measure metallicities. I will also describe the work carried out within the CALIFA and the MEGARA (*Multi-Espectrógrafo en GTC de Alta Resolución para Astronomía*, the optical IFU and MOS designed for the 10.4m Gran Telescopio CANARIAS) collaborations concerning the morphological classification of the CALIFA mother sample or the more technical tasks related to the data reduction and quality-control procedures in which I was deeply involved.

The first scientific result of this Ph.D. Thesis is the pilot study of the full bi-dimensional spectral cube of the nearby spiral galaxy NGC 5668 (Marino et al. 2012). Combining the IFU observations with panchromatic broad-band images, the surface brightness and color profiles were obtained and compared with chemo-spectrophotometric evolutionary models. We investigate the properties of the H II regions within NGC 5668 and the main result that we find is the discovery of a bar in its formative stages that produces an unusual flattening in metallicity gradient suggesting that not all galaxies

follow the smooth growth prediction of the *inside-out* scenario for the formation of disks. The second results presented in this Thesis is the revised calibration that I have performed on the widely used empirical oxygen calibrations based on the most comprehensive compilation of both CALIFA data and the T_e-based measurements from the literature. This novel approach make use of an unprecedent set ($\sim$4000) of H II regions and allows us to derive the most accurate calibration for external galaxies to date for both the O3N2 and N2 single-ratio indicators, in terms of all statistical significance, quality, and coverage of the parameters space (Marino et al. 2013). Finally, I have recently submitted my third 1st-author paper where I have carried out a combined analysis of the metallicity gradients obtained from CALIFA (based on the tools and calibrations presented in Marino et al. 2012, 2013) with the surface brightness and color profiles from the Sloan Digital Sky Survey (SDSS). Our analysis has already confirmed the presence of *U*-shaped color profiles in the outer parts of the vast majority of the CALIFA disk galaxies analyzed and a corresponding flattening in the ionized-gas metallicity gradients for the same radial ranges. This result relies upon the accuracy provided by the new calibrations and the techniques developed during the entire Thesis period, especially during the pilot analysis of NGC 5668.

The methodology, analysis and results of this dissertation demonstrate the strength and the urgency of using IFS data combined with multi-wavelength imaging for (I) understanding the nature of the physical and chemical properties of the gas-phase in spiral galaxies; (II) deriving the 2D distribution of metallicity of an entire galaxy; (III) studying their metallicity enrichment and evolution; (IV) testing fundamental relations such as the empirical metallicity calibrations or (V) the theoretical prediction of the *inside-out* scenario.

Acknowledgements

I would like to acknowledge all those persons who during these last four years, have provided me with their help, assistance and support, and to whom I will always be indebted. This paper is the report of all these personal and professional processes.

First and foremost, I cannot thank enough my supervisors, Armando Gil de Paz, Sebastián Sánchez and Francisco Sánchez for their guidance and for all the trust they put on me during the development of this Ph.D. Thesis. I will always remember their patience, warmth, sense of humor, steady support and expertise contributed to make my experience as student at the Complutense University of Madrid very rewarding one. Thank you guys for all!

I want to express my gratitude to the Spanish program of International Campus of Excellence Moncloa (CEI) which fully sponsored my studies and provided me with the financial support to carry out this research.

I feel especially grateful towards by the GUAIX (Extragalactic Astrophysics and Astronomical Instrumentation group) group at UCM: without all the hours of your time, effort, encouragement, laughters and coffees you kindly bestowed upon me, the completion of this Thesis would have not been possible. Thank you very much for your support, teachings and hospitality in Spain.

This Thesis makes uses of the data provided by the Calar Alto Legacy Integral Field Area (CALIFA) survey. Based on observations collected at the Centro Astronómico Hispano Alemán (CAHA) at Calar Alto, operated jointly by the Max-Planck-Institut für Astronomie and the Instituto de Astrofísica de Andalucía (CSIC). The CALIFA collaboration would like to thank the IAA-CSIC and MPIA-MPG, as major partners of the observatory, and CAHA itself, for the unique access to telescope time and support in manpower and infrastructures. I would also acknowledge the CAHA staff for their dedication to this project. We thank the *Viabilidad, Diseño, Acceso y Mejora* funding program, ICTS-2009-10, for supporting the initial developement of this project. As well the support from the Spanish *Programa Nacional de Astronomía y Astrofísica* under grant AyA2009-10368. I was also partially funded by the Spanish MICINN under the Consolider-Ingenio 2010 Program grant CSD2006-00070: First Science with the GTC. Finally, I would like to thanks the support from the *Plan Nacional de Investigación y Desarrollo* funding programs, AyA2012-30717 and AyA2013-46724P, of Spanish *Ministerio de Economía y Competitividad* (MINECO), as well as to the DAGAL network from the People's Program (Marie Curie Actions) of the European Union's Seventh Framework Program FP7/2007-2013/ under REA grant agreement number PITN-GA-2011-289313.

On the personal side, my family deserves my fondest gratitude for their love, patience, unfai-

ling encouragement and support that was the fuel that has kept me going on! Thanks also to all those important persons who made Madrid a special experience. It would take paragraphs and paragraphs to mention you all, but be sure that I will always keep in my heart and memory all the remarkable moments spent together, in so many different circumstances and situations. Thank you for your friendship, company, support, encouragement and love.

This dissertation is submitted for the degree of Doctor of Philosophy at the Complutense University of Madrid. The research described herein was conducted under the supervision of Prof. Armando Gil de Paz, Dr. Sebastián Sánchez and Prof. Francisco Sánchez in the Department of Astrophysics and Atmosphere Sciences at Complutense University, between 2011 and 2015. This work is to the best of my knowledge original, except where acknowledgements and reference are made to previous work. Neither this, nor any substantial similar dissertation has been or is being submitted for any other degree, diploma or other qualification at any other university.

Tarda en llegar
y al final, al final
hay recompensa
en la zona de promesas.
(Zona de promesas, G. Cerati)

Madrid, Junio de 2015

Raffaella Anna Marino

Contents

List of Figures

List of Tables

Symbols & Constants

Angstrom $\text{Å} = 10^{-10}$ m

Astronomical Unit $AU = 1.5 \times 10^{11}$ m

Boltzman constant $k = 1.3806503 \times 10^{-23}\ \mathrm{m^2\,kg\,s^{-2}\,K^{-1}}$

Cosmology[1] $\Omega_{\mathrm{matter}} = 0.308$

$\Omega_{\mathrm{vacuum}} = 0.692$

Hubble parameter $\mathrm{H}_0 = 67.8\ \times 10^3\ \mathrm{m\,s^{-1}\,Mpc^{-1}}$

Hubble time $\mathrm{t}_H = 13.798$ Gyr

Parsec $pc = 3.0857 \times 10^{16}$ m

Solar Effective Temperature $\mathrm{T}_{eff} = 5777$ K

Solar Luminosity $\mathrm{L}_\odot = 3.839 \times 10^{26}$ W

Solar Mass $\mathrm{M}_\odot = 1.98892 \times 10^{30}$ kg

Speed of light $c = 2.999792458 \times 10^8\ \mathrm{m\,s^1}$

Universal Gravitational $G = 6.67384 \times 10^{-11}\ \mathrm{N\,m^2\,kg^{-2}}$

[1] Planck Collaboration et al. 2015

Glossary

2MASS Two Micron All Sky Survey. Survey of the whole sky in the J, H and K_S bands (1.2 μm, 1.6 μm and 2.2 μm, respectively).

2dFGRS Two Degree Field Galaxy Redshift Survey.

AAT Anglo Australian Telescope.

AGB Asymptotic Giant Branch. A late stage in stellar evolution undertaken by low- to intermediate-mass stars.

AGN Active Galactic Nucleus. Very luminous and compact source in the center of a galaxy, possibly hosting a supermassive black hole.

ANU Australian National University Observatory.

AAO Anglo Australian Observatory.

APO Apache Point Observatory.

AQC Automatic Quality Control Tasks.

ASCII American Standard Code for Information Interchange.

CALIFA Calar Alto Legacy Integral Field Area Survey.

CAHA Calar Alto Hispano Alemá Observatory.

CAVEX Calar Alto Vistual EXtinction monitor.

CCD Charge Coupled Device.

CDM Cold Dark Matter.

CELs Collisional Excited Lines.

CFHT Canada France Hawaii Telescope.

CIGALE Code Investigating GAlaxy Emission. Software tool for study the evolution of galaxies by comparing modeled galaxy SEDs to observed ones from the far ultraviolet to the far infrared.

DAR Differential Atmospheric Refraction.

DQ Data Quality.

E3D Euro3D. Software tool for visualizing and analyzing integral field spectroscopy data.

E-ELT European Extremely Large Telescope.

ESO European Southern Observatory (also ESO/Uppsala Survey of the ESO(B) Atlas).

ETC Exposure Time Calculator.

EW Equivalent Width. In a spectral feature, width of a rectangle whose height is equal to the continuum level, and whose area is the same as that encompassed by the spectral feature.

ETGs Early Type Galaxies.

FC Folded Cassegrain.

FDR Focal Ratio Degradation.

FIR Far-Infrared (from 25-40 μm to 200-350 μm).

FITS Flexible Image Transport System. Standard image format used in astronomy.

FLAMES Fibre Large Array Multi Element Spectrograph on the VLT.

FMAT Fiber Mos Assignment Tool.

FMPT Fiber Mos Positioning Tool.

FRIDA inFRared Imager and Dissector for the Adaptive optics system of the GTC.

FoV Field of View.

FUV Far-Ultraviolet (1350-1750 Å).

FWHM Full Width at Half Maximum. Measurement of the width of a function (such as a spectral line or a PSF), defined as the difference between the two values of the x variable when the y one is equal to half of its maximum value.

GALEX Galaxy Evolution Explorer. Space telescope that observes in the FUV and NUV bands.

GMOS Gemini Multi Object Spectrograph.

GNIRS Gemini Near InfraRed Spectrograph.

GMT Giant Magellanic Telescope.

GTC Gran Telescopio CANARIAS.

GUI Graphical User Interface.

HRS Herschel Galaxy Reference Survey.

HST Hubble Space Telescope.

IC Index Catalogue.

ICF Ionization Correction Factor.

IFS Integral Field Spectroscopy. Technique that allows gathering two-dimensional simultaneously spectra of extended objects.

IFSps Integral Field Spectrographs.

IFU Integral Field Unit. Instrument designed to perform two-dimensional spectroscopy.

IGM Inter Galactic Medium.

ILR Inner Lindblad Resonance.

IMF Initial Mass Function. Function describing the mass distribution of newly born stars in a single cluster, in terms of number of stars per mass interval.

IR Infrared (from 0.7-1 μm to 350 μm).

IRAC Infrared Array Camera. Mid-infrared instrument onboard the *Spitzer* space telescope, providing images at 3.6 μm, 4.5 μm, 5.8 μm and 8.0 μm.

IRAF Image Reduction and Analysis Facility. Software to reduce and analyze astronomical data.

IRAS Infrared Astronomical Satellite. An infrared space observatory that performed an all-sky survey at 12 μm, 25 μm, 60 μm and 100 μm.

IRS Infrared Spectrograph. Instrument onboard *Spitzer* that provides low- and high-resolution mid-infrared spectra from 5.2 μm to 38 μm.

IRX-β Relation between the total-infrared to UV ratio (or infrared excess, IRX) and the slope of the UV spectrum (β).

ISM Interstellar medium. The gas and dust pervading space between stars.

ΛCDM Lambda Cold Dark Matter. Cosmological model that includes dark energy (in the form of a cosmological constant Λ) and non-baryonic dark matter moving at non-relativistic speeds.

LARR Lens Array coupled with a fiber bundle to PMAS.

LEDA Lyon-Meudon Extragalactic Database. Database of galaxies now referred to as HyperLeda, after having merged with the Hypercat database.

LCB Large Compact Bundle.

LINERs Low-Ionization Nuclear Emission-line Region galaxies.

LIRG Luminous Infrared Galaxy. Galaxy whose total infrared luminosity is larger than 10^{11} solar luminosities.

KINGFISH Key Insights on Nearby Galaxies: a Far-Infrared Survey with Herschel.

KMOS K-band Multi-Object Spectrograph at VLT.

KPNO Kitt Peak National Observatory.

JWST James Webb Space Telescope.

M Messier catalogue.

MaNGA Mapping Nearby Galaxies at APO.

MCS MEGARA Control System.

MEGADES MEGARA Galaxy Disk Evolution Survey

MEGARA Multi-Espectrógrafo en GTC de Alta Resolución para Astronomía.

MDRP MEGARA Data Reduction Pipeline.

MIPS Multiband Imaging Photometer. Camera onboard *Spitzer* observing in the far-infrared, at 24 μm, 70 μm and 160 μm.

MIR Mid-Infrared (from 5 μm to 25-40 μm).

MOPPS MEGARA Observing Preparation Sofware Suite.

MOS Multi-Object Spectrometers.

MRK Markarian Catalogue.

MW Milky Way.

MUSE Multi Unit Spectroscopic Explorer for the ESO-VLT.

NASA National Aeronautics and Space Administration.

NED NASA/IPAC Extragalactic Database. Database that compiles positions, basic data and bibliographic references for millions of extragalactic objects.

NGC New General Catalogue.

NIFS Near Infrared Spectrograph at AAT.

NIR Near-infrared (from 0.7-1 μm to 5 μm).

NIRSpec Near infrared Spectrograph for the JWST.

NTT New Technology Telescope. A 3.6 m telescope in La Silla (Chile) that incorporated for the first time active optics.

NUV Near-Ultraviolet (1750-2750 Å).

OASIS Optically Adaptive System for Imaging Spectroscopy mounted at CFHT.

OLR Outer Lindblad Resonance.

ORLs Optical Recombination Lines.

PA Position Angle. Angle between a galaxy's major axis and the north celestial pole, measured counterclockwise when north is up and east is left.

PACS Photodetector Array Camera and Spectrometer. One of the instruments onboard the Herschel Space Observatory, that can work either as an imaging photometer or an IFU in the spectral range from 57 μm to 210 μm.

PGC Principal Galaxies Catalogue.

PIFS Near Infrared Spectrograph at Hale Telescope.

PINGS PPAK IFS Nearby Galaxies Survey. Two-dimensional spectroscopic survey of 17 nearby galaxies, performed with the PPAK instrument.

PMAS PMAS, the Postdam Multi-Aperture Spectrophotometer mounted on the 3.5 m telescope in Calar Alto observatory.

PPak PMAS fiber pack. An off-axis fiber bundle that provides integral field spectroscopy observations in the optical range.

PSF Point Spread Function. Image of a point source yielded by an optical system.

R3D Software package for reducing fiber-based integral field spectroscopy data.

RC3 Third Reference Catalogue of Bright Galaxies. Catalog of thousands of nearby galaxies in the optical range.

RSS Row Stacked Spectra.

SAURON Spectroscopic Areal Unit for Research on Optical Nebulae Project at WHT.

SAMI Sydney university AAO MOS IFU.

SDSS Sloan Digital Sky Survey. Photometric and spectroscopic survey of more than a quarter of the sky in the optical range.

SED Spectral Energy Distribution. Variation with wavelength of an object's luminosity.

SFH Star Formation History. Temporal evolution of the star formation rate.

SFR Star Formation Rate. Mass of gas transformed into stars per unit of time.

SINGS Spitzer Infrared Nearby Galaxies Survey. Mid- and far-IR survey of 75 representative nearby galaxies, complemented with ground-based optical images.

SMEX NASA's Small Explorer.

S/N Signal-to-noise ratio.

SPIRE Spectral and Photometric Imaging Receiver. One of the instruments onboard the Herschel Space Observatory, that can work either as an imaging photometer or a spectrometer in the spectral range from 208 μm to 583 μm.

SPH Smoothed Particle Hydrodynamics. Numerical method that simulates fluids as made of discrete and smoothed elements.

SPHERE Spectro-Polarimetric High-contrast Exoplanet REsearch at VLT.

sSFR Specific Star Formation Rate. Ratio of the SFR and the total stellar mass.

STIS The Space Telescope Imaging Spectrograph Design.

THINGS The HI Nearby Galaxies Survey. Survey of 34 nearby galaxies performed with the Very Large Array at the 21 cm hydrogen line.

TIR Total Infrared (3-1100 μm).

UGC Uppsala General Catalogue.

ULIRG Ultra-Luminous Infrared Galaxy. Galaxy whose total infrared luminosity is larger than 10^{12} solar luminosities.

UV Ultraviolet (1350-2750 Å).

VENGA The VIRUS-P Exploration of Nearby Galaxies.

VIMOS Visible Multi-Object Spectrograph. Imager, multi-object spectrograph and integral field unit in the optical range, mounted on one of the telescopes (unit 3) of the Very Large Telescope facility.

VLA Very Large Array. Radio interferometer in New Mexico.

VLT Very Large Telescope. Array of four fixed 8.2 m telescopes and four movable 1.8 m ones at Cerro Paranal (Chile).

VPH Volume Phase Holographic.

VQC Visual Quality Control Tasks.

VVDS VIMOS-VLT Deep Survey.

WHT William Herschel Telescope.

XUV Extended Ultraviolet emission found in some spirals beyond their optical size.

1

Introducción

1.1 La composición química de las regiones H II como testimonio de la evolución de las galaxias

Nuestra visión del Universo, desde la sencillez del Big Bang a la complejidad observada en las galaxias actuales, ha ido cambiando de forma espectacular en las últimas décadas y está bajo continuas revisiones gracias a los avances en la tecnología de observación y en los recursos computacionales.

El camino hacia la comprensión de los procesos que dan lugar a la evolución de las galaxias ha sido arduo. Es sorprendente que hasta los años 1920 no se supiera de la existencia de galaxias distintas a la Vía Láctea. La opinión predominante hasta entonces era que el Universo consistía de la Vía Láctea y de un vacío alrededor de ésta. Hace cuatrocientos años, Galileo Galilei apuntó su telescopio a la Vía Láctea y descubrió que constaba de innumerables estrellas débiles que no son visibles a simple vista. Cerca de 150 años después, el filósofo Immanuel Kant especuló que la gravedad debe actuar entre las estrellas de la Vía Láctea en la misma forma que la gravedad es responsable de los movimientos de los planetas del Sistema Solar, y que otras nebulosas observadas podrían ser similares a la nuestra pero muy lejanas (es decir, serían Universos isla). Han pasado ya más de 90 años desde que el llamado *Gran Debate* entre Harlow Shapley y Heber Curtis en el que se estableció la verdadera naturaleza de las nebulosas gaseosas. El debate se resolvió finalmente por Edwin Hubble en 1923, que midió la distancia a Andrómeda usando Cefeidas y que demonstró que estas nebulosas espirales son, de hecho, galaxias enteras fuera de nuestra Vía Láctea (Hubble 1925). Desde entonces, el concepto de estos objetos, galaxias o Universos isla, situados más allá de la Vía Láctea, comenzó a extenderse.

Por otra parte, vale la pena mencionar que hasta la década de 1980 se consideraban a las estrellas como la forma dominante de la materia en el Universo. Así, nuevas ideas teóricas pusieron de manifiesto que la materia oscura originalmente descubierta por Zwicky (1933) podría consistir de partículas elementales neutras, no bariónicas (Cowsik & McClelland 1973; Peebles 1982), mientras que las imágenes de rayos X mostraron que la mayoría de los bariones en cúmulos ricos se encuentra en la forma de gas intergaláctico caliente (Forman & Jones 1982). Fruto de nuestro mejor conocimiento de las propiedades de las galaxias quedó claro que los bariones no son la forma dominante de la materia en nuestro Universo, y que las estrellas representan sólo una pequeña fracción de los bariones (e.g. Fukugita, Hogan & Peebles 1998).

A pesar de los importantes avances realizados en los últimos años en nuestra comprensión

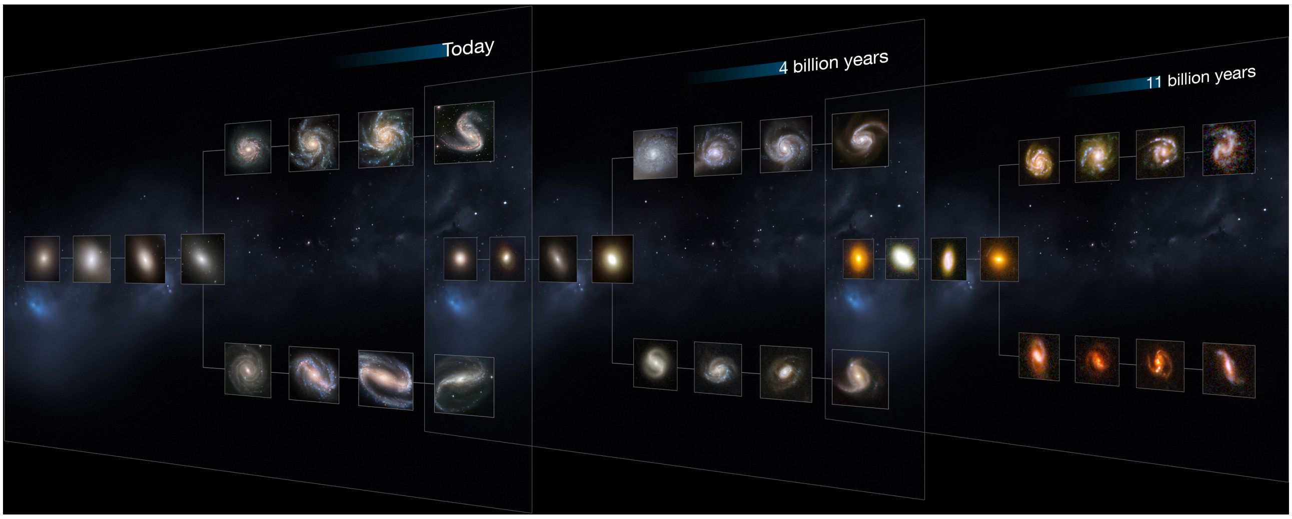

Figura 1.1: Esta imagen muestra cortes del Universo en diferentes instantes a lo largo de su historia (hoy en día, hace 4 y 11 mil millones años). La forma que se muestra a cada desplazamiento al rojo o época cosmológica es la del diagrama de Hubble, el cual describe y separa las galaxias de acuerdo a su morfología, ya sea espiral (S), elíptica (E) o lenticular (S0). A la izquierda de este diagrama se muestran las galaxias elípticas, con las lenticulares en el medio, y las galaxias espirales en dos ramas en el lado derecho. Las espirales de la rama inferior poseen barras, mientras que las de la rama superior carecen de ellas. El Universo actual esta poblado de galaxias muy luminosas y de gran tamaño, con formas complejas y morfología bien definidas. A medida que vamos más atrás en el tiempo, estas se vuelven más pequeñas y menos maduras, ya que estas galaxias se encuentran todavía en proceso de formación. *Créditos: NASA, ESA, M. Kornmesser*.

de la física bariónica, la formación y evolución de los discos galácticos siguen siendo todavía dos de los aspectos más importantes por entender en su totalidad, dentro del campo de la astronomía extragaláctica. La imagen actual sobre la formación de las galaxias en general se basa en el modelo jerárquico de agrupamiento de la Materia Oscura Fría (dentro del paradigma estándar de ΛCDM), el cual intenta explicar cómo se formaron las estructuras que observamos hoy en día como consecuencia del crecimiento de las fluctuaciones primordiales (inestabilidades gravitacionales) tras un período en que el Universo era extraordinariamente homogéneo, como lo ejemplariza el Fondo Cósmico de Microondas. De acuerdo al modelo ΛCDM la mayor parte de la materia en el Universo se encuentra en forma de materia fría (no relativista) no bariónica sujeta a interacciones gravitacionales y cuyo proceso de enfriamiento y virialización se realiza sin la emisión de fotones. Los últimos resultados del proyecto Planck confirman que nuestro Universo tiene una edad de 13.798 ± 0.037 millones años y se compone por un 4.82 ± 0.05 % de materia bariónica ordinaria, un 25 ± 4 % de materia oscura y un 69 ± 1 % de energía oscura (Colaboración Planck et al. 2015). De particular interés es el hecho de que, en el paradigma ΛCDM las galaxias representan sólo la punta del iceberg de un Universo dominado por alguna materia oscura desconocida, y de una forma aún más difícil de estudiar: la energía oscura. Así, la comprensión de la riqueza de morfologías, tamaños y luminosidades de las galaxias dentro un contexto cosmológico es una tarea de gran importancia pero de no menor dificultad (Mo, Mao & White 1998, MMW en adelante).

La mayor parte de la materia visible en el Universo está concentrada en las galaxias, que son los ecosistemas básicos en astronomía en el que se forman las estrellas, evolucionan y mueren durante un proceso que las mantiene en constante interacción con el medio interestelar (ISM). Las galaxias además representan balizas que nos permiten explorar nuestro Universo hasta escalas cosmológicas. A partir del trabajo pionero de Edwin Hubble (1926b, 1936), que fue quien propuso por primera vez un sistema de clasificación morfológica (el llamado *diagrama de Hubble*) para las galaxias, sabemos que el Universo está poblado por diferentes tipos de galaxias que se ordenan en tres categorías generales según la forma que presentan (originalmente en placas fotográficas): elípticas, espirales e irregulares; las galaxias del primer tipo son relativamente redondeadas en forma y están constituidas por un gran número de estrellas con una distribución de movimientos triaxiales, mientras que las espirales son discos planos dominados casi en su totalidad por las rotaciones ordenadas. Hoy en día, esta clasificación tiene una taxonomía más compleja y se actualiza continuamente utilizando no sólo las informaciones de las bandas ópticas, sino también en otras longitudes de onda. Otros tipos de galaxias son las galaxias de baja superficie de brillo, las galaxias enanas, galaxias ultra-débiles, esferoidales y galaxias en transición entre subclases (en muchos casos debido a efectos ambientales). La Figura 1.1 ilustra cómo se vería el diagrama de Hubble para la clasificación de galaxias en diferentes momentos de la historia del Universo.

El modelo estándar ΛCDM (Springel et al. 2006) proporciona un marco en el que puede llegar a entenderse los principales mecanismos de formación y evolución de la estructura a gran escala en el Universo. Sin embargo, la formación de las galaxias de disco ha demostrado ser particularmente difícil de entender. En el contexto ΛCDM las galaxias son sistemas que consisten en una estructura estelar embebida en un halo de materia oscura que crece en masa a partir del agrupamiento jerárquico de halos de menor masa. Sin embargo, la comprensión de la evolución de la componente bariónica bajo este escenario jerárquico para la materia oscura no es aún completa. Así, es bien sabido que las propiedades fotométricas, químicas, y cinemáticas de las galaxias a día de hoy son el resultado de varios mecanismos complejos tales como las condiciones iniciales en las que se formaron y también la interacción entre los procesos internos y externos, tanto rápidos como seculares. Aunque es difícil separar los efectos de todos estos mecanismos, cualquier teoría que pretenda explicar de forma satisfactoria la formación y evolución de las galaxias de disco tiene que ser capaz de dar cuenta de todos estos procesos.

El tipo más común de galaxias en una exploración limitada en magnitud dentro del Universo Local serían las galaxias espirales. Estas representan alrededor del 77 % de todas las galaxias observadas (20 % son elípticas y 3 % irregulares; Li & White 2009). En este trabajo de Tesis Doctoral vamos a prestar especial atención a los discos espirales observados dentro de la exploración CALIFA (Calar Alto Legacy Integral Field Area Survey)[1] que representa también el tipo más frecuente de objeto observado como parte de este proyecto (ver Capítulo §4 y §5). Las galaxias de disco consisten de una componente de disco formado por estrellas, polvo y gas frío (tanto atómico como molecular), una componente central de bulbo, un halo estelar, y un halo de materia oscura. A menudo se aprecian también brazos espirales y un alto porcentaje de galaxias espirales presentan también una componente central con forma de barra. Sus masas estelares típicas oscilan entre 10^9 y 10^{12} $M_\odot$, sus luminosidades

---

[1] `http://califa.caha.es/`

entre 10^8 y 10^{11} $L_\odot$, tamaños entre 5 y 100 kpc de diámetro, velocidades de rotación de unos 200-300 km/s y escalas de disco de aproximadamente 4 kpc. Sus discos a menudo se pueden separar en una componente delgada y una gruesa. El disco delgado está compuesto de estrellas jóvenes, mientras que el disco grueso contiene significativamente menos masa y sus estrellas son más viejas, más ricas en metales y son dinámicamente más calientes. Ya que nuestra propia galaxia es un espiral (barrada), la mayor parte de nuestra comprensión sobre la formación de galaxias espiral proviene de estudios realizados sobre los distintos componentes de la Vía Láctea.

Como ya se mencionó previamente, muchos aspectos relacionados con la formación y evolución de galaxias y, especialmente, sobre la evolución de las galaxias espirales permanecen sin explicación. Fueron White & Rees (1978) quienes en un primer lugar plantearon la formación de estas galaxias como un proceso en dos pasos según el cual las galaxias de disco se formarían por contracción disipativa dentro de los halos de materia oscura. Por un lado, las estructuras de materia oscura habrían crecido jerárquicamente colapsando en halos individuales con una cierta cantidad de momento angular adquirida de pares de marea. Por otro lado, el gas seguiría inicialmente la misma evolución de la materia oscura hasta que la disipación por emisión de luz de las primeras estrellas permitiera su contracción y virialización a tamaños cada vez más pequeños siempre que se pudiera transferir el momento angular total del objeto (que no se altera por la emisión de luz) hacia una componente de disco relativamente extensa. Este proceso de virialización a radios cada vez menores y la formación de un disco delgado ayudan ambos al aumento de la densidad del gas, lo que facilita un proceso de fragmentación y formación de estrellas en las nubes moleculares resultantes. Históricamente, se propusieron dos escenarios para la formación de la componente de disco (ver White & Rees 1978; Fall & Efstathiou 1980). El primero contemplaba un colapso monolítico de una nube de gas de gran tamaño, donde el disco se formaría por conservación del momento angular (Eggen et al. 1962), mientras que el segundo mecanismo se basaba en la coalescencia de progenitores más pequeños con un cierto momento angular total que también acabarían almacenados en un disco estelar (Searle & Zinn 1978).

Hoy en día el escenario más aceptado para la formación de discos (White & Frenk 1991; MMW) es el que se conoce como el escenario *inside-out* que combina un cierto colapso esférico inicial con un escenario jerárquico de fusiones de halos que darían lugar además a la formación de un disco grueso y una redistribución del momento angular efectiva en la componente de disco delgado. Este escenario predice una secuencia directa de eventos que comienzan con la formación de una protuberancia inicial debido a las altas densidades y tiempos de enfriamiento rápido de la parte más interna de una galaxia. Básicamente, un halo de materia oscura proporciona un potencial para que la nube de gas protogaláctica en rotación aumente su densidad y colapse por efecto de la gravedad. Durante el colapso, el gas se enfría a través de los procesos radiativos hasta que se alcanza el equilibrio y se virializa. Por otro lado, el halo de materia oscura gana momento angular a través de los pares de marea generados por la estructura a gran escala a su alrededor y por las numerosas fusiones que tienen lugar durante esta primera etapa. Debido a la conservación del momento angular esto da lugar a la formación de un disco relativamente grueso. Sin embargo, hasta que no disminuye el ritmo de fusiones (a $z<1$) no se empieza a formar un disco más delgado donde se produce el grueso de la formación estelar (debido a inestabilidades de Jeans en las que se rompe el equilibrio entre auto-gravedad y presión térmica) y donde además la trasferencia de momento angular es más efectiva debido a su gran abundancia de gas. La conservación del momento angular da lugar en este caso a la formación de perfiles de densidad superficial de masa exponenciales (Freeman 1970). Un análisis cuantitativo de este modelo y las diferentes teorías sobre la formación de discos se describe a continuación, aunque los detalles de su modelización van más allá del alcance de esta Tesis y se remite el lector a los trabajos originales y/o al libro ya clásico de Binney & Tremaine (1987, o a sus actualizaciones posteriores) para una revisión detallada.

Cualitativamente, de acuerdo con el escenario *inside-out*, se forma un disco con propiedades similares a las observadas sólo si el gas conserva la mayor parte de su momento angular; en una primera etapa los halos de materia oscura no bariónica se forman a partir de fluctuaciones primordiales, a continuación, se enfría el gas que se condensa en estos halos. Sus principales supuestos son: (I) la masa y momento angular del disco representan una fracción fija de la masa y momento angular del halo de materia oscura; (II) el disco es una estructura delgada, soportada por rotación y con un perfil de brillo superficial exponencial; (III) sólo dinámicamente sistemas estables pueden corresponder a los discos de galaxias reales; (IV) la estructura interna del halo se asume que sigue un perfil de densidad de Navarro, Frenck & White (1997); (V) el halo se asume que se mantiene esférico durante el colapso. En este contexto, se estarían formando estrellas a partir del gas desde el comienzo de la formación del disco, a partir de inestabilidades gravitacionales que conducen a la formación de nubes moleculares gigantes (Elmegreen & Elmegreen 1983). La estabilidad del disco se puede asegurar ya sea a través de la presión, cuando la escala de tiempo dinámica local es más grande que la escala de tiempo asociada a la velocidad del sonido en el gas, o por medio de la dispersión de velocidades de las estrellas cuando el período de los epiciclos es menor que la escala de tiempo dinámica local. Esto se conoce como el criterio de estabilidad de Toomre (1964), el cual establece una relación entre los parámetros de un disco gaseoso con rotación diferencial y que es aplicable en aproximación lineal, es decir, lejos de la resonancias entre el patrón espiral y el movimiento de rotación (co-rotación) y epicíclico (ILR y OLR) de las estrellas. Este criterio sólo se aplica a la estabilidad contra perturbaciones axisimétricas y también se utiliza para explicar la presencia de umbrales de formación de estrellas en las regiones exteriores de los discos de galaxias.

La evolución de las galaxias de disco no se detiene después de la formación inicial y es bien conocido que las galaxias siguen experimentando una importante evolución *secular*. El término *secular* se refiere a una evolución dinámica relativamente lenta debido a procesos internos inducidos por los brazos de una galaxia espiral, barras, rotación diferencial, vientos galácticos, los efectos causados por agujeros negros y por el entorno de la galaxia. Una visión esquemática de los diferentes procesos que determinan la evolución galáctica se presenta en la Figura 1.2 (Kormendy & Kennicutt 2004). La evolución secular interna juega un papel importante en la evolución de las galaxias espirales teniendo importantes consecuencias en la transferencia de momento angular y en la distribución de los componentes de una galaxia: estrellas, gas y polvo. Por otro lado, algunos de los efectos del entorno incluyen la acreción de gas o satélites en fusiones menores o lo que se conoce como acoso galáctico (encuentros cercanos con otras galaxias que resulta en un importante cambio en las propiedades observacionales de estas). En resumen, la evolución secular, tanto la interna como la debida a la interacción con el entorno son claves para entender y poner a prueba los modelos cosmológicos de formación y evolución de las galaxias.

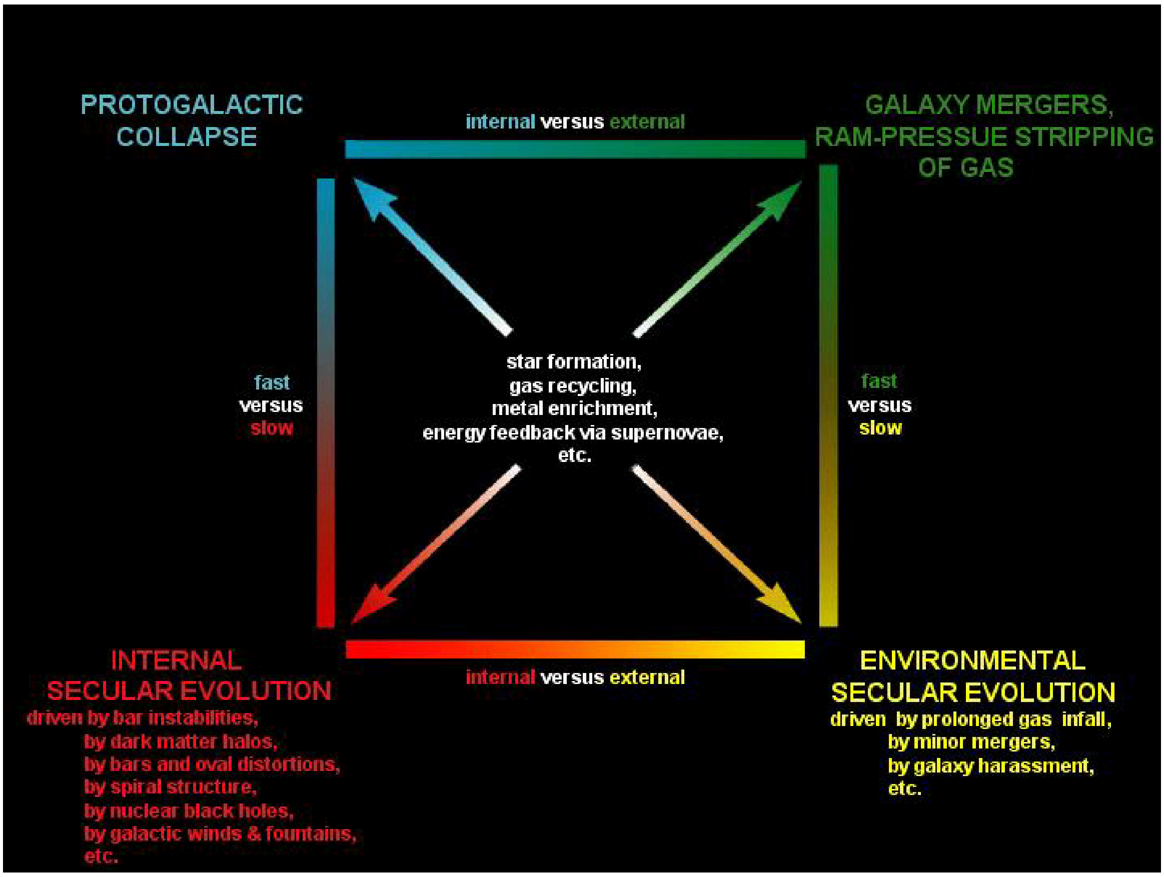

Figura 1.2: Esquema de Zwicky (1957) sobre los procesos que determinan la evolución galáctica de acuerdo a las actualizaciones del esquema proporcionados por Kormendy (1982a) primero y por Kormendy & Kennicutt (2004) más recientemente. Los procesos se dividen verticalmente en rápidos (arriba) y lentos (i.e. seculares; abajo). La evolución rápida ocurre en escalas de tiempo del orden de, o menores que, el tiempo de caída libre. Los procesos seculares normalmente requieren varios períodos de rotación galáctica para tener un efecto claro en los observables. Los procesos están divididos horizontalmente en los que ocurren internamente en una galaxia (izquierda) y los que son debidos al entorno, tales como las interacciones de galaxias (derecha). *Créditos: Kormendy & Kennicutt (2004).*

Típicamente, las galaxias de disco tienen dos brazos espirales dominantes (la amplitud más grande de los diferentes modos de Fourier es correspondiente a m=2) donde el patrón espiral gira más lentamente que las estrellas y se mantiene únicamente en el interior al radio de corotación, que es la zona donde se localizarán las regiones de formación de estrellas más activas. Bertil Lindblad (1925) fue el primero que apreció la existencia de dicha estructura espiral y su posible relación con la dinámica estelar y la evolución interna del disco. Existen dos teorías principales en la literatura para explicar el origen de la estructura espiral de los discos galácticos: la teoría de las ondas de densidad (Lin & Shu 1964) y la teoría de la formación estocástica auto-propagada de estrellas (Mueller & Arnett 1976). En el caso de las espirales de gran diseño (con brazos espirales bien definidos, muy abiertos y altamente simétricos) se prefiere el primer modelo. En este caso la estructura espiral se debe a la generación de una onda de densidad dinámica que se mantendría durante varios períodos galácticos. Los brazos espirales asociados serían entonces regiones más densas del disco que se mueven a una velocidad diferente a la de las propias estrellas. Las estrellas, por tanto, no se quedarían siempre en la posición que ahora vemos en ellas, sino que pasan a través de los brazos a medida que viajan en sus órbitas. El origen de la onda de densidad no se entiende completamente, aunque puede que parta de la generación de una onda de densidad cinemática producida por el valor casi constante de $\Omega - \kappa/2$ en los discos galácticos, aunque el papel de las interacciones con galaxias compañeras tampoco es descartable sobre todo en objetos con signos evidentes de interacción. La segunda teoría se basa en el supuesto de que la formación de estrellas en un sistema con rotación diferencial es capaz de auto-propagarse a través de la galaxia siguiendo un patrón espiral que se enrosca. Este escenario parte del hecho de que hay una pequeña probabilidad de formación de estrellas al azar dentro del disco que sería el substento para este mecanismo. El patrón de espiral observado sería fruto de la rotación diferencial del disco. Esta teoría es la más probable para explicar las propiedades las galaxias floculentas, donde los brazos espirales son irregulares, asimétricos y de bajo contraste.

Aproximadamente el 30 % de las espirales cercanas son floculentas, 10 % son de gran diseño, y el resto son multi-brazo, que se caracterizan por dos brazos simétricos en la parte interior del disco y una parte exterior muy ramificada con brazos formados por muchos segmentos. Las observaciones también confirman que las galaxias espirales aisladas tienden a ser floculentas mientras que los cúmulos densos con mayores oportunidades de interacción, tienden a ser de gran diseño. Aproximadamente en dos tercios de las espirales se observa la existencia de una componente adicional en la forma de barra, que se extiende desde el bulbo central, y en los extremos de los cuales comienzan comúnmente los brazos espirales. La proporción de espirales barradas en relación con las no barradas parece haber cambiado a lo largo de la historia del Universo. Es interesante hacer notar que observaciones con el satélite espacial Spitzer (entre otros) han puesto de manifiesto que nuestra propia Vía Láctea es una galaxia espiral barrada.

Por otra parte, en lo referente al escenario de formación de los discos de galaxias (es decir un escenario de crecimiento *inside-out* de discos dentro de un paradigma de agrupamiento jerárquico de ΛCDM) muchas de sus predicciones observacionales han sido ya puestas de manifiesto. Entre otras (I) el hecho de que las galaxias de disco tengan curvas de rotación planas, (II) los perfiles de brillo de la superficiál de los discos son muy cercanos a una función exponencial (lineal en brillo superficial), (III) las partes exteriores de los discos son generalmente más azules y presentan metalicidades más bajas que las partes internas, (IV) la abundancia de metales (i.e. elementos más pesados que el hidrógeno)[2] disminuye con la distancia galactocéntrica siguiendo un gradiente de metalicidad negativo casi universal. Esta predicción, en particular, es coherente con aquellas hechas por modelos espectrofotométricos y químicos de galaxias espirales cercanas (ver, por ejemplo, Boissier & Prantzos 2000). Estos modelos de evolución química (desarrollados originalmente para nuestra propia Galaxia) hacen uso de ingredientes de entrada (IMF, *yields* químicos, tiempos de vida estelares dependientes con la

---

[2] En astronomía, todos los elementos químicos más pesados que el Helio se denominan colectivamente como *metales*. Las reacciones nucleares durante los tres primeros minutos del Universo (la época de la nucleosíntesis primordial) producen principalmente hidrógeno (75 %) y helio (25 %), con una pequeña mezcla de metales, principalmente litio. Todos los otros metales en el Universo se formaron en tiempos posteriores como consecuencia de reacciones nucleares en las estrellas o durante procedimientos de captura neutrónica en las explosiones de supernova.

metalicidad, trazas evolutivas y librerías de espectros o modelos de atmósferas) y consideran los discos galácticos como un conjunto de anillos concéntricos que evolucionan de forma independiente y que están construidos por medio de la caída de gas de composición química primordial (ver sin embargo Bresolin et al. 2012). En términos de sus abundancias químicas, los modelos para la evolución de los discos espirales indican que estos se enriquecen de forma muy eficiente en un período muy corto de tiempo, alcanzando abundancias de oxígeno de $\sim$1/10 el valor solar en tan sólo 1 Gyr de evolución (Boissier & Prantzos 1999). En el Capítulo §3 se discute el caso de la galaxia NGC 5668, donde el modelo sencillo de crecimiento *inside-out* no es capaz de explicar las propiedades que observamos. Así, en general, se aprecia que aunque la mayoría de los discos espirales en galaxias cercanas presentan gradientes de metalicidad y color en sus partes interiores que son compatibles con las predicciones del escenario *inside-out*, más allá de una cierta distancia galactocéntrica (que en algunos modelos se asocia a un umbral de formación estelar) estos gradientes se aplanan e incluso se invierten siendo las estrellas más rojas y ricas en metales en dichas regiones exteriores. Algunos de los mecanismos (ajenos al escenario *inside-out*) que se proponen en este sentido se describirán más en detalle en el Capítulo §5 así como en un gran número de trabajos recientes en la literatura, incluyendo Bakos et al. (2008), Sánchez-Blázquez et al. (2009), Vlajić et al. (2009), Marino et al. (2012), Blanc et al. (2013).

Durante la última década, el estudio de la evolución de las galaxias en el Universo local ha sido tradicionalmente restringida al análisis fotométrico o, alternativamente, el análisis de espectros de rendija larga o de una única fibra óptica (e.g. SDSS). La disponibilidad generalizada de espectrómetros tipo Multi-Objeto (MOS, del inglés *Multi-Object Spectrographs*) y de Campo Integral (IFS, del inglés *Integral Field Spectroscopy*) con grandes campos de visión (FoV) nos ofrecen ahora la oportunidad de llevar a cabo exploraciones espectroscópicas sin precedentes, en el número de objetos/espectros abordados, de galaxias espirales y en las regiones H II dentro de estas, tanto a nivel local como para alto corrimiento al rojo. Este nuevo enfoque, tan ambicioso, se está aplicando ya en una nueva generación de exploraciones de IFS, lo que está dando lugar a un progreso significativo en el estudio de las galaxias de disco cercanas. Lo que antes era posible únicamente con datos de fotometría en banda ancha multi-frecuencia (desde el UV al infrarrojo, gracias principalmente a las exploraciones llevada a cabo por GALEX, SDSS, 2MASS, Spitzer, Herschel) se puede ahora cumplimentar y extender mediante el uso de espectroscopía 3D. Así, la calidad sin precedentes y la profundidad de estos nuevos conjuntos de datos de espectroscopía 3D nos están permitiendo (y esta Tesis es un claro ejemplo en ese sentido) alcanzar los bordes exteriores de los discos, donde las predicciones del, hasta cierto punto ingenuo, escenario *inside-out* de formación de discos descrito anteriormente podrían enfrentarse a sus tests más severos.

Muchos de los temas más candentes en el campo de la astrofísica extragaláctica llevan asociados el estudio de la física del gas ionizado. Por tanto, las regiones H II son lugares ideales para determinar la composición química y distribución de los elementos más pesados que el hidrógeno, que son responsables de las líneas prohibidas, de recombinación y de estructura fina emitidas en regiones H II y regiones de fotodisociación. En el caso del estudio de las nebulosas de emisión (tanto galácticas y extragalácticas), es claro que el uso de un conjunto de datos de espectroscopía 3D es crítico para obtener respuestas precisas a los problemas a los que nos enfrentamos en el estudio de estos objetos. Algunos de los temas que se pueden abordar en este sentido son: (1) la distribución de las regiones H II como un excelente trazador de la formación estelar reciente en galaxias espirales, (2) la interpretación detallada de sus espectros de líneas de emisión puede revelar detalles sobre la formación de la primera generación de estrellas y la formación de los elementos pesados en el Universo joven, (3) el análisis detallado de las propiedades físicas de estas regiones de gas ionizado (incluidas sus abundancias químicas relativas), lo que nos pueden dar pistas importantes sobre los mecanismos responsables de la formación de los discos de galaxias y (4) el estudio de estas regiones en el contexto de evolución de la galaxia, donde sus propiedas pueden aportar información como testimonio fósil de la historia de la formación de estrellas de una galaxia.

Como se discute en los Capítulos §3, §4 y §5, la profundidad, tamaño de la muestra y resolución espacial de las observaciones espectroscópicas IFS utilizadas para esta Tesis han permitido no solo la determinación de la abundancia metálica de las galaxias analizadas, sino también de su variación de galaxia a galaxia y de las discrepancias de abundancias entre las diferentes fases del ISM y entre éstas y la distribución de la luz de las estrellas. A lo largo de este trabajo, se considerará la medida de la abundancia de oxígeno como nuestro trazador de la metalicidad general en fase gaseosa y se hará uso de los dos términos de forma indistinta.

1.2 Objetivo y Estructura de esta Tesis

Con el fin de arrojar más luz sobre los mecanismos que gobiernan la evolución química de las galaxias, esta Tesis se centra en el análisis, con resolución espacial, de las abundancias químicas de regiones H II extragalácticas así como de las propiedades y efectos observacionales del polvo interestelar, de nuevo con resolución espacial. Así mismo, se estudiará como varían los resultados de este análisis de galaxia a galaxia y como son las discrepancias entre las varias abundancias entre las diferentes fases del ISM y entre estas y la abundancia química de las estrellas. Este trabajo se centrará especialmente en el estudio de las partes más externas de los discos donde el número de mecanimos responsables del enriquecimiento químico se esperan sean menos y más simples y donde los efectos de estos sean, por tanto, más notorios. Además, en estas regiones la menor abundancia de polvo debería servir de ayuda para minimizar el impacto de los (siempre difícilmente cuantificables) efectos del polvo interestelar sobre las medidas fotométricas y espectroscópicas.

En este sentido, las regiones de gas ionizado representan laboratorios ideales para derivar las abundancias químicas en el Universo local, ya que son regiones luminosas y de estructura relativamente simple, lo que las hace muy poderosas para la comprensión de las propiedades físicas y la evolución química del ISM en galaxias. En particular, en esta Tesis se van a utilizar los datos IFS pertenecientes a la exploración CALIFA para confirmar los resultados anteriores de medidas de gradientes de metalicidad en las regiones internas de los discos y para determinar la relación entre los gradientes relativamente planos de color observados en las partes externas con los gradientes de metalicidad, nunca medidos en tan detalle hasta la fecha. Finalmente, haciendo uso de este conjunto de datos sin precedentes, se podrán determinar los límites de predicción de diferentes indicadores de metalicidad a partir de las medidas de líneas de emisión intensas.

Las preguntas clave que pretendemos responder en este trabajo de Tesis Doctoral son las siguientes:

1. **¿Cómo han evolucionado las abundancias químicas de las galaxias espirales con el tiempo?** ¿Están creciendo estas abundancias de dentro hacia afuera tal y como se ha propuesto para explicar los gradientes de color y metalicidad en nuestra propia Vía Láctea, dentro del escenario *inside-out* de evolución de discos? Si existe un gradiente universal, ¿cómo podemos explicar todas las desviaciones (tanto en metalicidad como en color) recientemente medidos en las partes externas de los discos de varias galaxias cercanas respecto a lo predicho por este escenario?

2. **¿Son las diferentes calibraciones empíricas válidas para un amplio rango de propiedades físicas, incluyendo el desplazamiento al rojo, o su validez depende de los valores de estas y del método específico de diagnóstico utilizado?** Es bien sabido que hay varias técnicas en el literatura para derivar metalicidades del gas ionizado en regiones H II a partir de los flujos de sus líneas de emisión. Mediante el análisis del conjunto de datos espectroscópicos sin precedentes de la exploración CALIFA y de numerosos datos de la literatura con medidas de flujo en líneas aurorales hemos sido capaces de proporcionar calibraciones actualizadas de dichas técnicas así

como determinar las incertidumbres e intervalos de predicción de los métodos empíricos más utilizados.

3. **¿Es posible conciliar las características de los perfiles de luz, color y de abundancia química dentro de un escenario auto consistente?** Varios estudios recientes confirman la presencia de cambios de pendiente en las partes externas de los perfiles de brillo superficial y color de los discos de galaxias cercanas, pero todavía no está claro si existe una conexión entre estos y las propiedades de las abundancias de oxígeno en estas mismas regiones.

Abordar estos temas es un primer paso para futuros estudios detallados que harán uso de una nueva generación de Unidades de Campo Integral (IFU) como MUSE (por ejemplo, el proyecto MAD, *MUSE Atlas of Disks*) o MEGARA (como el proyecto MEGADES, *MEGARA Galaxy Disks Evolution Survey*). Así, en cierta medida, este trabajo puede ser también considerado como preparatorio para la futura explotación científica de estos instrumentos, que proporcionarán un salto cuantitativo en términos de eficiencia, resolución espacial y espectral.

La estructura de esta Tesis es la siguiente: En el Capítulo §2 se discute la importancia de las observaciones de espectroscopía 3D en astrofísica, incluyendo una breve explicación de las diferentes técnicas instrumentales utilizadas, incluidas sus ventajas e inconvenientes, y una revisión de las IFU más relevantes, con especial atención a aquellos proyectos en los que estoy más profundamente involucrada: PPak-CALIFA (*Calar Alto Legacy Integral Field Area Survey*) y MEGARA (*Multi-Espectrógrafo en GTC de Alta Resolución para Astronomía*). En este mismo Capítulo se ofrece un resumen de los trabajos realizados dentro de CALIFA y del proyecto MEGARA así como de la clasificación morfológica realizada sobre la muestra madre de CALIFA o los procedimientos más técnicos de reducción de datos y control de calidad en los que he participado más activamente. En el Capítulo §3 presento el análisis espectral bidimensional de un cubo que cubre de forma completa la extensión óptica de la galaxia espiral cercana NGC 5668. Se combinaron estos datos IFU con imágenes de banda ancha en diferentes longitudes de onda, desde el UV hasta el infrarrojo. Se obtuvieron perfiles radiales de brillo superficial y color que se compararon con modelos espectrofotométricos y químicos desarrollados en el contexto del escenario *inside-out* de evolución de discos. El análisis de las imágenes y de los perfiles radiales de abundancia química a partir del estudio de las propiedades de las regiones H II dentro NGC 5668 llevó al descubrimiento de una barra en sus primeras etapas de formación que ha dado lugar a un aplanamiento inusual del gradiente de metalicidad, lo que sugiere que no todas las galaxias siguen las predicciones de crecimiento de dicho escenario *inside-out*. El Capítulo §4 se centra en la derivación de nuevas calibraciones para la determinación empírica de la abundancia de oxígeno en galaxias. Este trabajo se basa en la recopilación más completa hasta la fecha de datos tanto de CALIFA como de la literatura con medidas de líneas intensas T_e. Este novedoso estudio hace uso de un conjunto sin precedentes ($\sim$4000) de regiones H II y nos permite obtener la calibración más precisa para galaxias externas hasta la fecha, tanto para el indicador O3N2 como para el de N2, en términos de su relevancia estadística, como de la calidad de los datos, y de su cobertura del espacio de parámetros. Este estudio fue un trabajo preparatorio necesario antes de que el análisis de NGC 5668 pudiera extenderse a una muestra estadísticamente significativa de galaxias. En el Capítulo §5, se lleva a cabo por primera vez un análisis combinado de los gradientes de metalicidad obtenidos a partir de los datos de la exploración CALIFA con los perfiles de brillo superficial y de color del Sloan

Digital Sky Survey (SDSS). El análisis detallado de 350 galaxias de disco de CALIFA confirma la presencia de perfiles de color en forma de U (*U-shaped*) en las partes exteriores de la gran mayoría de la muestra y una señal de aplanamiento correspondiente en los gradientes de metalicidad del gas ionizado para los mismos intervalos radiales en el caso de las galaxias con perfiles de tipo III. En §7 se discuten algunos proyectos de investigación futura, donde nos centramos en el estudio comparativo de la distribución 2D de la atenuación por polvo de estrellas y gas utilizando una muestra de unas pocas galaxias espirales extraídas del *Herschel Galaxy Reference Survey* que han sido observadas por nuestro grupo con la IFU PPak. En particular, el análisis conjunto de la extinción del continuo estelar y el gas ionizado nos permite investigar posibles variaciones en la geometría relativa de estrellas jóvenes y polvo o en la curva de extinción. También se analiza en este Capítulo la dependencia de estas magnitudes con la densidad superficial de polvo así como su temperatura y con la densidad de masa estelar y atenuación del continuo derivadas mediante el ajuste a distribuciones espectrales de energía pixel-a-pixel generadas por el código CIGALE[3]. Por último, las conclusiones generales de esta Tesis se resumen en §6.

Material adicional no incluido en el cuerpo principal de la Tesis se proporciona en tres apéndices. En el Apéndice A se presenta la mayor base de datos disponible hasta la fecha de medidas de flujos de líneas de emisión en regiones H II extragalácticas, incluyendo una recopilación de 603 regiones H II con mediciones precisas de la temperatura electrónica a partir de las medidas de líneas aurorales. En el Apéndice B se incluye el Atlas de discos de CALIFA donde se incluyen un total de 350 fichas (sólo 10 en la versión en papel de esta Tesis) que muestran los gradientes de brillo superficial, color y metalicidad de gas para cada galaxia. Las principales propiedades físicas derivadas así como la clasificación de los perfiles realizada en §5 también se incluyen en las Tablas B1 y B2 de este apéndice. En el apéndice C se ofrece una lista actualizada de publicaciones en las que he participado.

Esta Tesis se presenta como una recopilación de artículos. En particular, el trabajo presentado en §3 ha sido publicado en la revista Astrophysical Journal (2012, Volumen 754, A61), mientras que el de §4 se ha publicado en la revista Astronomy & Astrophysics (2013, Volumen 559, A114). El análisis presentado en §5 se publicará en breve en Marino et al. (2015, enviado). Con el fin de facilitar la comprensión de estos Capítulos y ponerlos en contexto dentro de los objetivos generales de la Tesis, cada uno de ellos incluye una breve introducción que ofrece información básica sobre los temas abordados más adelante en los artículos correspondientes. Por último, todos los Capítulos van precedidos de un breve resumen en español. También se proporciona una traducción completa al español de la Introducción y de las Conclusiones.

---

[3] `http://cigale.lam.fr/`

1

Introduction

1.1 The chemical composition of galaxies as testimony of their evolution

Our vision of the Universe, from the simplicity of the Big Bang to the complexity observed in present-day galaxies, has been changing dramatically in the last decades and it is under continual refinement thanks to the advances in observational technology and computational resources.

The road to our present-day understanding of galaxies has been a certainly long one. It was not definitively known until 1920s that galaxies exist outside of the Milky Way galaxy. The prevailing view until then was that the Universe consisted of the Milky Way and a presumed void of space beyond. Four hundred years ago, Galileo Galilei turned his telescope to the Milky Way and discovered it to consist of countless faint stars not visible to the naked eye. About 150 years later, the philosopher Immanuel Kant speculated that gravity should act between stars in the Milky Way in the same way that gravity is responsible for the motions of the planets in the Solar System, and that other observed nebulae might be similar but extremely distant “island universes”. It has been now over 90 years since the so-called *Great Debate* between Harlow Shapley and Heber Curtis that tried to establish the real nature of gaseous nebulae. The debate was finally settled by Edwin Hubble in 1923, who measured the distance to Andromeda using Cepheids and therefore proved that they are, in fact, entire galaxies outside our Milky Way (Hubble 1925). Since then the concept of these being galaxies or “island universes” located beyond our Milky Way began to spread. Moreover, is worth to mention that stars were accepted as the dominant form of matter in the Universe until the 1980s, when new theoretical ideas suggested that the dark matter discovered by Fritz Zwicky (1933) might consist of neutral, non-baryonic elementary particles (Cowsik & McClelland 1973; Peebles 1982), and X-ray images showed that most of the baryons in rich clusters are in the form of hot intergalactic gas (Forman & Jones 1982). It now seems clear that baryons are not the dominant form of matter in our Universe, and that stars account for only a small fraction of the baryons (e.g. Fukugita, Hogan & Peebles 1998).

The modern picture of galaxy formation is largely based on the hierarchical Cold Dark Matter model (ΛCDM standard paradigm), which attempts to explain how all the structures we observe today were formed as a consequence of the growth of primordial fluctuations (by gravitational instability) after a period when the Universe was remarkably homogeneous, as confirmed by the Cosmic Microwave Background. According to the ΛCDM model most of the matter in the Universe is in

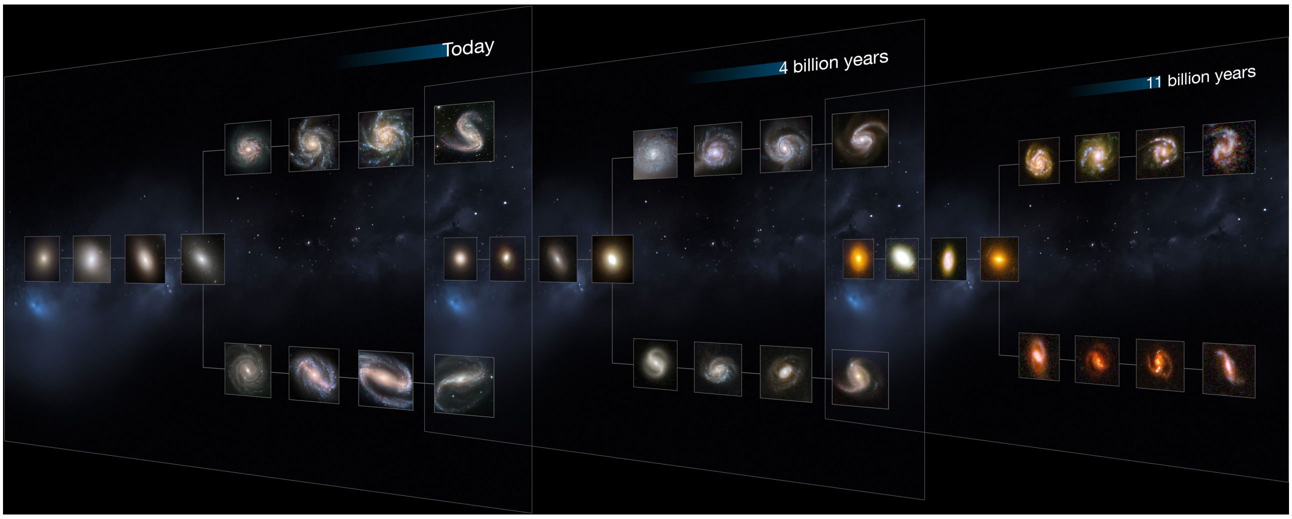

Figure 1.1: This image shows "slices" of the Universe at different times throughout its history (present day, and at 4 and 11 billion years ago). Each slice goes further back in time, showing how galaxies of each type appear. The shape is that of the Hubble tuning fork diagram, which describes and separates galaxies according to their morphology into spiral (S), elliptical (E), and lenticular (S0) galaxies. On the left of this diagram are the ellipticals, with lenticulars in the middle, and the spirals branching out on the right side. The spirals on the bottom branch have bars cutting through their centers. The present-day Universe shows big, fully formed and intricate galaxy shapes. As we go further back in time, they become smaller and less mature, as these galaxies are still in the process of formation. *Credits: NASA, ESA, M. Kornmesser*.

the form of non-baryonic cold matter characterized by non-relativistic velocity, gravitational interactions (collisionless), and cooling process without photons emission (dissipationless). The recent results from the Planck project confirm that our Universe is 13.798±0.037 billion years old, and is made up by 4.82±0.05% of ordinary baryonic matter, 25±4% of dark matter and 69±1% of dark energy (Planck Collaboration et al.2015). Despite significant progress in the recent past on our understanding of the baryonic physics, the formation and evolution of galactic disks remain two of the most important aspects but yet not fully understood topics in extragalactic astronomy. Of particular interest is the fact that, in the ΛCDM current paradigm, galaxies only represent the tip of the iceberg in a Universe dominated by some unknown "dark matter" and an even more elusive form of "dark energy". Understanding the majesty and variety of galaxies in a cosmological context is therefore an important, yet daunting task (Mo, Mao & White 1998, MMW hereafter).

Most of the visible matter in the Universe is concentrated in galaxies, which are the basic astronomical ecosystems in which stars form, evolve and collapse in constant interaction with the interstellar medium (ISM), but also they represent beacons that allow us to explore our Universe over cosmological scales. From the pioneering work of Edwin Hubble (1926b, 1936) who first proposed a classification scheme (the so-called *Hubble tuning-fork*) for galaxies, we know that the Universe is populated by different types of galaxies that are sorted in three general categories according to their observed shape: ellipticals, spirals and irregulars; the former are relatively roundish in shape and are supported almost entirely by random motions and a triaxial shape, while the spirals are flat disks supported almost entirely by ordered rotations. Nowadays, this classification has a more complex taxonomy and it is continuously updated using not only the informations of the optical bands but also the one of other wavelengths. Additional classes of galaxies are low surface brightness galaxies, dwarf galaxies, ultra-faint galaxies, spheroids and galaxies altered by environmental effects. Fig 1.1 illustrates how the Hubble tuning-fork method of galaxy classification looks over different times throughout the Universe's history.

The standard ΛCDM model (Springel at el. 2006) provides a framework in which the formation and evolution of the large scale structure of the Universe can be well understood. However, the formation of disk galaxies has proven to be particularly difficult to understand. In the ΛCDM context, galaxies are dynamically bound systems that consist of a stellar structure embedded in a dark-matter halo that can be formed in a "bottom up" process (or hierarchical clustering) in which smaller units merge and form larger units but actually is unable to describe the evolution of galaxies. It is well known that the current photometric, chemical, and kinematical properties of a galaxy are the results of several mechanisms that have taken place in them, such as the initial conditions under which they formed and also the interplay between internal/secular and external processes. Although is difficult to disentangle the effects of the various contributors, any successful theory for the formation of disk galaxies has to be able to account for all these processes.

The most common type of galaxies in the local Universe are spirals: they make up about 77% of all observed galaxies (20% are ellipticals and 3% irregulars, Li & White 2009). In this Ph.D. Thesis we will pay special attention to the spiral disks within the CALIFA, Calar Alto Legacy Integral Field Area Survey[1] project which seems to be the most frequent galaxy type in the local Universe (see Chapter §4 and §5). Disk galaxies consist of a disk component made up of stars, dust and cold gas (both atomic and molecular), a central bulge component, a stellar halo, and a dark-matter halo. They often reveal spiral arms and a central bar component. Their typical stellar masses are of the order of 10^9 to 10^{12} $M_\odot$, luminosities of 10^8 to 10^{11} $L_\odot$, sizes of 5 to 100 kpc in diameter, rotational velocities of 200-300 km/s and disk scale lengths of about 4 kpc. Their disks can often be separated into a thin and a thick disk component. The thin disk is typically composed of young stars while the thick disk contains significantly less mass and its stars are older, more metal rich and dynamically hotter. Since our own galaxy is a (barred) spiral, most of our understanding of spiral galaxy formation comes from studies of the different components within the Milky Way.

As already mentioned, many aspects of the galaxy formation and especially the formation of spiral galaxies remain unexplained. Historically, two important disk formation scenarios were proposed (see White & Rees 1978; Fall & Efstathiou 1980). The first is a monolithic collapse of a large gas cloud, settling into a rotating disk due to angular momentum conservation (Eggen et al. 1962). The second is the coalescence of smaller progenitors (Searle & Zinn 1978). White & Rees (1978) firstly outlined that the galaxy formation is a two-step process in which disk galaxies form by dissipative contraction within dark-matter halos. On one hand, the dark matter structures grow hierarchically collapsing into individual halos with a certain amount of angular momentum acquired from tidal torques. On the other hand, the gas follows the same dark matter evolution until cooling sets in and enables it to condense into the centers of its host dark-matter halos. Once the gas is condensed into a region small enough for its self-gravity to dominate over the background halo, the fragmentation process starts and stars begin to born within the molecular clouds.

---

[1] `http://califa.caha.es/`

Nowadays, the most popular picture for the formation of disks is the *inside-out* formation scenario (White & Frenk 1991; MMW) that combine spherical collapse and angular momentum redistribution. This scenario predicts a straightforward sequence of events beginning with the formation of an initial bulge due to the high densities and rapid cooling times of the innermost part of a galaxy. Basically, a dark matter halo provides a potential for a rotating protogalactic gas cloud to undergo gravitational collapse. During collapse, the gas cools via radiative processes until it reaches centrifugal equilibrium in the center of the halo. The dark-matter halo gains angular momentum through tidal torques from the surrounding large scale structure. Due to the conservation of angular momentum it collapses to a rotationally supported disk, formed *inside-out*. Stars can already form during collapse due to the compression of the gas by shocks and these will probably form the bulge component of the resulting disk galaxy. Most of the gas, however, is not able to do so and the bulk of the star formation happens once the disk is in place due to the Jeans instability (no balance between self-gravity and thermal pressure in a gas). The conservation of angular momentum also leads to the exponential surface density profiles (Freeman 1970). The semi-analytical model for disk formation proposed by MMW seems to constrain well the connection between disks and their dark-matter halos but sometimes is not able to reproduce some of the observed features of disk galaxies. A quantitative analysis of this model and the different theories of disk formation described above is beyond the scope of this Thesis and the reader is referred to the original papers and/or to the Binney & Tremaine (1987) book for a detailed review.

Qualitatively, according to the *inside-out* scenario, a realistic disk is formed only if the gas retains most of its angular momentum; at the first stage non baryonic halos are formed from primordial fluctuations, then gas cools and condense in these halos. Their main assumptions are: (I) the mass and angular momentum of the disk are fixed fractions of the mass and angular momentum of the dark matter halo; (II) the disk is a thin, centrifugally supported structure with an exponential surface brightness profile; (III) only dynamically stable systems can correspond to real galaxy disks; (IV) the inner structure of the halo is assumed to follow a Navarro Frank & White (1997) density profile; (V) the halo is assumed to remain spherical during collapse. In this context, stars are forming from the gas already during the formation of the disk, triggered by gravitational instabilities leading to the formation of giant molecular clouds (Elmegreen & Elmegreen 1983). Disk stability can be ensured either via pressure, when the local dynamical timescale is larger than the sound-crossing timescale, or via centripetal support quantified as the epicyclic period being smaller than the local dynamical timescale. This is known as the Toomre stability criterion (1964) that establish a relationship between parameters of a differentially rotating, gaseous disk and it can be used to approximate whether the system is stable. This criterion only applies to stability against axisymmetric perturbations and is also used to explain the presence of star formation thresholds in the outer regions of galaxy disks.

The evolution of disk galaxies does not stop after the initial formation and is well know that galaxies experiment the so-called *secular* evolution. The term *secular* refers to the relatively slow dynamical evolution due to internal processes induced by a galaxy's spiral arms, bars, galactic winds, black holes and environmental process. A schematic view of the different processes that drive the galactic evolution is presented in Figure 1.2 (Kormendy & Kennicutt 2004). The secular evolution plays an important role in the evolution of spiral galaxies with major consequences for galactic bulges, the transfer of angular momentum, and the distribution of the galaxy's constituents: stars, gas and

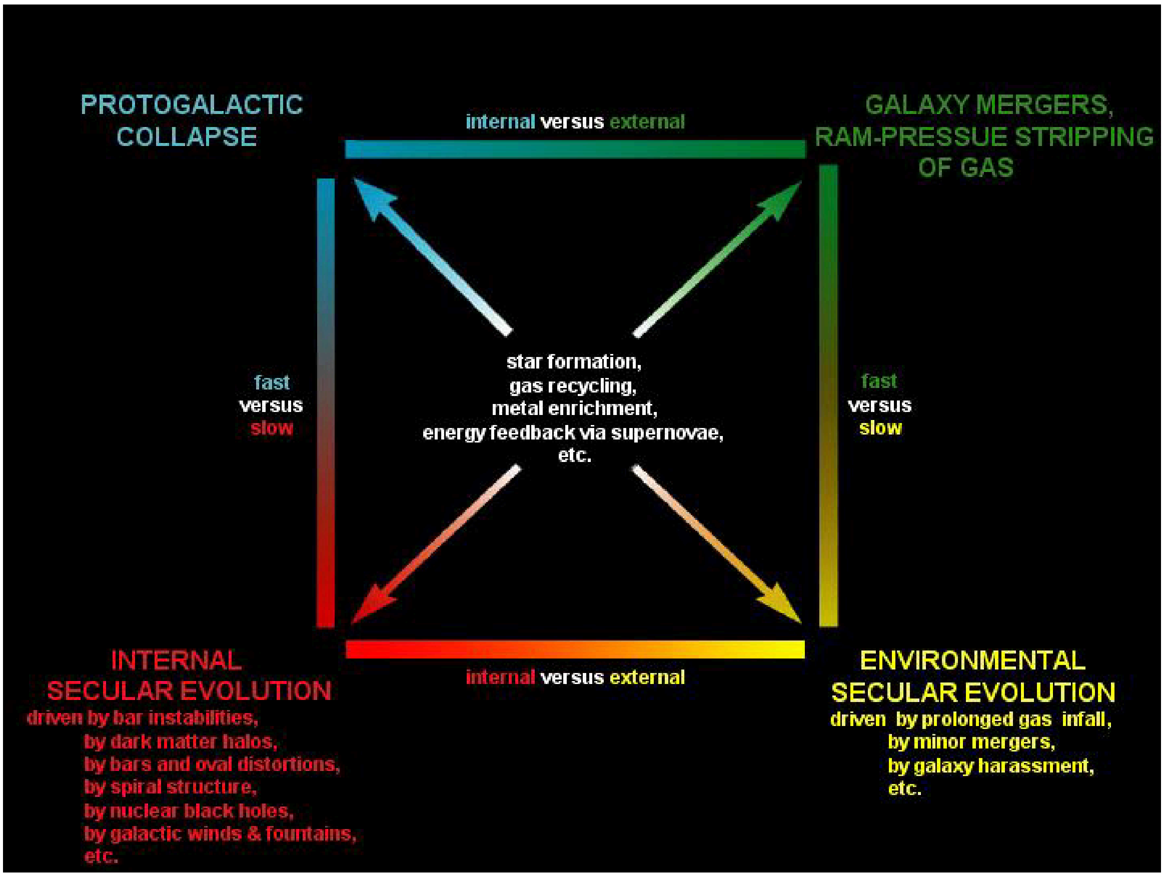

Figure 1.2: Morphological box (Zwicky 1957) of the galactic evolution processes. Updated from Kormendy (1982a), this figure is from Kormendy & Kennicutt (2004). Processes are divided vertically into fast (top) and slow (bottom). Fast evolution happens on a free-fall timescale. Slow means many galaxy rotation periods. Processes are divided horizontally into ones that happen internally in one galaxy (left) and ones that are driven by environmental effects such as galaxy interactions (right). The processes at center are aspects of all types of galaxy evolution. *Credits: Kormendy & Kennicutt (2004)*

dust. Examples for environmental effects are the accretion of gas or satellites in minor mergers or galaxy harassment (close encounters with other galaxies resulting in starbursts, warps or tidal tails). The internal/secular evolution and the environmental effects are in turn the key to understanding and testing cosmological models of galaxy formation and evolution.

Typically, disk galaxies have two dominant spiral arms (the larger amplitude of the different Fourier modes is the one for m=2), which in general are trailing arms (the spiral pattern rotates more rapidly than the stars as the spiral remains inside the coronation radius), that represent the primary sites of star formation. Our sun and solar system are located in one of the Milky way arms. Bertil Lindblad (1925) was the first who recognized that spiral arms are related to stellar dynamics and that they are long-lasting features with an important role in the internal evolution of the disk. Two main theories are proposed in the literature to explain the origin of spiral structure in galactic disks: the density wave theory (Lin & Shu 1964) and the theory of stochastic self-propagative star formation

(Mueller & Arnett 1976). Briefly, the first model is preferred for the so-called "grand design" spirals with well defined, open, highly symmetric and regular spiral arms. The spiral structure is based on a quasi-steady density wave maintained over many rotations of the galaxy. The spiral arms are over dense regions of the disk which move round at a different speed to the stars themselves. Stars therefore do not remain forever in the position that we now see them in, but pass through the arms as they travel in their orbits. The origin of the density wave is not understood completely but the spiral pattern is widely accepted the idea that the most unstable normal mode of a galactic disk are spiral arms and it may have to do with interactions. The second theory is based on the assumption of self-propagating star formation leading to a wave of star formation propagating through the galaxy. The "stochastic" part is because there is also a small probability of random star formation within the disk which keeps things going. The spiral pattern with trailing arms stems from differential rotation in the disk. This theory is more likely to cause "flocculent"[2] spirals with more irregular, asymmetric and subtle structures.

Roughly 30% of nearby spirals are flocculent, 10% are grand design, and the rest are "multi-armed" characterized by two symmetrical arms in the inner part of the disk and outer regions highly branched with many arm's segments. Observations also confirms that isolated spiral galaxies tend to be flocculent while those in dense clusters with increased opportunities for interactions, tend to be grand design. Approximately two-thirds of all spirals are observed to have an additional component in the form of a bar-like structure, extending from the central bulge, at the ends of which the spiral arms begin. The proportion of barred spirals relative to their barless cousins has changed over the history of the Universe. Our own Milky Way has been confirmed to be a barred spiral thanks to the observation performed by the Spitzer Space Telescope of stars in the galactic center. Moreover, some of the predictions of the *inside-out* scenario were observationally tested, among others (I) disk galaxies have flat rotation curves (II) the surface brightness profiles of disks are close to exponential, (III) the outer parts of disks are generally bluer with lower metallicity than the inner parts and populated by younger stars, (IV) the abundance of metals [3] (elements heavier than hydrogen) decreases with the galactocentric distance following an almost universal negative metallicity gradient since the inner regions arrive at the endpoint of their evolution more rapidly than the outer ones. This galactic chemical evolution model makes use of input ingredients (i.e. stellar IMF and yields, metallicity-dependent stellar lifetimes, evolutionary tracks and spectra) and considers the galactic disc as an ensemble of independently evolving concentric rings built by infall of gas of primordial composition (see however Bresolin et al. 2012). In terms of their chemical abundances, the models for the evolution of spiral disks indicate that they become self-enriched very efficiently in a very short period of time, reaching oxygen abundances of $\sim$1/10 the Solar value in only 1 Gyr of evolution (Boissier & Prantzos 1999). In Chapter §3 a detailed discussion of the chemical composition in galaxies is given as an example of one of the several issues that cannot be explained by the *inside-out* growth of galaxy disks. In this regard, many nearby spiral disks show that, while the color and metallicity gradients of the inner disk

---

[2] Flocculent refers to the "fleecy" appearance of the spiral-like structures

[3] In astronomy, all chemical elements heavier than helium are collectively termed "metals". The nuclear reactions during the first three minutes of the Universe (the epoch of primordial nucleosynthesis) produced primarily hydrogen (75%) and helium (25%), with a very small admixture of metals dominated by lithium. All other metals in the Universe were formed at later times as a consequence of nuclear reactions in stars.

are compatible with the *inside-out* scenario, beyond the star formation (SF) threshold radius (where SF rate drops sharply) the gradients flatten and even reverse getting redder and more metal rich toward the outer regions with different mechanisms being proposed (Bakos et al. 2008; Sánchez-Blázquez et al. 2009; Vlajic et al. 2009, Marino et al. 2012; Blanc et al. 2013).

Over the past decade, the study of the evolution of galaxies in the local Universe has been traditionally restricted to the photometric analysis or, alternatively, the analysis of long-slit or single-fiber spectra. The advent of Multi-Object Spectrometers (MOS) and Integral Field Spectroscopy (IFS) instruments with large fields of view (FoV) now offers us the opportunity to undertake a new generation of emission-line surveys in an increasingly large number of star-forming galaxies both locally and at high redshift. This novel approach is being implemented in a new series of ambitious IFS surveys around the world and have led to a significant progress in the study of nearby disk galaxies. Through the huge success of IFS techniques combined with images covering a wide wavelength range from the ultraviolet to the infrared (mainly from GALEX, SDSS, 2MASS, Spitzer, Herschel), we can now add another dimension to the study of nearby disks obtaining an authoritative description of galaxies. The unprecedented quality and depth of these datasets have allowed to reach the outer edges of disks, where the predictions of the simple *inside-out* model outlined above could face its most severe challenges and thanks to the availability of these new observing facilities we are able to infer the radial-dependence of several physical properties in numerous systems. Many important topics in astrophysics involve the physics of the ionized gas. Thus, H II regions are ideal places to trace the chemical composition, structure and distribution of those heavy elements relative to hydrogen that are responsible for forbidden and recombination and fine-structure lines. In the case of the study of nebulae (both Galactic and extragalactic H II regions), it has now become clear that the use of a bi-dimensional data is critical to obtain precise answers to the problems that these fields are facing. Some of the topics that can be addressed include: (1) the distribution of H II regions is an excellent tracer of recent massive star formation in spiral galaxies that shows to be strongly concentrated into the spiral arms. (2) The interpretation of their emission line spectra can reveal details on the formation of the first generation of stars and the formation of the heavy elements in the young universe.(3) The detailed bidimensional analysis of the physical properties of these ionized-gas regions can give us important clues on the mechanisms responsible for the formation of galaxy disks and is one of the fundamental parameters testimony of their evolution. (4) H II regions represent the fossil record of the formation history in a galaxy because they reflect the amount of gas that has been reprocessed by stars and exchanged with its environment over its lifetime.

As discussed in Chapters §3, §4 and §5, the depth and spatial resolution of the IFS spectroscopic observations described in this Thesis have allowed study not only of the global metallicity of galaxies but also of the variation across galaxies and the abundance discrepancies among different phases of the ISM and between these and the distribution of the star light. Throughout this work, I adopt the oxygen abundance as a tracer of the overall gas phase metallicity and use the two terms interchangeably.

1.2 Aim and Structure of this Thesis

In order to shed more light on the mechanisms that rule the chemical evolution of galaxies, this Thesis is focused on the spatial resolved analysis of the chemical abundances of the extragalactic H II regions. We have analyzed not only the global metallicity (and also extinction as a measure of this and of dust geometry) of galaxies but also the variation across galaxies and the abundance discrepancies among different phases of the ISM. In addition, we have compared these with the abundance of the stars paying special attention to the outer edges of disks. These ionized-gas regions represent perfect laboratories for deriving chemical abundances in the local Universe as they are powerful tools for understanding the physical properties and chemical evolution of the ISM in galaxies. In particular, in this dissertation I will use the IFS data belonging to the ongoing CALIFA Survey to test, confirm and extend previous results on metallicity gradients, while at the same time with this unprecedented dataset I will be able to better constrain the predictions coming from the theoretical models or to check and strengthen the diagnostic methods used to measure metallicities. The key questions I faced in this work are the following:

1. **How old are and how did spiral galaxies chemically evolve?** Are they growing *inside-out* as proposed to explain the color and metallicity gradients in our own Milky Way? If an universal gradient exists, how we can explain all the deviations (in metallicity but also in color) recently measured in the outskirts of several nearby disks?

2. **Are the different empirical calibrations applied to the extragalactic H II regions Universal (i.e. valid at low and high redshift)? Do they depend on the diagnostic method used?** It is well known that there are several techniques in the literature to derive gas metallicities of H II regions from their emission lines. With our unprecedented CALIFA spectroscopic dataset combined with literature data we made up the most ambitious compilation of H II region data with measurable auroral line fluxes that allows us to test the scatter of the most widely used empirical abundance calibrations.

3. **Is it possible to conciliate the light and abundance profiles features within a self-consistent scenario?** Several recent studies confirms the presence of breaks in their surface brightness and color profiles but is still unclear if a connection exists between these and the oxygen properties of the regions beyond that break radius.

Addressing these open questions is a first step for future detailed studies that can be only faced with the use of the new generation IFUs, such as MUSE or MEGARA. In that regard, this work can be also considered as a necessary preparatory step needed to fully exploit the capacities of these new, and certainly revolutionary, tools in terms of efficiency and spectral resolution.

The structure of this Thesis is as follows: In §2, I discuss the importance of IFS observations in astrophysics, including an introduction of the different techniques with their advantages and drawbacks, a brief review of the most important IFU (Integral Field Unit) surveys is also provided in this Chapter with special attention to the largest IFU projects up-to-date in which I am deeply involved:

PPak-CALIFA (*Calar Alto Legacy Integral Field Area Survey*) and MEGARA (*Multi-Espectrógrafo en GTC de Alta Resolución para Astronomía*). A summary is provided of the work made within the CALIFA and the MEGARA collaborations as the morphological classification of the CALIFA mother sample or the more technical phases of the data reduction and quality-control procedures in which I was deeply involved. In §3, I present the full bi-dimensional spectral cube analysis of the nearby spiral galaxy NGC5668. Combining the IFU data with panchromatic broad-band images the radial profiles and colors were obtained and compared with the chemo- spectrophotometric evolutionary models. The study of the properties of the H II regions within NGC5668 led to the discovery of a bar in its formative stages that produced an unusual flattening in metallicity gradient suggesting that not all galaxies follow the smooth growth prediction of the *inside-out* scenario for the formation of disks. Chapter §4 dealt with my re-derivation of the most widely used empirical oxygen calibrations based on the most comprehensive compilation to date of both CALIFA data and the T_e-based measurements from the literature. This novel approach makes use of an unprecedent set (∼4000) of H II regions and allows us to derive the most accurate calibration for external galaxies to date for both the O3N2 and N2 single-ratio indicators, in terms of all statistical significance, quality, and coverage of the parameters space. This study was a necessary preparatory work before the analysis of NGC5668 could be extended to a statistically-significant galaxy sample. In §5, I address for the first time a combined analysis of the metallicity gradients obtained from CALIFA with the surface brightness and color profiles from the Sloan Digital Sky Survey (SDSS). The detailed analysis of 350 CALIFA disk galaxies confirms the presence of U-shaped color profiles in the outer parts of the vast majority of the sample and a corresponding flattening in the ionized-gas metallicity gradients for the same radial ranges. Some planned paths of future research are posed in §6 where is outlined the comparative study of the 2D distribution of ionized-gas and dust and their properties using a sample of galaxies extracted from the Herschel Galaxy Reference Survey and that are being observed using the PPak IFU. In particular, the joint analysis of the stellar-continuum and ionized-gas attenuation allow us to investigate potential variations in the relative geometry of young stars and dust or in the extinction curve within different environments. I also analyze the relation between the dust surface density and temperature with the (population synthesis based) stellar mass density and continuum attenuation as given by the CIGALE[4] code for a pixel-by-pixel analysis applied to the normal star-forming galaxies. Finally, the general conclusions of this dissertation are summarized in §7.

Additional material not included in the main body of the Thesis is provided in the three final appendices. In Appendix A we present the largest accessible database of H II region emission-line data ever accomplished, including a compilation of 603 H II regions with accurate measurements of the electron temperature. In Appendix B the CALIFA Atlas of Disks is displayed comprising 350 fiches showing the gas metallicity, surface brightness and color profiles of every single galaxy. The main physical properties derived and the disk classification performed in §5 are also listed in Tables B1 and B2. In appendix C an updated list of publications is provided.

This dissertation is presented as a compilation of papers. In particular the work presented in §3 has been published in the Astrophysical Journal (2012, Volume 754, A61) while the one of §4

---

[4] `http://cigale.lam.fr/`

was published in the Astronomy & Astrophysics journal (2013, Volume 559, A114). The analysis presented in §5 will be soon published in Marino et al. (2015, submitted). In order to facilitate the comprehension of these Chapters and put them into general context of the Thesis, each one includes a brief introduction that provides some basic information on the subjects addressed later in the papers. Finally, all Chapters are preceded by a brief summary in Spanish. A complete translation to Spanish of the Introduction and Conclusion Chapters is also provided.

2

3D Spectroscopy in Astronomy: from CALIFA to MEGARA

Resumen

Tradicionalmente, el estudio de las propiedades de los discos de galaxias espirales se ha basado en el uso de imágenes en diferentes bandas fotométricas (cubriendo un rango amplio de longitudes de onda pero a menudo únicamente en el óptico e infrarrojo) y, en el mejor de los casos, espectros de rendija o de fibra única abarcando una parte muy pequeña de la extensión de estos discos.

Esto ha cambiado radicalmente con la disponibilidad de las primeras Unidades de Campo Integral (IFUs) en telescopios de la clase 4m durante la última década, con las que se empezaron a llevar a cabo las primeras exploraciones sistemáticas de galaxias externas en espectroscopía 3D: SAURON, ATLAS^{3D} y más recientemente CALIFA. A pesar la limitada apertura de los telescopios en los que estos instrumentos están instalados, lo ambicioso de sus proyectos observacionales les ha permitido marcar un camino para el estudio de las propiedades actuales y, a partir de estas, de la evolución pasada de las galaxias cercanas.

Lo exitoso de estos proyectos ha llevado a implementar proyectos aún más ambiciosos tales como el *Sydney university AAO MOS IFU* (SAMI) o el *Mapping Nearby Galaxies at APO* (MaNGA, IP: Kevin Bundy) ambos en telescopios de no más de 2.5 metros de diámetro. Esta limitada capacidad colectora ha llevado también a sacrificar la resolución espacial de muchos de estos instrumentos o su resolución espectral. Esto es algo que se se está solucionando ya mediante el uso de una nueva generación de IFUs tales como MUSE en el VLT o MEGARA en el telescopio español GTC, el más grande del mundo con un espejo de 10.4m de diámetro.

En este capítulo se presenta un sumario de las principales exploraciones en desarrollo y proyectadas para el estudio de las galaxias cercanas, con especial enfasis en las que estoy involucrada, CALIFA, cuyo aprovechamiento científico constituye el núcleo de esta tesis, y MEGARA, en cuyo desarrollo como instrumento he participado activamente durante estos últimos años y que fue diseñada para resolver todas aquellas cuestiones relacionadas con la evolución de los discos de galaxias que la instrumentación actual no es capaz de responder de forma precisa.

Obviamente, el uso de este tipo de instrumentos de alto multiplexado implica una gran complejidad en el procesado y análisis de los datos que proporcionan. Debido a ello también se hace una descripción detallada de estas peculiaridades (ventajas en muchos casos) asociadas al uso de datos de espectroscopía 3D, ya sean de CALIFA o de MEGARA en un futuro cercano.

2.1 Introduction

This Chapter is devoted to review the challenges of, and opportunities for, Integral Field Spectroscopy (IFS), and how these have led to new and different approaches to study nearby galaxies. For this purpose, a brief history of the development of IFS technique and instruments for ground and space based telescopes. Special attention is given to CALIFA, the Calar Alto Legacy Integral Field Area Survey (`http://califa.caha.es/`) and MEGARA, Multi-Espectrógrafo en GTC de Alta Resolución para Astronomía (`http://guaix.fis.ucm.es/megara`), two of the largest IFU (Integral Field Unit) projects up-to-date that represent the "alma mater" of this Thesis.

Our understanding of the physical processes that are taking place in galaxies has greatly improved in recent years thanks to the availability of new observing facilities that have allowed an efficient mapping of relatively extended nearby objects in a very efficient way and at different wavelength ranges with a spatial resolution of only a few arc seconds: NASA's GALEX SMEX mission in the Ultraviolet (Gil de Paz et al. 2007), Spitzer in the mid-infrared (e.g. SINGS; Kennicutt et al. 2003), and Herschel in the far-infrared (e.g. KINGFISH Herschel Key Program; Kennicutt et al. 2011) using the PACS and SPIRE instruments. In particular, these unprecedented sets of data have allowed us to get insights the properties of dust, gas and star formation in galaxies. A substantial instrumental effort has been done in the past decade with the aim to obtain high-spatial resolution spectroscopy with slits (e.g. STIS on HST, Woodgate et al. 1998), or with integral field spectrographs (IFSps) but with very small fields of view (FoV, e.g. TIGER and OASIS on the CFHT; Bacon et al. 1995, 2001b). Moreover, studies focused on the large-scale kinematics of galaxies traditionally make use of long-slit spectra obtained along at most a few position angles (e.g. Davies & Birkinshaw 1988; Statler & Smecker-Hane 1999). These studies rely on conventional observing techniques: they combine good-resolution broadband frames in different bands (to spatially isolate the different stellar populations and map the dust distribution), with narrow band imaging (needed to map the gas distribution, isolate the starburst regions, and derive their physical properties) and spectroscopy data (to derive the internal extinction, compute physical parameters and chemical abundances of the gas, and remove the contribution from emission lines); at most through a sequence of long-slit spectra sweeping the regions of interest.
Therefore, these studies require a great amount of observing time; besides, varying instrumental and atmospheric conditions make combining all the data together quite complicated. Long-slit spectroscopy has the additional problem of the uncertainty associated to the precise location of the slit and so the long-slit spectra are too limited to be useful for modeling and interpretation and have generally been used only to discuss the properties of emission lines. Long-slit spectroscopy lacks the essential two-dimensional information for decomposing the spatial flux distribution, and loses most of the source flux for a diffraction limited slit width and moderate atmospheric dispersion. In addition, flexure within the instruments complicates the acquisition of objects, and it is difficult to keep the object in the slit for long integration times. Besides, long-slit spectroscopy suffer from wavelength-dependent slit-losses due to differential atmospheric refraction (DAR). In these cases, what is really required is the ability to record a spectrum from each part of an extended object. This cannot be done with a long-slit (except by stepping the slit across the target by moving the telescope and recording separate exposures for each position and this is obviously very time-consuming). IFS attempts to solve the main disadvantages of traditional long-slit spectroscopy described above. These include

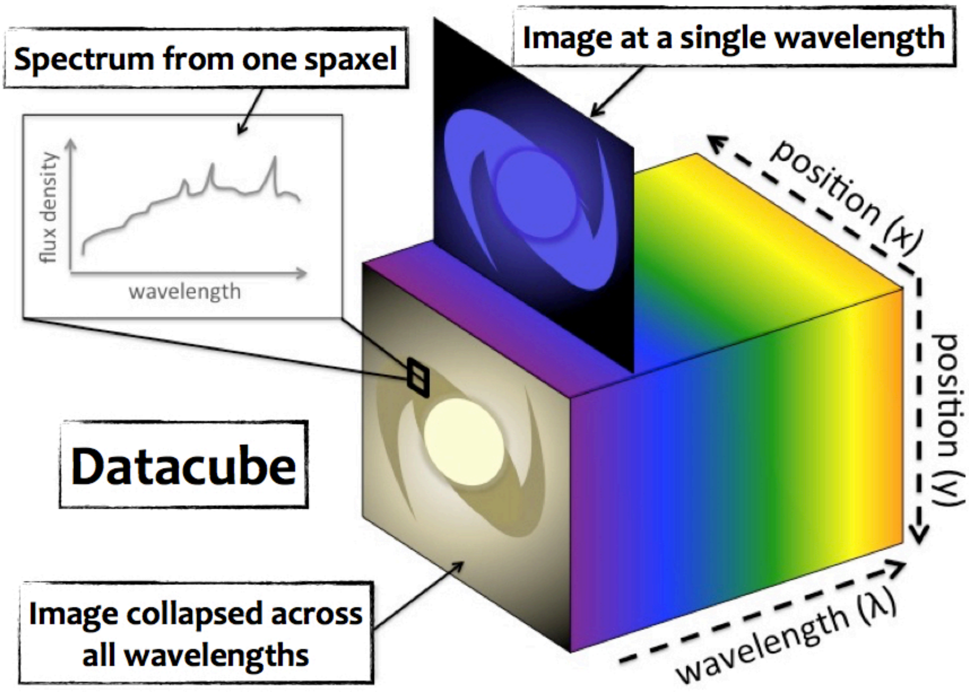

Figure 2.1: Schematic diagram of a datacube. A datacube provides information in three dimensions: two spatial dimensions (i.e., an image in [x,y]) and a third dimension of wavelength (λ). It is therefore possible to obtain an image of the target at a single wavelength or collapsed over wavelength slices. Furthermore, at every spatial spaxel of the datacube a spectrum can be extracted.

making poor use of the incident light when the object is extended, either intrinsically or due to poor seeing. Other techniques aim at deviating some of the limitations of long-slit spectroscopy, such as the Fabry-Perot scanning. This technique allows the observation of a large object in a single exposure but only at a single wavelength (which for very extended objects changes with the position of the source in the field) so that the full wavelength coverage is achieved via a series of exposures. As with stepped long-slit spectroscopy, this is an inefficient use of telescope time, at least in the case of nearby galaxies where the exquisite spatial resolution provided by these instruments might not be that critical.

Since the early 1980, the desire to simultaneously acquire spectral and spatial information in a single exposure under identical observing conditions motivated various groups to develop IFSps for astronomical telescopes. At same time, great deal of work was done in optical labs in an attempt to understand how the optical fibers, micro lenses and image slicers behave. The first astronomical spectrum through a fiber was taken in 1978 and the first fiber-optical multi-object spectroscopy (MOS) was performed using the Steward Observatory 2.3 m telescopes one year later (Hill et al. 1980). Almost at the same time Vanderriest (1980) used the design flexibility offered by optical waveguides to build the first fiber bundle prototype, which was installed at the Mauna Kea 2.2 m telescope. During those years it was more than doubtful whether this technique was going to be useful at all due to the fact that the scientific outcome was somewhat limited. It is worth mentioning that the topic of IFS had gained considerable momentum in the 1990s after superseding the initial phase of prototypes when a first generation of common user 3D spectrographs emerged at 4 m-class telescopes.

Historically, various designations have been invoked to describe IFS (area/imaging/2D/3D spectroscopy, etc) that basically consist of storing both spectral and spatial information simultaneously. Despite its relatively short history, 3D spectroscopy offers to the scientific community a new way to tackle astrophysical problems, and opens up new lines of research. We define integral field (3D) spectroscopy as an astronomical observing technique that creates a single exposure spectrum of (typically many) spatial elements (spatial pixels commonly shortened to "spaxel" this term, first introduced by the Euro3D consortium[1] is being used to differentiate between a spatial element on the IFU and a pixel on the detector) simultaneously over a two-dimensional FoV on the sky. The optical elements that accomplish the sampling of the sky are often called integral field units (IFUs), and thus IFS is also sometimes calles "IFU spectroscopy". Spaxels can have different shapes and sizes, depending on instrumental details and the type of IFU. Owing to this sampling method, each spaxel can be associated with its individual spectrum as shown in Figure 2.1. Once all of the spectra have been extracted from the detector frame it is possible to reconstruct maps at arbitrary wavelengths. The spectra can be arranged in a three-dimensional array which is most commonly called a "datacube". As spectroscopy involves one dimension per se (the wavelength scale), two-dimensional spectroscopy would arguably also describe the situation correctly. However, the datacube picture and the perhaps more "sexy" "3D" label have conventionally led to the now accepted terminology of tridimensional spectroscopy, which is adopted throughout this Thesis.

IFS data can be stored using different data formats. The raw data from an IFS observation usually consists of multiple of spectra laid out on the detector, each originating from an individual element of the IFU. There is a special data format for transportation of reduced 3D data different from the seemingly simple application of the standard FITS (a widely spread data format in the astronomical community all over the world) NAXIS=3 format, which actually has emerged from radio astronomy, where datacubes are a natural data product (Wells et al.1981). The peculiar virtue of IFS consists in the ability to create an individual spectrum for each spaxel simultaneously over the whole FoV. Thus, the final output of the data reduction processing is usually a set of row-stacked spectra (RSS hereafter). This data format consists mainly of a binary table, were the position of the spaxels on the sky are stored on the same row as the associated spectra. Datacubes are only valid to store reduced data from instruments that sample the sky-plane in a regular-grid (of rectangular spaxel) or for interpolated data. In that case the data are stored in a 3D FITS image, were the x and y axes stand for the two spatial dimensions, and the z axis corresponds to the dispersion axis. RSS format, however, is a 2D FITS image where the x and y axes contain the spectral and spatial information regardless of their position in the sky. It requires an additional file (a FITS or ASCII table), were the position of the different spatial elements on the sky is stored. The RSS format is widely used by IFUs where spectra are well-separated on the detector (i.e. not continuos such as in fiber spectrographs). The data reduction steps for an IFS observation are rather similar to those applied to other spectroscopic modes. IFUs have a

---

[1] `http://www.aip.de/Euro3D/`

few rather special requirements, however, notably for flat fielding and mapping data from 2D to 3D. Nowadays, more effort is dedicated to refining techniques for reducing, analyzing and interpreting the data obtained with 3D spectrographs. An example of the critical steps required to produce data ready for analysis is addressed in Section 2.4 where a comprehensive description of PPak (Verheijen et al. 2004) data is presented. IFS has a number of unique advantages over traditional observational techniques, which can be summarized as follows:

1. **Pointing:** This a posteriori advantage IFU is based on the fact that an IFU within its useful FoV has no physical aperture, so that there is no need to accurately center a given target of interest.
2. **Absence of slit effects:** These are essentially light losses caused by the finite width of a spectrograph slit. The severeness of the effect is a function of seeing FWHM in relation to the slit width (Jacoby & Kaler 1993), and a function of wavelength. 3D spectrographs based on the micro-pupil principle are totally unaffected by this problem, which is why these instruments are superior tools to measure subtle velocity field variations on small scales.
3. **Atmospheric refraction:** This effect is due to dispersion in the atmosphere, which causes a different angle of deflection as a function of wavelength for rays at oblique angles of incidence, i.e. for objects at airmass > 1 and depends on air temperature, pressure and relative humidity (Filippenko 1982). The net effect in a IFU translates merely into a shift in [x,y] as a function of wavelength, however no flux is lost due to light falling outside an aperture.
4. **Spatial binning:** From direct imaging data it is known that poor S/N in regions of low surface brightness can be improved by binning pixels, which contain more signal, and hence better S/N. Also in the case of the 3D spectroscopy we can co-add groups of spaxels with the same level of S/N through the use of a Voronoi tessellation which gives a gain scales that follows the square-root of the number of spaxels, this technique is also called “adaptive binning” (Cappellari & Copin 2003).
5. **Differential spectrophotometry:** 3D spectroscopy is the ideal method to perform spectrophotometry. Provided the observer is in the position to find a secondary or tertiary flux standard near the position of the target, one can apply the technique of “differential spectrophotometry”, analogous to the development of differential photometry (Barwig et al. 1987). This would make possible to continue observing even through thin clouds and compensate for transmission variations through the simultaneous observation of the standard star.
6. **Crowed field 3D spectroscopy:** Spectroscopy of individual sources embedded in densely populated stellar fields, or in bright nebular emission, or in a combination of both is a notoriously difficult undertaking, where the precise subtraction of the background component is often a challenge. Using the established techniques of PSF-fitting CCD photometry, it has been shown that the same methods applied to datacubes yield superior results when trying to disentangle point sources from a bright background (Roth et al. 2004).
7. **Ultra-deep faint object 3D spectroscopy:** Thanks to the advantage of their 2D FoV, a new generation of dedicated faint object 3D spectrographs, such as MUSE for the ESO-VLT, soon

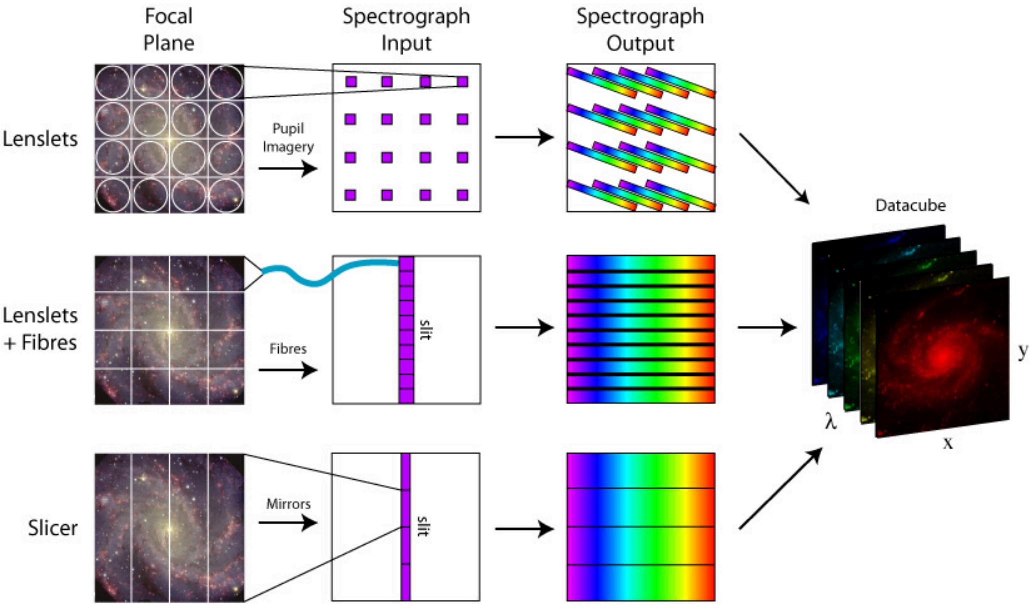

Figure 2.2: Cartoon illustration showing how the three major designs of present-day IFUs - a lenslet array (top), fiber (middle) and slicer (bottom) - sample the plane of the sky and the locations of the spectra along the 2D detector. *Credits: J. Allington-Smith.*

will give us the deepest views into the Universe ever obtained by carrying out unprecedented blind spectroscopic surveys.

In particular, we would highlight that IFS is the ideal observational technique to study nebular objects (e.g. external galaxies): each single exposure contains both spatial and spectral information in a large area of the galaxy, so in just one shot we collect information for all regions. Besides, the kinematical information also allows us to investigate what mechanisms trigger star formation as well those processes that cause rapid gas inflow or outflow and the movement of stars through spiral arms. In terms of observing characteristics, IFS provides simultaneous data for all spatial resolution elements under the same instrumental and atmospheric conditions, which guarantees a greater homogeneity of the data set. This makes 3D spectroscopy of stars and gas essential for understanding their formation and evolution and, depending of the spectral resolution of choice, also for deriving the dynamical structure of these systems.

2.2 3D spectroscopy instrumentation and techniques

The essence of an IFS lies in the coupling of two components: an IFU and the spectrograph. The purpose of an IFS is to acquire spectra over a two-dimensional area of the sky, where for each spatial location (or dissecting element) a spectrum is produced. The job of the IFU is to divide the 2D spatial plane into a continuous array or pseudo-slit. There are different methods of dissecting the FoV into spaxels (namely optical fiber bundles, lens array, optical fibers coupled to lens array or slicers) as described below and illustrated in Figure 2.2.

1. **Lenslet array:** The suggestion to use lens arrays for astronomical observations goes back to Courtès (1960), however it took quite a while until its implementation with TIGER, the first prototype of 3D spectrograph lens array-based. The basic concept consists of pupil-imaging spectroscopy using lenslets and the image of the telescope is projected onto a microlens array. At first glance, the lens array has one significant advantage: the absence of large gaps between the spaxels. Lens-array IFUs can, in principle, accommodate a large number of spaxels at the expense of wavelength coverage, therefore they are superior devices for high spatial resolution studies of objects on small scales. Thanks to the micropupil principle[2], the telescope focal plane is decoupled from the detector, which is a significant advantage for precision spectroscopy. The compact geometry of the spectra allows for compact opto-mechanical designs and also for highly efficient optical systems. A certain drawback of lens-array IFUs is the presence of diffraction and optical aberrations causing crosstalk between neighboring spectra, which occurs at different wavelengths (Lee et al. 2001; Roth et al. 2005). This undesirable effect, however, can largely be corrected for by software in the process of data reduction.

2. **Fibers (with or without lenslets):** Optical fiber bundles were the first and most simple technology to build up IFUs and this is currently the most common technique in use. The input image is formed at the entrance to a 2D bundle of optical fibers which transfer the light to the slit of the spectrograph. The flexibility of the fibers allows the round/rectangular FoV to be reformatted into one (or more) "slits", from where the light is directed to the spectrograph, and the spectra are obtained without wavelength shifts between them. There are a few problematic fiber properties, which, however, with proper care and a suitable design, can be handled fairly well. One of the more serious drawbacks for certain applications, especially when high spatial resolution is intended, is the non-contiguous sampling due to inevitable gaps in the bundle. A negative attribute of this coupling method is that the fibers do not work efficiently at low focal ratios resulting in focal ratio degradation (FRD), this can be overcome by placing an array of contiguous lenslets in front of the fibre bundle in order to focus all the light collected by that lenslet into the fibre (lenslet shapes are usually square or hexagonal and thus can be packed contiguously) simultaneously changing the focal ratio entrance to values close to F/3. One prominent example of fiber-based IFU is the Postdam Multi-Aperture Spectrophotometer (PMAS) at Calar Alto 3.5m telescope that will be described in detail in Section 2.4.

3. **Image-slicer:** Images-slicers have been around for a long time, primarily serving the high-resolution community, especially at NIR wavelengths. Indeed the slicer technique as a relatively small optical element is well-adapted for operation in a cryostat at low temperatures and allows for an overall compact opto-mechanical design. The input image is formed on a mirror that is segmented in thin parallel sections, sending each "slice" in a slightly different directions. These thin mirrors ultimately act as slits, or, in other words, as spaxels, dissecting the focal plane into narrow and long strips. A second segmented mirror is arranged to reformat the slices so that, instead of being above each other they are now laid out end to end to form the slit of the spectrograph. The advantage of this technique is that FRD is avoided and the slicing arrangement gives contiguous coverage of the field (is one spatial dimension) at potentially

---

[2] Instead of imaging the dispersed spaxels of the IFU, it is the microscopic entrance pupil behind each lenslet of a lensarray which is imaged onto the detector (hence the term "micropupil")

> high spatial resolution. Because this system uses only mirrors, it is especially suitable for the infrared since it is inherently achromatic and can be cooled to cryogenic temperatures. A potential disadvantages is that the optical system might be bulky and difficult to fabricate, especially if aimed at observing at the very demanding wavelengths below 5000−6000 Å. One of the most recent developments for the ground is MUSE, Multi Unit Spectroscopic Explorer, a dedicated faint object 3D spectrograph for the ESO-VLT.

In this dissertation I will focus my attention in the description of two fiber-feed IFUs: PPak and MEGARA. As discussed before, IFS optical observations with fibers are based on the idea of connecting the focal plane of the telescope with the spectrograph slit using a fiber bundle. In this way, when an extended object is observed, each fiber receives light coming from a particular region of the object. Each individual spectrum appears well separated on the detector; therefore, spatial information and spectral information are collected simultaneously. The wavelength limitations essentially depend on the characteristics of the spectrograph itself. The spatial resolution depends on the fiber sizes and the prevailing seeing conditions during the observation. The spatial coverage of the fiber systems is relatively small (for a counterexample see LeFévre et al. 2003), but they are very useful in the study of the small-size objects, such as the circumnuclear region of nearby active galaxies, blue compact dwarf galaxies, or gravitational lenses, as well for individual H II regions.
The early history of IFS, as discussed above, included the very first prototypes that quickly let to a first generation of facility instruments for 4m class telescopes. The latter have represented a significant step towards establishing 3D spectroscopy as a common user technique. In the late 1990's the light collecting power, superb image quality, and demand for new instrumentation of new 8−10m class telescopes prompted yet another generation of IFS, some of which were designed as IFUs in the original sense[3], i.e. add-on modules in front of conventional slit spectrographs. In the last few years investment in this type of instrumentation has been enormous and large telescopes all around the world are now equipped with IFU. In Table 2.1 a compilation of current, upcoming, and decommissioned, together with a summary of their characteristics is presented. These instruments are usually coming with their own data reduction pipeline, which is an important pre-requisite to open this non-trivial observing technique to the common user. Several IFS systems have become operational in ground-based and space telescopes as common user instruments over the past few years. Most of these systems are installed in large 8−10m class telescopes (and even in space; PACS@Herschel, NIRSpec@JWST see below) and are becoming a standard observational technique for almost all areas of astrophysical research. The most prominent new developments for the ground are MUSE (Bacon et al. 2004) as a 2nd Generation VLT instrument, and MEGARA (Gil de Paz et al. 2012) the future optical MOS and IFU for 10.4m GTC that will be described in detail in Sec. 2.5.

Briefly, MUSE (`http://www.eso.org/instruments/muse/`), a panoramic IFS, operates in the visible wavelength range from 0.47 to 0.93 μm at a resolution (R) of 2000−4000. Its main operating mode is the wide field mode combining IFS over a relatively wide field of view (1 arcmin^2) with sub-arcsec spatial resolution (0.3" to 0.4" FWHM). MUSE will also have a narrow field mode providing adaptive optics, extremely high angular resolutions (0.03" to 0.05" FWHM) over a small field of

---

[3] Multi-object spectroscopy (MOS) is similar to IFS, however, MOS is a technique designed to obtain spectra of multiple, separated (usually small) targets over a large FoV. Multi-object 3D spectroscopy is a major path for future instrumentation; with current designs, this is achieved using slit masks or positionable fibers/lenslets (see e.g. KMOS@VLT).

view (7.5×7.5 arcsec^2). The main scientific driver of MUSE instrument design is the study of the progenitors of normal galaxies out to a redshift of 6 but is also ideal for investigating the properties of low-z galaxies on scales of few parsecs.

Another example of IFU is the PACS Spectrometer (Poglitsch et al. 2010) on board the Herschel Space Telescope (Pilbratt et al. 2010) that is allowing us to explore excitation and cooling in a diverse variety of nearby resolvable environments. PACS operates between 51 and 220 μm with a resolution of $\sim$75$-$300km/s and instantaneous coverage of 1500 km/s, over a field of view of 47"×47". IFS systems will also be installed on board the James Webb Space Telescope (JWST) expanding IFS-based science into the mid-IR wavelength range. The JWST Near-InfraRed Spectrograph (NIRSpec) and Mid-InfraRed Instrument (MIRI) will have integral field capabilities covering the near-IR and mid-IR range in a low background environment. Future extremely large telescopes (diameter of 30 meters, or more) will also include IFS systems as part of the standard instrumentation as in the case of MOSAIC project (Jacoby, et al. 1998). There is, however, an important challenge ahead of us before the power of these systems is fully exploited. These future instruments will produce a huge amount (ten to hundred thousand) spatially separated spectra per exposure. Therefore emphasis has to be made on the development of new sophisticated software tools to automatically handle the calibration of the raw data and to facilitate their subsequent astrophysical analysis.

In the following sections, a brief summary of some recent IFU surveys is presented as well a detailed review of two ongoing IFU projects CALIFA and MEGARA making a special emphasis on my technical and scientific contributions to them, including the developments of some of those control software tools. Note that CALIFA and MEGARA are top priority projects for the GUAIX (`http://guaix.fis.ucm.es/`) group at UCM for which Integral Field Spectroscopy components is leading-edge ultimate driver both in its scientific and technological aspects.

Table 2.1: Compilation of 3D instrumentation. Source IFS WIKI PAGE `http://ifs.wikidot.com/`.

Telescope	Diameter (m)	3D Instrument	Format †	$\Delta\lambda$ (μm)	Max FoV arcsec^2	Max λ $\Delta\lambda$	Max Spaxel size arcsec
AAT	3.9	AAOmega-SPIRAL	F+L	0.37−0.95	11.2×22.4	15000	0.7
		AAOmega-SAMI	F	0.37−0.95	15×15	13000	1.6
ANU	2.3	WiFeS	IS	0.3−0.7	25×38	7000	0.5
APO	2.5	MaNGA	F	0.36−1.03	3°	2500	2.0
Calar Alto	3.5	PMAS-LARR	F+L	0.35−0.90	16×16	2200	1.0
		PMAS-PPak	F	0.35−0.90	74×65	2000	2.7
ESO-VLT	4×8.1	FLAMES	F+L	0.37−0.95	12×7	46000	0.52
		KMOS	IS	0.8−2.5	2.8×2.8	3500	0.2
		MUSE	IS	0.47−0.93	60×60	3000	0.2
		SINFONI	IS	1.10−2.45	8×8	4000	0.12×0.25
		SPHERE	IS	0.95−1.7	1.8×2.5	30	5.1×4.1
		VIMOS	F+L	0.36−1.15	54×54	3000	0.67
GEMINI	2×8.1	GMOS	L	0.4−1.1	5×7	4300	0.2
		GNIRS	IS	0.9−2.5	3.15×4.8	5900	0.15
		NIFS	IS	0.94−2.40	3×3	6000	0.103×0.04
GTC	10.4	FRIDA	IS	0.9−2.5	1.3×1.2	30000	0.02
		MEGARA	F+L	0.36−1.0	12.5×11.3	10000	0.6
Hale	5.0	PIFS	IS	1−5	5.4×9.6	1300	0.167
HJS	2.7	VIRUS-P	F	0.35−0.68	1.7×1.7	6850	4.16
JWST	6.5	MIRI	IS	5−28	7×7	4000	···
		NIRSpec	IS	0.6−5	3×3	3000	···
Keck	2×10	OSIRIS	L	1.0−2.4	4.8×6.4	3800	0.1
Magellan	2×6.5	IMACS	L	0.4−0.9	50×50	10000	0.2
SUBARU	8.3	KYOTO-3DII	L	0.36−0.92	3.6×2.8	1200	0.096
WHT	4.2	INTEGRAL	F	0.37−0.80	33.6×29.4	1800	2.7
		OASIS	L	0.4−1.0	10.3×7.4	4400	0.26
		SAURON	L	0.45−0.70	41×33	4400	0.94
Herschel	3.5	PACS	IS	51−220	47×47	4000	9.4

Notes: † The different coupling methods are expressed with the following formats: Lenslets (L), Fibers (F) and Image Slicer (IS).

2.3 IFU surveys, a panoramic view of galaxy evolution

Much of our recently acquired understanding of the architecture of the Universe and its constituents comes from large spectroscopic surveys (e.g., 2dFGRS, SDSS, VVDS, zCOSMOS, PINGS, SAURON, VIRUS-P among others). Such surveys have not only constrained the evolution of global quantities such as the cosmic star formation rate, but also enabled us to link this with the properties of individual galaxies morphological types, stellar masses, metallicities, etc.
As claimed in Sánchez et al. 2012 (S12 hereafter), the major advantages of this recent generation of surveys are: (I) the large number of objects sampled, allowing for meaningful statistical analysis to be performed on an unprecedented scale; (II) the possibility to construct large comparison/control samples for each subset of galaxies; (III) a broad coverage of galaxy subtypes and environmental conditions, allowing for the derivation of universal conclusions; and (IV) the homogeneity of the data acquisition, reduction and (in some cases) analysis. Surveys such as SDSS or zCOSMOS, do provide more detailed astrophysical information because they are designed to improve our understanding of galaxy evolution by the characterization of the properties of numerous individual targets. A negative attribute of this surveys is that they are generally limited to one spectrum per galaxy, often with aperture losses that are difficult to control, as for example, the 3" diameter of the fiber used in the SDSS project (Abazajian et al. 2009). IFS surveys of large samples of galaxies are therefore needed to derive the spatial distributions of galaxy properties in two dimensions and to provide enough statistics at low and high redshift. Despite the several advantages of this technique (as described in Sec. 2), until the past decade, IFS has rarely been used in a “survey mode” to investigate large samples. Some notorious exceptions are, among others, *a)* the SAURON survey (de Zeeuw et al. 2002) which main aim was the study of the central regions of 72 nearby early-type galaxies and bulges of spirals, and *b)* its extension ATLAS^{3D} survey (Cappellari et al. 2011) focused on the analysis of 260 objects at $z < 0.01$; *c)* the PINGS project (Rosales-Ortega et al. 2010) at the CAHA 3.5m aimed to mapping dozen very nearby galaxies; *d)* the SINS project obtained with SINFONI at ESO’s Very Large Telescope (Förster-Schreiber et al. 2006); *e)* the Disk Mass Survey (Bershady et al. 2010) that provided very high spectral resolution using PPak and SparsePak of 46 face-on spirals; *f)* the VENGA project (Blanc et al. 2013), that is observing a sample of 32 face-on spirals with VIRUS-P; *g)* and the SIRIUS project, currently studying 70 (U)LIRGS at z<0.26 using different IFUs (Arribas et al. 2008). In the last few years the number of these surveys has exploded thanks to the ATLAS^{3D}, CALIFA (Sánchez et al. 2012 and Walcher et al. 2014, W14 hereafter), MaNGA (Law et al. 2014) and SAMI nearby galaxies (Croom et al. 2012). In general, all the surveys try to select a sample representative of the population of galaxies at low redshifts because their common aim is to understand the nature of galaxies as a fossil record of their evolution through cosmological times. However, they are all affected by non-trivial sample selection criteria and most of their differences are on the technical details of the selected IFU or the adopted setup. Table 2.2 presents a comparison view between the largest aforementioned surveys.

Each of the IFUs surveys is very complementary to each other. For example, while ATLAS^{3D} provides the highest spatial resolution and better spatial sampling for the individual galaxies, it offers a limited wavelength range and FoV compared to the size of galaxies and it is mainly focused on the study of ETGs. In other cases, like MaNGA, the total number of objects is the main statistical advantage, since it would provide with the average characteristics properties of the main population

Table 2.2: Comparison of the current ongoing IFU Surveys. *Source Sánchez et al. 2014*.

Specification	ATLAS^{3D}	CALIFA	MaNGA	SAMI
Sample Size	260	600	10,000	3,400
Selection	M>$10^{9.8}$ †	45" < D_{25} < 80"	M>10^{9}	M>$10^{8.2}$
Radial coverage	$<1\,R_{\rm eff}$	$>2.5\,R_{\rm eff}$	$\sim 2\,R_{\rm eff}$	$1-2\,R_{\rm eff}$
S/N at $1R_{\rm eff}$	~ 30	15−30	10−30	
Wavelength range()	4800−5380	3700−7500	3600−10300	3700−7350
Instrumental resolution (km/s)	105	85−150	50−80	28−75
Spaxel Size	1″	2.7″	2.0″	1.6″
Spatial FWHM	1.5″	2.5″	2″	2″
Telescope size	4.2m	3.5m	2.5m	3.5m

Notes: † Only E/S0 types are included in ATLAS^{3D}. Masses are in unit of $M_{\odot}$. D_{25} is the standard diameter measured at 25 mag/□″.

of galaxies for many different galaxy types with better statistical significance than any of the other survey. In the case of SAMI the main advantage is the wide range of galaxy masses sampled and the higher spectral resolution in the red wavelength range. Finally, in the case of CALIFA, it provides the widest spatial coverage compared to the spatial size of the galaxies, and one of the best spatial physical resolutions. However, the sample is more limited than the one studied by MaNGA or SAMI but CALIFA represents the first of those surveys and the only one completed already. Thus, CALIFA provides with the only panoramic view of galaxy properties already in hand as discussed in the next section and summarized by *The CALIFA's Mandala* shown in Figure 2.3.

2.4 CALIFA, Calar Alto Legacy Integral Field Area Survey

The CALIFA survey (S12) is one of the most ambitious large projects ever carried out at the Centro Astronómico Hispano-Alemán at the Calar Alto observatory (Almería, Spain). The CALIFA observations started in July 2010 with 250 observing nights awarded and are performed using the PMAS (Roth et al. 2005) at CAHA 3.5m in the PPak mode (Verheijen et al. 2004). The PPak IFU has a hexagonal FoV of $74'' \times 65''$, sufficient to cover the full optical extent of the galaxies up to two to three effective radii (R_{eff}), on average. This is possible due to the diameter selection of the sample (W14) indeed CALIFA comprises a diameter (45" < D_{25} <80", D_{25} is the standard diameter measured at 25 mag/□″) selected sample of ∼600 galaxies (from the parent SDSS 7^{th} catalog) in the local Universe (0.005 < z < 0.03). These redshift limits were imposed to ensure that all interesting spectral features can be observed with a fixed spectral setup of the instrument and that the sample would not be dominated by dwarf galaxies. As illustrated in Figure 2.4, PPak is made up of 331 science fibers, 36 sky background fibers, and 15 calibration fibers with diameters of 2.7″, and it has a 100% covering factor when a three-pointing dithering scheme is adopted. The CALIFA spectra allow us to investigate the most prominent emission lines from our H II regions covering the wavelength range of 3700−7300 ÅÅ in two overlapping setups: V500 (from 3745 Å to 7300 Å with a resolution of ∼ 850) and V1200 (from 3700 Å to 4750 Å with a resolution of ∼ 1650). Making use of the IFS advantages, CALIFA provides a more comprehensive view of individual galaxy properties than any

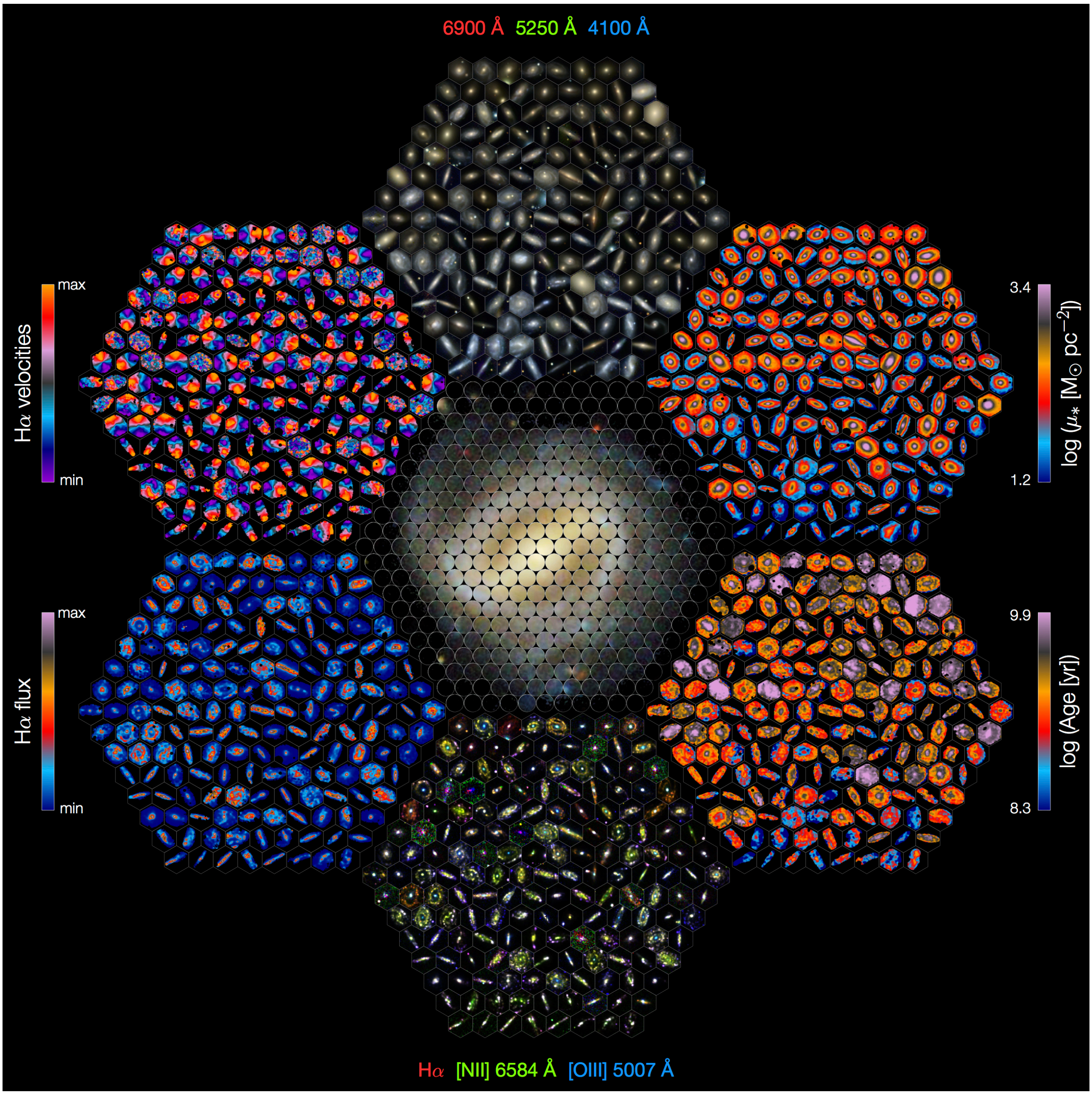

Figure 2.3: CALIFA "panoramic view" (also referred to us *CALIFA's Mandala*) of the different dataproducts obtained for a set of 100 galaxies within the CALIFA survey extracted randomly from the 2nd Data Release (García Benito et al 2015). The six hexagons shown here are: 1) true-color maps showing the light distribution (top center); 2) stellar mass surface densities (upper right); 3) luminosity weighted stellar ages (lower right); 4) three-color image representing the ionized gas distribution for Hα, [NII]λ6583 and [OIII]λ5007 (bottom center); 5) Hα emission (lower left) and 6) ionized gas kinematics maps (upper left). The CALIFA logo is placed at the central hexagon. *Credits: R. García Benito, F. Rosales-Ortega, E. Pérez, C.J. Walcher, S. F. Sánchez & the CALIFA team.*

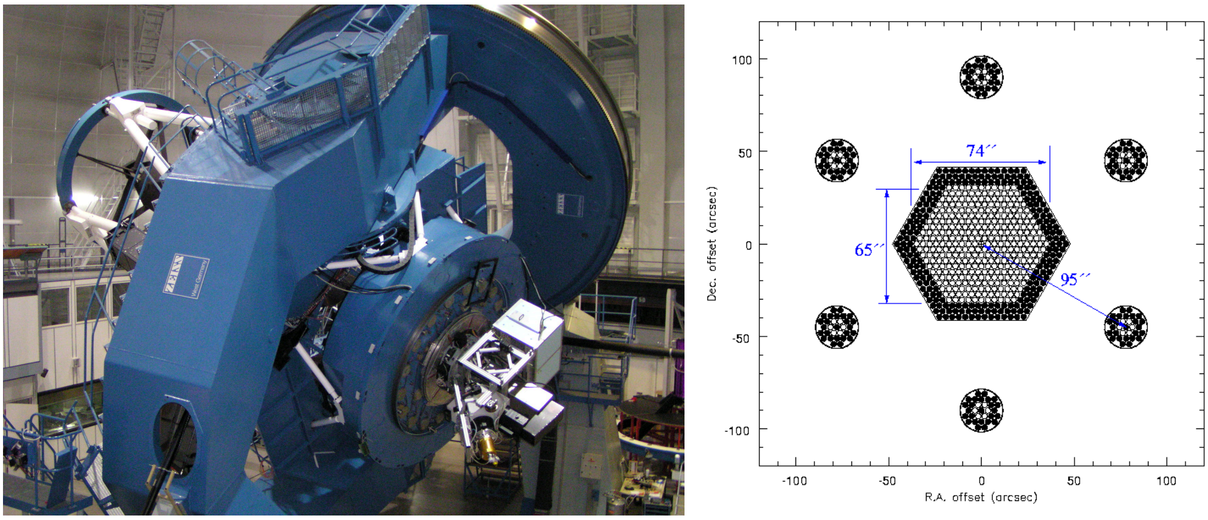

Figure 2.4: *Left:* The PMAS-PPak instrument mounted at the Cassegrian focus of the 3.5m telescope at CAHA. *Right:* PPak-IFU geometrical layout and dimensions. The central hexagonal is made up of 331 object fibers, surrounded by six sky-IFUs. Note, that only the white circles represent active fibers, while the black ones are protective buffers. Each circle represents the combined fiber core, cladding and buffer material. While the physical size of the central IFU is just 4 mm, its coverage on the sky is more than 1 arcminute. *Credits: CAHA observatory.*

traditional spectroscopic survey. The defining drivers for the CALIFA project are: *(a)* deriving the stellar population content both in age and metallicity; *(b)* tracing the distribution of ionized gas and estimate chemical abundances for the gas phase over entire galaxies and a large sample; *(c)* measuring the kinematical properties, both from emission and absorption lines over the whole Hubble sequence using a homogeneous dataset; and *(d)* map entire galaxies in their emission- and absorption-line properties in an unprecedented way. Compared with previous IFS surveys, CALIFA offers an unique combination of sample size, wide range of morphological types and wide range of masses, sampling the Color-Magnitude diagram for $M_g > -18$ mag as shown in Figure 2.5 along with an accurate spatial sampling, with a typical spatial resolution of 1 kpc for the entire sample. This allows to obtain spatially resolved spectroscopic properties of most relevant structures in galaxies (spiral arms, bars, bulges, H II regions, etc). CALIFA can also be viewed as a way to provide a valuable bridge between large single-aperture surveys such as SDSS and more detailed studies of individual galaxies with PPak (e.g. PINGS), SAURON, VIRUS-P, and other instruments. CALIFA is conceived as a public legacy survey and one of the main goals of the CALIFA collaboration is to grant public access of the fully reduced datacubes. In November 2012, the 1^{st} Data Release[4] (Husemann et al. 2013, H13 hereafter) was delivered comprising 200 datacubes corresponding to 100 galaxies within the CALIFA sample. On October 2014, the 2^{nd} Data Release[5] (García Benito et al. 2015, G15 hereafter) was delivered to the scientific community including 400 datacubes (200 galaxies) with an improved data reduction. The actual statistics comprise a total of 554 observed object with the V500 setup until February 2015, of which 498 has also been observed with the V1200 setup.

---

[4] `http://califa.caha.es/DR1/`

[5] `http://califa.caha.es/DR2/`

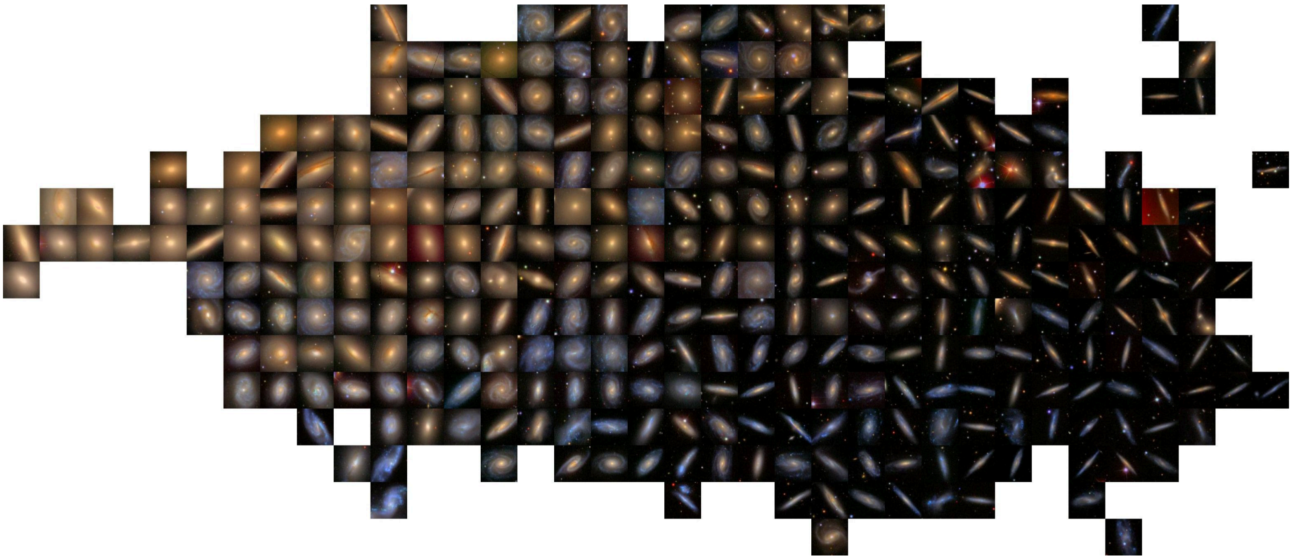

Figure 2.5: Postage stamp (90" × 90") true-color images of a subset of galaxies within the CALIFA mother sample that illustrates the large variety of galaxy types covered by the survey. The galaxies are ordered following the $u-r$ vs. r color-magnitude diagram. The figure spans from $M_r \sim -23$ mag from the left end, to $M_r \sim -18$ mag to the right end, and from $u-r\sim$ 3.5 mag from the top end, to $u-r\sim$ 1.5 mag to bottom end.

CALIFA-like observations were collected during the feasibility studies (Mármol-Queraltó et al. 2011; Viironen et al. 2012) and the PINGS project as predecessor of this survey. First results based on those data sets already explored their information content (e.g., Marino et al. 2012; Rosales-Ortega et al. 2011, 2012; Sánchez et al. 2011, 2012b). So far, a number of science goals have been addressed using the data from the CALIFA survey:

(I) New techniques have been developed to understand the spatially resolved star formation histories (SFH) of galaxies (Cid Fernandes et al. 2013; 2014); a solid evidence that mass-assembly in the typical galaxies happens from the inside-out (Pérez et al. 2013). The SFH and metal enrichment of bulges and early-type galaxies are fundamentally related to the total stellar mass, while for disk galaxies it is more closely related to the local stellar mass density (González-Delgado et al. 2014a,b); this includes the derivation of the spatially-resolved SFR (Catalán-Torrecilla et al. 2015).

(II) New tools were developed within the CALIFA collaboration to detect and extract the spectra of H II regions (Sánchez et al. 2012b), building the largest catalog currently available (6000 H II regions and aggregations). This catalog has been used to define a new ionized-gas phase oxygen abundance calibrator, anchored to electron temperature measurements (Marino et al. 2013). From these, the dependence of the mass-metallicity relation with star formation rate (Sánchez et al. 2013), and the local mass-metallicity relation (Rosales-Ortega et al. 2012) were also explored. These results suggest that all galaxies present a common gas-phase oxygen abundance radial gradient with a similar slope, when normalized to the effective radius (Sánchez et al. 2014). More recently, this result has been confirmed by the analysis of the stellar abundance gradient in the same sample (Sánchez-Blázquez et al. 2014; Marino et al. 2015, submitted).

(iii) The origin of the low intensity, LINER-like, ionized gas in galaxies was also analyzed within CALIFA. These regions are clearly not related to star formation activity, neither to AGN activity. They seem to be related to post-AGB ionization in most of the cases (Kehrig et al. 2012; Singh et al. 2013; Papaderos et al. 2013).

(iv) This project provides a unique tool to understand the aperture and resolution effects in larger single-fiber (e.g., SDSS) and IFS surveys (e.g., MaNGA, SAMI) thanks to the study made on the effects of the signal dilution in different gas and stellar population properties (Mast et al. 2014), and also the new empirical aperture correction for the SDSS data proposed by Iglesias-Páramo et al. (2013).

(v) The local properties of the ionized gas and stellar population of galaxies hosting supernovae (SNe) have been also analyzed. Core collapse SNe are found to be correlated with younger stellar populations, while SNeIa show no correlation with the stellar age (Galbany et al. 2014).

(vi) CALIFA is the first IFS survey that allows gas and stellar kinematic studies for all morphologies with sufficient spectroscopic resolution to study the kinematics of the ionized gas (García-Lorenzo et al. 2015); the effects of bars in the kinematics of galaxies (Barrera-Ballesteros et al. 2014); the effects of the interaction stage on the kinematic signatures (Barrera-Ballesteros et al. 2015); the bar pattern speeds in late-type galaxies (Aguerri et al. 2015).

(vi) The effects of a first stage merger on the gas and stellar kinematics, star formation activity and stellar populations of the Mice merging galaxies (Wild et al. 2014) were also studied in detail.

The CALIFA survey has produced so far significant advances in our knowledge of the stellar and gas composition in galaxies, their kinematical structure, and the overall star formation history and chemical enrichment. New local relations within galaxies were found, tightly connected to the global relations described using classical spectroscopic surveys. In summary, CALIFA opens to the astronomical community the possibility to further analyze the spatially-resolved properties of galaxies presenting a panoramic view of galaxy properties in the local Universe.

2.4.1 Technical and scientific contribution to the CALIFA Survey

As I mentioned before, during my Ph.D. Thesis I was fully involved in both the technical and the scientific aspects of the CALIFA project. My contribution encompasses several aspects: I was working over 1 year carrying out the observations at CAHA observatory of the feasibility studies for the CALIFA galaxies. As part of the CALIFA Data Quality (DQ) Control Team, I am involved in all the technical phases of the data reduction and quality-control procedures along with the scientific analysis of the CALIFA galaxies. In particular, I was part of the team that performed the visual morphological classification of the sample and of the DQ group at UCM. Also, as member of the Ionized-Gas Working Group, I have led a review study on the most widely used empirical oxygen calibrations based on the most comprehensive compilation of both CALIFA data and the T_e-based measurements from the literature. As detailed described in Chapter 4, this novel study makes use of an unprecedent set ($\sim$4000) of H II regions and allows us to derive the most accurate calibration for external galaxies to date for both the O3N2 and N2 single-ratio indicators, in terms of all statistical significance, quality, and coverage of the parameters space (more details in Marino et al. 2013). Finally, I have carried out a combined analysis of the metallicity gradients obtained from CALIFA (based on the tools and calibrations presented in Marino et al. 2012, 2013) with the surface brightness and color profiles from the SDSS. Our analysis has confirmed the presence of U-shaped color profiles in the outer parts of the vast majority of the 350 CALIFA disk galaxies analyzed and weak flattening signal in the ionized-gas metallicity gradients for the same radial ranges (see Chapter 5). In this section I will briefly describe the visual morphological classification performed and all those technical aspects carried out within the CALIFA collaboration (the update list of papers published within this Ph.D. is given in Appendix C).

2.4.1.1 Data reduction of the CALIFA observation

The reduction of IFS observations has an intrinsic complexity given the nature of the data and the vast amount of information recorded in a single observation. The reduction of the CALIFA data is performed using a fully automatic pipeline developed specifically for the project. The pipeline uses the routines included in the R3D package (Sánchez 2006a), following the standard steps for fiber-based IFS (e.g., Sánchez 2006a; Sandin et al. 2010). The pipeline was upgraded and improved during the project on the basis of the quality tests performed on the acquired data (the latest data products were reduced with the CALIFA pipeline v1.5 version, the reader is referred to G15 for a detailed description of the pipeline improvements). In the following list, I present a summary of the reduction procedures applied, manually for some specific processing steps in the case of galaxies analyzed in Chapters 3 and 6 and in a fully-automatized way for the CALIFA survey. A sketch of a typical reduction sequence of the PPak data is also presented in Figure 2.6. For a detailed discussion on the latest pipeline improvements the reader is referred to H13 and G15.

1. **Pre-reduction:** It consists in all the "classical" corrections applied to the CCD[6] data: removal of electronic signatures and realignment of the frames; application of the bias subtraction and cosmic-ray rejection to the raw images.

---

[6] The CCD used for PPak is a new 4k×4k E2V detector installed at the telescope in October 2009.

2. **Identification of the position of the spectra on the detector for all pixels along the dispersion axis:** In order to find the location of each spectrum at each wavelength along the CCD, we need a continuum exposure (e.g. a dome-flat), that, in the case of instruments that suffer from flexures (i.e. displacement of the spectra in the CCD at different positions of the telescope such as PMAS), should be taken with the telescope pointing to the same location of your science exposure. To ensure a continuous behavior, once the peak intensities are identified (i.e., the spectra traced), a low-polynomial function is fit to the resulting trace.

3. **Extraction of each individual spectrum:** After tracing the location of the spectra on the CCD, the next reduction step is to extract, for each spectrum, the flux corresponding to each spectral pixel along the dispersion axis. The simplest method to perform this extraction is to co-add the flux within a certain aperture (~ 5 pixels) around the *trace* of the spectra in the raw data, and store it in a 2D image (RSS). To continue with the reduction it is needed reduce the sky-flat exposures (or the corresponding dome-flats) that you are going to use to determine the fiber-flat. For each frame, we extract both the science frame (or sky-flat frame), and the corresponding arc frame, necessary to next steps of the reduction.

4. **Cross-talk correction:** By construction, the projected spectrum of each fiber in the CCD contaminates the adjacent one in an amount that depends on the distance between adjacent spectra and the width of the projected distribution along the cross-dispersion. This effect is known as cross-talk, and it can blur signal of faint objects or create artificial structures. Given that this effect is an incoherent contamination it is preferable to keep it as low as possible (maximum 10%) and a *Gaussian-suppression* technique is applied in order to asses the level of contamination. At this step, the IFS data can be stored using different data formats: datacubes or RSS files. In the case of PPak the data are stored in 2D FITS image where the X and Y axis contain the spectral and spatial information respectively, regardless of their position in the sky. This format requires a position table (either a FITS or ASCII table) where is indicated the position of the different spatial elements on the sky.

5. **Distortion correction of the extracted spectra:** Most of the spectrographs do not disperse the light homogeneously along the cross-dispersion axis. The dispersion is distorted, being larger in the edges of the slit than in the center. This distortion is sometimes called the “C distortion” due to its shape on the CCD (see the curvature and distortions of the Extracted Spectra shown in Figure 2.6). In the case of fiber-feed spectrographs, additional distortions are introduced due to the way the fibers are placed in the pseudo-slit. The distortions have to be corrected fiber-to-fiber before finding a common wavelength solution. The R3D software package performs this correction by a two steps procedure, using arc calibration lamp exposures.

6. **Determination of the wavelength solution:** In order to derive the wavelength coordinates on the CCD, the emission lines of an arc exposure are first identified using an interactive routine. Calibration data cubes were taken at the beginning and at the end of the night by illuminating the instrument with an arc (e.g. HeHgCd) lamp. The distortion-corrected spectra of the arc are then transformed to a linear wavelength coordinate system by 1D spline interpolation.

7. **Fiber-to-fiber transmission correction (FiberFlat):** The light-path from the focal plane of the telescope to the detector is different from spectrum to spectrum. They suffer from differential

positioning with respect to the axis of the optical system. Besides, the entrance cone in each of the fibers is different due to small differences in the positioning of each fiber with respect to the focal plane of the telescope. Each fiber, although done with the same material, have slightly different one-to-one transmissions, with a clear wavelength dependency. The location of the final edge of the fiber along the slit is different one each other along the slit view of the spectrograph, with slight misalignments. Finally, each spectrum suffer a different distortion due to the differential position with respect to the optical axis of the spectrograph. In general all these effects produces a differential transmission to optical element that are translated in what is normally named a differential fiber-to-fiber transmission. To correct for this effect it is required to obtain an exposure of a continuum illuminated source, such as the twilight sky, that is reduced following the same procedure as a science frame.

8. **Flux-calibration:** The final step of the reduction, at the level of the CCD frames, is to determine the transformation between counts measured and real flux per second, that is normally called flux calibration. For doing so it is required to have observed during the night a set of standard spectrophotometric calibration stars (e.g. from the Oke Catalogue; Oke 1990). We should apply all the previous reduction steps to the calibration star frame, in order to be able to use it for measuring the ratio between counts per second and physical flux per second. This ratio will be later applied to the science data to "flux-calibrate" them. Note that, if the conditions are not photometric, this method yields a *relative* flux calibration; the *absolute* one is achieved with the comparison with broad-band photometry as described below. R3D includes a procedure that finally provides the transformation function from observed counts to intensity, taking into account also the airmass and extinction of the observations of both the spectrophotometric standard stars and the science targets. To apply this procedure the extinction measured by the Calar Alto Vistual EXtinction monitor (CAVEX) at the moment of the observations is used, and the average extinction curve for the observatory is derived (Sánchez et al. 2007a). The procedure ensures a good relative flux calibration from the blue to the red part of the spectra, as long as the weather conditions throughout the night are stable. If more than one standard star is observed, the pipeline performs a comparison between the transformations derived using each of them, in order to estimate the photometric stability of the night considered.

9. **Sky Subtraction:** One of the most difficult steps in the data reduction is the correct subtraction of the Earth's atmosphere emission (easily identified in the Object+Sky Spectra panel of Figure 2.6 as bright vertical lines). If the observed target does not fill all the FoV of the IFU, an option is to subtract the sky spectrum obtained using the spaxel free from object emission, following the same procedure adopted e.g. for the sky subtraction of the spectrophotometric standard star frames. In the case of PPak there are also a set of 36 fibers located at $\sim$90" of the center of the science bundle, grouped in 6 small bundles; the purpose of these fibers is to sample the sky. An individual inspection of all the sky fibers is required in order to avoid any contamination from foreground or background objects, e.g. bright foreground stars or H II regions in the galaxy. The procedure adopted to derive the night-sky spectrum, in the case of extended CALIFA galaxies, is to combine the spectra from these fibers, performing a 2σ clipping rejection and then subtract the combined spectrum from all science frames.

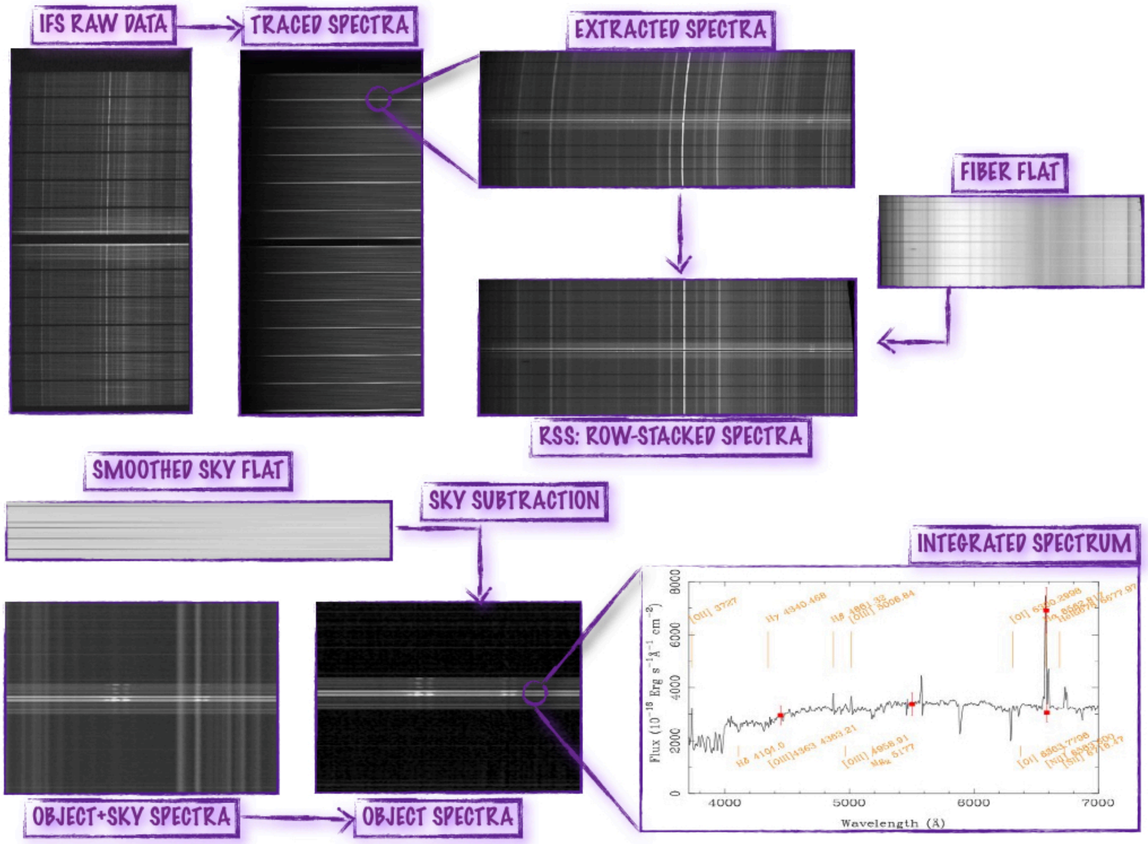

Figure 2.6: Graphical summary of a typical reduction sequence of the CALIFA IFS raw data obtained with PMAS in the PPak mode. Each horizontal line corresponds to the projection of a spectrum along the dispersion axis.

10. **Re-arranging the spectra in the sky: Cube and dithers reconstruction:** The location of the spectra in the sky is given by a certain position table that relates each spectrum with a certain fiber, as these are located at a fixed position with respect to each other in the PPak IFU. Once the three frames corresponding to each particular pointing are reduced, the science spectra corresponding to these three dithered exposures are combined in a single frame of 993 spectra. The images are rescaled to a common intensity and response function by comparing the integrated spectra within an aperture of 30"diameter. In the case of PPak is possible to create a cube of data for the central hexagonal IFU, by interpolating at each wavelength the intensities at each spatial location creating an artificial squared grid pattern. This is done by adopting a flux-conserving variation of Shepard's interpolation method (Shepard 1968).

11. **Mosaic reconstruction:** This step is not required in the case of the CALIFA galaxies due to their diameter selection requirement. The mosaic reconstruction was done for galaxies NGC 5668, NGC 3395 and NGC 3396 as explained in Chapters 3 and 6. A single RSS file for the whole mosaic is built by adding pointings previously normalized to a reference ("master") pointing. The master pointing is that having the best sky subtraction and most optimal observing conditions regardless of the geometric position of the pointing in the mosaic. This

procedure makes use of the overlapping fibers between different pointings (11 fibers in total) to re-scale each new added pointing using the flux ratio in the continuum region 5869−5893 Å between the two pointings (the newly added and the master one).

12. **Differential Atmospheric Refraction (DAR) correction:** DAR effects (Filippenko 1982) are corrected once the data are spatially resampled to a datacube with a regular grid. In the case of IFS data, the DAR can be corrected empirically, after the observations, without requiring to know the original orientation of the instrument and without need of a compensator (Emsellem et al. 1996; Arribas et al. 1999; Roth et al. 2004). To do so, the centroid of the observed object or even better a nearby field star is derived at each wavelength by determining its barycenter in an image slice extracted from the datacube, within a range of 20 Å around the considered wavelength. Then, the shifts along the wavelength are determined by comparing the corresponding coordinates to a common reference. A polynomial function (of order 3 in the case of PPak) is fitted to each shift (*X* and *Y*) along the wavelength to increase the accuracy of the determined offset (e.g. Wisotzki et al. 2003). Then, the full datacube is shifted by resampling and shifting each image slice at each wavelength. In the case of mosaicking galaxies, a total theoretical DAR value using a Calar Alto public tool was performed, obtaining a value of 1”. In those cases the differential atmospheric refraction can be considered negligible compared with the fiber size (2.7” in diameter). In general, the empirical correction produces similar results to the theoretical one. In the case of CALIFA this step is done on the individual pointings before the cube reconstruction.

13. **Absolute Flux Re-Calibration:** The absolute flux re-calibration is computed using the SDSS photometry, available for all targets by construction of the sample. Out of the five SDSS band (*ugriz*), the *g* (λ_{eff}=4694 Å) and *r* (λ_{eff}=6178 Å) filters are covered almost completely by the V500 grating data, while the *u* (λ_{eff}=3594 Å) is only partially covered by both the V500 and V1200 grating data. Therefore, the V500 grating data and the SDSS *g* and *r* images are used to perform a primary flux recalibration by measuring the counts of each galaxy in the SDSS image inside a 30" diameter aperture (the photometric accuracy is better than 0.05 mag). Then, the 30" diameter integrated spectrum is extracted from the reduced datacubes and is convolved with the SDSS *g* and *r* bands to derive the absolute spectrophotometry. Using these two data pairs, a scaling solution is found, by adopting the average of the flux ratio in both bands. The secondary flux calibration is obtained in a similar way using the V1200 grating. In new versions (those used in DR2 and beyond) of the CALIFA pipeline this step is as follow: an image registration is performed to the SDSS images that re-scale the flux and found the best astrometric solution.

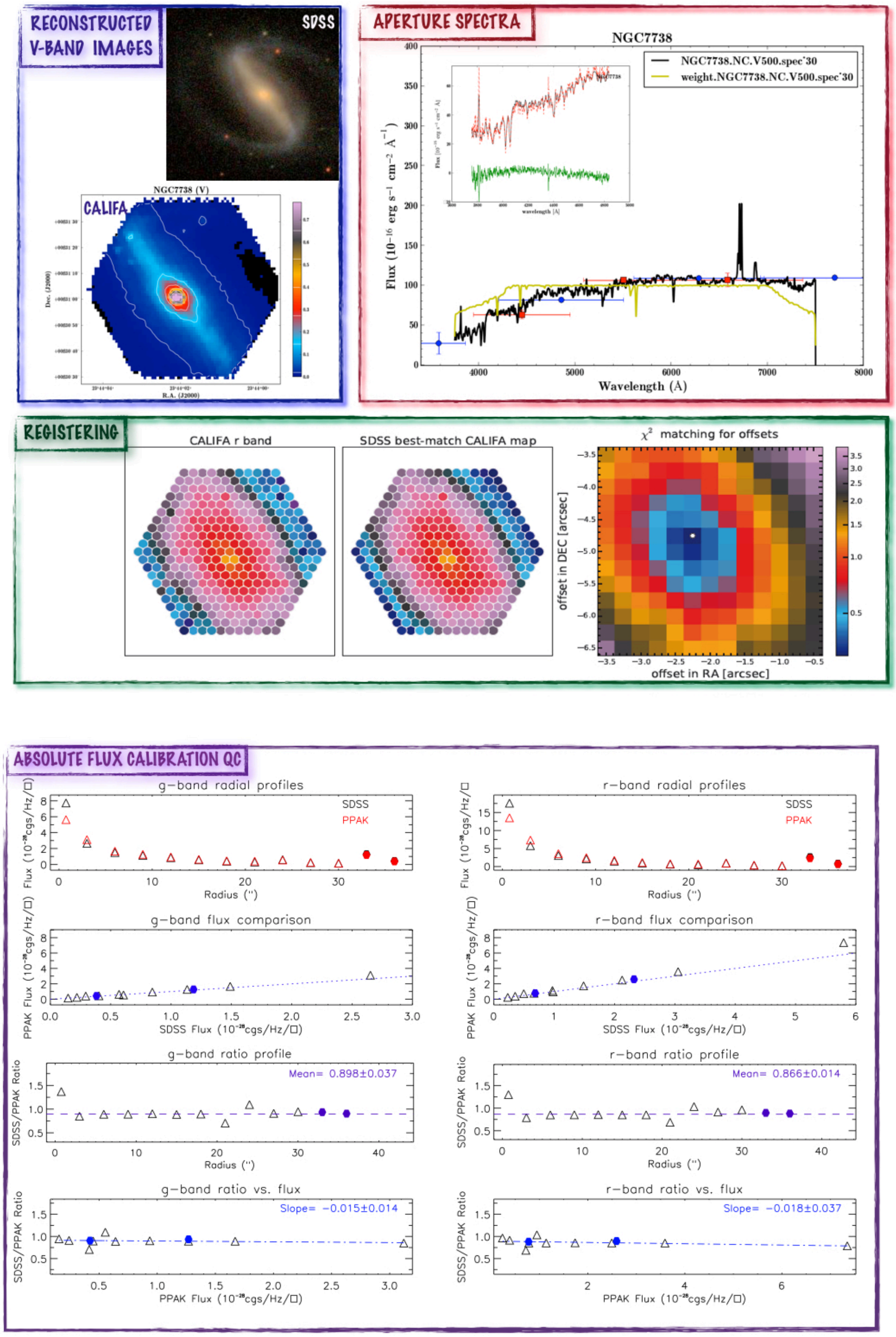

Figure 2.7: *Top*: Schematic view of the three visual quality control diagnostic checks performed for the CALIFA sample. *Bottom*: Absolute flux calibration plots performed for the SDSS g-, r- bands.

2.4.1.2 Quality Control for the CALIFA data.

Monitoring the data quality is a critical issue in a legacy project like CALIFA which involves large amounts of data. So far, the two CALIFA data releases have provide to the community science-grade data of 200 galaxies. The quality control of the CALIFA data necessarily involves different levels of assessment, including automatic and manual checks. In the case of CALIFA DR1 our UCM QC group have performed several tests on the absolute flux calibration of the CALIFA data cubes that basically consists in the comparison of the integrated spectra within an aperture of 30" with the fluxes derived from the SDSS *g*- and *r*-band images. On the other hand for the CALIFA DR2, a first step in the quality control is carried out automatically during the new data reduction. A set of tables and figures allow the CALIFA Data Quality Control Team (in which I have actively participated) to check the quality of the data and to identify possible problems in the data reduction. Overall, the final data quality for CALIFA depends on a number of independent factors such as (I) general instrument reliability and temperature stability, (II) ambient conditions during observations, and (III) the robustness of the data reduction pipeline. We define a set of parameters and QC flags related to the astrometric, spectroscopic and photometric characterization of the data reduction for each galaxy. The QC results obtained are summarized in H13 and G15 to which the reader is referred for a detailed discussion on the automatic quality control (AQC) checks. Here I will emphasize my contribution to visual quality control (VQC) checks performed for the whole CALIFA sample. VQC checks are performed separately on the pipeline output for the V500 and the V1200 gratings; additional tests are performed on the COMBO[7] cubes as well. Starting points for V500 and V1200 are the plots provided by the AQC. VQC parameters are organized by diagnostic and could be sorted in three categories:

1. Check for anomalies in the “reconstructed” V-band image, and comparison with SDSS postage stamp images for the V500, V1200 and COMBO cubes.

2. Check for consistency between the V500, V1200 and COMBO spectrum and the photometric data points and for anomalous shapes and bumps, drops etc. As shown in Figure 2.7 the black line is the spectrum obtained integrating all spaxels within 30" (in the case of V500 and COMBO, 20" for V1200) and dots are photometric points derived from SDSS images integrated within the same aperture. The blue dots are *u*, *g*, *r*, and *i*−band fluxes from the corresponding SDSS images. The red squares represent the B, V, and R Johnson bands. The inset panel in the V500 spectrum of the galaxy NGC 7723 shows with a black line the spectrum obtained integrating all spaxels within 20" in V500, red dashed is the spectrum obtained integrating all spaxels within 20" in V1200, green is the difference V500-V1200. Systematic residuals with a continuous curvature and absolute values up to 10−20% are considered acceptable.

3. Check the registering procedure of the pointings relative to SDSS (hence if there are also problems with the astrometry). For each of the three pointings a χ^2 surface plot is analyzed. Lack of a clear minimum, strange shapes in the χ^2 levels or a minimum significantly larger than unity imply that the matching was not successful so these objects are worth analyzing in further

---

[7] The CALIFA COMBO data are the result of a coherent combination of the V500+V1200 ones and it is produced where wavelength range short-ward of 4600 Å is taken from matched V1200 data cube and long-ward of 4600 Å is taken from the original V500 datacube

detail. The last row (top panel) in Figure 2.7 shows the $r-$band integral of each fiber in the CALIFA pointing (first panel), the projection of the SDSS $r-$band image (second panel) and χ^2 surface plot (third panel).

4. Check the automatic absolute flux calibration performed by the pipeline. In this regard, our group at UCM performed a new absolute flux calibration of all the CALIFA spectra, comparing them with the improved photometry provided by the 8th data release of SDSS, to independently measure any systematic offset and quantitatively cross-check the achieved accuracy in the absolute photometry of the CALIFA data. The mean SDSS/CALIFA *g*-, *r*- band ratio found was 1.06 ± 0.13 and 1.00 ± 0.10, respectively, which shows that the absolute photometric calibration of CALIFA data is better than 15%. The bottom panel of Figure 2.7 shows the $r-$band integral of each fiber in the CALIFA pointing (first panel), the projection of the SDSS $r-$band image (second panel) and χ^2 surface plot (third panel).

2.4.1.3 CALIFA Galaxy Explorer page

As it can be a challenge for the general user to judge *a priori* which CALIFA dataset could be useful for their specific scientific interest, the team has prepared a CALIFA Galaxy Explorer page[8] (hereafter CGE) that provides a presentation card for each individual CALIFA galaxy released to the scientific community. It is a powerful tool for a quick-look reference of the galaxy properties and the actual content of the CALIFA public released data. The CGE is linked to each object in the output table of the CALIFA retrieval tool and the page is structured in three different levels. In the first level, a false-color (*gri* bands) SDSS postage stamp image is presented together with a short table containing the galaxy name, galaxy equatorial coordinates (in J2000 format) and the designated CALIFA ID. Alternative names of the galaxies can be found through a direct link to NED together with the redshift, the SDSS *u, g, r, i,* and *z* band Petrosian magnitudes, and the corresponding Galactic extinction in each band. In the second level, the user finds the CALIFA data products and their content. A compact visualization of the CALIFA data (see Figure 2.8) shows the reconstructed V-band image, the stellar population age distribution, the gas velocity field, and the Hα+[NII]$\lambda\lambda$6543,6583 emission-lines 2D distribution at first glance. A third level is available only within the collaboration where we report our data products, as the visual morphological classification of the galaxies described in the next paragraph. More detailed galaxy information is shown in a separate table which includes additional parameters available through the Hyperleda[9] database (Makarov et al. 2014).

2.4.1.4 The morphological classification of the CALIFA galaxies.

Despite the time that has passed since it has first proposed, the gold standard for galaxy classification among astronomers is still the Hubble classification (Hubble 1926). With a few minor modifications, this classification has stood in place for almost 90 years and is often known colloquially as the "Hubble Tuning Fork" diagram because of the shape of the pattern in which it is traditionally represented.

---

[8] `http://www.caha.es/CALIFA/public_html/?q=content/califa-explorer`

[9] `http://leda.univ-lyon1.fr/`

Hubble's scheme divides galaxies into 3 broad classes, namely *ellipticals, spirals and irregulars*, depending on properties such as the amount of flattening for elliptical galaxies and the nature of the arms for spiral galaxies (originally recorded on photographic plates). The Hubble sequence is the most commonly used system for classifying galaxies and is now considered somewhat too simple but the basic ideas still hold. In summary, elliptical galaxies have a basic circular shape but they are slightly flattened. Hubble gave the ellipticals numbers from zero to seven, which characterize the ellipticity of the galaxy, "E0" is almost round, "E7" is very elliptical. Hubble named the galaxies that reminded him of whirlpools or the whirling blades of pinwheels as spirals galaxies. For spirals were assigned letters from "a" to "c" which characterize the compactness of their spiral arms ("Sa" spirals are tightly wound whereas "Sc" are more loose). Spiral galaxies are also sub-divided into two groups: normal spirals and barred spirals. Hubble found that some galaxies are difficult to put in the context of the tuning fork diagram. Those include irregular galaxies which have odd shapes, dwarf galaxies which are very small, and cD galaxies which are very large elliptical galaxies residing in the centers of some clusters of galaxies. A fourth class contains *lenticular* galaxies, or "S0", that are

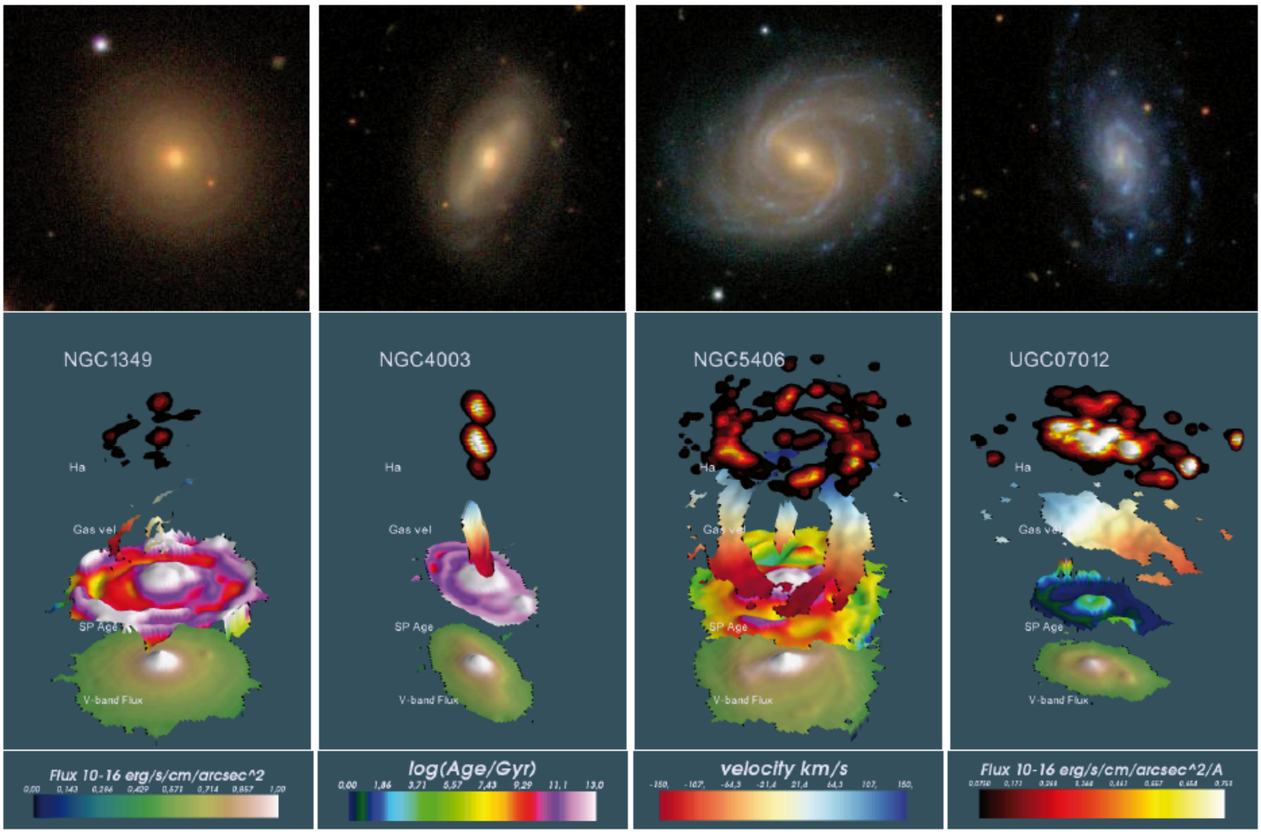

Figure 2.8: *Top panels:* SDSS postage stamp images of four representative CALIFA target galaxies, with a FoV of 90" × 90". *Bottom panels:* Corresponding examples of quick-look CALIFA 3D visualization images shown on the CALIFA Galaxy Explorer page . From bottom to top it shows the reconstructed V-band light distribution, the stellar population luminosity-weighted age distribution, the Hα+[NII]$\lambda\lambda$6543,6583 emission-lines 2D distribution inferred from the CALIFA V500 datacube. The associated color bars are shown below increasing from left to right.

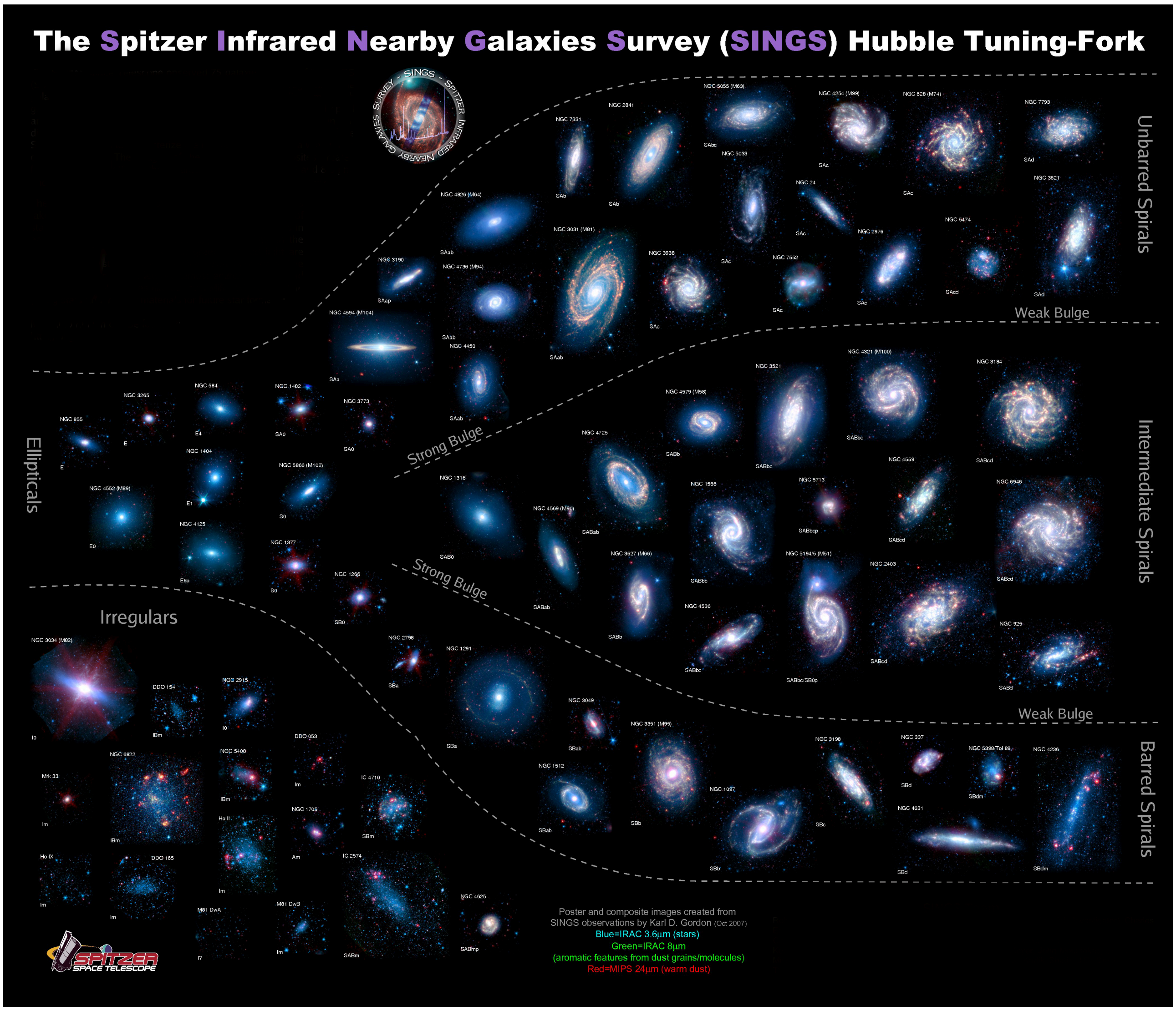

Figure 2.9: The Spitzer Infrared Nearby Galaxies Survey (SINGS) Hubble Tuning-Fork. A total of 75 SINGS galaxies are displayed arranged in a tuning fork based on their optical morphology. The color images of each galaxy were created from the SINGS IRAC 3.6 μm (blue), IRAC 8.0 μm (green), and MIPS 24 μm (red) images. *Credits: Karl Gordon.*

between ellipticals and spirals and consist of a large bulge with a small flattened disk around them without visible spiral structure.

Since Hubble's time, tens of thousands of spatially-resolved galaxies have been imagined using different kinds of telescopes and instruments. For a time the Hubble tuning fork was thought to be an evolutionary sequence, although not to the eyes of Hubble himself, where galaxies might evolve from one type to another progressing from left to right across the tuning-fork diagram. Nowadays, multiple extensions to this diagram came about after Hubble's discovery and is still unclear which is the right evolutionary path of galaxies within it. De Vaucouleurs et al. (1991), for example, distinguished between $s-$shapes and rings, thus making the tuning fork 3D. A particularly detailed version was produced by the Spitzer Infrared Nearby Galaxies Survey (SINGS) team at these wavelengths as shown in Fig 2.9. In our case, one of the defining characteristics of the CALIFA sample is that it contains galaxies of all morphological types. When looking through the morphological classifications available from public databases we found that these were incomplete for our sample (e.g. Galaxy Zoo 2, 535 matches to Willett et al. 2013) or missing a consistent classification in Hubble subtypes (e.g. NED). We therefore undertook our own reclassification. To sort galaxies by morphology within the CALIFA survey we carried out a by-eye classification. Five members of the CALIFA collaboration (myself included) used r and i SDSS postage stamps to classify all 939 galaxies in the CALIFA mother sample according to the following criteria:

1. E or S or I for elliptical, spiral, irregular
2. 0-7 (for Es) or 0, 0a, a, ab, b, bc, c, cd, d, m (for S) or r (for I)
3. B for barred, otherwise A
4. Merger features

The five classifications obtained were combined, clipping outlier measurements in the calculation of the mean, but keeping them as minimum and/or maximum values. Figure 2.10 shows the resulting morphology histogram (Walcher et al. 2014). We verify that the CALIFA mother sample covers a broad range in galaxy morphology.

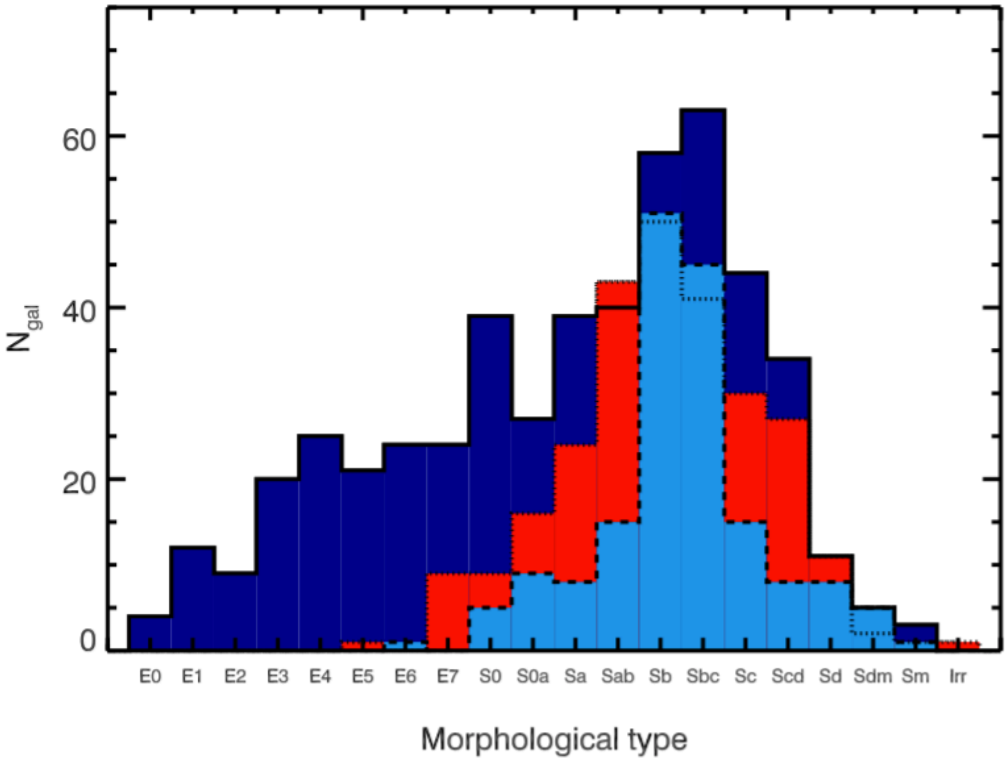

Figure 2.10: The distribution of morphological types in the CALIFA sample from our own classification. Independent histograms are drawn for non-barred (meanbar = A, fullline, dark blue), strong barred (meanbar=B, dashed, blue) and weak barred (meanbar = AB, dotted, red) galaxies.

2.5 MEGARA, Multi-Espectrógrafo en GTC de Alta Resolución para Astronomía

MEGARA is an optical IFU and MOS designed for the 10.4m Gran Telescopio CANARIAS (GTC) in La Palma, Spain (Gil de Paz et al. 2012, 2014; G14 hereafter). In Figure 2.11 a general 3D view of MEGARA on the GTC telescope is shown. The instrument consists of two different subsystem, one located at the Folded Cassegrain (FC) focus, where the IFU and the robotic positioners of the MOS are placed and the other one at the Nasmyth platform, where the MEGARA spectrograph is placed and kept static.

The FC unit and the spectrograph are connected by means of a 40m-long fiber link. MEGARA offers one IFU bundle covering $12.5'' \times 11.3''$ with a spaxel size of $0.62''$ (Large Compact Bundle; LCB, which makes use of 100μm-core optical fibers). The MEGARA MOS mode will allow observing up to 100 objects in a region of 3.5’ × 3.5’ around the IFU. Eight of these bundles will be devoted to the determination of the sky during the observation with the LCB IFU, so only 92 of these positioners will be available for MOS observations and will be controlled by the MEGARA Control System (MCS).

The MEGARA spectrograph is a fully-refractive optical system composed by a collimator with 5 lenses (including an aspheric singlet and two doublets) and a camera with 7 lenses (three singlets and two doublets). The spectrograph is composed by a pseudo-slit, where fibers are placed simulating a long slit 119mm in length that follows the curvature of the entrance focal plane (with a radius of 1075mm). The pseudo-slits will be moved using two translation stages mounted on $X-Y$ that will allow exchanging the pseudo-slit in use between that of LCB or MOS modes, and also will be used as a focusing mechanism that will be configured in the z-axis.

The disperser elements are Volume Phase Holographic (VPH) gratings and both the LCB IFU and MOS capabilities of MEGARA will provide intermediate-to-high spectral resolutions [the requirement is $\mathrm{R}_{FWHM} \sim$6,000, 12,000 and 18,700, respectively for the low-resolution (LR), mid-resolution (MR) and high-resolution (HR) modes; the reader is referred to Table 1 of G14 for a summary of the characteristics of the two MEGARA modes and the corresponding spectral resolutions required for each set of VPHs.

MEGARA Folded Cassegrain subsystems include all components that collect and conduct the light from the Folded Cassegrain focal plane to the spectrograph entrance. Those elements are basically: (a) a Field Lens to correct from lack of telecentricity providing a telecentric focal plane for the microlens arrays, (b) the cover, that allows obtaining very low cross-talk observations with half the FoV and multiplexing of the MEGARA default mode, (c) the microlenses, that change the focal number of the telescope allowing a good coupling with fibers (that will couple the light at the focal plane of the telescope, f/17, into the optical fibers, f/3), (d) the fiber bundles, (e) the Fiber MOS that allows to position 92 minibundles in a dedicated area of the focal plane, (f) the interface plate that supports the LCB IFU in the central area of the focal plane, (g) the Folded-Cassegrain Rotator Adapter that provides the interface with the FC rotator at GTC and (h) the pseudo-slit plate that positions fibers at the Spectrograph entrance. The camera focuses the light onto an E2V 231-84 deep-depleted 4k×4k 150 μm pixels CCD that is located in a custom cryostat designed and built by the INAOE partner.

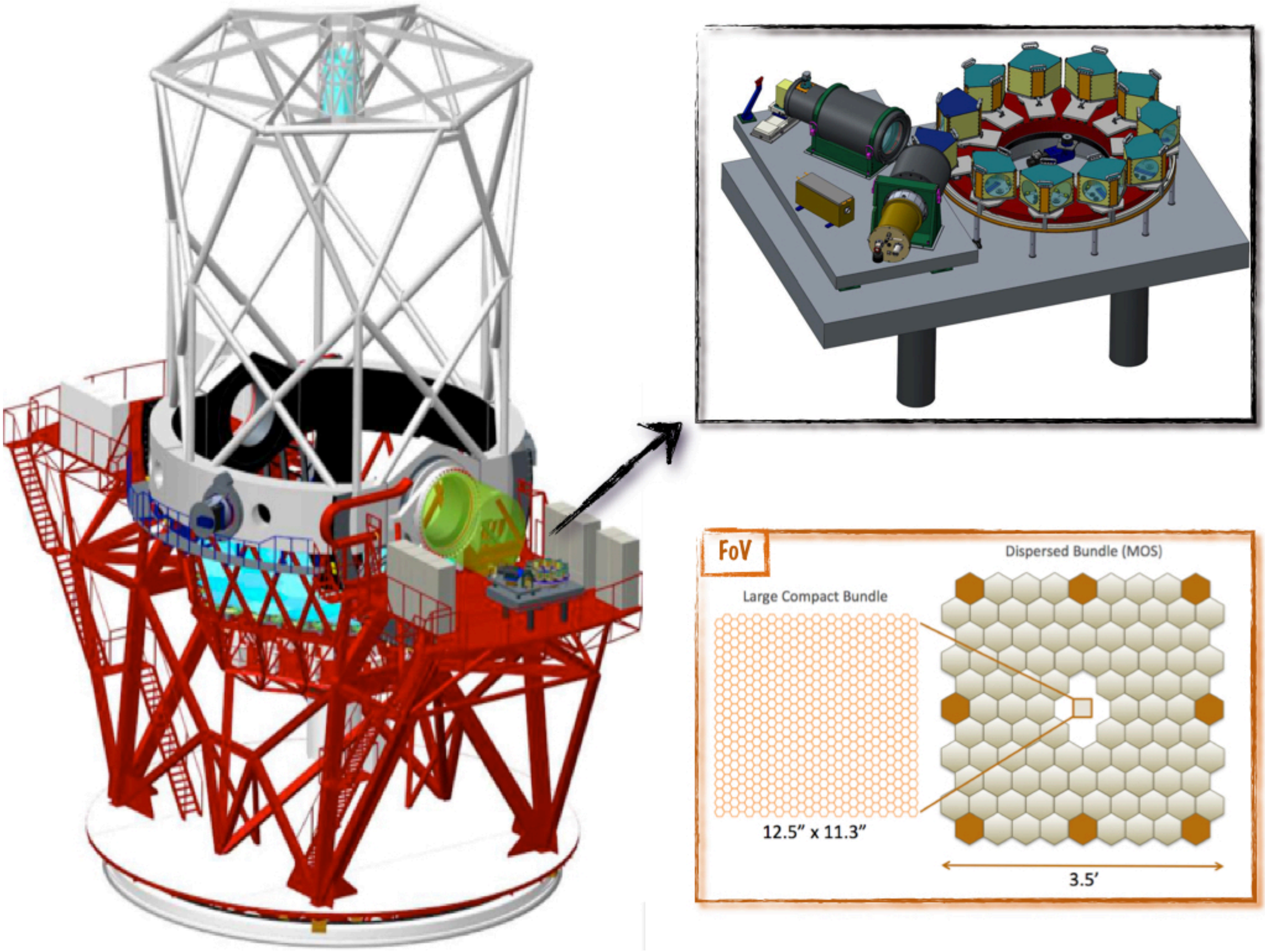

Figure 2.11: 3D drawing of the two main elements of MEGARA installed at the GTC. Insets shows the MOS and IFU FoV (bottom right of the figure) and the spectrograph (top right of the figure) in a Nasmyth platform, both connected by fiber bundles.

The MCS will be responsible for all mechanisms in MEGARA (focal-plane cover, Fiber-MOS robotic positioners, pseudo-slit exchange and focusing, shutter, and VPH wheel and insertion mechanism) and for the Data Acquisition System (DAS) and will follow the GTC standards defined by GRANTECAN. As mentioned before, I was involved in the MSC team and a detailed discussion of the MSC tasks on which I participated will presented in Section 2.5.2.

The consortium responsible for the design and construction of the instrument includes the Universidad Complutense de Madrid (UCM, Spain) where the MEGARA Principal Investigator (Armando Gil de Paz) is located, the Instituto Nacional de Astrofísica, Óptica y Electrónica (INAOE, México), the Instituto de Astrofísica de Andalucía (IAA-CSIC, Spain), and the Universidad Politécnica de Madrid (UPM, Spain). After being selected in a competitive Conceptual Design Review in September 2010, the instrument successfully passed its Preliminary (March 2012) and Detailed Design Reviews (Optics: May 2013; Full: December 2014). On May 2014 the UCM, as leader institution, signed the Full Detailed Design, Construction, and the Assembly, Integration and Verification contract with GRANTECAN S.A. for a target delivery date at GTC on December 2016. GTC/MEGARA shall fill a gap currently existing of a IFS facility providing high spectral resolution, wide FoV, and high sensitivity at the same time. Thus, MEGARA will be the first spectrograph capable of observing the emission coming from faintest and diffuse objects in a wide range of redshift providing the astronomer with unprecedented capabilities to explore the Universe: from the star forming regions, planetary nebulae and massive stars in our galaxy and nearby galaxies and being the next workhorse instrument for the GTC scientific community. See the MEGARA IFU during its assembly in Figure 2.11.

The following subsections summarize my contribution to the MEGARA project, in particular I will make special emphasis on the two MEGARA aspects in which I was more deeply involved: the MEGADES project, (*MEGARA Galaxy Disks Evolution Survey*; see Section 2.5.1) and the MEGARA MOPSS tools, (*MEGARA Observing Preparation Software Suite*; see Section 2.5.2).

2.5.1 MEGARA Science

The scientific interests that have driven the MEGARA design can be grouped in two categories: the study of Galactic and extragalactic nebulae and the study of point sources (or close to point sources) with intermediate-to-high surface densities. Among the former we include the study of planetary nebulae, nearby galaxies, and the high-redshift IGM (diffuse Lyman-α) emission and among the latter Galactic open stellar clusters, resolved stellar populations in Local Group galaxies, intermediate-redshift dwarf and starburst galaxies, and high-redshift cluster galaxies are the main subject of our research activities. What is common to all the scientific interests of our Science Team is the need for an intermediate-to-high spectral resolution. In some of the cases above this need is a mere consequence of velocity resolution (kinematics) but in many cases is given by the need of reducing line blending, either directly when lines from different elements ought to be measured in stars or via a reduction in the degeneracy of the properties of composite stellar populations. The MEGARA Science Team encompasses researchers with a broad range of scientific interests belonging to institutions of all members of the GTC community (Spain, Mexico and UF). This guarantees that, as a facility instrument, MEGARA will also successfully serve to the interests of the entire astronomical communities of the GTC Consortium members. Figure 2.12 summarizes the main lines of research behind MEGARA and the corresponding senior team members with interest in each of these topics.

Among the study of astrophysical nebulae, our team has a strong interest in the understanding of the evolution of galaxy disks through the analysis of the velocity ellipsoids and the 2D spatial distribution of spectral indices and chemical abundances of stars and gas. This goal constitutes the core of *MEGADES*, the *MEGARA Galaxy Disks Evolution Survey* in which I am deeply involved. This analysis is fundamental to disentangle the roles of the secular processes involved in the shaping of the present-day properties of disks, i.e. in-situ star formation, stellar migration and satellite accretion and (minor-) merging among others. In addition to the study of the unresolved stellar populations in galaxy disks, MEGADES will also allow pursuing the study of the interplay between the massive-star formation and the interstellar medium and the long-standing problem of the abundance discrepancies in H II regions and the potential identification and analysis of chemo-dynamical phenomena. This study will be complemented with the MOS observations of resolved-stars in the Local Group galaxy M 33. Its inclination, location in the sky and relatively undisturbed morphology makes of the M33 disk an ideal laboratory to analyze the 2D distribution of single-star abundances and kinematics that could provide further clues on the role of the different processes that shape the photometric, chemical and dynamical evolution of galaxy disks. In this context, as a pilot study for the MEGARA science cases, I have

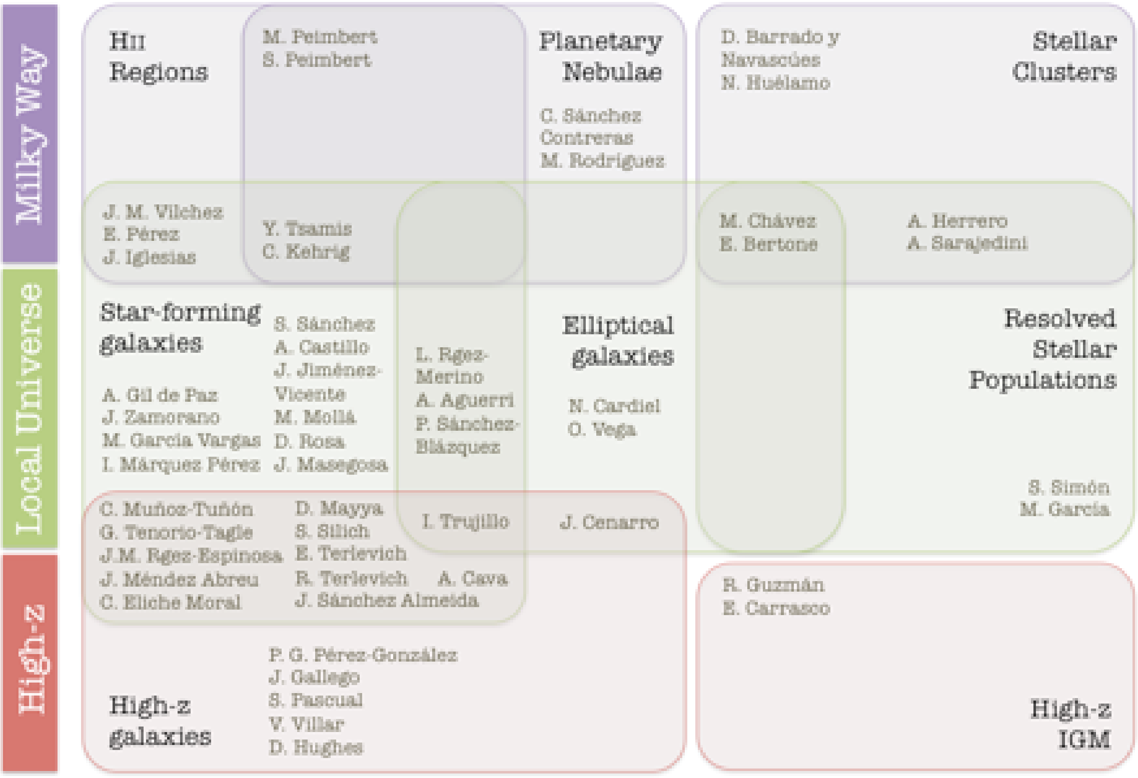

Figure 2.12: Areas of main scientific interest of the MEGARA Science Team. We note that these include most of the areas of research in Astronomy (excluding the study of the Sun and the Solar System). The main interest of the UPM group is e-Science with focus in Astronomy, which, as a general discipline, shares interests with all of the above.

analyzed the full bi-dimensional spectral cube of the nearby spiral galaxy NGC 5668 (as described in Chapter 3). In summary, we combine the PPak-IFU data with panchromatic broad-band images to obtain the radial profiles and colors and we have compared them with the chemo-spectrophotometric evolutionary models. In this regard, we use the PPak data to investigate the properties of the H II regions within NGC 5668 and the main result that we find is the discovery of a bar in its formative stages that produces an unusual flattening in metallicity gradient suggesting that not all galaxies follow the smooth growth prediction of the *inside-out* scenario for the formation of disks. This work has served as a proof of concept of what CALIFA first and soon MEGARA, in combination with GTC, can tells us on the evolution of galaxy disks.

2.5.2 MEGARA Control System

As a rather complex instrument, with both IFU and MOS capabilities, spectral resolutions reaching R=20,000 and up to 11 spectral setups simultaneously available for each of its modes, MEGARA includes a large number of work packages, among which the MEGARA Control System (MCS) is one of the most critical. The MCS includes the hardware and software components that are required to provide the MEGARA control and the integration of the instrument in the GTC Control System (GCS). The MCS should also provide the capabilities to move the different mechanisms of the instrument, to readout the data from the detector controller, the necessary routines for the Inspector Panels and the Sequencer strategies. Finally, the MEGARA project includes the design and development of the software tools that shall be developed by the MEGARA Consortium to facilitate the preparation of the observing programs and the exploitation of the data provided by the instrument to the GTC community, which is referred as the MEGARA Observing Preparation Software Suite (MOPSS).

The MOPSS is composed by the Exposure Time Calculator (ETC), the Simulator, the Fiber Assignment (FMAT) and the Fiber MOS Positioning (FMPT) Tools , the Off-line MEGARA Data Reduction Pipeline and the On-line Pipeline. The MCS is being designed to fulfill, as much as possible the GCS standards and shall be delivered to GTC in order to be integrated in the GCS. The On-line MEGARA pipeline routines and quick-look application shall be developed by MEGARA and the GTC control team will integrate these within the GCS. MEGARA MOPSS and the Off-line MEGARA Data Reduction Pipeline shall be developed as stand-alone tools that shall not follow the GTC standards and shall be made available to the MEGARA Science Users. More specifically, within the MCS Team, I was collaborating in the development of different software packages of the MOPSS softwares that will control and monitor the internal activities of the instrument. On the other hand, thanks to the expertise acquired within the CALIFA project, I was involved in the Data Reduction Pipeline components implemented to reduce and analyze the acquired data that runs integrated in the GTC Control System. The main objectives of both tools are the following:

1. The MEGARA ETC tool shall simulate the signal-to-noise (S/N) ratios that will be obtained for the continuum and a spectral line of a target for a given exposure time, MEGARA setup, and night atmospheric conditions. The tool is intended to derive also SNRs versus wavelength in the case that a source spectrum is provided as input, as well as the expected MEGARA output spectra in one fiber assumed to be centered on the source.

2. The MEGARA Simulator tool is intended to create a set of images simulating the output of the MEGARA instrument depending on the observational strategy for a given input source. The tool includes the expected sky contribution to the final spectrum, considers the wavelength range of the selected MEGARA configuration, and simulates the output observation of the provided input source as a function of the input observational parameters chosen by the user. The Simulator returns a MEGARA frame in FITS format with the simulated spectra corresponding to the projection of each spaxel on the detector plane, including the expected sky contribution and the effects inherent to the observation (bias, flat, geometrical distortion, non-linear dispersion, crosstalk, differential atmospheric refraction), as well as its RSS frame.

3. The Fiber Assignment Positioning tool will allow the user to prepare a Configuration Plan composed for several Configuration Blocks for the MEGARA MOS mode by assisting the user in the assignment of their sources to the different in-use robotic positioners of the MEGARA MOS (up to 92 positioners). The current release supports both manual and automatic assignment through a user-friendly GUI.

4. The Fiber MOS Positioning tool shall determine the optimal assignment of the 92 positioners used in the MOS mode for an input list of source coordinates in the 3.5' × 3.5' to cover as many sources as possible, and provide in which order must be the positioners be moved to avoid collisions among adjacent ones (minimizing the time to configure them at the same time).

5. The MEGARA Data Reduction Pipeline (MDRP) supply the users with data corrected from instrument signatures, which can be used at different stages of data acquisition and analysis. These processed data will be in physical units, from which the users can start their scientific analysis, without the need of additional data processing. The user shall be able to modify the predefined parameters of the MDRP to customize data processing. The On-line MEGARA pipeline routines shall be provide part of the off-line functionality (MEGARA shall provide these routines to GTC to facilitate the GTC control team the development of this application).

As said before, my principal technical contribution within the MEGARA project was on the MEGARA Simulator. The last version of the MEGARA Simulator provides simulated output CCD frames that would be taken with MEGARA for a given instrumental configuration, atmospheric conditions, and flux distribution in the observed input source. The MEGARA Simulator is written in Python and it has been created to be multi-platform and easy to install. The required supporting software exists in a precompiled form for most platforms (Unix, Linux, MacOSX, MS Windows). Apart from testing MEGARA for the proposed science cases, this tool will be extremely useful for the development of the MEGARA data reduction pipeline, because the pipeline must reproduce the operations done by the Simulator but in the inverse direction (starting from raw CCD frames data provided by MEGARA, it must obtain the reduced and calibrated 3D datacube of the source). Therefore, a definitive quality control test to the pipeline will be to use as input simulated MEGARA CCD frames, to see if the reduced data resulting from the pipeline are similar to the simulated data obtained with the Simulator at each step.

The MEGARA Simulator consists on two independent packages: the Image Simulator and the Simulator, as shown in the upper panel of Figure 2.13. The Image Simulator creates the 2D RSS from

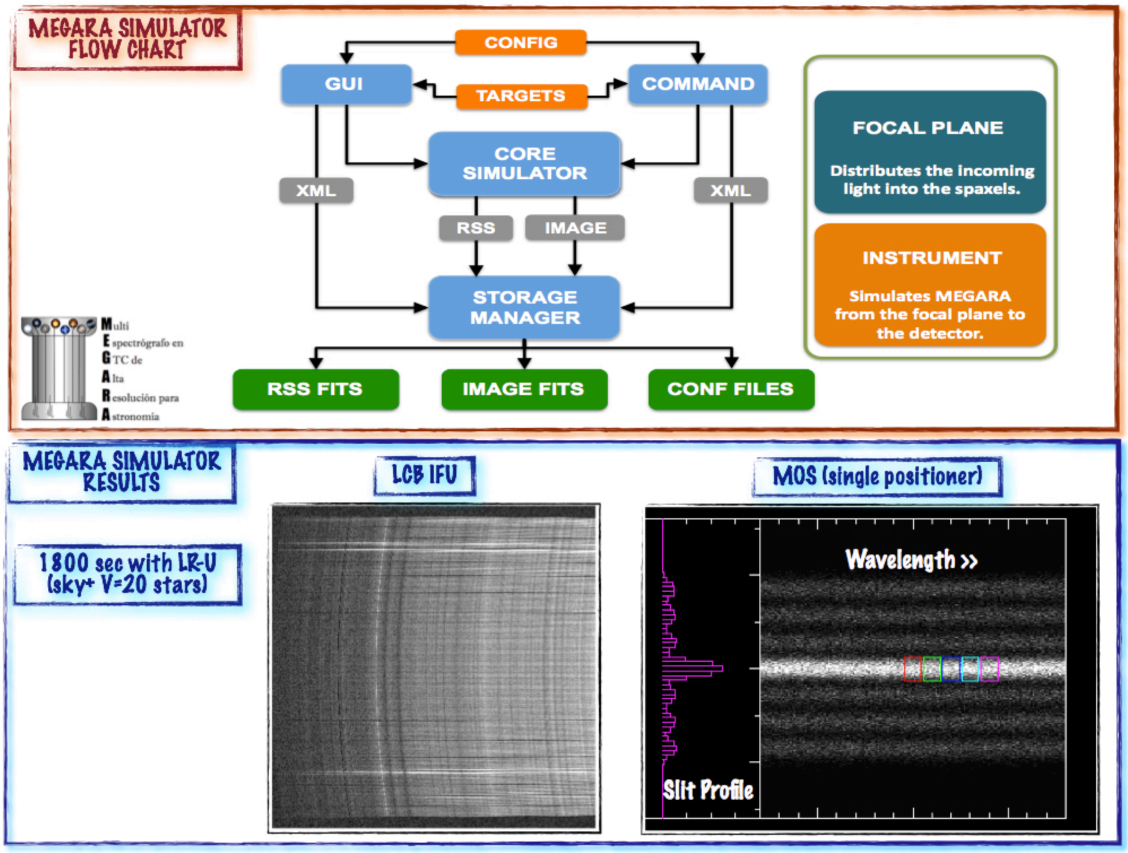

Figure 2.13: *Top panel:* MEGARA Image Simulator flow chart. *Bottom panel, Left:* Simulated MEGARA CCD frame of two stars with V=20 mag, with the blue low resolution (LR-U VPH with R∼6000). *Right:* Simulated MEGARA light distribution of a point source in the 7 fibers of a MOS mini-bundle.

the target object. Basically, this package determines which fraction of the object's emitted light passes through each fiber. Only the differential atmospheric refraction effect is considered at this stage. This 2D RSS feeds the simulator. The Simulator creates a sky+object model, considering the VPH wavelength range and resolution, as well as all transmission curves and telescope characteristics, includes the different noise sources in the resulting sky+object RSS, creates the corresponding MEGARA CCD frame, and includes the effects associated to the observation that are removed through a typical reduction process (bias, flat, geometrical distortion, non-linear dispersion, cross-talk and soon also cosmetic defects and cosmic rays). The MEGARA Simulator works in a command-line mode at present. Future versions will also incorporate a GUI, but the command-line tool will be kept due to its versatility. Some preliminary results are shown in the lower panel of Figure 2.13. In this case we have simulated the observation of two calibrating stars with an apparent magnitude in the Johnson V band of 20 mag for both LCB IFU and MOS modes.

3

IFS and multi–wavelength imaging of NGC 5668: an unusual flattening in metallicity gradient

Resumen

El escenario más aceptado para la evolución de los discos de galaxias espirales es el que se conoce como escenario *inside-out* según el cual, tras una etapa dominada por numerosas fusiones de galaxias espirales, donde se formarían tanto la componente de bulbo como el disco grueso. Además, la formación de estrellas tendría lugar de forma secular en un disco delgado rico en gas. Este disco delgado contendría la mayor parte del momento angular del sistema y mostraría una formación estelar retrasada en sus partes externas (de mayor momento angular) comparada con las partes internas. Esto daría lugar a la existencia a perfiles de brillo superficial exponenciales, gradientes de color y metalicidad negativos, lo que está de acuerdo con las propiedades más notorias de los discos de galaxias espirales.

Existen, sin embargo, un gran número de propiedades observacionales, especialmente en las parte más externas de los discos, que no se pueden explicar dentro de este escenario simple de evolución *inside-out*. A fin de probar este escenario en detalle e intentar explicar el origen de algunas de estas discrepancias es necesario llevar a cabo un análisis combinado de las abundancias químicas de los discos y de las propiedades fotométricas de los mismos. Este análisis, además, debe hacerse con resolución espacial y en dos dimensiones si se pretende obtener más información sobre los mecanismos responsables de la evolución de los discos, dentro o no del escenario *inside-out*. A fin de determinar las abundancias metálicas de los discos es especialmente útil el estudio de las regiones H II presentes en ellos, debido a que nos pueden servir para determinar las abundancias de oxígeno (e incluso cocientes de abundancias N/O) hasta grandes distancias (tanto galactocéntricas como heliocéntricas). Como se mencionó anteriormente este análisis debe combinarse con medidas de la distribución de luz en diferentes bandas fotométricas, desde el UV hasta el infrarrojo, a fin de separar los efectos de extinción de aquellos asociados a la evolución de la población estelar y así poder combinar la información sobre esta con la proporcionada con el análisis de abundancias.

Con este objetivo, este capítulo describe nuestro esfuerzo para añadir una dimensión más al clásico estudio basado únicamente en datos de fotometría multi-banda en el caso de la galaxia espiral cercana NGC 5668. Para esta galaxia disponemos de datos de espectroscopía 3D de la IFU PPak instalada en el telescopio de 3.5m de Calar Alto y de datos de imagen UV, óptica e infrarroja de las misiones/exploraciones GALEX, SDSS y Spitzer, respectivamente. Los principales resultados que se

encuentran son una atenuación media del gas ionizado de $A_V \sim 1$ mag, y que esta es mayor que la del continuo por un factor 3. Respecto a la abundancia de oxígeno, se encuentra que mientras que dentro de una distancia galactocéntrica de $\sim$4.4 kpc esta sigue un gradiente típico observado en otras galaxias espirales, pero más allá de esta distancia el gradiente se aplana. Además, se ha llevado a cabo la comparación de los perfiles multi-frecuencia de brillo superficial de esta galaxia con las predicciones de los modelos espectro-fotométricos y químicos de Prantzos & Boissier (2000; desarrollados en el contexto del escenario *inside-out*). Tanto las desviaciones de los perfiles de color como la forma de la distribución radial de metalicidad sugieren la presencia de un mecanismo secundario que no está incluido dentro de los mecanismos considerados en este modelo. Este mecanismo parecer ser la trasferencia radial de gas (con la consiguiente alteración de la historia de formación estelar) inducida por la presencia de una barra joven. Este estudio ha sido publicado en la revista Astrophysical Journal en el año 2012 (Volumen 754, pág. A61).

3.1 Introduction

As discussed in Chapter §1, the most successful picture of galaxy formation is the hierarchical ΛCDM scenario in which galaxy disks are growing from *inside-out*. Although this scenario has been around for a long time now, it has only been recently that the inside-out growth of galaxy disks has been applied and quantified beyond the Milky Way. It is widely known that measuring chemical abundances can infer details about the thermonuclear reactions that occurred in the young ionizing stars or in the case of H II regions to discover details of the chemical evolution of the ISM in the host galaxy. Furthermore, ionized nebulae are remarkably efficient machines for converting ultraviolet continuum energy from OB stars, originally diluted over wide bandpasses, into a few narrow, intense, optically-thin emission lines. Their relative structural simplicity and their characteristic emission spectrum have made them ideal laboratories to study the physical and chemical properties of the gas and stars in our Galaxy and beyond. In this Thesis, I shall focus on the determination of the gas phase abundances from the emission lines of H II regions located in nearby galaxies; in particular I will describe the pilot study of the galaxy NGC 5668 in this Chapter while the CALIFA sample of galaxies will be analyzed in Chapters §4 and §5. These works demonstrate the strength and the urgency of using IFS data in deriving the 2D distribution of metallicity of an entire galaxy to study their metallicity enrichment and evolution as well to test fundamental relations such as the empirical metallicity calibrations or the theoretical prediction of the inside-out scenario.

The complexity of the IFS data makes advisable to start with a pilot study where all the tools and analysis techniques to be later employed in a statistically significant sample are developed. The key players in this Thesis constitute one of the most important component of the ISM within galaxies: H II regions. Although a comprehensive review of all the properties of extragalactic H II regions is beyond the scope of this Thesis, a brief discussion is needed to provide a context for the subject of the measurement of abundance gradients. The ISM of a galaxy consists of the gas and dust distributed between the stars. It is the final result of the mixture of gas remaining from the formation of the galaxy, gas ejected by stars, and gas accreted from outside (such as infalling diffuse gas or the interstellar medium of other galaxies that have been accreted). The interstellar gas is very diffuse − the densest case is the Galactic gas where the particle number density is $\sim 10^3$ to 10^9 atomic nuclei m^{-3} − and could be observed in different forms as single neutral atoms, or some is in the form of simple molecules, while some exists as ions. Whether gas is found as atoms, molecules or ions depends on its temperature, density and the presence of radiation fields, primarily the presence of ultraviolet radiation from nearby stars. Qualitatively speaking, the chemical composition is about 90% hydrogen, 9% helium plus a trace of heavy elements (expressed by numbers of nuclei). Note that the oxygen alone constitutes nearly 50% by mass of the elements heavier than helium on which we are particularly interested (Dinerstein 1990).

There are different types of extragalactic H II regions according to their environments. These include: (1) disk H II regions in spiral (on which we are particular interested) and irregular galaxies; (2) gas-rich dwarf irregular galaxies with spectra dominated by that of H II regions; and (3) nuclear and near-nuclear regions sometimes called “starburst” or “hotspot” H II regions (e.g. Kennicutt, Keel, and Blaha 1989). As claimed above, I will particularly focus on the extragalactic H II regions, the hot component of the ISM within disk galaxies (excluding the hot coronal component). They are the special places where hot stars produces a large flux of ultraviolet photons, and any Lyman continuum photons (i.e. photons with λ<912Å) will photoionise hydrogen producing a region of H+ (i.e. H II ions). This process produces a huge variety of observable emission lines and continua in the ultraviolet, optical, infrared and radio parts of the spectrum; their interpretation will be exhaustively described in Chapter §4. Here, I will describe how we can constrain and test the inside-out scenario of galaxy disk formation by making use of 3D spectroscopy of a large sample of H II regions.

As extensively described in Chapter §1, the inside-out scenario predicts a faster formation of the inner disk relative to the outer part that naturally results in a decline with the galactocentric distance of the metal content (among other properties) mainly due to the longer collapsing timescales of the outermost region of galaxy disks. Therefore, negative metallicity gradients rise spontaneously from this kind of disk growth via radially dependent gas infall and star formation rate (Matteucci & Francois 1989). From the theoretical point of view, the shape of the gradient can be a key ingredient for models of galaxy formation. For this reason, a chemical evolution model has been included in modern cosmological simulation codes as an attempt to explain the existence of radial gradients (and the G-

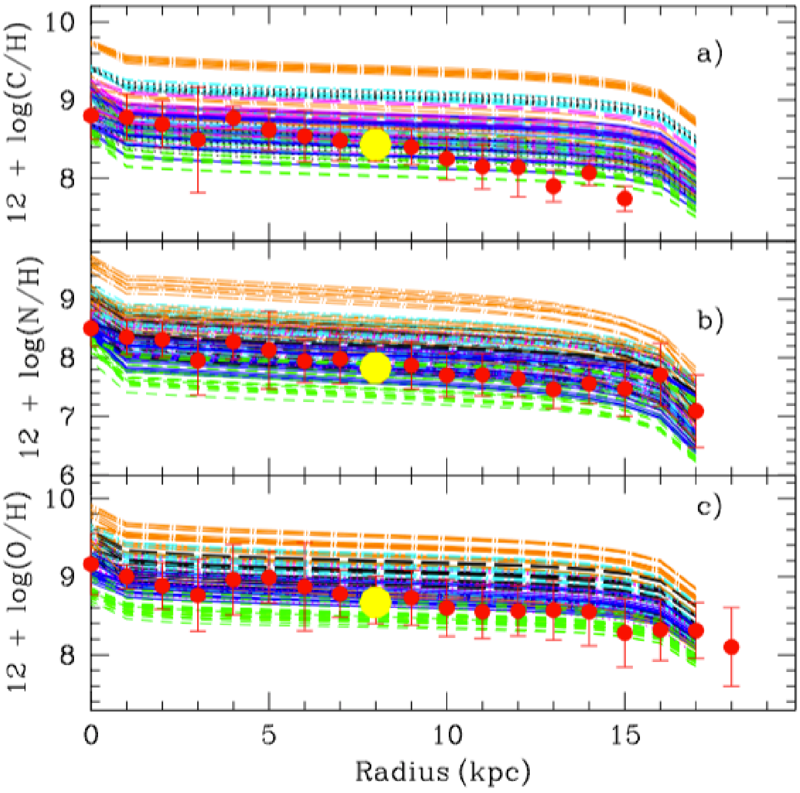

Figure 3.1: Theoretical radial distributions of elemental abundances expressed in units of 12+log(X/H): a) C, b) N and c) O, in the case of a MWG disk for 144 models. The observational data are plotted as red dots with error bars. The larger yellow dots represent the Solar abundance. Color line coding depends on which IMF is assumed to compute the chemical evolution model (see the original work of Mollá et al. 2015 for a detailed explanation of the plot and grids).

dwarf metallicity distribution in our Milky Way) as well as the classical closed-box model (Pilkington et al. 2012). As an example in Fig 3.1, from the recent work of Mollá et al. (2015), the predicted radial abundance gradients in the case of a Milky Way-like galaxy (i.e. late type spirals, MWG hereafter) are shown for a set of 144 galactic chemical evolution models. The chemical evolution models shown in this figure are computed within the same consistent framework: same total mass, molecular cloud and star formation efficiencies, and infall prescriptions. Different combinations of stellar yields for massive stars (6 sets), low + intermediate mass stars (4 sets), and IMFs (Salpeter (1955); Miller & Scalo (1979); Ferrini et al. (1990); Kroupa (2002); Chabrier (2003) and Maschberger (2013)) are considered in this work. These theoretical results nicely match with the observational data (red dots) compiled by these authors and show that the decline of the metal content is mainly due by the combined effects of a SFR and an infall of gas which vary with the galactocentric radius within a galaxy.

Since the seminal work of Searle (1971), who first found radial abundance gradients in nearby galaxies using collisionally excited lines (CELs, Kennicutt et al. 2003) of oxygen and nitrogen (the primary coolants in these H II ionized regions), a lot of work has been done and several relations have been proposed in order to get a more complete vision of the metallicity distribution within disk galaxies. There are a number of methods in the literature for estimating the metal content of a galaxy and in Chapter §4 I will provide a more detailed description of many of these. Here, as an example of the complexity of this topic, is worth to emphasize that in the case of our MW, the ISM oxygen abundance has been derived using: open clusters (e.g. Janes 1979; Twarog et al. 1997; Friel et al. 2002; Yong et al. 2012; Frinchaboy et al. 2013), Cepheids (e.g. Caputo et al. 2001; Lemasle et al. 2013; Korotin et al. 2014), OB stars (e.g. Fitzsimmons et al. 1990; Rolleston et al. 2000; Daflon & Cunha 2004), red giant stars (e.g. Hayden et al. 2013; Boeche, et al. 2014; Bovy et al. 2014), planetary nebulae (e.g. Maciel et al. 2003; Pottasch & Bernard-Salas 2006; Stanghellini & Haywood 2010; Henry et al. 2010), and H II regions (e.g. Peimbert 1978; Shaver et al. 1983; Afflerbach et al. 1997; Deharveng et al. 2000; Rudolph et al. 2006; Esteban et al. 2013). In the case of NGC 5668 or the CALIFA galaxies, the access to all these sources of chemical information is difficult and our main tool to trace the metallicity behavior of our galaxies will be the measurements of the optical metal-sensitive line fluxes within H II regions. Indeed, H II regions are *fossil records* of the star formation activity and their history of chemical enrichment.

Another important result from the observational side has recently come from Sánchez et al. (2014, S14 hereafter) where we have demonstrated that up to $\sim$2 disk effective radii all galaxies within the CALIFA sample present a gas-phase oxygen abundance radial gradient with a similar slope (α=$-$0.12 dex/R$_{eff}$), when normalized to the effective radius. In Fig 3.2 is presented an updated version of the universal gradient published in S14, now computed using 550 CALIFA galaxies together with the new calibration proposed in Marino et al. (2013). This result is in agreement with the predictions of the standard inside-out scenario on a relatively quick self enrichment with oxygen abundances and an almost universal negative metallicity gradient once this is normalized to the galaxy optical size (see the theoretical predictions of Boissier & Prantzos 1999a, 2000). However is still controversial whether the slope of the oxygen gradient is constant all over the disk or not. For instance, a flattening in the outskirts of spiral galaxies has been claimed by several author both in case of our Milky Way (Vilchez & Esteban (1996) and Fich & Silkey (1991)) as for nearby galaxies, (e.g. Bresolin et al. 2009; Yoachim et al. 2010; Rosales-Ortega et al. 2011; Bresolin et al. 2012 and Marino et al.2012) and likewise chemodynamical models also predict a plateau of the abundance gradient at large galactocentric distance. Finally, the theory of viscous evolution of a star-forming disk (e.g. Lin & Pringle 1987, Ferguson & Clarke 2001) predicts an angular momentum redistribution and gas flows, which in turns could lead to a flattening in the outer part of the radial gas- phase abundance gradient within disks as well.

With the purpose of fully understand which is the actual metallicity trend, this Thesis aims at adding another dimension to the study of nearby spiral galaxies thanks to the use of IFU data. In this pilot study, we combine our PPak data with images covering a wide wavelength range from the ultraviolet to the infrared. Thus, in order to improve our understanding of the mechanisms that drive the evolution of disk galaxies, we start by analyzing the full optical bi-dimensional spectral cube of the nearby spiral galaxy NGC 5668, obtained with the PPak IFU at the CAHA 3.5 m telescope. From these data we obtain the 2D spatial distribution maps of the attenuation of the ionized gas, and chemical abundances of oxygen. We find a mean ionized-gas attenuation of $A_V \sim$1mag, with the gas attenuation appearing larger than the continuum attenuation by a factor of 3. With respect to the oxygen abundance, we find that, while inwards of $\sim$4.4kpc the derived O/H ratio follows the radial gradient typical of the disks of spiral galaxies, beyond this radius it flattens out. In addition, the multi-wavelength surface brightness profiles of NGC 5668 are compared with those predicted by chemo-spectrophotometric evolutionary models of galaxy disks by Prantzos and Bossier (2000) in the context of the inside-out scenario of disk formation. Both the deviations of the color profiles and the shape of the metallicity radial distribution indicate that a secondary mechanism, possibly gas transfer induced by the presence of a young bar, must have played a role in shaping the recent chemical and star formation histories of NGC 5668 beyond what is predicted by the inside-out scenario. This study has been published in the Astrophysical Journal in 2012 (Volume 754, A61) under the title "Integral Field Spectroscopy and multi-wavelength imaging of the nearby spiral galaxy NGC 5668: an unusual flattening in metallicity gradient" and it demonstrates the strength of the combination of IFU and multi-wavelength imaging data in deriving the physical properties of H II regions in nearby galaxy as well the power in constraining the theoretical model as for NGC 5668 that does not follow the simplistic (somewhat naive) prediction of the inside-out scenario.

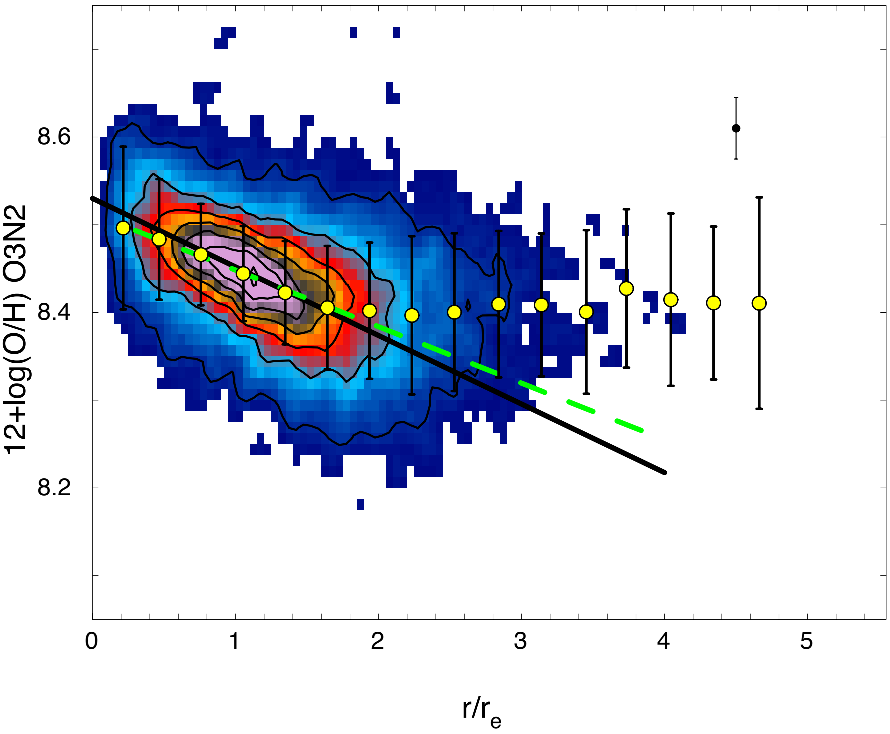

Figure 3.2: Radial distribution for the oxygen abundance derived using the O3N2 indicator and the calibration proposed by Marino et al. (2013), after scaling to the average value at the disk effective radius for each galaxy. Note that, the universal slope found here is α=$-$0.06 dex/R$_{eff}$ and it was obtained using more than 10,000 CALIFA H II regions (S. F. Sánchez, private communication). The image and contours show the density distribution of H II regions in this parameter space. The solid-yellow points represent the average oxygen abundances, with their corresponding standard deviations. The average error of the derived oxygen abundance (without considering systematic errors) is shown by a single error bar located a the top-right side of the panel. The dashed-green line shows the result of the best linear regression to the data.

3.2 Marino et al. (2012) ApJ, 754, 61

INTEGRAL FIELD SPECTROSCOPY AND MULTI-WAVELENGTH IMAGING OF THE NEARBY SPIRAL GALAXY NGC 5668*: AN UNUSUAL FLATTENING IN METALLICITY GRADIENT

R. A. Marino[1,2], A. Gil de Paz[1], A. Castillo-Morales[1], J. C. Muñoz-Mateos[3], S. F. Sánchez[2], P. G. Pérez-González[1,6], J. Gallego[1], J. Zamorano[1], A. Alonso-Herrero[4], and S. Boissier[5]
[1] CEI Campus Moncloa, UCM-UPM, Departamento de Astrofísica y CC. de la Atmósfera, Facultad de CC. Físicas, Universidad Complutense de Madrid, Avda. Complutense s/n, 28040 Madrid, Spain; ramarino@fis.ucm.es
[2] Centro Astronómico Hispano Alemán, Calar Alto (CSIC-MPG), C/Jesús Durbán Remón 2-2, E-04004 Almeria, Spain
[3] National Radio Astronomy Observatory, 520 Edgemont Road, Charlottesville, VA 22903-2475, USA
[4] Instituto de Fisica de Cantabria, CSIC-UC, Avenida de los Castros s/n, 39005 Santander, Spain
[5] Laboratoire dÁstrophysique de Marseille, OAMP, Université Aix-Marseille & CNRS UMR 6110, 38 rue Frédéric Joliot-Curie, 13388 Marseille cedex 13, France
Received 2012 January 10; accepted 2012 May 18; published 2012 July 6

ABSTRACT

We present an analysis of the full bidimensional optical spectral cube of the nearby spiral galaxy NGC 5668, observed with the Pmas fiber PAcK Integral Field Unit (IFU) at the Calar Alto observatory 3.5 m telescope. We make use of broadband imaging to provide further constraints on the evolutionary history of the galaxy. This data set will allow us to improve our understanding of the mechanisms that drive the evolution of disks. We investigated the properties of 62 H II regions and concentric rings in NGC 5668 and derived maps in ionized-gas attenuation and chemical (oxygen) abundances. We find that while inward of $r \sim 36''$ ~ 4.4 kpc ~ 0.36 $(D_{25}/2)$ the derived O/H ratio follows the radial gradient typical of spiral galaxies, the abundance gradient beyond $r \sim 36''$ flattens out. The analysis of the multi-wavelength surface brightness profiles of NGC 5668 is performed by fitting these profiles with those predicted by chemo-spectrophotometric evolutionary models of galaxy disks. From this, we infer a spin and circular velocity of $\lambda = 0.053$ and $v_c = 167$ km s^{-1}, respectively. The metallicity gradient and rotation curve predicted by this best-fitting galaxy model nicely match the values derived from the IFU observations, especially within $r \sim 36''$. The same is true for the colors despite some small offsets and a reddening in the bluest colors beyond that radius. On the other hand, deviations of some of these properties in the outer disk indicate that a secondary mechanism, possibly gas transfer induced by the presence of a young bar, must have played a role in shaping the recent chemical and star formation histories of NGC 5668.

Key words: galaxies: abundances – galaxies: evolution – galaxies: individual (NGC 5668) – galaxies: ISM – galaxies: kinematics and dynamics – techniques: spectroscopic

Online-only material: color figures

1. INTRODUCTION

The evolution of galactic disks is one of the most important and yet not fully understood topics in extragalactic astronomy. Despite significant progress in the recent past regarding our understanding of the history of both thick and thin disks, important questions remain unanswered: How old are the disks seen in the spiral galaxies today? How did they chemically evolve? Are they growing inside-out, as proposed to explain the color and metallicity gradients of the Milky Way (MW)? Do they have an edge? How efficient is stellar radial diffusion?

Until recently, the study of the properties of spiral disks has been limited to broadband imaging data and/or long-slit spectroscopy, which has severely limited the reach of previous works. Radial color profiles have been widely used to probe the inside-out scenario of disk evolution (Bell & de Jong 2000; MacArthur et al. 2004; Pohlen & Trujillo 2006; Muñoz-Mateos et al. 2007). However, radial variations of metallicity and dust extinction conspire to create color gradients similar to those due to changes in stellar age alone. Analysis of color–magnitude diagrams (CMDs) allows for more robust measurements of stellar ages as a function of radius, but these kinds of studies are currently limited to very nearby galaxies where individual stars can be resolved (de Jong et al. 2007; Barker et al. 2010; Gogarten et al. 2010). Long-slit spectra overcome the problems of broadband photometry, but at the expense of focusing along a pre-defined spatial axis (Yoachim & Dalcanton 2008). Our effort is committed to adding another dimension for studying nearby spiral galaxies thanks to the use of wide-field Integral Field Spectrometers (IFS) combined with images covering a wide wavelength range from the ultraviolet to the infrared. This paper presents an analysis of the Integral Field Unit (IFU) data taken for NGC 5668 within a more ambitious project aimed at mapping a sample of a dozen nearby galaxies included in the *Herschel* Galaxy Reference Survey (Boselli et al. 2010) using mosaics obtained with two of the largest IFUs available to date: the Pmas fiber PAcK (PPAK) IFU of the Potsdam Multi-Aperture Spectrophotometer (PMAS) at the Calar Alto (CAHA) 3.5 m telescope and the VIsible MultiObject Spectrograph at the ESO Very Large Telescope.

The evolution of galaxy disks is a complex process because many factors are mechanisms that might alter their photometric, chemical, and kinematical properties: minor mergers, the formation of bars or rings, density waves, stellar diffusion, gas infall, and, in the case of galaxies in clusters, also ram pressure stripping and galaxy harassment. Despite this rather discouraging scenario, a picture for the formation of disks has

---

* Based on observations collected at the German-Spanish Astronomical Center, Calar Alto, jointly operated by the Max-Planck-Institut für Astronomie Heidelberg and the Instituto de Astrofísica de Andalucía (CSIC).

[6] Associate Astronomer at Steward Observatory, University of Arizona, AZ, USA.

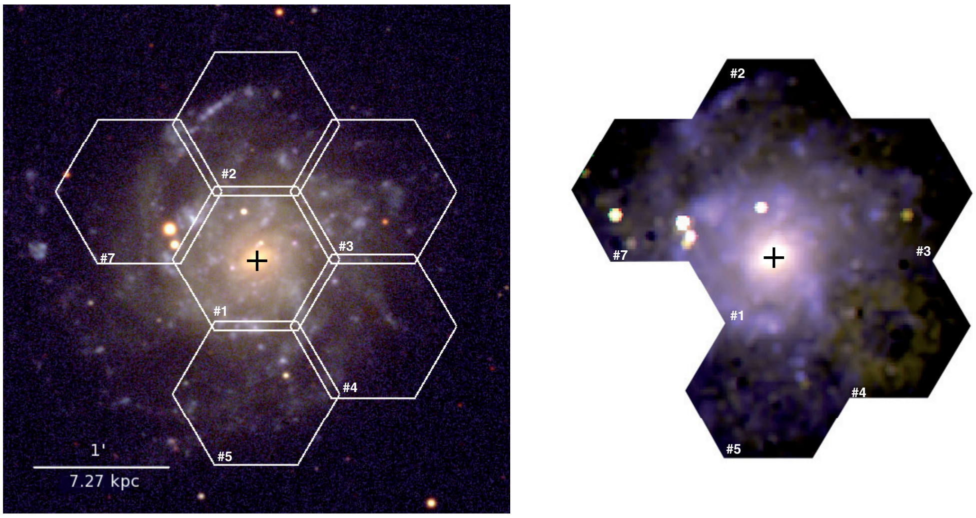

Figure 1. Left: SDSS optical *ugr* image (from 4458 to 7706 Å) of NGC 5668 centered at R.A.(2000) $14^{\mathrm{h}}33^{\mathrm{m}}24\overset{\mathrm{s}}{.}3$ and decl.(2000) $+04^{\circ}33'24\overset{''}{.}3$. North is up and east is to the left. Plate scale is $0.396''\mathrm{pixel}^{-1}$. Right: synthetic false-color image obtained from the PPAK data cube and the response curves of the SDSS *u*, *g*, and *r* filters. Note that the luminous spot in pointing 7 is caused by cross-talk effects from a nearby (on the CCD) field star. Plate scale is $1''\mathrm{pixel}^{-1}$ in this case. Center and orientation are the same as in the left panel.

emerged in recent years that attempts to explain most of their observational properties: the inside-out formation scenario. Although this scenario has been around for a long time now, the inside-out growth of galaxy disks has only recently been applied and quantified beyond the MW. Both the extinction-corrected color gradients in nearby galaxies (Muñoz-Mateos et al. 2007) and weak dependence of the mass–size relation with redshift (Trujillo et al. 2004, 2006; Barden et al. 2005) support an inside-out scenario for the evolution of disks. However, there are several observational results that conflict with or, at least, cannot be explained by this otherwise elegant scenario. In this regard, many nearby spiral disks show that while the color and metallicity gradients of the inner disk are compatible with the inside-out scenario, beyond the star formation threshold radius (Martin & Kennicutt 2001) the gradients flatten and even reverse by getting redder toward the outer regions (Bakos et al. 2008; Azzollini et al. 2008; Vlajić et al. 2009). In the specific case of the chemical abundances, the models based on the standard inside-out scenario of galaxy disk formation predict a relatively quick self-enrichment with oxygen abundances one-tenth the solar value after only 1 Gyr of evolution (Boissier & Prantzos 1999). These models also predict an almost universal negative metallicity gradient once this is normalized to the galaxy optical size d[O/H] of ~ -0.8 dex/R_{25} (Prantzos & Boissier 2000). Regarding this, the few observational abundance measurements obtained to date in the outer edges of disks show a flattening or even an increase in the abundance toward the outermost parts of the disk. This is also true in the case of the extended UV disks recently discovered by the *Galaxy Evolution Explorer* (*GALEX*) satellite (Gil de Paz et al. 2005, 2007; Thilker et al. 2007), which show oxygen abundances that are rarely below one-tenth the solar value. In this regard, Bresolin et al. (2009a) found that the normalized radial metallicity gradient in M83 changes from -0.030 dex kpc^{-1} in the inner disk to -0.005 dex kpc^{-1} in the outer parts (see also Bresolin et al. 2012). We also refer the reader to Yoachim et al. (2010) for another recent example in this same regard. Similar results were obtained on the metallicity gradient of the outer disk of NGC 300 from single-star CMD analysis (Vlajić et al. 2009).

In this work, we present the pilot study of the full bidimensional spectral cube of the nearby spiral galaxy NGC 5668 (Figure 1), obtained with the PPAK IFU at the CAHA observatory 3.5 m telescope. Despite the relatively modest collecting area of the CAHA 3.5 m telescope, the broad spectral coverage (from 3700 to 7000 Å) and adequate spectral resolution (R = 500) of PPAK with the V300 grating make this instrument one of the best tools for studying stellar populations, dust content, and physical conditions of the gas (temperature, density, and chemical abundances) in spatially resolved galaxies.

2. THE NEARBY SPIRAL GALAXY NGC 5668

NGC 5668 is a nearly face-on late-type spiral galaxy classified as an Sc(s)II–III type according to Sandage & Tammann (1987) and as an SA(s)d by de Vaucouleurs et al. (1991). There is a weak bar or oval inner structure $12''$ in size visible on the optical image, which leads to a small shoulder in the surface brightness profile published by Schulman et al. (1994). The outer disk (beyond $R = 100''$) is slightly asymmetric and more extended toward the north. For this work, we adopted a distance of ~25 Mpc, $(m - M) = 31.99$ mag, assuming a cosmology with $H_0 = 73$ km s^{-1} Mpc^{-1}, $\Omega_{\mathrm{matter}} = 0.27$, and $\Omega_{\mathrm{vacuum}} = 0.73$, for a recession velocity of 1813 km s^{-1} corrected to the reference frame defined by the 3 K microwave background radiation (Fixsen et al. 1996).[7] A broadband optical image of this galaxy from the Sloan Digital Sky Survey (SDSS; York et al. 2000) is shown in Figure 1. The galaxy presents an inclination of 18° and a total magnitude of $B = 12.13 \pm 0.03$ mag (Schulman et al. 1996). The total mass within the optical disk was estimated to be $5.7 \times 10^{10}\ M_{\odot}$ (Schulman et al. 1996).[8] NGC 5668 has been found to host a number of High-velocity Clouds (HVCs) by Schulman et al. (1996) using the Arecibo telescope. These authors detected high-velocity wings in the line shape, which were attributed to HVCs in the galaxy. HVCs and High Residual

---

[7] Source: NASA/IPAC Extragalactic Database (http://nedwww.ipac.caltech.edu/)

[8] They adopted a distance of 30 Mpc, consistent with a cosmology with $H_0 = 50$ km s^{-1} Mpc^{-1}.

Table 1
Global Properties of NGC 5668

Name	NGC 5668	Source
Morphological type	SA(s)d	de Vaucouleurs et al. (1991)
	Sc(s)II–III	Sandage & Tammann (1987)
R.A.(2000)	$14^{\rm h}33^{\rm m}24\overset{\rm s}{.}3$	Dressel & Condon (1976)
Decl.(2000)	$+04^\circ27'02''$	Dressel & Condon (1976)
B	12.13 ± 0.03 mag	Schulman (1996)
R	11.28 ± 0.01 mag	Schulman (1996)
L_B	$(2.7 \pm 0.6) \times 10^9\ L_\odot$[a]	Schulman (1996)
$L_{\rm H\alpha}$	$(1.0 \pm 0.3) \times 10^8\ L_\odot$[a]	Schulman (1996)
$L_{\rm FIR}$	$(5.8 \pm 1.2) \times 10^9\ L_\odot$[a]	Schulman (1996)
D_{25}	$3\overset{\prime}{.}3 \pm 0\overset{\prime}{.}2$	Jiménez-Vicente & Battaner (2000)
Heliocentric systemic velocity	1582 ± 5 km s^{-1}	Schulman (1996)
Distance	24.8 ± 1.7 Mpc	Fixsen (1996)
Inclination	18°	Schulman (1996)
P.A.	145°	Schulman (1996)
Total dynamical mass	$5.7 \times 10^{10}\ M_\odot$	Schulman (1996)
$E(B-V)$	0.037 mag	NED

Note. [a] Corrected for Galactic and internal extinction.

Table 2
NGC 5668 Observational Log

Pointing[a] (1)	Obs. Date (UT) (2)	Offsets (arcsec) (3)	Exposure Time (s) (4)	Air Mass (5)	Seeing (arcsec) (6)
1	2007 Jun 22	(0,0)	3 × 1000	1.21	1.1
2	2007 Jun 22	(0, 60)	4 × 1000	1.38	1.1
3	2007 Jun 22/23	(52, 60)	3 × 1000	1.75	1.1
7	2007 Jun 23	(52, −60)	3 × 1000	1.21	1.2
5	2007 Jun 23	(0, −60)	3 × 1000	1.36	1.2
4	2007 Jun 23/24	(−52, 60)	3 × 1000	1.74	1.0

Notes. (1) NGC 5668 pointings. (2) Observation date. (3) Pointing offsets; the original pointing of the telescope is at R.A.(2000) $14^{\rm h}33^{\rm m}24\overset{\rm s}{.}3$ and decl.(2000) $+04^\circ33'24\overset{''}{.}3$. (4) Exposure time in seconds and the number of images obtained for each pointing. (5) and (6) Mean air mass and seeing values.
[a] Pointing number 6 in the default mapping strategy used with PPAK at the CAHA observatory has offsets ($-52''$, $-60''$) relative to the center of the mosaic and was not observed in the case of NGC 5668.

Velocity Regions (residual velocity field and the shell/chimney candidates, regions which have a systematic deviation from rotational velocity) were found also in the ionized gas and interpreted as regions with vertical motions related to ongoing star-forming processes in the disk on the basis of Fabry–Perot Hα observations (Jiménez-Vicente & Battaner 2000). Schulman et al. (1996) also computed $L_{\rm FIR} = (5.8 \pm 1.2) \times 10^9\ L_\odot$ and $L_{\rm H\alpha} = (1.0 \pm 0.3) \times 10^8\ L_\odot$.

Such high FIR and Hα luminosities (and therefore star formation rates (SFRs)) would naturally result in a high supernova (SN) rate in this galaxy. Indeed, NGC 5668 is known as an "SNe factory" due to the discovery of multiple SN explosions in the recent epoch, namely, SN2004G (Nakano et al. 2004), and SN1952G, SN1954B (Boffi et al. 1999). The main properties of NGC 5668 are summarized in Table 1. NGC 5668 has also been recently observed by a number of instruments and facilities, including SAURON at the William Herschel Telescope (WHT), SDSS, *Spitzer* and as a part of the Medium-deep Imaging Survey of *GALEX*. This data set in combination with the PPAK mosaic obtained as part of this work should allow a very detailed analysis of the evolution and chemical-enrichment history of NGC 5668.

3. OBSERVATIONS AND DATA REDUCTION

3.1. IFS Observations

We have observed the nearly face-on spiral galaxy NGC 5668 with the PPAK IFU of PMAS at the CAHA observatory 3.5 m telescope (Kelz et al. 2006). The observations were carried out on 2007 June 22–24. We used the PPAK mode that yields a total field of view of $74'' \times 65''$ (hexagonal packed) for each pointing. We covered a total area of roughly 2×3 arcmin^2 with a mosaic of six PPAK pointings (see Figure 1). We used for the V300 grating covering a wavelength range of 3700–7100 Å(10 Å FWHM, corresponding to $\sigma \sim 300$ km s^{-1} at Hβ). With this spectral configuration, we covered all the optical strong emission lines in which we are interested. A total of 112 individual images were taken during the observing run. These images include 19 on-source frames for the 6 pointings obtained in NGC 5668 (see Table 2 for a summary of the science observations), bias frames (22 in total), sky flats (19), focus images (6), HgCdHe arcs (14), tungsten-lamp flats (14), observations of the spectrophotometric standard star Hz44 (3), and dome flats (6). The spatial sampling is determined by a hexagonal array of 331 densely packed optical fibers for the object (science fibers), 36 fibers for the sky, and 15 calibration fibers. Each fiber has a diameter of $2\overset{''}{.}68$ and a pitch of $3\overset{''}{.}458$ with a high filling factor in one single pointing (65%). For a more exhaustive description of the instrument, see Kelz et al. (2006).

3.2. IFS Data Reduction

The reduction procedure applied to NGC 5668 follows the techniques described in Sánchez (2006) using R3D. This is a software package developed specifically for the reduction of fiber-based IFS data, which has been extensively used for the reduction of PMAS data, in combination with IRAF[9] packages and Euro3D software (Sánchez 2004). Six pointings were observed for NCG 5668, leading to total covered area of

---

[9] IRAF is distributed by the National Optical Astronomy Observatory, which is operated by the Association of Universities for Research in Astronomy, Inc., under cooperative agreement with the National Science Foundation.

2×3 arcmin^2. Each pointing results from the combination of three or four images, each one with an exposure time of 1000 s. Our combined raw mosaic includes a total of 2292 spectra (1982+310 science+internal calibration spectra) covering the spectral range 3700–7131 Å. The pre-reduction of the IFS data consists of all standard corrections applied to the CCD that are common to the reduction of any CCD-based data.

1. *Bias subtraction.* A master bias frame was created by averaging all the bias frames observed during the night and subtracted from the science frames.
2. *Cosmic-ray rejection.* We median combined different exposures (at least three) of the same pointing. This procedure is able to remove 95% of all cosmic-ray events from each pointing.

After these corrections, the IFS data reduction consists of

1. *Spectra extraction.* We identified the position of the spectra on the detector for each pixel along the dispersion axis. We then co-added the flux within an aperture of 5 pixels around the trace of the spectra and we extracted the flux corresponding to the different spectra at each pixel along the dispersion axis. Finally, the one-dimensional extracted spectra are stored in a row-staked-spectra (RSS) file.
2. *Wavelength calibration.* We corrected for all distortions and determined the wavelength solution by using an arc calibration lamp exposure. Calibration data cubes were taken at the beginning and at the end of the night by illuminating the instrument with an HgCdHe lamp. The V300 wavelength calibration was performed using 14 lines in the considered spectral range. The rms of the best-fitting polynomial (order 4) was 0.45 Å (i.e., FWHM/20).
3. *Fiber-to-fiber transmission.* We corrected the differences in fiber-to-fiber transmission by using twilight sky exposures from which a Fiber-Flat frame was computed.
4. *Sky emission subtraction.* For each pointing, a sky image of 300 s (shifted $+5'$ in decl.) was taken. We median combined the different sky images to create a sky frame, which was then subtracted from the science data frame.
5. *Relative flux calibration.* We relative flux calibrated our data using observations of the spectrophotometric standard star Hz44 ($\alpha(2000) = 13^{\rm h}23^{\rm m}35\overset{\rm s}{.}37$, $\delta(2000) = +36^\circ08'00''.0$, Oke 1990) obtained during the night with the same instrumental setup as for the object. We applied all of the previous steps to the calibration star frame and extracted the standard star spectrum from the brightest $2''.7$ wide PPAK fiber centered on the star. Finally, we derived the ratio between counts per second and flux. In this way we obtained the instrumental response, which was applied to the science frames in order to flux calibrate them. Note that although this procedure also provides an absolute calibration for the data, this is uncertain due to potential flux loses during the observation of the standard star and variations in the transparency throughout the night.
6. *Differential atmospheric refraction* (*DAR*) *correction.* We calculated a total theoretical DAR value using a Calar Alto public tool, obtaining a value of $1''$ (the mean value of air mass used is 1.3). In this case the DAR can be considered negligible compared with the fiber size ($2''.7$ in diameter). Therefore, we considered the DAR correction not to be required for this data cube. In any case, we never obtained any flux measurements from regions with less than five adjacent fibers in size.
7. *Locating the spectra in the sky.* A position table that relates each spectrum to a certain fiber gives the location of the spectra in the sky.
8. *Mosaic reconstruction.* We built a single RSS file for the whole mosaic by adding pointings previously normalized to a reference (“master”) pointing. The “master” pointing is that having the best sky subtraction and most optimal observing conditions regardless of the geometric position of the pointing in the mosaic. In our case this “master” pointing was number 5 (offsets (0,−60); see Figure 1). This procedure makes use of the overlapping fibers between different pointings (11 fibers in total) to re-scale each new added pointing using the flux ratio in the continuum region 5869–5893 Å between the two pointings (the newly added and the “master” one).
9. *Absolute flux re-calibration.* We also computed an absolute flux re-calibration based on SDSS photometry. Only two of the five filters of SDSS (g and r, $\lambda_{\rm eff} = 4694$ and 6178 Å, respectively) are used because these are the ones for which their passbands are fully covered by our spectra. We convolved the whole data cube of NGC 5668 with the SDSS g- and r-filter passbands to derive the absolute spectrophotometry. First, we measured the AB magnitude within the footprint of the entire PPAK mosaic and in seven concentric annuli for both PPAK and SDSS images. Then, these magnitudes were converted to fluxes using the prescription in the SDSS documentation[10] in order to calculate the flux ratio in both bands. The resulting average scaling factor found is 0.9 for the two data pairs. This result implies a factor of 0.04 in magnitude. Note that the error in SDSS photometry alone is estimated to be 2% mag. In our case, we have an uncertainty of 5% in fluxes, so the total absolute error associated with line fluxes is 8%. Obviously, relative measurements are more precise. All results shown in the following analysis (and in Table 3) are re-calibrated based on these SDSS photometry measurements.

3.3. *Imaging Observations*

In order to complement the IFS data of NGC 5668 presented here, we have also compiled multi-wavelength broadband images acquired with different facilities: UV imaging data from *GALEX*, optical data from SDSS, and near-IR data from *Spitzer* (see Figure 2). The *GALEX* telescope (Martin et al. 2005) observed NGC 5668 as part of its Medium-deep Imaging Survey. Images at both the FUV ($\lambda_{\rm eff} = 151.6$ nm) and NUV ($\lambda_{\rm eff} = 226.7$ nm) bands are available for this galaxy. The final pixel scale is $1''.5$ pixel^{-1}, and the point-spread function (PSF) has an FWHM of $\sim 5''$–$6''$ in both bands (Morrissey et al. 2007). At the distance of NGC 5668, this corresponds to a physical scale of ∼700 pc. The uncertainty of the zero point, which is calibrated against white dwarfs, is estimated to be less than 0.15 mag (Gil de Paz et al. 2007).

Optical images in the $ugriz$ bands were retrieved from the SDSS (York et al. 2000) Data Release 7 (DR7) archive (Abazajian et al. 2009). The two different scans on which NGC 5668 lies were flux-matched and mosaicked together using a custom-built task in IRAF. We applied the photometric calibration specified in the SDSS DR7 Flux Calibration Guide,[11] relying on the calibration factors of the scan used as reference when creating the mosaic. According to the information provided by the

---

[10] http://www.sdss3.org/dr8/algorithms/fluxcal.php

[11] http://www.sdss.org/dr7/algorithms/fluxcal.html

Table 3
Spectra Emission Lines

ID (1)	$F_{[\mathrm{O\,II}]}/F_{\mathrm{H}\alpha}$ (2)	$F_{[\mathrm{O\,III}]}/F_{\mathrm{H}\alpha}$ (3)	$F_{[\mathrm{N\,II}]}/F_{\mathrm{H}\alpha}$ (4)	$F_{[\mathrm{S\,IIa}]}/F_{\mathrm{H}\alpha}$ (5)	$F_{[\mathrm{S\,IIb}]}/F_{\mathrm{H}\alpha}$ (6)	$F_{\mathrm{H}\alpha}$ (7)	A_V (8)
				Rings			
1	...	...	...	...	...	...	...
2	2.68 ± 0.43	...	0.32 ± 0.05	0.28 ± 0.05	0.27 ± 0.05	18.20 ± 2.51	1.57
3	1.92 ± 0.31	0.15 ± 0.04	0.31 ± 0.05	0.26 ± 0.04	0.24 ± 0.04	19.40 ± 2.41	1.52
4	1.77 ± 0.29	0.21 ± 0.05	0.26 ± 0.04	0.25 ± 0.04	0.20 ± 0.04	13.94 ± 1.77	1.23
5	1.13 ± 0.21	0.21 ± 0.05	0.29 ± 0.06	0.25 ± 0.06	0.23 ± 0.05	4.96 ± 0.71	0.35
6	1.70 ± 0.32	0.28 ± 0.06	0.26 ± 0.05	0.25 ± 0.05	0.19 ± 0.05	9.36 ± 1.41	1.00
7	1.83 ± 0.24	0.36 ± 0.05	0.21 ± 0.03	0.23 ± 0.03	0.18 ± 0.03	10.61 ± 1.18	1.33
8	1.30 ± 0.18	0.40 ± 0.06	0.17 ± 0.03	0.21 ± 0.03	0.17 ± 0.03	7.12 ± 0.78	0.88
9	2.29 ± 0.41	0.47 ± 0.09	0.20 ± 0.05	0.24 ± 0.05	0.25 ± 0.05	7.86 ± 1.29	1.64
10	2.04 ± 0.48	0.61 ± 0.14	0.15 ± 0.06	0.23 ± 0.07	0.19 ± 0.06	4.36 ± 0.93	1.33
11	1.81 ± 0.58	0.35 ± 0.13	...	0.21 ± 0.09	0.21 ± 0.09	2.80 ± 0.80	1.19
12	...	...	...	...	...	...	...
13	...	...	...	...	...	...	...
14	1.99 ± 0.87	0.64 ± 0.28	...	...	...	1.80 ± 0.75	1.10
15	1.50 ± 0.43	0.66 ± 0.18	...	...	...	2.03 ± 0.53	0.76
				H II regions			
1	1.14 ± 0.14	0.64 ± 0.04	0.09 ± 0.02	0.28 ± 0.03	0.19 ± 0.03	2.23 ± 0.09	0.65
2	1.19 ± 0.37	0.48 ± 0.11	0.20 ± 0.09	...	...	0.50 ± 0.05	0.12
3	1.55 ± 0.23	0.49 ± 0.04	0.15 ± 0.02	0.24 ± 0.02	0.13 ± 0.01	11.36 ± 0.28	2.02
4	1.52 ± 0.09	0.24 ± 0.02	0.16 ± 0.01	0.21 ± 0.01	0.17 ± 0.01	12.27 ± 0.16	1.36
5	1.33 ± 0.06	0.37 ± 0.01	0.17 ± 0.01	0.22 ± 0.01	0.15 ± 0.01	13.32 ± 0.14	1.18
6	...	...	0.01 ± 0.01	0.28 ± 0.05	0.25 ± 0.05	5.39 ± 0.43	2.46
7	1.83 ± 0.42	0.44 ± 0.08	0.02 ± 0.01	0.28 ± 0.05	0.13 ± 0.03	3.68 ± 0.21	1.64
8	1.44 ± 0.12	0.29 ± 0.04	0.09 ± 0.03	0.18 ± 0.03	0.21 ± 0.04	11.39 ± 0.50	1.31
9	1.57 ± 0.11	0.46 ± 0.03	0.12 ± 0.02	0.12 ± 0.02	0.10 ± 0.02	32.00 ± 0.91	2.06
10	1.72 ± 0.07	0.41 ± 0.01	0.17 ± 0.01	0.17 ± 0.01	0.13 ± 0.01	12.39 ± 0.16	1.22
11	2.00 ± 0.22	0.62 ± 0.05	0.14 ± 0.02	0.26 ± 0.02	0.20 ± 0.02	4.75 ± 0.18	1.30
12	2.05 ± 0.26	0.67 ± 0.04	0.11 ± 0.02	0.24 ± 0.02	0.14 ± 0.02	10.02 ± 0.30	1.98
13	2.31 ± 0.23	0.34 ± 0.06	0.18 ± 0.05	0.26 ± 0.06	0.14 ± 0.05	4.27 ± 0.25	0.39
14	1.76 ± 0.80	0.32 ± 0.10	0.20 ± 0.05	0.16 ± 0.06	...	23.48 ± 1.85	2.60
15	0.48 ± 0.08	0.57 ± 0.05	0.10 ± 0.04	0.15 ± 0.05	0.12 ± 0.04	6.27 ± 0.25	0.73
16	1.18 ± 0.09	0.47 ± 0.02	0.15 ± 0.01	0.17 ± 0.01	0.11 ± 0.01	15.94 ± 0.23	1.61
17	3.93 ± 0.76	0.96 ± 0.16	0.18 ± 0.07	0.22 ± 0.06	0.22 ± 0.09	19.32 ± 1.93	2.89
18	1.26 ± 0.37	...	0.22 ± 0.03	0.29 ± 0.03	0.13 ± 0.03	6.84 ± 0.30	1.93
19	1.48 ± 0.17	0.29 ± 0.04	0.26 ± 0.03	0.27 ± 0.03	0.18 ± 0.03	11.43 ± 0.50	0.90
20	0.51 ± 0.12	0.41 ± 0.04	0.25 ± 0.03	0.28 ± 0.04	0.17 ± 0.03	1.375 ± 0.05	0.12
21	1.85 ± 0.14	0.29 ± 0.03	0.22 ± 0.02	0.15 ± 0.02	0.11 ± 0.02	16.73 ± 0.59	0.89
22	2.40 ± 0.62	0.26 ± 0.10	0.18 ± 0.05	0.35 ± 0.05	0.24 ± 0.04	4.30 ± 0.34	1.87
23	0.93 ± 0.04	0.97 ± 0.01	0.09 ± 0.01	0.12 ± 0.01	0.10 ± 0.01	11.94 ± 0.12	0.92
24	1.69 ± 0.15	0.26 ± 0.03	0.23 ± 0.02	0.22 ± 0.02	0.16 ± 0.02	7.36 ± 0.18	1.31
25	1.57 ± 0.27	0.71 ± 0.07	0.24 ± 0.04	0.14 ± 0.03	0.10 ± 0.03	2.41 ± 0.12	1.06
26	1.41 ± 0.51	0.14 ± 0.05	0.31 ± 0.07	0.33 ± 0.07	0.21 ± 0.05	9.14 ± 1.68	0.88
27	...	2.19 ± 0.48	...	0.15 ± 0.07	...	31.30 ± 4.64	4.59
28	1.74 ± 0.47	0.17 ± 0.05	0.30 ± 0.05	0.26 ± 0.04	0.19 ± 0.04	20.57 ± 2.59	1.67
29	1.28 ± 0.20	0.21 ± 0.03	0.25 ± 0.03	0.24 ± 0.03	0.19 ± 0.03	14.89 ± 0.93	1.08
30	1.34 ± 0.24	0.24 ± 0.05	0.25 ± 0.04	0.25 ± 0.04	0.16 ± 0.03	11.61 ± 0.71	1.15
31	1.30 ± 0.08	0.38 ± 0.02	0.18 ± 0.01	0.18 ± 0.01	0.11 ± 0.01	9.23 ± 0.12	1.14
32	1.13 ± 0.09	0.33 ± 0.02	0.18 ± 0.01	0.15 ± 0.01	0.11 ± 0.01	29.66 ± 0.59	1.18
33	1.43 ± 0.13	0.20 ± 0.02	0.24 ± 0.02	0.19 ± 0.02	0.12 ± 0.01	30.84 ± 1.21	1.30
34	2.30 ± 0.59	0.41 ± 0.10	0.14 ± 0.04	0.24 ± 0.03	0.13 ± 0.03	6.59 ± 0.41	2.20
35	3.42 ± 0.38	0.39 ± 0.06	0.35 ± 0.04	0.35 ± 0.04	0.21 ± 0.04	50.93 ± 3.45	1.50
36	2.32 ± 0.15	0.66 ± 0.03	0.14 ± 0.01	0.19 ± 0.01	0.12 ± 0.01	17.41 ± 0.34	1.96
37	1.15 ± 0.05	0.36 ± 0.01	0.18 ± 0.01	0.14 ± 0.01	0.11 ± 0.01	57.29 ± 1.04	1.00
38	1.55 ± 0.23	0.15 ± 0.04	0.26 ± 0.03	0.24 ± 0.03	0.15 ± 0.03	13.94 ± 0.79	1.25
39	2.68 ± 0.92	0.96 ± 0.14	...	...	...	7.80 ± 0.59	2.74
40	3.32 ± 1.16	0.51 ± 0.11	0.15 ± 0.03	0.26 ± 0.03	0.09 ± 0.02	25.61 ± 1.71	3.63
41	1.06 ± 0.05	0.32 ± 0.01	0.16 ± 0.01	0.19 ± 0.01	0.15 ± 0.01	14.14 ± 0.16	1.06
42	2.21 ± 0.45	0.27 ± 0.07	0.24 ± 0.05	0.23 ± 0.04	0.20 ± 0.04	7.85 ± 1.30	1.84
43	0.76 ± 0.16	0.20 ± 0.03	0.22 ± 0.03	0.23 ± 0.03	0.18 ± 0.03	18.11 ± 1.75	1.22
44	1.78 ± 0.19	0.15 ± 0.03	0.32 ± 0.03	0.23 ± 0.02	0.24 ± 0.02	28.78 ± 2.28	1.47
45	2.99 ± 0.41	0.12 ± 0.04	0.29 ± 0.04	0.27 ± 0.04	0.21 ± 0.03	25.34 ± 3.02	1.75
46	1.33 ± 0.25	0.15 ± 0.05	0.25 ± 0.05	0.26 ± 0.05	0.21 ± 0.04	11.02 ± 1.50	1.06
47	1.45 ± 0.20	0.16 ± 0.04	0.25 ± 0.04	0.26 ± 0.04	0.21 ± 0.04	6.23 ± 0.71	0.34

Table 3
(Continued)

ID (1)	$F_{[\text{O II}]}/F_{\text{H}\alpha}$ (2)	$F_{[\text{O III}]}/F_{\text{H}\alpha}$ (3)	$F_{[\text{N II}]}/F_{\text{H}\alpha}$ (4)	$F_{[\text{S IIa}]}/F_{\text{H}\alpha}$ (5)	$F_{[\text{S IIb}]}/F_{\text{H}\alpha}$ (6)	$F_{\text{H}\alpha}$ (7)	A_V (8)
48	3.60 ± 0.75	0.26 ± 0.08	0.26 ± 0.06	0.29 ± 0.07	0.18 ± 0.05	15.20 ± 2.89	1.71
49	1.64 ± 0.05	0.75 ± 0.01	0.10 ± 0.01	0.11 ± 0.01	0.10 ± 0.01	16.48 ± 0.16	1.09
50	1.22 ± 0.19	0.20 ± 0.04	0.25 ± 0.04	0.25 ± 0.04	0.21 ± 0.04	9.11 ± 1.05	0.72
51	1.56 ± 0.11	0.34 ± 0.03	0.21 ± 0.02	0.20 ± 0.02	0.17 ± 0.02	22.45 ± 1.29	0.93
52	1.14 ± 0.11	0.31 ± 0.03	0.22 ± 0.02	0.22 ± 0.02	0.19 ± 0.02	21.20 ± 1.41	1.01
53	1.52 ± 0.05	0.40 ± 0.01	0.18 ± 0.01	0.19 ± 0.01	0.16 ± 0.01	29.32 ± 0.54	1.02
54	1.65 ± 0.06	0.66 ± 0.02	0.12 ± 0.01	0.15 ± 0.01	0.12 ± 0.01	10.30 ± 0.12	0.94
55	1.72 ± 0.08	0.63 ± 0.02	0.12 ± 0.01	0.22 ± 0.01	0.16 ± 0.01	15.11 ± 0.18	1.33
56	0.81 ± 0.05	0.18 ± 0.02	0.11 ± 0.02	0.24 ± 0.02	0.16 ± 0.02	3.30 ± 0.16	0.00
57	11.5 ± 2.4	0.78 ± 0.16	0.18 ± 0.04	0.18 ± 0.04	0.16 ± 0.04	153.29 ± 30.27	3.93
58	1.83 ± 0.08	0.70 ± 0.02	0.11 ± 0.02	0.15 ± 0.02	0.13 ± 0.03	6.07 ± 0.16	0.86
59	3.22 ± 0.25	0.45 ± 0.04	0.13 ± 0.04	0.19 ± 0.03	0.27 ± 0.04	6.09 ± 0.27	1.51
60	2.26 ± 0.14	0.36 ± 0.03	0.10 ± 0.03	0.17 ± 0.03	0.16 ± 0.04	4.80 ± 0.18	1.06
61	7.2 ± 1.3	0.78 ± 0.11	. . .	0.17 ± 0.05	0.21 ± 0.07	20.34 ± 1.59	3.57
62	3.24 ± 0.61	. . .	0.28 ± 0.05	0.25 ± 0.05	0.21 ± 0.04	34.30 ± 5.43	2.30
Total[a]	1.31 ± 0.17	0.35 ± 0.05	0.16 ± 0.04	0.21 ± 0.03	0.15 ± 0.03	3.93 ± 0.14	1.03

Notes. (1) Region identification numbers. (2)–(7) Emission-line flux ratios along with their errors. These ratios are measured relative to Hα, where the Hα fluxes are measured in units of 10^{-16} erg s^{-1} Å^{-1} cm^{-2} arcsec^{-2} and are absolute flux calibrated. The line fluxes listed are those of: [O II] λ3727; [O III] λ5007; [N II] λ6548; and [S II] λ6717, λ6731 (from left to right). (8) A_V is calculated from the Balmer decrement by adopting an MW extinction law ($A_V/A_{\text{H}_\beta} = 1.164$; Cardelli et al. 1989).
[a] The term *total* refers to the integrated spectrum. In this case, the flux line ratio values are in units of 10^{-12} erg s^{-1} cm^{-2}.

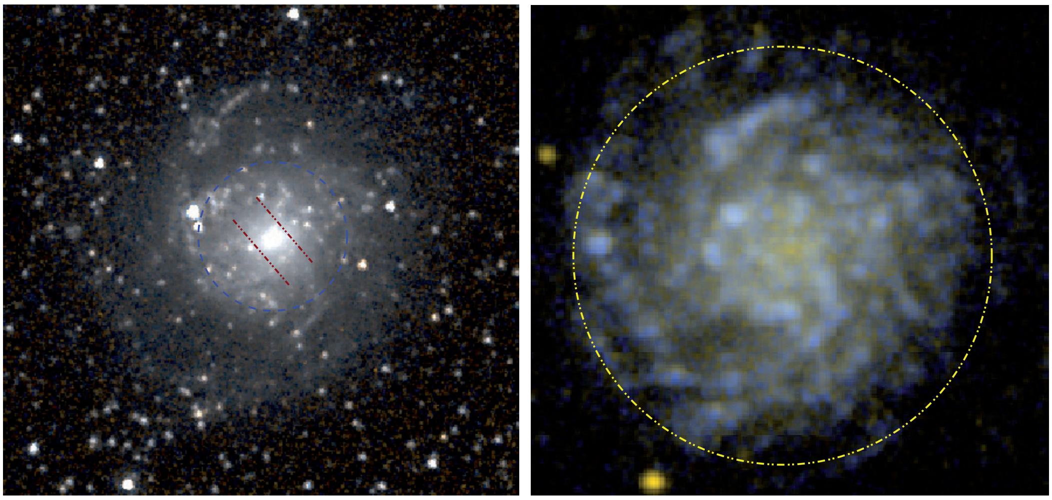

Figure 2. Left: IRAC color image of NGC 5668, using the 3.6 μm and 4.5 μm images. Since these bands primarily probe old stars, no significant color variations are found. The red dashed lines show the width of the weak bar visible in the optical images (~12″ in size) and the blue dashed circle corresponds to the break radius of the metallicity gradient (r ~36″). Right: *GALEX* color image, using the FUV and NUV bands as the blue and red channels, respectively, and a linear combination of both in the green one. The diameter of the yellow dashed circle is the optical one quoted in the RC3 catalog, at 25.5 mag arcsec^{-}2 in the B band (~3′.3). Both frames are 250″ in size. North is up and east is to the left.

SDSS project, the photometric relative errors are of the order of 2%–3%. The plate scale is 0″.396 pixel^{-1} with a PSF FWHM of 1″.4 (170 pc at the distance of the galaxy).

Near-IR images at 3.6 μm and 4.5 μm were taken by *Spitzer* (Werner et al. 2004) using the IRAC instrument (Fazio et al. 2004). The corresponding Post Basic Calibrated Data were downloaded from the *Spitzer* archive.[12] These images are already flux calibrated and delivered in units of MJy sr^{-1}. The pixel scale is 0″.6 pixel^{-1}, and the PSF has an FWHM of 1″.7 in both channels, probing a spatial extent of 200 pc (Reach et al. 2005). The photometric error (~2%) is dominated by the aperture corrections that need to be applied to account for the scattered light on the array. This total uncertainty is estimated to be around 10%[13] in this case.

4. ANALYSIS

4.1. Spectroscopy

Many important topics in astrophysics involve the physics of ionized gases and the interpretation of their emission-line spectra. Powerful constraints on theories of galactic chemical evolution and on the star formation histories (SFHs) of galaxies can be derived from the accurate determination of chemical abundances either in individual star-forming regions or distributed

---

[12] *Spitzer* Proposal ID 69: A Mid-IR Hubble Atlas of Galaxies, PI: G. Fazio.

[13] http://ssc.spitzer.caltech.edu/irac/calib/extcal/

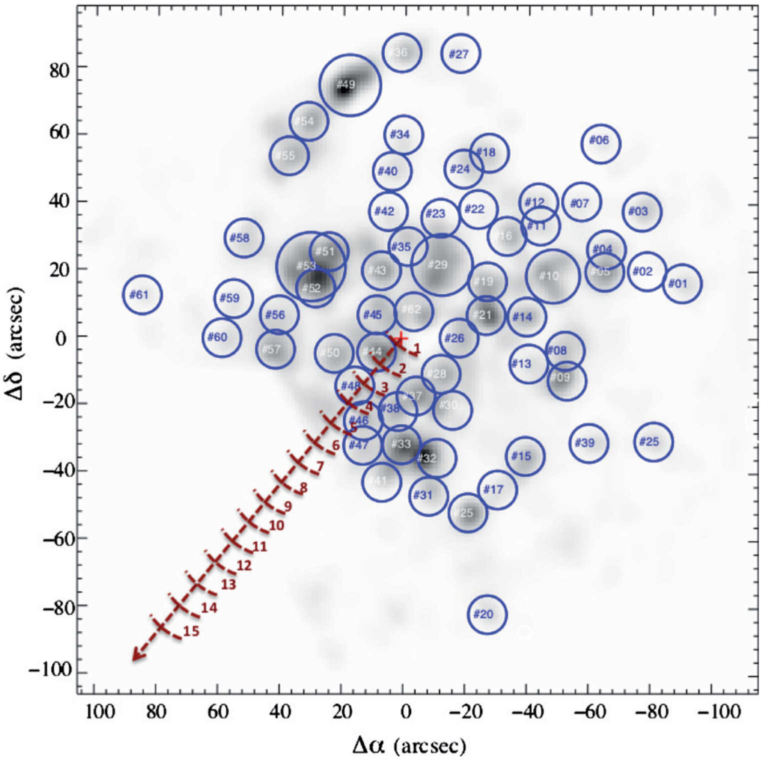

Figure 3. PPAK continuum-subtracted Hα emission map. The H II regions selected in NGC 5668 are shown as blue circles; see Section 4.1.1 for details. The red dashed lines indicate the radii of the rings and the red cross represents the central fiber of the mosaic. North is up and east is to the left.
(A color version of this figure is available in the online journal.)

across galaxies or even in galaxies as a whole. In this sense, chemical abundance is a fossil record of star formation history (SFH). In addition, the distribution of H II regions is an excellent tracer of recent massive star formation in spiral galaxies. The previous evolutionary history of the gas and the local ionization, density, and temperature are important features for understanding the physical conditions prevailing in the regions where they are emitted.

For all these reasons, our first aim is to identify H II regions in our target, or at least H II complexes (see Figure 3).[14] We extract from the PPAK data cube the emission-line fluxes corresponding to each of these regions. Furthermore, we also compute two-dimensional maps of the flux of strong emission lines, such as [O II] $\lambda\lambda$3726, 3729[15]; [O III] $\lambda\lambda$4959, 5007; Hβ; [N II] λ6548; Hα; [N II] λ6583; and [S II] $\lambda\lambda$6717, 6731.

4.1.1. Region Selection

In spiral galaxies, H II regions are strongly concentrated along the spiral arms and in the galactic plane and are the best objects for tracing the structure of spiral arms in galaxies. We are interested in the study of the optical emission lines from H II regions because they represent the primary means of performing gas-phase diagnostics in galaxies (Pagel 1986; Osterbrock & Ferland 2006). These data were analyzed using IRAF and E3D (Sánchez 2004) tasks and some custom-made IDL (Interactive Data Language) scripts. In order to select the H II regions of NGC 5668, we computed a synthetic Hα image (the brightest emission line in the optical spectrum of H II regions under most physical conditions) from the data cube using E3D. The spectral window for the Hα line was defined as a narrow wavelength range from 6589 Å to 6613 Å. Two bands (6457–6553 Å and 6667–6730 Å) close to the Hα line were also extracted for continuum subtraction. We normalized the "continuum" maps to match the width of the Hα intensity map. From the synthetic Hα image, we can then identify H II regions. We visually selected 62 H II complexes in the galaxy from this image (see Figure 3). The apertures were defined so that they would approximately reach the same surface brightness level in Hα. We also imposed the conditions that these apertures would be large enough to include at least five PPAK fibers (in order to minimize atmospheric refraction effects) and that each region would be isolated from bright neighbors. As a result of the conditions imposed, the majority of regions are the sum of five PPAK fibers, except in the case of regions 17, 37, and 62, which are the superposition of one bright and several marginally resolved faint H II regions, and region 58, which extends 15″ in the SE–NW direction approximately following the spiral pattern of the galaxy's northern arm. See Figure 3 for the positions and sizes of the regions of interest selected for this study. We extracted the spectrum coming from each region by averaging the signal for each fiber belonging to a particular region.

In many spiral galaxies of early and intermediate Hubble type (Sa-Sc), active star formation is organized in a ring-like structure that often contains a large fraction of the entire star formation activity of the galaxy. To investigate this and the ubiquitous

---

[14] Hereafter we use the terms "H II regions" and "H II complexes" indistinctly, even although individual H II regions are not spatially resolved at the physical resolution achieved in our IFS data.

[15] The [O II] $\lambda\lambda$3726, 3729 doublet is spectrally unresolved in our data, therefore, and hereafter we will refer to it as [O II] λ3727.

radial variation of the physical properties in spiral galaxies, we also selected 18 concentric annuli, centered on the peak of the optical-continuum emission. A width of about 5″ proved to be a good compromise in terms of the trade-off between spatial resolution and depth. The outermost ring analyzed is located at $R_{\rm last} = 95''$.

In a first step we analyze the data to verify the quality of the spectra extracted in all regions: we identify and eliminate bad fibers (e.g., those placed on bright field stars or affected by cross-talk), and we interpolate over the spectrum at the position of the brightest sky lines to clean out our spectra. We trim the wavelength range in each spectrum to avoid the poor instrumental efficiency at the very edges. This leads to a useful wavelength range of 3702–6997 Å.

4.1.2. Emission-line Fluxes

The radiation emitted by each element of volume in a region depends upon the abundance of the elements, determined by the previous evolutionary history of the galaxy, and the local ionization, density, and temperature. The most prominent spectral features are emission lines, many of which are collisionally excited lines. In the V300 grating setup, the main emission lines observed are [O II] λ3727 doublet; [O III] λλ4959, 5007; Hβ; [N II] λ6548; Hα; [N II] λ6583; and [S II] λλ6717, 6731.

We identified two different types of regions according to the intensity of the continuum: (1) regions where the continuum was bright enough so some absorption features were clearly visible and, therefore, the spectrum of the underlying stellar population could be fit using stellar population synthesis models, and (2) regions with fainter and/or noisier continua where no spectral absorption features could be identified.[16]

We refer to Section 4.1.3 for a description of the procedure followed to fit the underlying continuum in the case of the former regions; here we discuss the procedure followed to derive accurate emission-line fluxes in regions with negligible or noisy continua. Initially, we have identified 73 H II regions in our synthetic Hα image but we excluded some of these regions because of their low signal-to-noise ratio (S/N) or because they were later identified as bad columns or field stars.

We first masked out the main emission lines and used a third-order polynomial function to fit the continuum. We then selected two spectral ranges excluding emission lines in three different wavelength ranges [O II] λ3727, Hβ, and Hα regions, and measured the continuum level in each of these ranges. In a second step, we averaged the two continua and subtracted the result from each emission-line spectra in order to obtain a *decontaminated* flux. We analyzed the spectra using the IRAF package ONEDSPEC and STSDAS. For well-isolated emission lines, such as [O II] λ3727, Hδ, Hγ,[17] [O III] λ5007, we fit the emission-line profile to a single Gaussian function. For partially blended emission lines, such as the [N II] λ6548; Hα; [N II] λ6583 triplet, and [S II] λλ6717, 6731 doublet, we used the task NGAUSSFIT that fits simultaneously multiple Gaussian functions. We calculated the typical S/N of our data. In the case of [O II] λ3727, the S/N ranges are between 3.4 and 23. In the case of Hβ, we obtain similar S/N values, ranging between 2.5 and 23. For the part of our spectra where the Hα emission line is located, the S/N values vary between 6 and 67.

Table 4
Hα Equivalent Widths in Emission from the Ring Spectra

Ring	$EW^{\rm em}_{\rm H\alpha}$ (Å)	Radius (″)	Ring	$EW^{\rm em}_{\rm H\alpha}$ (Å)	Radius (″)
1	[a]	1	9	38.34	40
2	8.75	5	10	37.85	45
3	18.65	10	11	36.5	50
4	29.32	15	12	24.04	55
5	25.56	20	13	34.98	60
6	39.18	25	14	50.18	65
7	44.97	30	15	100.1	70
8	44.00	35	16	128.5	75[b]

Notes. These values are not corrected for underlying stellar absorption.

[a] No line emission was detected.

[b] In this table, we present the value for ring 16 that it is not shown in any of the other tables in the paper since only the Hα line could be detected in the spectrum and its flux (and EW) measured.

Before analyzing the data in terms of chemical abundances or SFR, the observed emission-line fluxes must be corrected for various effects. For example, the presence of dust between the zone of the emission and the observer or the possible underlying stellar absorption in the case of the hydrogen recombination lines can alter considerably the intrinsic emission-line fluxes. We correct for underlying stellar absorption in the hydrogen Balmer lines using the values obtained from the analysis of the ring spectra (see Section 4.1.3 for fitting details). These best-fitting equivalent widths in absorption show very little variation with a radius ranging between −1.9 and −2.3 Å in Hβ and −1.7 and −1.8 Å in Hα. We apply an average correction of −2 and −1.7 Å, respectively, for Hβ and Hα, to the spectra of the 58 H II regions where the continuum emission was too faint for carrying out a full spectral fitting. The emission fluxes were then corrected for reddening using the Hα/Hβ Balmer decrements after adopting an intrinsic ratio of 2.86 (Osterbrock & Ferland 2006). Additionally, we verified that in the case of regions with a high equivalent width in emission (typically no less than 5 Å in Hβ), the corrected Hβ/Hγ ratios were consistent with the predictions for the case B recombination value at a typical T_e of $\sim 10^4$ K. In Table 3, we present the results obtained from the analysis of H II regions and concentric annuli in NGC 5668.

Following a similar analysis on a pixel-by-pixel basis, we also generate maps of ionized-gas extinction, radial velocity, emission-line fluxes, and stellar-absorption equivalent width. In Figure 4, we present the maps of the Hα line flux, [O II] λ3727 doublet flux, Hα continuum intensity, and the equivalent width (EW). Note that while the EW(Hα) in emission gets locally higher as we move toward the outer parts of the disk, this is mainly due to the decrease in the intensity of the adjacent underlying (*R*-band) continuum. Indeed, when we compute the azimuthally averaged EW(Hα) from the ring spectra, this changes less dramatically, with values ranging from 20 to 50 Å in all cases except for the very outer rings (see Table 4). The very high EW(Hα) values measured in the rings beyond ∼70″ are likely due to strong Hα emission associated with the bright H II complex located in the galaxy Northern spiral arm. Note that in the very outer disk, where the total SFR is low, stochasticity in the number and luminosity of H II regions might lead to significant fluctuations in the EW(Hα) compared with values

---

[16] The limit in the continuum intensity between the two types of spectra was set to 1×10^{-16} erg s^{-1} Å^{-1} . For those spectra where the continuum was fainter (in either Hβ or Hα) than this number, no attempt to carry out a full spectral fitting to the continuum was attempted.

[17] Note that we detect these lines only in 23 H II regions, so we do not use Hδ and Hγ to derive physical properties.

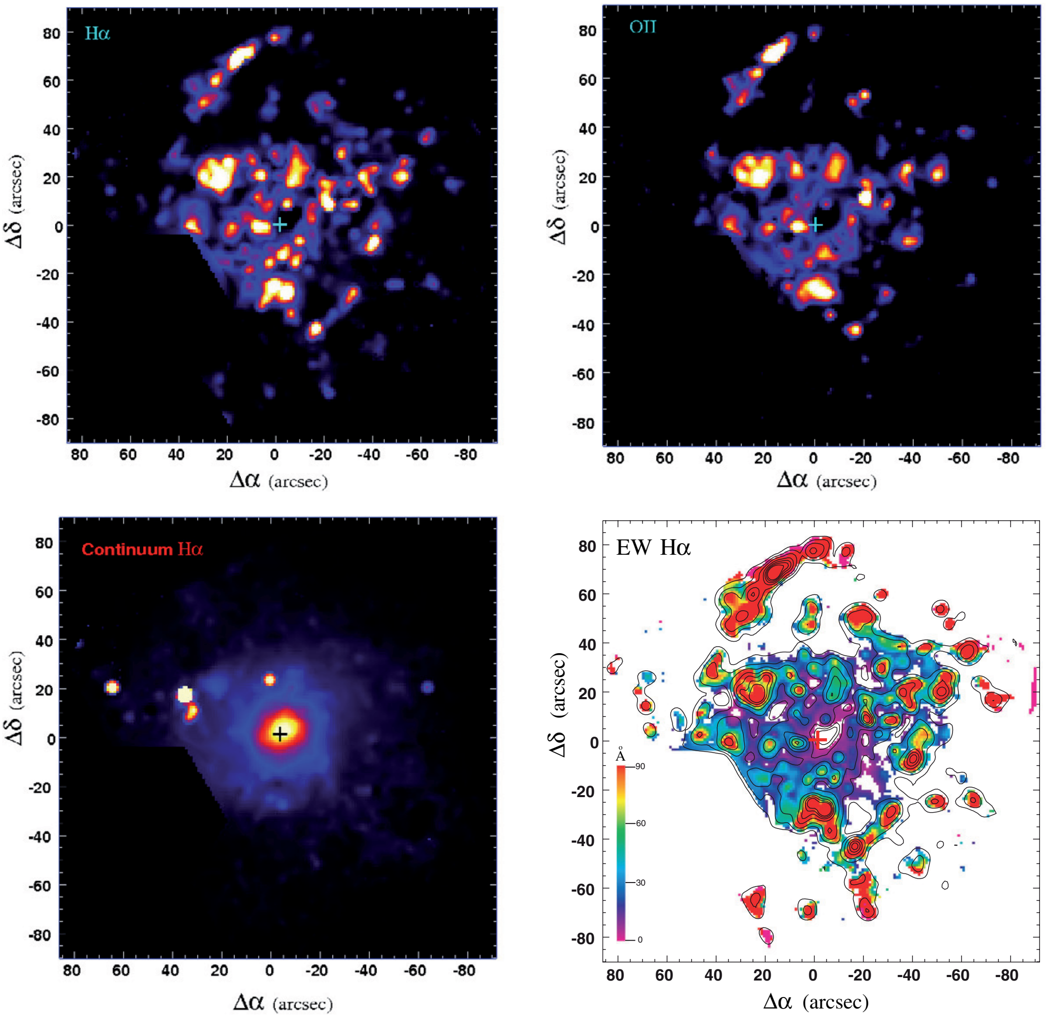

Figure 4. NGC 5668 synthetic maps. Top: emission lines map at Hα (left) and [O II] λ3727 doublet (right). Bottom: Hα continuum (left) and EW (right); we calculated these maps assuming an average absorption equivalent width in H_β of −2 Å. Hα emission-line fluxes in this plot are represented by the isocontours. The mosaic center is marked with a cross. North is up and east is to the left in all cases.

(A color version of this figure is available in the online journal.)

averaged over timescales of a few hundred Myr or even a rotation period.

4.1.3. Stellar-absorption Correction

As discussed above, for the rings and some H II regions the continuum is sufficiently strong enough to allow us to clearly identify absorption features in their spectra. In this way we can fit the absorption and emission components in the spectra simultaneously. The spectra of the 18 concentric annuli are plotted in Figure 5. In this case, we made use of an IDL script that finds the best-fitting stellar population synthesis model among the ones in libraries by Bruzual & Charlot (2003, hereafter BC03) and Sánchez-Blázquez et al. (2006, also known as MILES). This procedure allowed us to measure intensities for the emission lines already corrected for stellar continuum absorption (nebular continuum emission is negligible at the EW(Hα) measured anywhere in this object). Both libraries yield good fits to our spectra, yet the analysis presented here is based on the results obtained using the BC03 library since this provides a good coverage of physical parameters and good spectral resolution and has been more extensively tested than MILES. We explore the whole range in age and metallicity in the BC03 library for simple stellar populations (SSPs) with a spectral resolution of 3 Å across the whole wavelength range from 3200 Å to 9500 Å. These templates have 11 values in age (5, 25, 100, 290, 640, 900 Myr, and 1.4, 2.5, 11, 13, 17 Gyr) and each of them has six different metallicity values: $z = 0.0001$, 0.0004, 0.004, 0.008, 0.02, 0.05. Our fitting program is able to find the model that best fits the underlying stellar population (stellar continuum) in this BC03 stellar library by minimizing the residuals between the model and observed spectra for a set of input parameters. The program finds the best-fitting parameters for the recession velocity, velocity dispersion, normalization factor, and stellar continuum attenuation in the V band for each region.

In order to attenuate the stellar continuum as a function of wavelength, we adopt a dependence of the optical depth with a wavelength of the form $\lambda^{-0.7}$, which, according to the results of

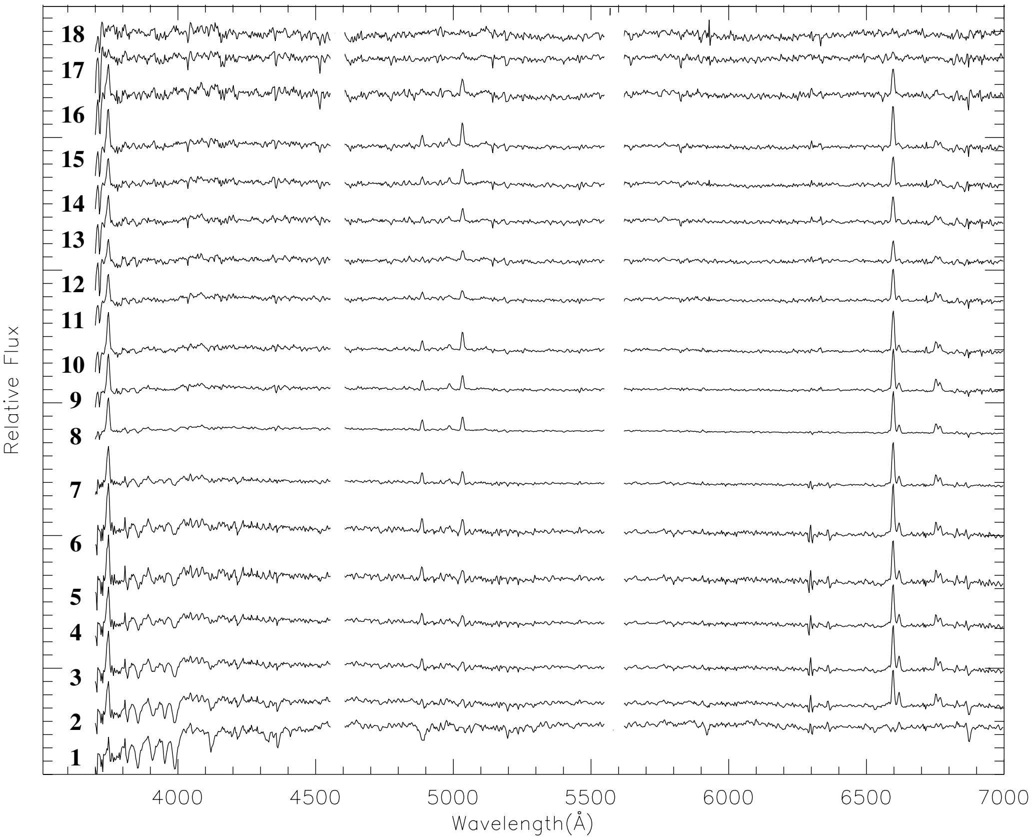

Figure 5. PPAK spectra extracted from the rings selected in NGC 5668. From bottom to top we show the spectra of rings with an increasing radius. The spectra are obtained summing all fibers within each ring. Two bright sky line residual ranges are masked. These spectra are plotted in linear scale and shifted in the y-axis for better visualization.

Charlot & Fall (2000), is a good approximation to the extinction law in star-forming galaxies at these wavelengths. This analysis provides us with the best-fitting SSP model for each spectrum along with best-fitting values for the recession (tropocentric) velocity, velocity dispersion, normalization factor, and continuum dust attenuation.

Note that the age and metallicities derived are, in general, highly uncertain, but, on the other hand, the Hα and Hβ equivalent widths in absorption are much more precise (see Mármol-Queraltó et al. 2011 for a detailed description on the feasibility in the derivation of the properties of the underlying stellar population). The residual spectrum obtained after the subtraction of the best-fitting SSP model is then used for the subsequent analysis of the emission-line fluxes.

We calculate the errors in all line fluxes from the rms in the spectra (in the region adjacent to each emission feature) after the best-fitting stellar synthesis model has been subtracted. We assume that these rms measurements were due mainly to photon noise and to sky subtraction. These errors were scaled to those spectra for which the fainter continuum emission prevented carrying out a full spectral fitting. Finally, we used the errors in the continuum to calculate the errors associated with the line fluxes.[18]

4.2. Integrated Spectrum

Some advantages of using IFUs are that all the spectra are obtained simultaneously and that we can use the IFU as a large-aperture spectrograph. From our data cube, we add up the spectra of all the fibers to create an integrated spectrum of NGC 5668 (see Figure 6). In this figure, we also compare this spectrum with the corresponding fluxes derived from the SDSS photometry. Note that the g' and r' bands overlap completely with our spectral range. Since the spectroscopy data were not taken under photometric conditions and given that some flux losses are expected as part of the PPAK observations of our spectrophotometric standard star, an 8% difference was found between the two data sets. This offset, which is wavelength independent, has already been applied to the spectrum shown in Figure 6, although it was not applied to our spectral data cube and the line fluxes measured hereafter. Similar wavelength-independent offsets are also found in other works based on PPAK spectroscopic observations (Rosales-Ortega et al. 2010, 2011). In any case, this does not have any impact on the physical

---

[18] The errors are calculated from the residual fit models of the underlying stellar population; we are assuming that these residuals are primarily due to photon noise and sky subtraction. We note that we have pointings with a slightly different spatial resolution and several combinations of exposure time and number of individual exposures; for this reason the continuum level emission and the associated noise was derived for each pointing separately. The sky subtraction to the spectra of NGC 5668 was done, see the data reduction steps in Sánchez (2006), by median average the 331 sky spectra. The resulting spectrum was then subtracted from the cube of NGC 5668. The analysis of these sky-subtracted spectra showed that the error in the continuum level emission increases linearly with the number of fibers (but not to the square root). This indicates that for apertures including a large number of fibers the total error is dominated by the sky-subtraction error.

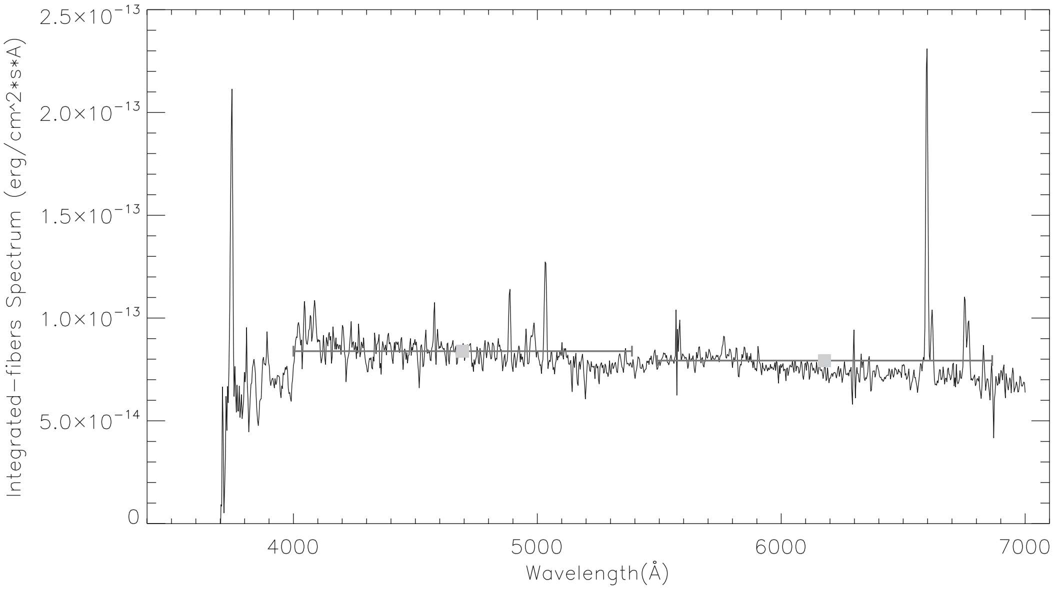

Figure 6. Integrated spectrum of NGC 5668 is shown as a black line. The SDSS g'- and r'-band photometry data are shown as gray squares. Horizontal error bars represent the FWHM of each filter.

properties derived (dust attenuation, oxygen abundance, and electron density) as these are determined by the ratio of emission-line fluxes alone. In Table 3 (last row), we present the emission-line flux ratios found for the integrated fiber spectrum of NGC 5668.

4.3. Imaging

Prior to the measurement of the surface brightness profiles in NGC 5668, foreground stars, background galaxies, and cosmetic artifacts had to be masked out from our multi-wavelength imaging data. Radial profiles were obtained using the IRAF task ELLIPSE. We measured the mean intensity within concentric circular annuli centered on the galaxy's nucleus, using a radial increment of 6″ between adjacent annuli. Photometric errors were derived as explained in Gil de Paz & Madore (2005) and Muñoz-Mateos et al. (2009b). The uncertainty of the mean intensity at a given radius is computed as the quadratic sum of two terms: the Poissonian noise of the galaxy's light and the error in the sky level. The latter was the result of the combination of both pixel-to-pixel variations and large-scale background errors.

5. RESULTS

5.1. Attenuation

More than 80 years have passed since Trumpler's discovery of color excesses provided the first definitive proof of the existence of interstellar dust (Trumpler 1930). However, the nature of interstellar dust still remains unclear and how dust both reddens and attenuates the light from the stars is one of the least understood of the physical phenomena which take place in galaxies.

The dust content of galaxies is a critical issue given its important impact on the observational properties of galaxies (mainly in the optical and UV). The extinction in a galaxy depends first on the amount of dust and its composition, and also on the distribution of dust relative to the light sources (Calzetti 2001). For instance, some authors favor a foreground screen dust geometry model (Calzetti et al. 1994, 1996), while others propose hybrid models with the dust partially distributed in a foreground screen and partially concentrated in the star-forming regions (Charlot & Fall 2000). In this subsection, we discuss the methods used to estimate dust attenuation. We calculate the attenuation of the stellar continuum from the UV data available on NGC 5668 and these estimates are then compared with the ionized-gas attenuation derived from the Balmer decrement in both individual H II regions and concentric annuli.

5.1.1. UV-continuum Attenuation

In this case, we estimate the attenuation of the stellar continuum using UV data alone. Because the UV radiation is preferentially emitted by young stars (∼100 Myr) and because the dust is most efficient in attenuating UV light, rest-frame UV observations can lead to incomplete and/or biased reconstructions of the recent star formation activity and SFH of galaxies where dust absorption is expected to be significant, unless proper corrections are applied. Radiative transfer models suggest that the total-IR (TIR; 3–1100 μm) to UV luminosity ratio method (i.e., Buat 1992; Xu & Buat 1995; Meurer et al. 1995, 1999) is the most reliable estimator of the dust attenuation in star-forming galaxies because it is almost completely independent of the extinction mechanisms (i.e., dust/star geometry, extinction law; see Xu & Buat 1995; Meurer et al. 1999; Gordon et al. 2000; Witt & Gordon 2000). However, this would require having both far-infrared data at the same resolution as the UV data. In the case of galaxies at the distance of NGC 5668, this would provide very little spatial information on the radial variation of the dust attenuation even if data from state-of-the-art infrared facilities such as *Herschel* would be available. Even though IRAC and MIPS images for NGC 5668 are available in the *Spitzer* archive, and we can theoretically obtain profiles in 8, 24, 70, and 160 μm, the poor resolution at 160 μm (38″) would yield a TIR profile with just a couple of data points. Under certain circumstances, the UV attenuation can be indirectly estimated using the slope of the UV spectrum

Table 5
UV-continuum Attenuation Results

Radius ($''$) (1)	A_{FUV} (mag) (2)	A_{NUV} (mag) (3)	$E(B-V)_{\mathrm{Cardelli}}$ (mag) (4)	$A_{V,\mathrm{Cardelli}}$ (mag) (5)	$E(B-V)_{\mathrm{Calzetti}}$ (mag) (6)	$A_{V,\mathrm{Calzetti}}$ (mag) (7)
6	1.98	1.40	0.18	0.54	0.17	0.69
12	1.51	1.13	0.14	0.44	0.14	0.56
18	1.33	1.03	0.13	0.40	0.12	0.51
24	1.20	0.95	0.12	0.37	0.12	0.47
30	1.04	0.87	0.11	0.34	0.11	0.43
36	0.90	0.80	0.10	0.31	0.10	0.39
42	1.01	0.86	0.11	0.33	0.10	0.42
48	1.04	0.87	0.11	0.34	0.11	0.43
54	1.23	0.97	0.12	0.38	0.12	0.48
60	1.20	0.96	0.12	0.37	0.12	0.47
66	0.95	0.83	0.10	0.32	0.10	0.41
72	0.84	0.77	0.10	0.30	0.09	0.38
78	0.84	0.77	0.10	0.30	0.09	0.38
84	0.93	0.82	0.10	0.32	0.10	0.40
90	0.75	0.73	0.09	0.28	0.09	0.36
96	0.40	0.59	0.07	0.23	0.07	0.29
102	0.62	0.67	0.08	0.26	0.08	0.33
108	0.58	0.66	0.08	0.26	0.08	0.32
114	0.90	0.80	0.10	0.31	0.10	0.40

Notes. (1) Radius in arcsec. (2) Far-UV attenuation values in magnitudes. (3) Near-UV attenuation values in magnitudes. (4) and (5) Galactic color excess from UV data and attenuation values calculated via Cardelli law, ($E(B-V) = A_{\mathrm{NUV}}/8.0$) $R_V = 3.1$, expressed in magnitudes. (6) and (7) Galactic color excess from UV data and attenuation values calculated via Calzetti law, ($E(B-V) = A_{\mathrm{NUV}}/8.22$) $R_V = 4.05$, expressed in magnitudes.

(denoted as β), in the sense that redder UV colors are indicative of larger attenuations. This so-called infrared excess (IRX)–β relation has been widely used in starburst galaxies, where most of the UV light comes from newly born stars (Calzetti et al. 1994; Heckman et al. 1995; Meurer et al. 1999). In normal star-forming spirals, more evolved stars can also contribute to the UV flux, shifting the IRX–β relation to redder UV colors and increasing the overall scatter (Bell 2002; Buat et al. 2005; Seibert et al. 2005; Cortese et al. 2006; Gil de Paz et al. 2007; Dale et al. 2007). The use of radial profiles instead of integrated measurements seems to reduce the global scatter (Boissier et al. 2007; Muñoz-Mateos et al. 2009a).

Here, we apply the IRX–β relation provided by Muñoz-Mateos et al. (2009a) to FUV–NUV measurements obtained from the *GALEX* images of NGC 5668. This relationship was specifically calibrated for normal nearby spirals, so it should be applicable to NGC 5668 as well. However, before applying this technique to subregions, we checked this assumption using the total galaxy IR luminosity of NGC 5668 from the *IRAS* fluxes quoted by Wang & Rowan-Robinson (2009) leading to a TIR flux of $\log(F_{\mathrm{TIR}}) = 13.64 \times 10^{-23}$ (erg s^{-1} cm^{-2}). This value combined with the FUV flux obtained from our *GALEX* FUV image leads to $\log(\mathrm{TIR/FUV}) \sim 0.18$. On the other hand, for a global UV color of FUV–NUV = 0.27, the IRX–β yields $\log(\mathrm{TIR/FUV}) \sim 0.39$. This is somewhat larger than the observed value, but still lies within the 1σ scatter around the IRX–β relation of Muñoz-Mateos et al. (2009b). Thus, using the radial profiles described in Section 4.3, we determined the radial variation of the FUV–NUV color in steps of $6''$. The UV color was then used to obtain profiles of TIR/FUV and TIR/NUV ratios using the prescriptions of Muñoz-Mateos et al. (2009b). These values were then transformed into dust attenuation in the FUV (A_{FUV}) and NUV (A_{NUV}) by means of the recipes by Cortese et al. (2008), which take into account the IR excess associated with the extra dust heating due to the light from old stars. The resulting attenuation profiles are shown in Table 5. Note that the absolute uncertainty in the TIR/FUV ratio from the FUV–NUV is larger than the relative change in such a ratio across the galaxy (see Muñoz-Mateos et al. 2009b).

Now that we have derived the extinction in the UV, we can calculate the extinction in other bands using an attenuation curve. Such reddening corrections have normally been undertaken using a number of extinction curves, including those of Seaton (1979; in the UV), Cardelli et al. (1989), Savage & Mathis (1979), Ardeberg & Virdefors (1982), and Fitzpatrick (1999). These "standard" curves are often used interchangeably, on the understanding that they should give broadly similar results. The parameterized curve by Cardelli et al. (1989) is commonly used to fit the extinction data both for diffuse and dense interstellar medium (ISM). In our case, the continuum attenuation is obtained using at different wavelengths two different extinction laws (Cardelli et al. 1989; Calzetti 2001). We based our calculation on the NUV data, adopting the relation with the color excess $E(B-V)$ given by Cardelli et al. (1989), $E(B-V) = A_{\mathrm{NUV}}/8.0$, and for Calzetti et al. (1994), $E(B-V) = A_{\mathrm{NUV}}/8.22$ (Gil de Paz et al. 2007). We then adopt the average values of $R_{V,\mathrm{Cardelli}} = 3.1$ and $R_{V,\mathrm{Calzetti}} = 4.05$. For sake of clarity, Figure 7 plots only the results obtained in the case of the Calzetti extinction law as the two curves are consistent within the errors (but offset by -0.09 mag in the case of the Cardelli law).

5.1.2. *Ionized-gas Emission-line Attenuation*

We now make use of the Balmer decrement in individual H II regions and concentric annuli for determining the amount of dust extinction in the ionized-gas emission along the line of sight. The relative ratios of the Balmer lines of hydrogen are often used as extinction indicators due to the fact that they are observationally convenient (being in the optical band), strong, and their intrinsic relative flux ratios are fairly well detemined

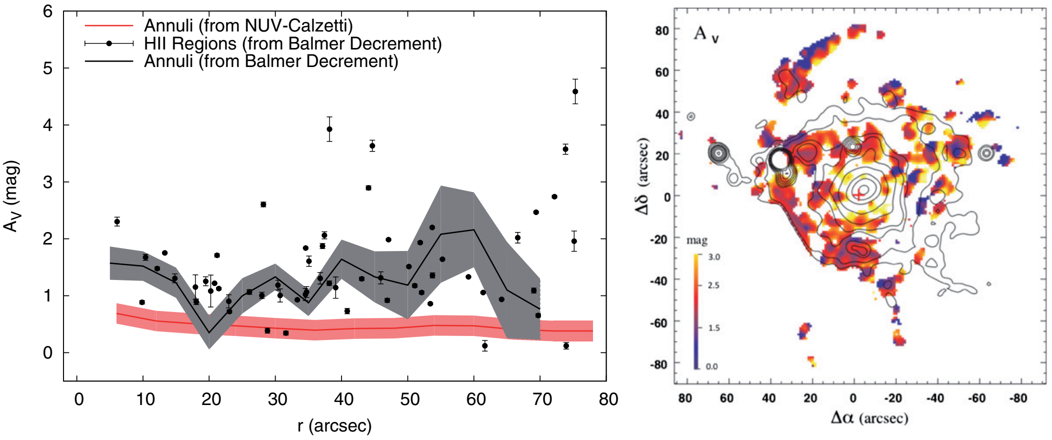

Figure 7. Left: representation of the radial variation of dust attenuation. Filled circles represent the values obtained from individual H II regions based on the Balmer decrement measurements. The black line represents Balmer decrement data for the concentric annuli. The red line is the attenuation (and $\pm 1\sigma$ error band) calculated from the slope of the UV continuum (or, equivalently, the FUV–NUV color) adopting a Calzetti extinction law. Right: dust extinction map (MW + internal) of the ionized gas in NGC 5668 computed from the Hα/Hβ ratio. The Hα continuum values are represented as isocontours. North is up and east is to the left.

(A color version of this figure is available in the online journal.)

from atomic theory. Under case B, conditions with temperatures $\sim$10,000 K and electron densities $\sim$100 cm^3, the theoretical Hα/Hβ ratio should be close to 2.86 (Osterbrock & Ferland 2006). Since extinction is more severe in Hβ than in Hα wavelengths, the net effect is to increase the observed Balmer line ratio. As we discussed above, the results are dependent on the dust model of choice. Here, we assume that the dust is located in a uniform screen between us and the gas and that the extinction law in the optical is similar to the Galactic one, as parameterized by Cardelli et al. (1989).

5.1.3. Optical-continuum Attenuation

The last method that we have used for the extinction is based on our IDL fitting program for the underlying stellar population (see Section 4.1). From the output values for each concentric annuli, we find a mean value of $A_V \sim 1.7$ mag. This value has a very large uncertainty due to the limited wavelength range of our spectroscopic observations, which leads with strong age–metallicity-extinction-SFH degeneracies (see Gil de Paz & Madore 2002). The results are summarized in Figure 7. In general, the ionized-gas dust attenuation has a mean value of $\sim$1.5 mag, which is in agreement with what is found in other spiral disks (Gil de Paz et al. 2007). We find that the gas attenuation is larger than the continuum attenuation by $\langle E(B-V)_{\rm continuum}\rangle = 0.36 \times \langle E(B-V)_{\rm ionized-gas}\rangle$ when the Calzetti attenuation law is adopted; note that ionized-gas color excess (derived from the Balmer decrement) is corrected for a MW foreground reddening, $E(B-V) = 0.037$. This is somewhat expected given that, as shown in Calzetti et al. (2000) and Stasińska & Sodré (2001), in nearby spiral galaxies there is evidence that stars, gas, and dust are typically decoupled (see, e.g., Maíz-Apellániz et al. 1998), so the attenuation inferred from the Hα/Hβ ratio is typically higher than that inferred from the spectral continuum of the same wavelength (e.g., Calzetti et al. 1994; Mayya & Prabhu 1996; Calzetti 1997). Poggianti et al. (1999) and Poggianti & Wu (2000) explain such results are due to selective-dust-extinction effects where a large fraction, but not all, of the dust in galaxies is associated with star formation regions, which absorb a significant fraction of the light emitted by the young stars.

5.2. Electron Density

The electron density, N_e, is one of the key physical parameters that characterize gaseous nebulae. Most of the density estimates found in the literature are based on measurements of a sensitive emission-line ratio. In the presence of internal variations of electron density, however, these single line ratio measurements may not be representative of all ionizing zones. The measurements are based on the fact that a relation exists between the collisional de-excitation of atoms and electron density (Osterbrock & Ferland 2006). If an ion emits similar amounts of energy from different energy levels at nearby wavelengths, then the ratio of the emission-line intensities can be used to obtain an estimate of the electron density and there are two line ratios that can be used: [O II] $\lambda\lambda$3726, 3729 or [S II] $\lambda\lambda$6717, 6731. In our case, we make use of the [S II] $\lambda\lambda$6717, 6731 line ratio and the electron density of the region responsible for the [S II] emission can be determined as

$$R([\mathrm{S\,II}]) = \frac{I([\mathrm{S\,II}]\,\lambda6717)}{I([\mathrm{S\,II}]\,\lambda6731)} \simeq 1.49\left(\frac{1+3.77x}{1+12.8x}\right), \qquad (1)$$

where x, the density parameter, is defined as $x = 10^{-4}\cdot n_e\cdot t^{-1/2}$. Solving this equation for the density parameter, we can obtain N_e by assuming $T_e = T_{[\mathrm{S\,II}]}/10^4$, where $T_{[\mathrm{S\,II}]}$ is the electron temperature of the region responsible for the [S II] emission (McCall et al. 1985). Thus, in order to properly estimate this electron density, a previous knowledge of the electron temperature of the region responsible for the [S II] emission lines is required. Assuming the calibration of T[N II] as a function of the R_{23} line ratio (see Equation (2)) given by Thurston et al. (1996) and an average difference of 3000 K between T[N II] and T[S II] (with the former being lower; Garnett 1992), we estimated $T_{[\mathrm{S\,II}]}$ in the equation above. Note that although this estimate for the temperature is not very precise (as it does not rely on the use of temperature-sensitive line ratios), it is accurate enough for correcting the densities obtained from the [S II] $\lambda\lambda$6717, 6731 line ratio for temperature effects. The large uncertainties associated with the determination of T[S II] prevent us from extracting further conclusions from the density measurement derived. Despite that, we find a mean value for N_e

Table 6
Abundance Gradient Fits

Fits Type	$r_{\rm BREAK}$	Segment	$12 + \log(\mathrm{O/H})$ at $r = 0$	Gradient		
				(dex/″)	(dex kpc^{-1})	(dex/R_{25})
Single slope	...	...	8.640 ± 0.047	-0.0042 ± 0.0009	0.0346 ± 0.0074	0.416 ± 0.089
Double slope unweighted	40″	Inner	8.876 ± 0.056	-0.013 ± 0.002	0.1073 ± 0.0165	1.29 ± 0.20
		Outer	8.269 ± 0.012	0.002 ± 0.002	0.002 ± 0.019	0.198 ± 0.198
Double slope weighted	36″	Inner	8.949 ± 0.053	-0.017 ± 0.002	0.140 ± 0.016	1.683 ± 0.198
		Outer	8.269 ± 0.012	0.002 ± 0.002	0.002 ± 0.019	0.198 ± 0.198

of 190 cm^{-3} for the H II regions in agreement with the typical value densities in H II regions ($N_e \sim 10^2$ cm^{-3}; Osterbrock & Ferland 2006).

5.3. Chemical Abundances

H II regions identify the sites of recent massive star formations in galaxies. The rapid evolution of these stars, ending in SNe explosions, and the subsequent recycling of nucleosynthesis products into the ISM, make H II regions essential probes for the present-day chemical composition of star-forming galaxies across the universe. The study of nebular abundances is therefore crucial for understanding the chemical evolution of galaxies. Obtaining a direct measurement of chemical abundances in H II regions requires a good estimate of the electron temperature. Unfortunately, this implies detecting very faint auroral lines such as [O III] λ4363 or [N II] λ5755, that are very faint at the abundance levels of most spiral disks. Thus, we must use instead calibrations based on the predictions of photoionization models or on empirical measurements for strong lines. Among the various strong-line methods, the R_{23} indicator originally proposed by Pagel et al. (1979) stands out as arguably the most popular:

$$R_{23} = \frac{f([\mathrm{O\,III}]\,\lambda\lambda 4959, 5007) + f([\mathrm{O\,II}]\,\lambda\lambda 3726, 3729)}{f(\mathrm{H}\beta)}. \tag{2}$$

Like all strong-line diagnostics, R_{23} as an abundance indicator has a statistical value, based on the fact that the hardness of the ionizing radiation correlates with metallicity. Numerous calibrations of R_{23} in terms of the nebular chemical composition can be found in the literature. We choose as the best set of values for the oxygen abundance those given by the Kewley & Dopita (2002) recipe, which basically adopts a calibration of the [N II]/[O II] ratio for oxygen abundances above half-solar and their own calibration of R_{23} for abundances below that value.[19] The R_{23} abundance diagnostic depends strongly on the ionization parameter, for this reason we also calculated it following the indications given in Kewley & Dopita (2002). These authors used a combination of stellar population synthesis and photoionization models to develop a set of ionization parameter and abundance diagnostics based only on the use of strong optical emission lines. These techniques are applicable to all metallicities. In particular, for metallicities above half-solar, the ratio [N II]/[O II] provides a very reliable diagnostic since it is an independent ionization parameter and does not have a local maximum. This ratio has not been used historically because of concerns about reddening corrections. However, the use of classical reddening curves is sufficient to allow this [N II]/[O II] diagnostic to be used with confidence as a reliable abundance indicator. Note that the calibration of the [N II]/[O II] line ratio as a diagnostic of $12 + \log(\mathrm{O/H})$ relies on the dependence of the (N/O) abundance ratio on the oxygen abundance. Thus, no attempt has been made to derive the nitrogen abundance in this work.

The iterative method used as part of this recipe allows both these parameters to be obtained without the need of using temperature-sensitive line ratios involving very faint emission lines that are particularly elusive in the case of spiral disks. One drawback of using R_{23} (and many other emission-line abundance diagnostics; see Pérez-Montero & Díaz 2005) is that it depends also on the ionization parameter q defined here as $q = S_{\rm H0}/n$, where $S_{\rm H0}$ is the ionizing photon flux through a unit area and n is the local number density of hydrogen atoms. Some calibrations have attempted to take this into account (e.g., McGaugh 1991), but others do not (e.g., Zaritsky et al. 1994). Another difficulty in the use of R_{23} and many other emission-line abundance diagnostics is that they are double valued in terms of the abundance ($12 + \log(\mathrm{O/H})$). Thus, one of the main difficulties in its adoption is related to the necessity of locating which of two branches (upper and lower) a given H II region belongs to, since R_{23} is degenerate (Bresolin et al. 2009a). This is because at a low abundance the intensity of the forbidden lines scales roughly with the chemical abundance while at high abundance the nebular cooling is dominated by the infrared fine structure lines and the electron temperature becomes too low to collisionally excite the optical forbidden lines. When only double-valued diagnostics are available, an iterative approach that explicitly solves for the ionization parameter, as the one used here that is based on the Kewley and Dopita logical flow diagram, helps to resolve the abundance ambiguities. In Tables 6 and 7, we present, the results respectively, derived for the abundance gradient Fits and the values obtained for both H II regions and concentric annuli. The metallicity values vary between $12 + \log(\mathrm{O/H}) = 8.15$ and $12 + \log(\mathrm{O/H}) = 8.7$ (i.e., from approximately 1/3 the solar oxygen abundance to nearly the solar value). The lack of some regions in this table is due to the poor signal to noise or simply non-detection of Hβ emission (12 regions).

Simulations of the line flux errors were carried out in order to derive the errors in the oxygen abundances. These simulations assumed a Gaussian probability distribution for each line flux and that these were not correlated between the different lines. The resulting errors, which are shown in Table 7, could then be considered as upper limits to the actual line flux errors (where a contribution of correlated errors is expected).

In order to quantify the abundance gradient, we have carried out three linear regressions to the data points, the first one is a fit to all points weighted by their errors ($\chi^2_{\rm red} = 1.45$); the gradient has a value of -0.035 dex kpc^{-1} (-0.0042 dex arcsec^{-1}). The second and the third fits are double fits to the data with a free parameter, the radius of break, but one is weighted by the errors (black solid line) and the other is unweighted (black dashed line; yield both $\chi^2_{\rm red} = 0.54$).

---

[19] We used the value of $12 + \log(\mathrm{O/H})_\odot = 8.93$ as in Kewley & Dopita (2002).

Table 7
Ionized-gas Diagnostics in the H II Regions and Concentric Annuli

ID (1)	12 + log(O/H) (2)	q (3)	N_e (4)	T_e (5)	Offsets (6)
		Rings			
1	. . .	. . .	1137	53359	(−3.6,2.5)
2	. . .	. . .	206	11036	. . .
3	8.69 ± 0.11	8.9E+06	122	9822	. . .
4	8.60 ± 0.16	9.5E+06	186	9685	. . .
5	8.63 ± 0.32	2.2E+07	138	8362	. . .
6	8.61 ± 0.18	1.1E+07	169	9721	. . .
7	8.50 ± 0.13	1.5E+07	154	10184	. . .
8	8.29 ± 0.18	1.7E+07	106	9215	. . .
9	8.50 ± 0.12	1.6E+07	84	11308	. . .
10	8.21 ± 0.63	1.7E+07	27	11204	. . .
11	. . .	. . .	256	10124	. . .
12	. . .	. . .	248	15785	. . .
13	. . .	. . .	287	16225	. . .
14	. . .	. . .	242	11186	. . .
15	. . .	. . .	56	10296	. . .
		H II regions			
1	7.96 ± 0.74	2.5E+07	123	9549	(−71.9,17.1)
2	7.43 ± 1.08	2.0E+07	. . .	9229	(−62.8,20.3)
3	8.34 ± 0.12	1.7E+07	. . .	9984	(−31.5,35.8)
4	8.36 ± 0.07	1.1E+07	. . .	9247	(−52.1,25.9)
5	8.22 ± 0.11	1.6E+07	. . .	9211	(−51.7,20.1)
6	. . .	. . .	272	. . .	(−50.7,53.6)
7	7.00 ± 1.20	. . .	. . .	10372	(−45.7,38.5)
8	8.30 ± 0.21	. . .	405	9229	(−40.4,−0.5)
9	8.34 ± 0.10	1.7E+07	. . .	9935	(−39.9,−7.1)
10	. . .	. . .	10	10084	(−38.2,18.9)
11	8.38 ± 0.11	1.7E+07	68	11163	(−34.9,32.2)
12	8.33 ± 0.11	1.8E+07	33	11368	(−34.5,38.2)
13	8.43 ± 0.38	1.3E+07	. . .	11047	(−31.8,−3.9)
14	8.60 ± 0.22	1.5E+07	. . .	9940	(−31.3,8.4)
15	8.39 ± 0.70	1.1E+08	352	7959	(−30.9,−28.0)
16	8.17 ± 0.08	2.0E+07	30	9175	(−26.2,29.5)
17	8.45 ± 0.36	1.8E+07	. . .	15032	(−23.6,−36.8)
18	. . .	. . .	. . .	8371	(−21.6,51.2)
19	8.58 ± 0.20	1.3E+07	11	9295	(−21.1,17.6)
20	8.55 ± 0.97	7.4E+07	12	7556	(−21.0,−69.4)
21	8.62 ± 0.09	1.3E+07	116	10033	(−20.7,8.8)
22	7.80 ± 1.00	1.1E+07	142	10992	(−18.6,36.5)
23	8.18 ± 0.08	3.9E+07	78	10008	(−15.9,−42.8)
24	8.48 ± 0.12	1.1E+07	12	9657	(−14.8,47.1)
25	8.50 ± 0.23	2.8E+07	37	10573	(−14.2,−58.0)
26	8.72 ± 0.25	1.0E+07	42	8739	(−13.6,2.8)
27	. . .	. . .	. . .	19479	(−12.5,77.3)
28	8.70 ± 0.15	1.0E+07	103	9507	(−8.9,−6.5)
29	8.61 ± 0.26	1.4E+07	29	8659	(−9.2,21.9)
30	8.58 ± 0.25	1.4E+07	194	8860	(−7.5,−15.0)
31	8.25 ± 0.15	1.7E+07	. . .	9175	(−5.7,−36.6)
32	8.50 ± 0.23	. . .	. . .	8699	(−3.7,−27.9)
33	8.69 ± 0.09	1.2E+07	73	8941	(−2.3,−12.2)
34	8.39 ± 0.21	1.5E+07	. . .	11198	(0.8,55.9)
35	8.66 ± 0.07	1.2E+07	. . .	7534	(1.3,23.3)
36	8.41 ± 0.04	1.6E+07	. . .	11831	(1.3,77.6)
37	8.48 ± 0.24	2.1E+07	116	8804	(1.4,−24.9)
38	8.64 ± 0.17	1.0E+07	50	9067	(3.3,−15.6)
39	. . .	. . .	. . .	13102	(3.3,−69.3)
40	8.47 ± 0.18	1.3E+07	. . .	13174	(3.8,46.5)
41	. . .	. . .	168	8506	(5.3,−31.0)
42	8.57 ± 0.13	1.1E+07	. . .	10684	(4.8,35.9)
43	8.61 ± 0.39	1.2E+07	54	7507	(6.6,20.5)
44	8.74 ± 0.05	9.1E+06	242	9523	(7.9,−0.7)
45	. . .	. . .	149	11738	(7.8,8.9)
46	8.57 ± 0.26	9.1E+06	126	8596	(11.4,−18.7)
47	8.51 ± 0.24	1.1E+07	241	8870	(11.5,−25.1)
48	8.63 ± 0.12	8.5E+06	130	13086	(13.6,−9.6)
49	8.42 ± 0.11	2.8E+07	170	10808	(14.8,68.9)
50	8.54 ± 0.30	1.4E+07	201	8500	(19.0,−1.1)
51	8.47 ± 0.14	1.7E+07	118	9599	(20.3,25.5)
52	8.53 ± 0.27	1.9E+07	137	8655	(23.8,15.9)
53	8.31 ± 0.10	1.5E+07	158	9683	(25.0,21.6)
54	8.43 ± 0.08	2.6E+07	. . .	10588	(25.6,59.5)
55	8.44 ± 0.08	2.4E+07	54	10645	(30.7,50.5)
56	. . .	. . .	50	6785	(33.3,8.9)
57	8.57 ± 0.16	8.1E+06	259	23652	(34.3,−0.0)
58	8.34 ± 0.21	1.9E+07	170	11032	(42.5,29.0)
59	8.34 ± 0.37	1.0E+07	1318	12890	(45.2,13.2)
60	7.96 ± 0.83	1.1E+07	335	10993	(48.3,2.9)
61	. . .	. . .	619	19051	(69.1,14.2)
62	. . .	. . .	60	12023	(−3.2,4.3)

Notes. (1) H II regions and annuli identification. (2) Oxygen abundances along with the corresponding errors. (3) Ionization parameter q defined as $q = S_{\mathrm{H0}}/n$. (4) Electron density in units of cm^{-3}. (5) Electron temperature in Kelvin. (6) Offset coordinates of the H II regions in units of arcsec.

The Kewley & Dopita recipe allows us to make use of the most optimal abundance indicator among [N II]/[O II], [N II]/Hα, and R_{23}. We find that the three abundance diagnostics (shown in the bottom panel of Figure 8 with different colors) are homogeneously mixed, as shown in Figure 8. Thus, the [N II]/Hα and R_{23}-based abundance values are well mixed and can be derived at almost any galaxy radius, while the [N II]/[O II] indicator is lost in some H II regions, mostly at large radii. This is, as pointed out in Kewley & Dopita (2002), because nitrogen is predominantly a primary nucleosynthesis element in the range 12 + log(O/H) $\leqslant$ 8.6 (see also Figure 3 in Kewley & Dopita 2002) and the calibration of the (N/O) abundance ratio and the [N II]/[O II] line ratio is not sensitive to the oxygen abundance under these circumstances.

The results are summarized in Table 6 and Figure 8 where we plot the three gradients as a function of the de-projected galactocentric radius. We find that inward $r \sim 36''$ ($\sim$4.4 kpc) the O/H ratio follows an exponential profile with a slope of 0.140 ± 0.016 (dex kpc^{-1}) and $12 + \log(\mathrm{O/H})_{r=0} \simeq 8.9$, similar to the normalized radial gradient found in other spiral disks. The outer abundance trend flattens out to an approximately constant value of $12 + \log(\mathrm{O/H})_{r=0} \simeq 8.27$ (with a slight gradient of 0.002 ± 0.019 (dex kpc^{-1})) and could even reverse (see Section 6 for a discussion on the possible causes for such flattening). The abundance gradient derived, -0.035 dex kpc^{-1} (-0.0042 dex arcsec^{-1}), is somewhat shallower than the one for the MW (-0.08 dex kpc^{-1}; Boissier & Prantzos 1999 and references therein). A similar trend was found from the analysis of the spectra of the concentric annuli. The analysis of these spectra was limited to the innermost nine annuli, because beyond this ring both the continuum and line emission become too faint to derive reliable emission-line fluxes. In Figure 8, we plot the change in abundance for all annuli with a solid black line (bottom panel) where the uncertainties associated are represented by the gray shaded area. The blue dashed line represents the metallicity profile predicted by the best-fitting model of Boissier & Prantzos (1999, 2000, hereafter BP2000 models). This profile has been shifted by 1 dex to match the metallicity scale derived from our spectroscopic data. Note that

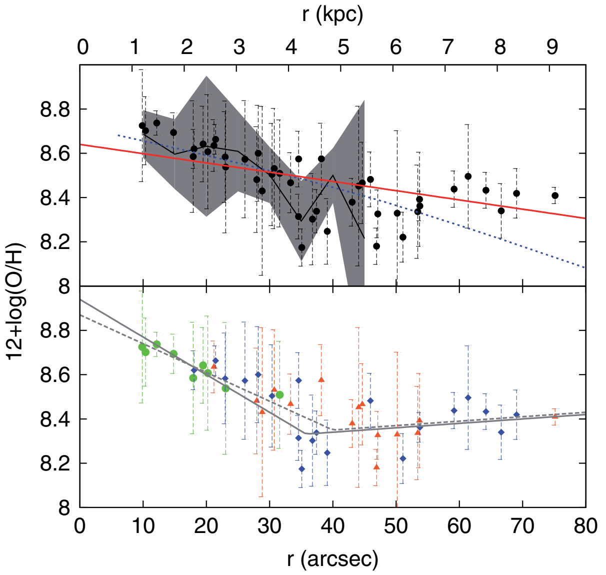

Figure 8. Radial abundance gradient in NGC 5668, where filled symbols correspond to individual H II regions while the gray shaded area represents the values obtained for the concentric annuli. Top panel: the red line symbolizes the linear regression fit to the H II region data. We obtained a single gradient of 0.035 ± 0.007 dex kpc^{-1}. The blue dashed line represents the gradient obtained from the models of Boissier & Prantzos (1999; BP2000), with an offset of 1 dex in the metallicities plotted (see the text for details). Bottom panel: in this plot, we draw two types of fits: the gray line reproduces a double fit weighted by the errors; the gradient has a value of 0.140 ± 0.016 for inner part and 0.002 ± 0.019 dex for outer part. The gray dashed line reproduces the unweighted double fit that yields gradient values of 0.1073 ± 0.0165 (inner) and 0.002 ± 0.019 (outer). The color coding of the points represents the different line ratios used to calculate the metallicity for the central point of the ratios probability distribution (based on Kewley & Dopita 2002 recipe): green points are calculated from [N II]/[O II], red triangles represent the values obtained with [N II]/Hα, and blue diamonds show R_{23}-based values. Note that the presence of three uncertain points (regions 13, 17, and 59 have an error major of 0.3) has no influence on the fitting parameter values.

(A color version of this figure is available in the online journal.)

this kind of zero-point offsets in metallicity are not unexpected due to the significant uncertainties in the yields used in the disk evolution models (see discussion in Muñoz-Mateos et al. 2011); besides, even the empirical oxygen abundances can be subject to large systematic offsets (Moustakas et al. 2010). The relative changes in metal abundances and therefore their radial profiles, on the other hand, are much more robust to these unknowns.

5.4. Galaxy Disk Modeling

In order to gain further insight into the evolution of NGC 5668, we have fitted its multi-wavelength surface brightness profiles with the BP2000 models. These models describe the chemical and spectrophotometric evolution of spiral disks as a function of only two variables: the dimensionless spin parameter, λ, and the circular velocity in the flat regime of the rotation curve, V_C. Within these models, galactic disks are simulated as a set of concentric rings that evolve independently from each other (for simplicity, radial mass or energy flows are not considered). The gas infall rate at each radius decreases exponentially with time, with a timescale that depends on both the total mass of the galaxy and the local mass surface density at that radius. Once in the disk, gas is transformed into stars following a Kennicutt–Schmidt law multiplied by a dynamical term, which accounts for the periodic passage of spiral density waves. The mass distribution of each new generation of stars follows a Kroupa (2001) initial mass function (IMF). The finite lifetimes of stars of different masses is taken into account; when they die, they inject metals into the ISM, thus affecting the metallicity of subsequent stars. The local metallicity at the time of formation is taken into account when determining the lifetimes, yields, evolutionary tracks, and spectra of each generation of stars. The model was first calibrated against several observables in the MW (see Boissier & Prantzos 1999) and then extended to other galaxies with different values of λ and V_C (BP2000), using several scaling laws derived from the Λ-Cold Dark Matter framework of galaxy formation (Mo et al. 1998).

For each pair of values of λ and V_C, the model outputs radial profiles at different wavelengths, which can then be compared to the actual profiles of our Galaxy. In order to probe the spatial location of stars of different ages—and therefore better constrain the model predictions—we measured surface brightness profiles at all *GALEX* FUV and NUV bands, the *ugriz* bands from SDSS, and the 3.6 and 4.5 μm *Spitzer* bands. The radial variation of internal extinction in the UV was estimated indirectly from the FUV−NUV color profiles, as explained in Section 5.1.1. The UV extinction was then extrapolated to the optical and near-IR bands, assuming a MW extinction curve, convolved with a sandwich model to account for the relative geometry of stars and dust (see Muñoz-Mateos et al. 2011 for details).

We compared these extinction-free profiles with the model predictions for a grid of values of λ and V_C, and used an χ^2 minimization algorithm to find the best-fitting values. The results of the fit are shown in Figure 9, and in Figure 10 we present the residuals. Each panel corresponds to a different wavelength. The gray profiles are only corrected for foreground MW extinction, whereas the black ones are corrected for internal extinction as well. The red and blue dashed lines bracket the region of the profile used for the fit. On the one hand, starlight inside $r \simeq 20''$ is dominated by emission coming from the bulge and the oval. On the other hand, beyond $r \simeq 125''$ the S/N becomes very low, and contamination from background sources could be an issue. The model that best reproduces simultaneously all multi-wavelength profiles is shown with a red line. The shaded band encompasses all models whose χ^2 is less than twice the χ^2 of the best model ($\chi^2_{\rm min} \simeq 0.8$).[20] The resulting χ^2 of the fitting model is obtained after a two-stage-fitting procedure because, as one would expect, this model does not reproduce the very small-scale variations of the surface brightness profiles of our disk. So in a first run of the fitting procedure we assume that the total uncertainty for each point is due to the quadratic sum of the zero-point and photometric errors, plus an extra uncertainty in the model predictions of 10%. These values represent the initial guess for the intrinsic error of the model and in this stage the χ^2 is ~5. In the second step, we calculate the rms of the best-fitting model with respect to the galaxy profiles and we pass these error profiles to the code as initial uncertainties to start the second run. In this way the new reduced χ^2 values are close to unity. In principle, when we

---

[20] Note that the scatter of the data points around the model is not entirely due to noise, but also to real features of the galaxy that a smooth model cannot reproduce. This precludes applying the classical statistical formula to translate the χ^2 distribution into confidence intervals. The criterion of using $\chi^2 \leqslant 2\chi^2_{\rm min}$ is just orientative, based on the results shown in Figure 9. Note also that we are not using the χ^2 distributions in a strict statistical way, since many of the required mathematical conditions (Gaussianity of errors, etc.) are not met (see Muñoz-Mateos et al. 2011 for a more extensive discussion).

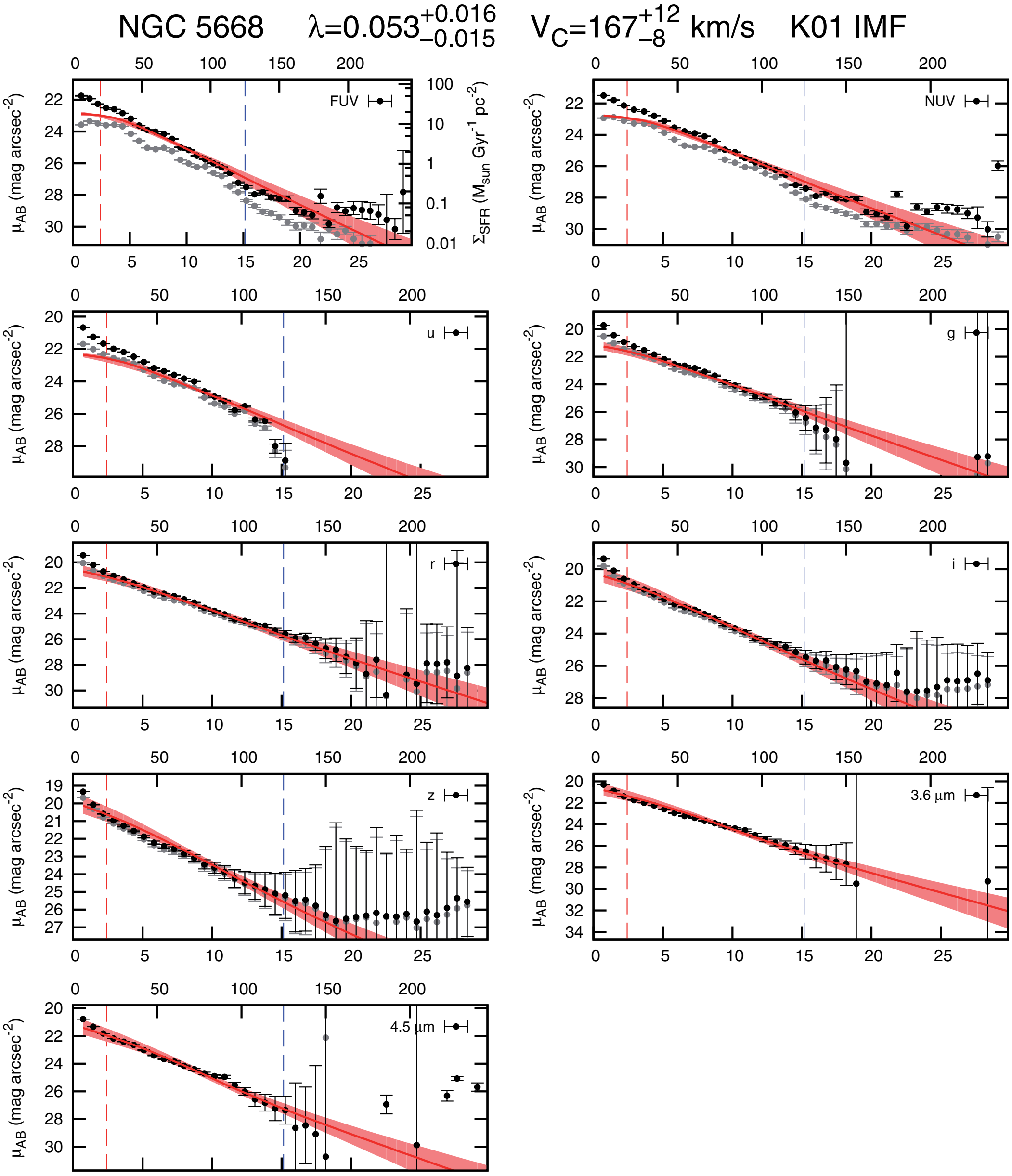

Figure 9. Best-fitting model of NGC 5668 using the Kroupa (2001) IMF. The gray profiles are only corrected for foreground Milky Way extinction, whereas the black ones are also corrected for internal attenuation. The latter profiles are the ones used to constrain the disk evolution models in the radial range spanned between the red and blue vertical lines (in order to exclude the bulge and the low S/N outer parts). The best-fitting model is shown as a red solid line, and the red shaded band comprises all models with $\chi^2 \leqslant 2\chi^2_{\rm min}$. The radius along the semimajor axis is shown both in kpc (bottom x-axis) and arcseconds (top x-axis).

(A color version of this figure is available in the online journal.)

fit a set of data points with a given model, it is often implicitly assumed that deviations between the observed data points and the model are due to the measured uncertainties of the former. However, in practice one also has to account for the fact that the models themselves are not a perfect representation of nature and have their own "uncertainties." The model yields smooth profiles that, by construction, cannot reproduce the fine structure of the actual profiles. In order to account for this, we performed this fit for NGC 5668 in a two-stage fashion (see also Section 5 of Muñoz-Mateos et al. (2011) for a detailed discussion). When fitting the multi-wavelength profiles, we should not ignore the internal degeneracy in the determination of the λ and $V_{\rm C}$ values as these are not completely independent parameters. For this reason in Figure 11, we show the two-dimensional χ^2 distribution obtained for NGC 5668 in the case of fitting all bands simultaneously and in the case of each band separately. The corresponding best-fitting values are $\lambda = 0.053^{+0.016}_{-0.015}$ and $V_{\rm C} = 167^{+12}_{-8}$ km s^{-1}. Where the errors are those expected when one is interested in deriving each of the two quantities separately.

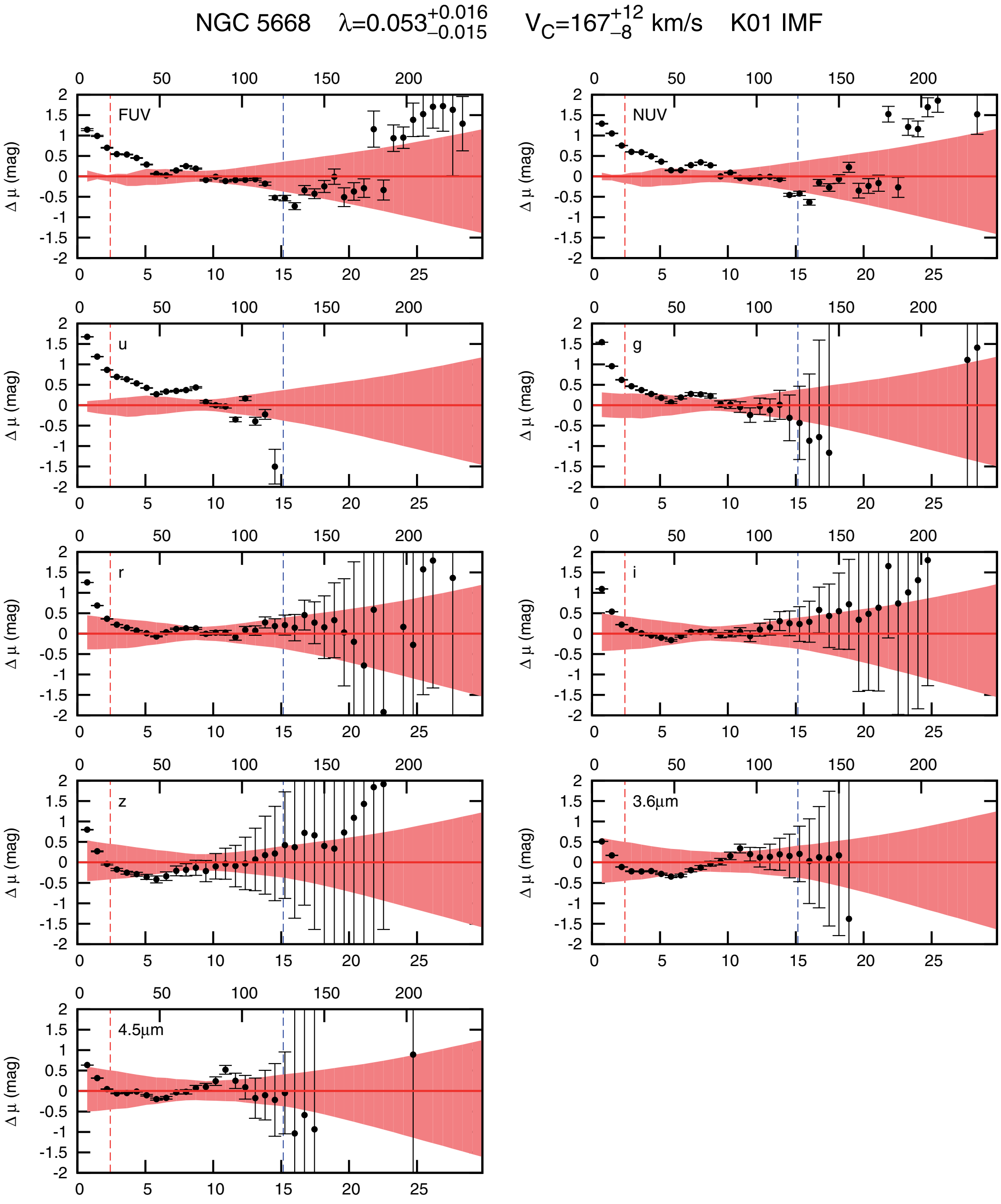

Figure 10. Residuals of the best-fitting BP2000 model of NGC 5668 using the Kroupa (2001) IMF. The red line represents the best-fitting model and the red shaded area represents all models with $\chi^2 \leqslant 2\chi^2_{\rm min}$. The black points are the residuals of the black profile corrected for internal and foreground Milky Way attenuation. The radius along the semimajor axis is shown both in kpc (bottom x-axis) and arcseconds (top x-axis).

(A color version of this figure is available in the online journal.)

In general, all bands are successfully reproduced by the BP2000 models, but the fit is not equally good at all wavelengths. For example, we can appreciate in the top panels of Figure 10 that in the cases of FUV, NUV, and u-band data the quality of the fit is not so good because these bands are more sensitive to the recent variations in the SFH and on the recipe used to calculate the extinction (or even limitations intrinsic to the models in order to reproduce the UV part of the spectrum at certain metallicities, as explained in Figure 9 of Muñoz-Mateos et al. 2011). The deviations in UV bands from the BP2000 models are compatible with the typical range of errors, as pointed out in Muñoz-Mateos et al. (2011).

While the BP2000 models provide a good fit to the overall shape of the surface brightness profiles of NGC 5668 (see Figure 9), the analysis of the deviations from these otherwise idealized models could give important clues on the details of the SFH of this galaxy (e.g., gas and/or stellar radial transfers). In this regard, Figure 12 shows that while the best-fitting model predicts a systematic bluing in the colors toward the outer parts of the disks, the measured colors flatten or even get redder

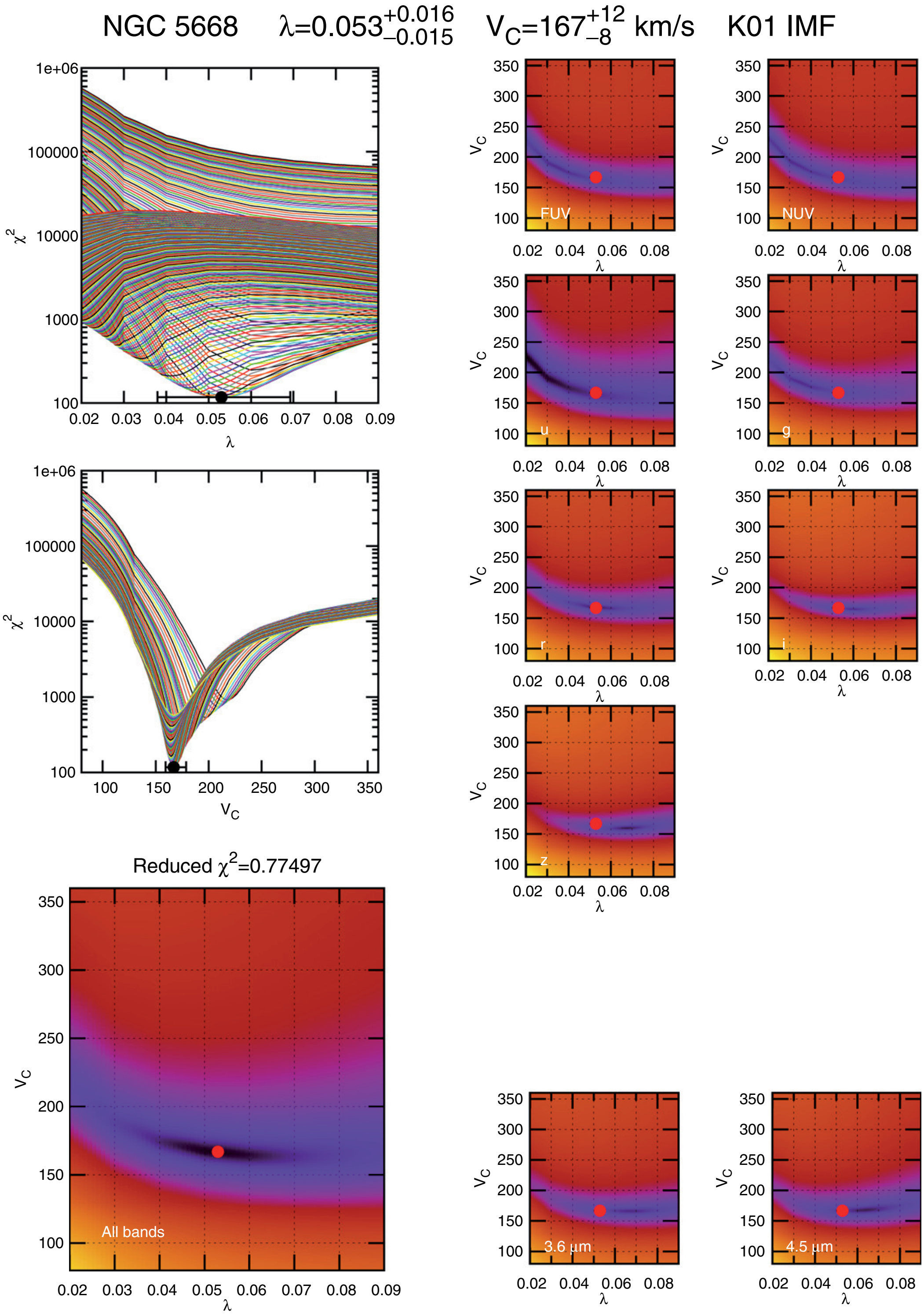

Figure 11. Two-dimensional χ^2 distribution of the disk evolution model fitting procedure. In the top left panel, we plot χ^2 as a function of the spin (λ) for different circular velocities (V_C). The best-fitting value and its estimated uncertainty are marked with a circle with error bars. The middle left plot is analogous and shows χ^2 as a function of V_C for different spins. These are projections of the surface shown in the bottom left panel, where the red dot marks the best model. While we constrain the model by fitting all bands at the same time, we keep track of the individual χ^2 distributions at each wavelength. These are shown in the small panels to the right (the red point has been replicated in all of them for clarity). The missing small panels would correspond to J, H, and K Two Micron All Sky Survey images that we decided to exclude from this analysis as they are not deep enough to provide additional information. For more details, see Muñoz-Mateos et al. (2011).

(A color version of this figure is available in the online journal.)

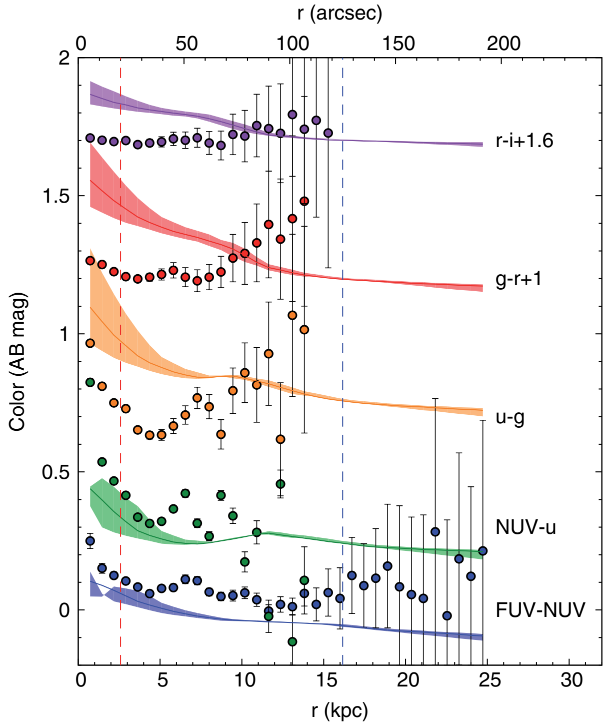

Figure 12. Observed color profiles of NGC 5668 (points) corrected for internal extinction as in the black points of Figure 9. These observed colors are compared with the ones predicted by the best-fitting model to light profiles (lines and bands). The red and blue vertical dashed lines bracket the spatial range used during the fit. Note that since the fit is performed simultaneously at all radii and all wavelengths from the FUV to 4.5 μm, departures up to a few tenths of a magnitude are expected for a particular color and radius.

(A color version of this figure is available in the online journal.)

beyond ~30″–40″. This radius interestingly coincides with the position where the slope of the metallicity gradient changes sign. We also find small offsets ($\leqslant$0.2 mag) between the observed and predicted colors. This is partially due to uncertainties in the model predictions for some of these colors.

The model has to reproduce at the same time the shape of the observed surface brightness profiles in all bands simultaneously and in addition it has to reproduce the "average" level of surface brightness. This kind of fitting introduces some limits in the range of the model parameters in a way that the colors of these models are located in a relatively narrow range as a consequence of the high degeneration within those model (surface brightness) profiles that match the data at all wavelengths simultaneously.[21]

Small variations of a few tenths of a magnitude will not have a significant impact on the overall shape of the surface brightness profiles, but will reveal themselves more clearly in the color profiles (see Muñoz-Mateos et al. 2011). On the other hand, the SFHs of the different annuli in the model are tied to one another (due to the analytical way in which we implement radial changes) but the actual SFH within the galaxy will exhibit more complex radial variations from one ring to the next.

6. DISCUSSION

The analysis presented above shows that most of the properties of the disk of NGC 5668 can be well reproduced by the chemical and spectrophotometric BP2000 models. This is true both for the global metallicity gradient as well as for the shape of the galaxy surface brightness profiles. This is also true for the rotation curve (see Figure 13). However, there are observables (chemical abundances and colors) and, especially, radial intervals among them that are not so well fitted by these simple models. The objective must then be to establish the mechanism(s) that drive the departures of these observables and the associated star formation and chemical histories in NGC 5668 from those predicted by the *inside-out* scenario of the disk formation on which the BP2000 models are based on. In particular, we ought to explain the bimodality (Chiappini et al. 2001) of the abundance gradient (and color profiles) measured in NGC 5668: flatter in the outermost regions and steeper in the inner ones.

6.1. Bimodal Distribution Mechanisms

The re-distribution of stars, gas, and dust in galaxies can have important consequences in the metallicity distribution and, in particular, in deviations of the chemical and photometric properties of disks with respect to the predictions of static disk evolution models. In this regard, radial changes (up- or down-bending) in the slope of the abundance gradient of nearby spiral galaxies (Vílchez & Esteban 1996) are detected and are often related to gaseous and stellar radial mixing processes (Spitzer & Schwarzschild 1953; Barbanis & Woltjer 1967; Shaver et al. 1983; Fuchs 2001; Sellwood & Binney 2002; Roškar et al. 2008; Haywood 2008; Bresolin et al. 2009b; Vlajić et al. 2009).

The existence of this kind of bimodal gradients are often proposed to have been induced by the presence of a bar-like potential (Díaz et al. 1990; Vila-Costas & Edmunds 1992; Edmunds & Roy 1993; Zaritsky et al. 1994). Indeed, in the case of strong-barred galaxies a change from a shallow to a steep metallicity profile is commonly observed and explained in the context of radial mixing of the gas induced by the bar (Martin & Roy 1995; Roy & Walsh 1997). On the other hand, bars can also lead to a steepening of the metallicity profile toward the inner disk if the gas transfer results in significant star formation in situ (Friedli et al. 1994; Martin & Roy 1995; Roy et al. 1996; Roy & Walsh 1997).

This latter behavior has been found in dynamical simulations of the formation of bars (Friedli et al. 1994; Friedli & Benz 1995). In these simulations, the presence of a steep-shallow break in the metallicity profile is the result of an intense chemical enrichment by star formation in the bar combined with the dilution effect of the outward flow beyond the break. According to these models the presence of such a break indicates that the bar has recently formed, i.e., in the last Gyr. Observationally, the metallicity distribution of a number of galaxies hosting young bars has been successfully reproduced by this or a similar scenario (Roy & Walsh 1997; Considère et al. 2000).

However, other mechanisms have been also proposed to explain bimodal metallicity distributions. Thus, in the context of the spiral density wave theory, star formation is expected to be proportional to $\Omega - \Omega_p$ (Oort & Peixóto 1974). In Jensen et al. (1976), this prediction was successfully tested against the metallicity gradients measured in a number of grand-design spirals. Should this scenario be valid, one would expect to find a minimum in the chemical abundance at the position of the

---

[21] One could decide to fit only the color profiles instead. However, that would lead to solutions that might not fit the overall shape of the surface brightness profiles and that would be very sensitive to uncertainties in the model predictions regarding specific colors (associated with limitations in the yields, stellar libraries at non-solar abundances, and uncertainties in the luminosity at near-infrared and UV wavelengths; see Maraston et al. 2006 and Muñoz-Mateos et al. 2011, respectively).

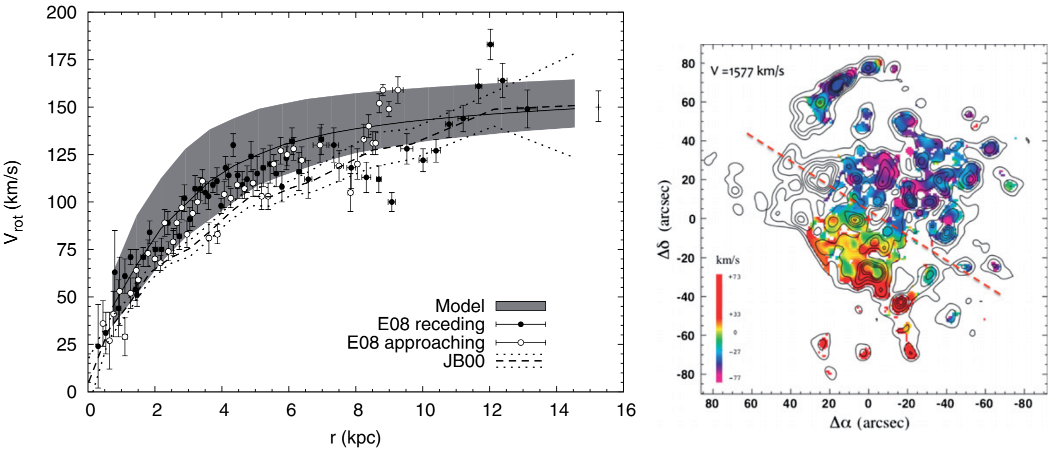

Figure 13. Left: comparison between the observed and predicted rotation curve of NGC 5668. The black solid line shows the rotation curve corresponding to the model that best fits the multi-wavelength profiles, and the gray band shows the associated uncertainty. The empirical data come from the Fabry–Perot Hα studies of Jiménez-Vicente & Battaner (2000) and Epinat et al. (2008). The rotation curve of the former is plotted with a dashed line, the dotted ones showing the corresponding errors. The values of Epinat et al. (2008) are marked with solid points (receding side of the disk) and open ones (approaching side). Since NGC 5668 is almost face-on, small variations in the adopted inclination angle could re-scale the empirical rotation curves. The vertical tickmark near the end of the curve shows the variations induced by changes of ±1° in the inclination angle. Right: Hα velocity map of the ionized gas derived from the Hα emission line (Hα is represented by isocontours). North is up and east is to the left. One pointing was masked out because the derived velocity values were not reliable.

(A color version of this figure is available in the online journal.)

corotation radius (see also the recent works by Acharova et al. 2005; Scarano 2010), especially in the case of galaxies where the spiral structure is long-lived and quasi-stationary (McCall 1986; Acharova et al. 2005). This is to the fact that $\Omega - \Omega_p$ is null (by definition) at corotation and, therefore, star formation should be less efficient resulting in a lesser degree of metal enrichment. In this scenario, a maximum in the colors should also be observed at the approximate position of the corotation radius as the optical–near-infrared colors would be dominated by those of the underlying stellar population since the current day SFR is expected to be low.

Finally, a flattening of the outer color and metallicity profiles is believed to be also caused by the increasing contribution of old migrated stars to the stellar content of disks (Zaritsky et al. 1994; Binney 2001; Sellwood & Binney 2002; Roškar et al. 2008; more recently, Minchev et al. 2011; Roškar et al. 2011). In this case, as we move further out into the outer disk we find progressively older stars, which have been migrating for a longer period of time, leading to a positive age and color gradient in these regions. With regard to the metal abundance and according to the simulations of Roškar et al. (2008), radial migration leads to the mixing of the old stellar populations, which results in flatter gradients at early times and in the very outer regions of the present-day disks as these regions are primarily populated by migrated stars. In the few observational and theoretical studies on the luminosity-weighted age profiles of the disks, a similar flattening or even an up-bending is found (Bakos et al. 2008; Sánchez-Blázquez et al. 2009, 2012; Yoachim et al. 2010). While some authors favor stellar migration as the main driver of the shaping of these age profiles (Yoachim et al. 2010), some others indicate that this might be due to a decrease in the star formation in the external parts of the disk with time caused by a reduction of the volume density of the gas in these regions (Sánchez-Blázquez et al. 2009).

The different scenarios proposed above to explain a steep-shallow break in the metallicity gradient of galaxies, namely, a young bar, reduced star formation at the corotation radius, stellar migration, or evolution of the star formation threshold with redshift have different imprints not only on the specific shape of the metallicity gradient but also on other properties such as the colors. In the case of NGC 5668, the change in the shape of the metallicity gradient takes place at a radius of ∼36″ (4.4 kpc or 2.8 disk-scale lengths), well within the region where in situ star formation takes place in the disk, at an approximate surface brightness of ∼22 mag arcsec^{-2} (3.6 μm *Spitzer* band). At this radius the contribution of migrated stars to either the colors, luminosity-weighted age, or chemical abundance is expected to be negligible compared with that from stars formed in situ (see Bakos et al. 2008; Vlajić et al. 2009). Again, as this brake takes place well within the star-forming disk of NGC 5668, changes in the color and metallicity gradients associated with a possible evolution of the star formation threshold with redshift is highly unlikely. With respect to the possibility that the minimum in the metal abundance profile of NGC 5668 could be due to the presence of the corotation radius at this break, two things can be said. First, NGC 5668 is a rather flocculent spiral,[22] where spiral density waves are expected to be weak or absent and, consequently, the effects of the spiral arms on the radial distribution of the star formation should be minimal (if any; McCall 1986). Second, the color profiles in $(u - g)$ and $(g - r)$ show a minimum at the position of the metallicity break, which is the opposite to what we would expect if that position corresponds to the corotation radius.

6.2. Bar Formation in NGC 5668

The only scenario that remains to be analyzed in detail is the possibility that the deviations of the metallicity and color profiles from those predicted by the best-fitting BP2000 model of NGC 5668 are due to the presence of a nascent bar and the effects associated with it. It is well known that one of the most important drivers in the evolution of galaxies are

---

[22] The lack of strong spiral arms in NGC 5668 is evident even after the examination of the IRAC near-infrared images of the object (see Scarano 2010 and references therein).

bars (or non-axisymmetric central light distributions or ovals; Athanassoula 1994). Bars exist in about two-thirds of disk galaxies (Sellwood & Wilkinson 1993) and isolated galaxies are known to be able to develop a barred morphology spontaneously from internal instabilities caused by cooling processes (Miller & Prendergast 1968; Kalnajs 1978; Binney & Tremaine 1987; Sellwood & Wilkinson 1993). These gravitational instabilities are commonly the result of enhanced gas accretion in the disk (Lindblad et al. 1996). Some of the observational properties of NGC 5668 already reveal a potential active gas-accretion phase in this galaxy, such as the presence of both HVCs and HRVCs (Jiménez-Vicente & Battaner 2000 and references therein) and the high total SFR in this object.

In this regard, another relevant parameter is the H I content of NGC 5668 compared with objects of similar total mass and morphological type. In order to find out whether the H I content NGC 5668 is particularly high or low, we resort to the so-called H I deficiency parameter. This quantity, defined by Haynes & Giovanelli (1984), compares—in logarithmic scale—the observed H I mass of a given galaxy and the typical H I mass of isolated galaxies of similar morphological types and linear sizes. The difference between both values is performed in such a way that positive H I deficiencies correspond to galaxies with less gas than similar field galaxies, and vice versa. Following the prescriptions of Haynes & Giovanelli (1984), we find that an Sd galaxy with the same optical diameter as NGC 5668 is expected to have $\log(M_{\rm H\,I}) = 9.66$. Solanes et al. (1996) extended the work of Haynes & Giovanelli (1984) to a larger sample of galaxies. While they only include Sa-Sc galaxies in their sample, we can safely apply the fitting coefficients of Sc's to our Sd spiral (Solanes et al. 2001). By doing so we obtain a reference H I mass of $\log(M_{\rm H\,I}) = 9.64$, completely consistent with the previous estimation. According to Schulman et al. (1996), the actual H I mass of NGC 5668 is $\log(M_{\rm H\,I}) = 10$, which implies a negative H I deficiency of ~ -0.35. Considering that the usual 1σ scatter of the H I mass for a given type and size is 0.2–0.3 dex (including all types of galaxies), we conclude that our Galaxy is roughly 1σ–2σ gas richer than its *normal* counterparts. While this difference might not be significant, it shows that, if anything, NGC 5668 has a larger H I content than the average of the spiral galaxy population of its type. Schulman et al. (1994) found in NGC 5668 a weak bar or oval inner structure of $12''$ size visible in both optical and near-infrared images. Athanassoula (1994) found that in spiral galaxies having oval structures or weak bars, star formation can occur prolifically along them, especially in the central parts and at the two ends of the bar region. This would result in bluer colors in these regions. The presence of a local minimum in color at a galactocentric distance of ∼30–40 arcsec seems to favor this scenario for NGC 5668. Note, however, that the oval seen in its images is significantly smaller than the radius where the minimum in color and metallicity is found. One possible explanation for this difference might come from the fact that while the light from the superposition of x_1 orbits that shape the oval is only clearly seen in the central $12''$, the instabilities associated with it could take place further out, where the superposition of these orbits is not yet significant enough for being detected via photometry only (Debattista et al. 2006).

Another possible explanation for the existence of the oval distortion in NGC 5668 is the possible interaction of NGC 5668 with UGC9380 (Schulman et al. 1996). This is a dwarf galaxy at a relative distance of 200 kpc to the southeast of NGC 5668, with a systemic velocity of 1690 km s^{-1} and a relative velocity of ∼108 km s^{-1}. A recent or ongoing tidal interaction between these two galaxies could have produced the high-velocity features in NGC 5668 and triggered the formation of both the oval and the incipient bar, as reported by *N*-body simulations of minor mergers (Eliche-Moral et al. 2006, 2011).

The fact that these blue colors do not extend all the way from this galactocentric distance to the center of the galaxy is likely due to a combination of different effects. First, the secular inside-out model for the evolution of the disk of NGC 5668 predicts a reddening of ∼0.2 mag (0.15 mag) in $u - g$ $(g - r)$ from $36''$to $6''$ (see Figure 12). Moreover, the reddening in the (FUV − NUV) color indicates a change of ∼0.09 mag in the $B - V$ color purely due to dust attenuation $[E(B - V)]$ within this same radial range. Finally, the light contribution of the bulge in the center, despite being small, can also lead to relatively red colors. These three effects are superimposed on the change in colors induced by star formation in the bar region and whose effects on the colors appear to be noticeable only at both its ends.

Regarding the age of this young bar, in the case of the barred galaxy NGC 3359, Martin & Roy (1995) calculated the age of the bar by using the equation of turbulent transport in a shear flow (Roy & Kunth 1995). Below we repeat this exercise for the case of NGC 5668. If we consider a Cartesian coordinate system centered in the galaxy center and we take x_2 as the radial direction of the local circular orbit (we do not take in account perpendicular effects), $l \sim 300$ pc as the mean free path of clouds between collisions (Roberts & Hausman 1984), we can then calculate the time for the gas to diffuse in a length Δx_2 in the radial direction as

$$\tau_{x_2} = \frac{\Delta {x_2}^2}{vl}. \qquad (3)$$

In our case $\Delta x_2 = 4.4$ kpc, which coincides with $r_{\rm BREAK}$ which is the radius at which we detect the flattening of the metallicity gradient and the minimum in the color profiles. From the radial velocity map kindly provided by J. Jiménez-Vicente (2010, private communication; see also Jiménez-Vicente & Battaner 2000), we determine the maximum of the non-circular motions to be $v = 10$ km s^{-1}. This yields $\tau_{x_2} \sim 10^9$ yr, which can be considered as an upper limit to the bar age since the radial transport induced by a bar is a stationary flow. The lower limit is given by a simple division of $\Delta x_2/v$. The best estimate for the age of the young bar in NGC 5668 is then $10^8 \mathrm{yr} \leqslant \tau_{x_2} \leqslant 10^9$ yr.

In summary, while the overall observational properties of NGC 5668 are well fitted by the inside-out scenario of disk formation, the deviations in the color and metallicity profiles are best interpreted in the context of the presence of a nascent bar where significant in situ star formation is (or have been recently) taking place. The formation of the bar is believed to be due to instabilities in the gas-rich inner disk of NGC 5668, possibly helped in the interaction with a companion. This scenario is compatible with the relatively large H I content and SFR of NGC 5668 and with the presence of HVCs and HRVCs in its velocity field, evidence of significant non-rotational gas motions in the disk.

7. CONCLUSIONS

In this paper, we have carried out an extensive and detailed study of the chemical and photometric properties of the nearby spiral galaxy NGC 5668. This detailed study has been possible thanks to the combined use of Integral Field Spectroscopy (IFS) in the optical and panchromatic broadband imaging of the entire system. The main conclusions from this work are the following.

1. Dust-attenuation profiles have been obtained using a number of methods. The mean continuum attenuation is A_V ∼0.4 mag. We find a significantly larger ionized-gas attenuation than that of the continuum in agreement with the predictions of Calzetti (2001).
2. We have derived dust-attenuation-corrected emission-line fluxes for a total of 62 individual H II complexes and 18 concentric annuli centered on the position of the nucleus of NGC 5668. Based on the strong-line method of Kewley & Dopita (2002) oxygen-abundance measurements have been obtained. We find a bimodal radial distribution in metallicity with a steep negative gradient with slope −0.14 ± 0.09 (dex kpc^{-1}) within a galactocentric distance of 36″ and a shallower (or even positive) metallicity gradient beyond that point, 0.002 ± 0.002 (dex kpc^{-1}).
3. Surface brightness and color profiles from the UV to the near-infrared have also been obtained. These profiles nicely match the predictions of the chemo-spectrophotometrical models for the evolution of galaxy disks (BP2000 models) for a circular velocity of $v_{\rm circ} = 167\,{\rm km\,s^{-1}}$ and a spin parameter of $\lambda = 0.053$. This best-fitting model also agrees with the overall shape of the galaxy metallicity gradient and rotation curve, although it cannot reproduce the steep-shallow metallicity break or the moderate bluing in some of the color profiles ($u - g$, $g - r$) around the position of the metallicity break.
4. Out of the different mechanisms proposed in the literature to explain the change in the slope of the metallicity profile in spiral disks (and the color profile), only the presence of a bar in its formative stages agrees well with the other observational properties of NGC 5668: the position of the metallicity break in disk-scale lengths, the bluing in the colors at that position, the large H I content and SFR of the galaxy, the presence of HVCs and HRVCs in the galaxy velocity field, and even the detection of an oval in the central region of the galaxy.

We thank the anonymous referee for reviewing the manuscript, and for the comments and suggestions that helped to improve the content of the paper. We also thank Carmen Eliche-Moral, Fabián Rosales-Ortega, Judit Bakos, and Sheila Kannappan for helpful discussions. R. A. Marino was also funded by the Spanish program International Campus of Excellence Moncloa (CEI). We thank the Calar Alto Observatory for the allocation of the director's discretionary time to this program. We acknowledge support from the Spanish Programa Nacional de Astronomía y Astrofísica under grant AYA 2009-10368. We are also partially funded by the Spanish MICINN under the Consolider-Ingenio 2010 Program grant CSD2006-00070: First Science with the GTC. J.C.M.M. receives financial support from NASA JPL/*Spitzer* grant RSA 1374189. He also acknowledges support from the National Radio Astronomy Observatory, which is a facility of the National Science Foundation operated under cooperative agreement by Associated Universities, Inc. This work is based in part on observations made with the *Spitzer Space Telescope*, which is operated by the Jet Propulsion Laboratory, Caltech under NASA contract 1407. *GALEX* is a NASA Small Explorer launched in 2003 April. We gratefully acknowledge NASA's support for construction, operation, and scientific analysis of the *GALEX* mission. This research has made use of the NASA/IPAC Extragalactic Database (NED) which is operated by the Jet Propulsion Laboratory, and the California Institute of Technology, under contract with the National Aeronautics and Space Administration. This paper makes use of the Sloan Digital Sky Survey data. Funding for the SDSS and SDSS-II has been provided by the Alfred P. Sloan Foundation, the Participating Institutions, the National Science Foundation, the U.S. Department of Energy, the National Aeronautics and Space Administration, the Japanese Monbukagakusho, the Max Planck Society, and the Higher Education Funding Council for England. The SDSS Web site is http://www.sdss.org/. The SDSS is managed by the Astrophysical Research Consortium for the Participating Institutions. The Participating Institutions are the American Museum of Natural History, the Astrophysical Institute Potsdam, the University of Basel, the University of Cambridge, Case Western Reserve University, the University of Chicago, Drexel University, Fermilab, the Institute for Advanced Study, the Japan Participation Group, Johns Hopkins University, the Joint Institute for Nuclear Astrophysics, the Kavli Institute for Particle Astrophysics and Cosmology, the Korean Scientist Group, the Chinese Academy of Sciences (LAMOST), the Los Alamos National Laboratory, the Max-Planck-Institute for Astronomy (MPIA), the Max-Planck-Institute for Astrophysics (MPA), New Mexico State University, the Ohio State University, the University of Pittsburgh, the University of Portsmouth, Princeton University, the United States Naval Observatory, and the University of Washington.

REFERENCES

Abazajian, K. N., Adelman-McCarthy, J. K., Agüeros, M. A., et al. 2009, ApJS, 182, 543
Acharova, I. A., Lépine, J. R. D., & Mishurov, Y. N. 2005, MNRAS, 359, 819
Ardeberg, A., & Virdefors, B. 1982, A&A, 115, 347
Athanassoula, E. 1994, in Proc. of the Conf. held at The University of Kentucky, Lexington, ed. I. Shlosman (Cambridge: Cambridge Univ. Press), 143
Azzollini, R., Trujillo, I., & Beckman, J. E. 2008, ApJ, 679, L69
Bakos, J., Trujillo, I., & Pohlen, M. 2008, ApJ, 683, L103
Barbanis, B., & Woltjer, L. 1967, ApJ, 150, 461
Barden, M., Rix, H., Somerville, R. S., et al. 2005, ApJ, 635, 959
Barker, M. K., Ferguson, A. M. N., Irwin, M., Arimoto, N., & Jablonka, P. 2009, AJ, 138, 1469
Bell, E. F. 2002, ApJ, 577, 150
Bell, E. F., & de Jong, R. S. 2000, MNRAS, 312, 497
Binney, J. 2001, in Galaxy Disks and Disk Galaxies, ed. J. G. Funes, S. J., & E. M. Corsini (San Francisco, CA: ASP), 63
Binney, J., & Tremaine, S. 1987, Galactic Dynamics (Princeton, NJ: Princeton Univ. Press)
Boffi, F. R., Sparks, W. B., & Macchetto, F. D. 1999, A&AS, 138, 253
Boissier, S., Gil de Paz, A., Boselli, A., et al. 2007, ApJS, 173, 524
Boissier, S., & Prantzos, N. 1999, MNRAS, 307, 857
Boissier, S., & Prantzos, N. 2000, MNRAS, 312, 398
Boselli, A., Eales, S., Cortese, L., et al. 2010, PASP, 122, 261
Bresolin, F., Gieren, W., Kudritzki, R., et al. 2009a, ApJ, 700, 309
Bresolin, F., Kennicutt, R. C., & Ryan-Weber, E. 2012, ApJ, 750, 122
Bresolin, F., Ryan-Weber, E., Kennicutt, R. C., & Goddard, Q. 2009b, ApJ, 695, 580
Bruzual, G., & Charlot, S. 2003, MNRAS, 344, 1000
Buat, V. 1992, A&A, 264, 444
Buat, V., Iglesias-Páramo, J., Seibert, M., et al. 2005, ApJ, 619, L51
Calzetti, D. 1997, AJ, 113, 162
Calzetti, D. 2001, PASP, 113, 1449
Calzetti, D., Armus, L., Bohlin, R. C., et al. 2000, ApJ, 533, 682
Calzetti, D., Kinney, A. L., & Storchi-Bergmann, T. 1994, ApJ, 429, 582
Calzetti, D., Kinney, A. L., & Storchi-Bergmann, T. 1996, ApJ, 458, 132
Cardelli, J. A., Clayton, G. C., & Mathis, J. S. 1989, ApJ, 345, 245
Charlot, S., & Fall, S. M. 2000, ApJ, 539, 718
Chiappini, C., Matteucci, F., & Romano, D. 2001, ApJ, 554, 1044
Considère, S., Coziol, R., Contini, T., & Davoust, E. 2000, A&A, 356, 89
Cortese, L., Boselli, A., Buat, V., et al. 2006, ApJ, 637, 242
Cortese, L., Boselli, A., Franzetti, P., et al. 2008, MNRAS, 386, 1157
Dale, D. A., Gil de Paz, A., Gordon, K. D., et al. 2007, ApJ, 655, 863

Debattista, V. P., Mayer, L., Carollo, C. M., et al. 2006, ApJ, 645, 209
de Jong, R. S., Seth, A. C., Radburn-Smith, D. J., et al. 2007, ApJ, 667, L49
de Vaucouleurs, G., de Vaucouleurs, A., Corwin, H. G., Jr., et al. (ed.) 1991, Third Reference Catalogue of Bright Galaxies (New York: Springer)
Díaz, A. I., Terlevich, E., Pagel, B. E. J., Vílchez, J. M., & Edmunds, M. G. 1990, RevMexAA, 21, 223
Dressel, L. L., & Condon, J. J. 1976, ApJS, 31, 187
Edmunds, M. G., & Roy, J. 1993, MNRAS, 261, L17
Eliche-Moral, M. C., Balcells, M., Aguerri, J. A. L., & González-García, A. C. 2006, A&A, 457, 91
Eliche-Moral, M. C., González-García, A. C., Balcells, M., et al. 2011, A&A, 533, A104
Epinat, B., Amram, P., & Marcelin, M. 2008, MNRAS, 390, 446
Fazio, G. G., Hora, J. L., Allen, L. E., et al. 2004, ApJS, 154, 10
Fitzpatrick, E. L. 1999, PASP, 111, 63
Fixsen, D. J., Cheng, E. S., Gales, J. M., et al. 1996, ApJ, 473, 576
Friedli, D., & Benz, W. 1995, A&A, 301, 649
Friedli, D., Benz, W., & Kennicutt, R. 1994, ApJ, 430, L105
Fuchs, B. 2001, MNRAS, 325, 1637
Garnett, D. R. 1992, AJ, 103, 1330
Gil de Paz, A., Boissier, S., Madore, B. F., et al. 2007, ApJS, 173, 185
Gil de Paz, A., & Madore, B. F. 2002, AJ, 123, 1864
Gil de Paz, A., & Madore, B. F. 2005, ApJS, 156, 345
Gil de Paz, A., Madore, B. F., Boissier, S., et al. 2005, ApJ, 627, L29
Gogarten, S. M., Dalcanton, J. J., Williams, B. F., et al. 2010, ApJ, 712, 858
Gordon, K. D., Clayton, G. C., Witt, A. N., & Misselt, K. A. 2000, ApJ, 533, 236
Haynes, M. P., & Giovanelli, R. 1984, AJ, 89, 758
Haywood, M. 2008, MNRAS, 388, 1175
Heckman, T., Krolik, J., Meurer, G., et al. 1995, ApJ, 452, 549
Jensen, E. B., Strom, K. M., & Strom, S. E. 1976, ApJ, 209, 748
Jiménez-Vicente, J., & Battaner, E. 2000, A&A, 358, 812
Kalnajs, A. J. 1978, in Structure and Properties of Nearby Galaxies (IAU Symp. 77), ed. E. M. Berkhuijsen & R. Wielebinski (Dordrecht: Reidel), 113
Kelz, A., Verheijen, M. A. W., Roth, M. M., et al. 2006, PASP, 118, 129
Kewley, L. J., & Dopita, M. A. 2002, ApJS, 142, 35
Kroupa, P. 2001, MNRAS, 322, 231
Lindblad, P. A. B., Lindblad, P. O., & Athanassoula, E. 1996, A&A, 313, 65
MacArthur, L. A., Courteau, S., Bell, E., & Holtzman, J. A. 2004, ApJS, 152, 175
Maíz-Apellániz, J., Mas-Hesse, J. M., Muñoz-Tuñon, C., Vílchez, J. M., & Castañeda, H. O. 1998, A&A, 329, 409
Maraston, C., Daddi, E., Renzini, A., et al. 2006, ApJ, 652, 85
Mármol-Queraltó, E., Sánchez, S. F., Marino, R. A., et al. 2011, A&A, 534, A8
Martin, C. L., & Kennicutt, R. C., Jr. 2001, ApJ, 555, 301
Martin, D. C., Fanson, J., Schiminovich, D., et al. 2005, ApJ, 619, L1
Martin, P., & Roy, J. 1995, ApJ, 445, 161
Mayya, Y. D., & Prabhu, T. P. 1996, AJ, 111, 1252
McCall, M. L. 1986, PASP, 98, 992
McCall, M. L., Rybski, P. M., & Shields, G. A. 1985, ApJS, 57, 1
McGaugh, S. S. 1991, ApJ, 380, 140
Meurer, G. R., Heckman, T. M., & Calzetti, D. 1999, ApJ, 521, 64
Meurer, G. R., Heckman, T. M., Leitherer, C., et al. 1995, AJ, 110, 2665
Miller, R. H., & Prendergast, K. H. 1968, ApJ, 151, 699
Minchev, I., Famaey, B., Combes, F., et al. 2011, A&A, 527, A147
Mo, H. J., Mao, S., & White, S. D. M. 1998, MNRAS, 295, 319
Morrissey, P., Conrow, T., Barlow, T. A., et al. 2007, ApJS, 173, 682
Moustakas, J., Kennicutt, R. C., Jr., Tremonti, C. A., et al. 2010, ApJS, 190, 233
Muñoz-Mateos, J. C., Boissier, S., Gil de Paz, A., et al. 2011, ApJ, 731, 10
Muñoz-Mateos, J. C., Gil de Paz, A., Boissier, S., et al. 2007, ApJ, 658, 1006
Muñoz-Mateos, J. C., Gil de Paz, A., Boissier, S., et al. 2009a, ApJ, 701, 1965
Muñoz-Mateos, J. C., Gil de Paz, A., Zamorano, J., et al. 2009b, ApJ, 703, 1569
Nakano, S., Kushida, R., Kushida, Y., & Itagaki, K. 2004, IAU Circ., 8272, 1
Oke, J. B. 1990, AJ, 99, 1621
Oort, A. H., & Peixóto, J. P. 1974, J. Geophys. Res., 79, 2705
Osterbrock, D. E., & Ferland, G. J. 2006, Astrophysics of Gaseous Nebulae and Active Galactic Nuclei (2nd. ed; Sausalito, CA: University Science Books)
Pagel, B. E. J. 1986, PASP, 98, 1009
Pagel, B. E. J., Edmunds, M. G., Blackwell, D. E., Chun, M. S., & Smith, G. 1979, MNRAS, 189, 95
Pérez-Montero, E., & Díaz, A. I. 2005, MNRAS, 361, 1063
Poggianti, B. M., Smail, I., Dressler, A., et al. 1999, ApJ, 518, 576
Poggianti, B. M., & Wu, H. 2000, ApJ, 529, 157
Pohlen, M., & Trujillo, I. 2006, A&A, 454, 759
Prantzos, N., & Boissier, S. 2000, MNRAS, 313, 338
Reach, W. T., Megeath, S. T., Cohen, M., et al. 2005, PASP, 117, 978
Roberts, W. W., Jr., & Hausman, M. A. 1984, ApJ, 277, 744
Rosales-Ortega, F. F. 2011, NewA, 16, 220
Rosales-Ortega, F. F., Kennicutt, R. C., Sánchez, S. F., et al. 2010, MNRAS, 405, 735
Roškar, R., Debattista, V. P., Loebman, S. R., Ivezić, Ž., & Quinn, T. R. 2011, MNRAS, submitted (arXiv:1110.4413)
Roškar, R., Debattista, V. P., Quinn, T. R., Stinson, G. S., & Wadsley, J. 2008, ApJ, 684, L79
Roy, J., Belley, J., Dutil, Y., & Martin, P. 1996, ApJ, 460, 284
Roy, J., & Kunth, D. 1995, A&A, 294, 432
Roy, J., & Walsh, J. R. 1997, MNRAS, 288, 715
Sánchez, S. F. 2004, Astron. Nachr., 325, 167
Sánchez, S. F. 2006, Astron. Nachr., 327, 850
Sánchez-Blázquez, P., Courty, S., Gibson, B. K., & Brook, C. B. 2009, MNRAS, 398, 591
Sánchez-Blázquez, P., Marcolini, A., Gibson, B. K., et al. 2012, MNRAS, 419, 1376
Sánchez-Blázquez, P., Peletier, R. F., Jiménez-Vicente, J., et al. 2006, MNRAS, 371, 703
Sandage, A., & Tammann, G. A. 1987, A Revised Shapley-Ames Catalog of Bright Galaxies (Carnegie Inst. Washington Publ., Washington, D.C.: Carnegie Inst. Washington)
Savage, B. D., & Mathis, J. S. 1979, ARA&A, 17, 73
Scarano, S., Jr. 2010, Bull. Astron. Soc. Braz., 29, 65
Schulman, E., Bregman, J. N., Brinks, E., & Roberts, M. S. 1996, AJ, 112, 960
Schulman, E., Bregman, J. N., & Roberts, M. S. 1994, ApJ, 423, 180
Seaton, M. J. 1979, MNRAS, 187, 73P
Seibert, M., Martin, D. C., Heckman, T. M., et al. 2005, ApJ, 619, L55
Sellwood, J. A., & Binney, J. J. 2002, MNRAS, 336, 785
Sellwood, J. A., & Wilkinson, A. 1993, Rep. Prog. Phys., 56, 173
Shaver, P. A., McGee, R. X., Newton, L. M., Danks, A. C., & Pottasch, S. R. 1983, MNRAS, 204, 53
Solanes, J. M., Giovanelli, R., & Haynes, M. P. 1996, ApJ, 461, 609
Solanes, J. M., Manrique, A., García-Gómez, C., et al. 2001, ApJ, 548, 97
Spitzer, L., Jr., & Schwarzschild, M. 1953, ApJ, 118, 106
Stasińska, G., & Sodré, L., Jr. 2001, A&A, 374, 919
Thilker, D. A., Bianchi, L., Meurer, G., et al. 2007, ApJS, 173, 538
Thurston, T. R., Edmunds, M. G., & Henry, R. B. C. 1996, MNRAS, 283, 990
Trujillo, I., Förster Schreiber, N. M., Rudnick, G., et al. 2006, ApJ, 650, 18
Trujillo, I., Rudnick, G., Rix, H., et al. 2004, ApJ, 604, 521
Trumpler, R. J. 1930, PASP, 42, 214
Vila-Costas, M. B., & Edmunds, M. G. 1992, MNRAS, 259, 121
Vílchez, J. M., & Esteban, C. 1996, MNRAS, 280, 720
Vlajić, M., Bland-Hawthorn, J., & Freeman, K. C. 2009, ApJ, 697, 361
Wang, L., & Rowan-Robinson, M. 2009, MNRAS, 398, 109
Werner, M. W., Roellig, T. L., Low, F. J., et al. 2004, ApJS, 154, 1
Witt, A. N., & Gordon, K. D. 2000, ApJ, 528, 799
Xu, C., & Buat, V. 1995, A&A, 293, L65
Yoachim, P., & Dalcanton, J. J. 2008, ApJ, 682, 1004
Yoachim, P., Roškar, R., & Debattista, V. P. 2010, ApJ, 716, L4
York, D. G., Adelman, J., Anderson, J. E., Jr., et al. 2000, AJ, 120, 1579
Zaritsky, D., Kennicutt, R. C., Jr., & Huchra, J. P. 1994, ApJ, 420, 87

4

The O3N2 and N2 abundance indicators revisited

Resumen

La medida de la abundancia química en regiones H II extragalácticas es vital para: (I) el estudio del enriquecimiento químico de galaxies individuales en zonas específicas y para (II) la el estudio de la evolución del contenido en metales con el desplazamiento al rojo.

Los métodos más comunes para la determinación de la abundancia metálica en el gas ionizado en galaxias se basa en el análisis de cocientes de líneas de emisión en el óptico. En este capítulo se presenta el trabajo realizado en Marino et al. (2013) donde se proporciona una versión mejorada y actualizada de las calibraciones ya clásicas de los métodos de líneas intensas de Pettini & Pagel (2004; PP04 a partir de aquí) mediante el uso de los datos obtenidos dentro de la exploración CALIFA y de datos de la literatura.

El cálculo de las abundancias del gas ionizado en regiones H II tiene como punto de partida la definición de la estructura de ionización de la región correspondiente. Una suposición válida es el conocido como modelo de dos fases propuesto por Strömgren (1939). Este modelo asume que el gas alrededor de las estrellas más calientes y masivas está segregado en dos volúmenes bien diferenciados; es decir, hay dos zonas de ionización, una que incluye las especies de alta ionización tales como O++, Ne++,N++, y otra de menor grado de ionización que incluiría especies del tipo O+, N+, S+. La región se considera no isoterma y para cada zona de ionización es necesario derivar una cierta temperatura electrónica, a partir de líneas sensibles a la temperatura de especies características de cada una de las zonas, típicamente de [O III] en el primer caso y de [N II] o [O II] en el segundo. Una vez estas temperaturas y densidades son conocidas (n_e y T_e) las abundancias iónicas se pueden calcular a partir de diferentes cocientes de líneas. Este es el método conocido como directo o basado en T_e (Osterbrock & Ferland 2006). En el óptico las líneas más sensibles a la densidad son [O II]λ3726/λ3729 y [S II]λ6717/λ6731, mientras que las sensibles a la temperatura son [O III]λ4363, [N II]λ5755, [S III] λ 6312 y [O II]λ7320/λ7330. Además, la medida de al menos un cociente de líneas de las serie de Balmer es necesario para determinar la enrojecimiento por polvo. Las abundancias se pueden derivar entonces tanto a partir de líneas de recombinación (ORLs: Liu et al. 2006) o de las mucho más brillantes líneas de excitación colisional (CELs: Kennicutt et al. 2003; Pérez-Montero & Díaz 2005, PMD05 a partir de ahora, Kewley & Ellison 2008, KE08 a partir de ahora), o una combinación de ambas.

Desafortunadamente, en muchos casos no se disponen de medidas precisas de líneas sensibles a la temperatura. En ese caso se utilizan relaciones empíricas entre la temperatura (o directamente la abundancia química) y los cocientes de ciertas líneas de excitación colisional brillantes. Estos métodos alternativos se conocen como métodos indirectos y son los únicos disponibles en galaxias con desplazamiento al rojo intermedio y alto y fueron propuestos por primera vez por Pagel et al. (1979). Desde entonces se han introducido un gran número de estimadores indirectos (basados bien en calibraciones empíricas o en las predicciones de modelos de fotoionización), tales como O3N2[1], N2[2], R23[3], N2O2[4] entre otras. Las incertidumbres en las condiciones de excitación y estratificación de las diferentes regiones dentro de la nebulosa da lugar a que existan discrepancias en la determinación de la abundancia de oxígeno que llegan a ser de un factor $\sim 2-3$ (ver López-Sánchez et al. 2012 para una revisión reciente sobre este tema; LS12 a partir de ahora).

A pesar de las dificultades, el hecho de que en objetos distantes o en regiones H II débiles se dependa únicamente de las calibraciones de líneas intensas hace de estas de gran utilidad y relevancia evolutiva. A pesar del importante trabajo realizado recientemente (ver, por ejemplo, Israelian and Meynet 2008), ha llegado el momento de redefinir las calibraciones más populares de O3N2 y N2 usando la gran cantidad de datos observacionales disponibles en la actualidad, especialmente en el rango de alta metalicidad donde, hasta la fecha, sólo de disponía de predicciones teóricas y no de datos empíricos (ver PP04).

En Marino et al. (2013) se presenta una revisión de los calibradores empíricos de abundancias más usados, O3N2 y N2, mediante la comparación con medidas directas. Además, este trabajo proporciona, por primera vez, intervalos de confianza en función del valor del calibrador medido, gracias a la disponibilidad de medidas en multiples líneas de emisión (a partir del uso del método ONS; Pilyugin et al. 2010). Nuestro conjunto de datos incluye una compilación de 603 medidas de abundancias directas (método basado en T_e) en regiones H II de galaxias cercanas y de medidas basadas en el método ONS para 3423 regiones y complejos H II de galaxias de la muestra CALIFA. Los métodos derivados en Marino et al. (2013) se puede utilizar de forma empírica para derivar abundancias de oxígeno con errores aleatorios de 0.18 y 0.16 dex, respectivamente para el indicador O3N2 y N2, respectivamente. La compilación de las medidas utilizadas se presenta en el Apéndice A y en el artículo correspondiente publicado en la revista Astronomy & Astrophysics (2013, Vol. 559, A114). Como resultado a destacar, además del impacto conseguido por este trabajo en la comunidad, está el hecho de que las abundancias obtenidas usando estimadores previos estaban muy probablemente sobre-estimadas.

---

[1] O3N2=log(([O III]λ5007/Hβ) $\times$ (Hα/[N II]λ6584)); Alloin et al. 1979

[2] N2=log(Hα/[N II]λ6584); Storchi−Bergmann et al. (1994); Denicoló et al. (2002)

[3] R23=log(([O II]λ3727+[O III]λ5007)/Hβ); Pagel et al. 1979, 1980

[4] N2O2=log([N II]λ6584/ [O II]λ3727); Dopita et al. (2000)

4.1 Introduction

The chemical abundance of extragalactic H II regions are paramount for: (I) the study of the enrichment by heavy elements at a given position within a galaxy, and (II) the overall chemical enrichment in the Universe as a function of time by looking at galaxies over a wide redshift range (Peimbert et al. 2000). Most common methods for measuring the metal content of the ionized gas in galaxies rely on the analysis of their optical emission line ratios making H II regions the main target measuring element abundances in galaxies at any cosmological distance. In this Chapter I will present the most popular techniques widely used within the scientific community in deriving gas-phase chemical abundances. In particular, I will describe the work presented in Marino et al. (2013) where we provided an updated version of the seminal work of Pettini & Pagel 2004 (PP04 hereafter) but using the homogeneously-processed CALIFA dataset on emission-line flux measurements.

H II regions represent the most common form of interstellar material which emits strongly in the optical spectral range with fairly complete information about their elemental composition. The derivation of gaseous chemical abundances in these regions is based on the definition of the ionization structure. A valid assumption to understand how H II regions work is the original two-phase model of the ISM, or the so-called H II/H I region dichotomy, introduced by Strömgren (1939). This model assumes that the gas surrounding hot stars is segregated into physically distinct volumes, separated from their neutral environment by sharp boundaries; so there are two zones of ionization, one including all high ionization ions like O++, Ne++,N++, and another one including the lower ones, like O+, N+, S+. The H II region is considered non isothermal and for each ionization zone an electron temperature has to be assumed; typically, the electron temperature derived from the [O III] temperature sensitive lines is assigned to the high-ionization zone, whereas the electron temperature derived from the [N II] or [O II] lines is assumed for the low-ionization zone. Once the electron temperatures and densities are known, the abundance of each ion can be calculated from its corresponding equilibrium equation and line intensities measured in the spectra and the total abundance of a given element will be the sum of its different ions (see Shields 1990 for a review). Thus, when the physical properties of the ionized gas are well known (n_e and T_e) ionic abundances can be derived directly from the measured line fluxes; this is the so-called *direct* or T_e-based method (Osterbrock & Ferland 2006). Within the optical window, useful and popular density diagnostics for H II regions include the: [O II]λ3726/λ3729 and [S II]λ6717/λ6731 doublets; while the temperature sensitive lines include: [O III]λ4363, [N II]λ5755, [S III] λ6312, [O II]λ7320,λ7330. In addition, the measurement of the Balmer decrement is needed to correct the spectra from dust reddening and attenuation. The abundances of metals can be derived using either the faint recombination lines (ORLs: Liu et al. 2006) or the much brighter collisionally excited lines (CELs: Kennicutt et al. 2003; Pérez-Montero & Díaz 2005, PMD05 hereafter; Kewley & Ellison 2008, KE08 hereafter), or a combination of both. The standard method of deriving nebular abundances from emission lines is explained in great detail in bibliographic references on the physics of gaseous nebulae (Aller 1984; Osterbrock 1989).

Unfortunately, in some cases not all the ionic abundances are known and it becomes necessary to make use of ionization-correction factors (ICFs) in order to calculate the total abundance from the ionic abundances derived. These ICFs are very useful and can be computed using photoionization models together with the thermal parameters of the H II region obtained from different diagnostic line-intensity ratios. Therefore, in this case in order to derive abundances one has to rely on the so-called *indirect* abundance calibrations. The strong line methods rely on empirical relationships between different optical emission line ratios and metallicities determined via the T_e-method or predictions based on pure photoionization models, based on observations of large samples of H II regions. Pagel et al. (1979) first proposed the use of strong nebular lines of O and H to infer the oxygen abundance for giant extragalactic H II regions. Since then, many more calibration methods have been introduced providing more and more reliable estimates of the abundance of a given element from a combinations of their optical bright emission lines like O3N2[5], N2[6], R23[7], N2O2[8] among others. The difficulty of observationally determining T_e also led to the development of theoretical calibrations based on the predictions of grids of photoionization models (e.g. Dopita & Evans 1986; McGaugh 1991, M91 hereafter; Zaritsky et al. 1994, Z94 hereafter; Kewley & Dopita 2002, KD02 hereafter). Another approach is to simultaneously fit all the strong emission lines and use theoretical models to generate a probability distribution of metallicities and statistically estimate abundances (see Tremonti et al. 2004, hereafter T04; Pérez-Montero 2014; Dopita et al. 2013).

A number of relations have been proposed in the literature to derive metal abundances and temperatures from the metallicity-sensitive emission lines ratios. In this regard, we highlight the recent comparative review of López-Sánchez et al. (2012, LS12 hereafter) and similar previous studies from PMD09, KE08 and López-Sánchez & Esteban (2010). It is now widely accepted that abundance measurements can be affected by multiple systematic uncertainties that yield non−negligible offsets when abundances obtained from different methods are compared as shown in Figure 4.1 from KE08. Determining chemical abundances is not an easy task given the difficulty in the detecting faint auroral emission lines, such as [O III]λ4363. Besides, the field is at a crossroads as no consensus has been reached on (I) the long-standing "abundance discrepancy" problem (e.g. Peimbert et al. 1993; Esteban et al. 2009): for several Galactic and extragalactic H II regions the metal abundances relative to hydrogen, derived from the analysis of their faint ORLs are systematically larger than those obtained from the bright CELs, which can then be based on T_e measurements or strong-line methods (see Kennicutt et al. 2003; PMD05; KE08) of the same elements. In addition, there are still several relevant issues that have to be considered and need to be explained, including: (II) the presence of possible chemical inhomogeneities in the ionized regions (e.g. Tsamis & Pequignot 2005; Tsamis et al. 2011), that are intimately related to nucleosynthesis and the physics of metal dispersion and mixing in the ISM, (III) the effect of the complex geometry of the H II regions in the observed ionization structure, a fact nicely illustrated by 3D photoionization modelling (Ercolano et al. 2007, 2011) and likely linked to the ionizing photons leakage (Giammanco et al. 2005), and (IV) the fact that our knowledge of the ionizing spectra of hot massive stars is still plagued by many and profound uncertainties, specially in the extreme ultraviolet domain.

---

[5] O3N2=log(([O III]λ5007/Hβ) × (Hα/[N II]λ6584)); Alloin et al. 1979

[6] N2=log(Hα/[N II]λ6584); Storchi−Bergmann et al. (1994); Denicoló et al. (2002)

[7] R23=log(([O II]λ3727+[O III]λ5007)/Hβ); Pagel et al. 1979, 1980

[8] N2O2=log([N II]λ6584/ [O II]λ3727); Dopita et al. (2000)

In general, the discrepancies when computing oxygen abundances are typically within a factor of $\sim 2-3$ as illustrated in the comparative plot (Figure 4.1) for 10 different metallicity calibrations, including direct, theoretical and empirical methods applied to 27,730 star-forming galaxies from the SDSS; this is most worrying as the abundance of oxygen is the measure of metallicity in distant star-forming galaxies and the evolution of metallicity with redshift is being called to provide a fundamental

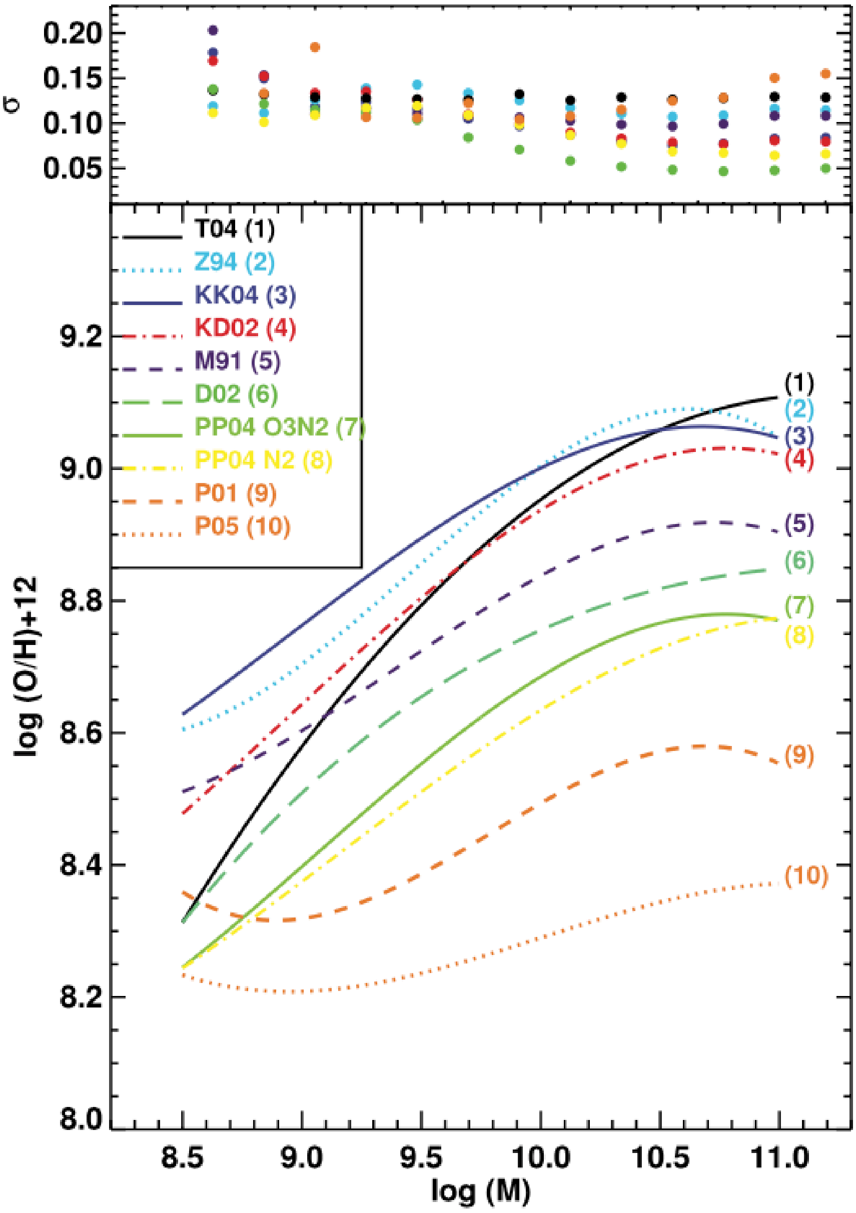

Figure 4.1: The robust best-fitting mass-metallicity (MZ) relations calculated using different metallicity calibrations (T04; Z94; Kobulnicky & Kewley (2004); KD02; M91; Denicoló et al. (2002); PP04; Pilyugin (2001); Pilyugin & Thuan (2005)). The top panel shows the rms scatter in metallicity around the best relation for each calibration in 0.1 dex bins of stellar mass. The y-axis offset, shape, and scatter of the MZ relation differs substantially, depending on which metallicity calibration used (see KE08 for a detailed explanation of the plot and discussion).

test on the evolution of galaxies. These results show that the choice of metallicity calibration has a significant effect on the shape and oxygen distribution suggesting that it is critical to use the same metallicity calibration when comparing different luminosity-metallicity or mass-metallicity (MZ) relations.

Despite of this discouraging scenario, empirical calibrations can be very useful to derive abundances for large samples of objects and they became, in practice, the only way to estimate the metallicity of distant (star-forming) galaxies, they are rather robust when used to derive properties, that changes from galaxy to galaxy or within galaxies. Though an important amount of work on the study of gas abundances in galaxies has been carried out during the last years (see e.g. Israelian and Meynet 2008 and references therein), the time has arisen to redefine the observational problem of chemical abundances at the scale of the entire galaxy disks. As exposed before, two of the most popular calibrations of the oxygen abundance are the O3N2 and N2 indicators. The most widely used calibration of these was introduced by PP04 who were actually the first to establish a relationship between these strong-line ratios and the H II region metal abundances. Figure 4.2 shows the O3N2 and N2 calibrations found by these authors using a set of 137 H II regions, all these values belong to T_e-based measurements except for few points (black squares) in the higher metallicity regime that come from photoionization models.

Thanks to the advent of modern IFU and the increasingly large number of emission line measurements, the study of chemical abundances in galaxies has entered in a new era. In this regard, in Marino et al. (2013) we reviewed the most widely used empirical oxygen calibrations, O3N2 and N2, by using new direct abundance measurements in order to give a precise determination of the prediction intervals of these indicators that were lacking until this work. Our analysis is based on the most comprehensive compilation of both T_e-based and multiple strong-line (ONS-based) ionized-gas abundance measurements in external galaxies to date in terms of all statistical significance, quality, and coverage of the parameters space. Our dataset compiles the T_e-based abundances of 603 H II regions extracted from the literature but also includes new measurements from the CALIFA survey. Besides providing new improved empirical calibrations for the gas abundance, we also present a comparison between our revisited calibrations with a total of 3423 additional CALIFA H II complexes with abundances derived using the ONS calibration (Pilyugin et al. 2010). Our (M13) O3N2 and N2 calibrations can be empirically applied to derive oxygen abundances calibrations relative to either direct-abundance determinations with errors of 0.18 dex and 0.16 dex, respectively. They show shallower abundance dependencies and statistically significant offsets compared to the classical calibrations as the ones of PP04, Nagao et al. (2006) and Pérez-Montero & Contini 2009. The T_e-based H II compilation is presented in Appendix A and this study has been published in the Astronomy & Astrophysics journal (2013, Volume 559, A114) with title “The O3N2 and N2 abundance indicator revisited: improved calibrations based on CALIFA and T_e-based literature data”. Our methodology has provided extremely useful informations for our current understanding of the chemical evolution of galaxies suggesting that the metallicity calibration used before our analysis led to an overestimation (on the basis of our assumptions) of the oxygen abundance in external galaxies.

Note that the assumed formalism along M13 was that the gas is in thermal equilibrium, with the electrons following a Maxwell-Bolzmann equilibrium energy distribution defined by a single electron tempetarure (T_e). However, this is an idealized situation far from the reality. There are two different formalisms that address inhomogeneities in the equilibrium of the plasma. One of them is the κ-formalism (e.g. Dopita et al. 2013), that assumes that the plasma has not reached the equilibrium, and the electron do not follow the M-B distribution, but a different one, the κ-distribution, described in solar system plasmas near the equilibrium. A more general one is the *t2* formalism (Peimbert et al. 1967), in which it is assumed that the plasmas is described by a set of electron temperatures like was a mix of plasmas at equilibrium each of them. Therefore for each of them it is needed a T_e, and the plasma is described as a first order by the medium temperature and the medium of the squared temperatures, *t2* (which is somehow an indication of how far the plasma is from an equilibrium defined by a single temperature). When $\kappa=\infty$ or $t2=0$ the plasma is at equilibrium defined by a single electron temperature.

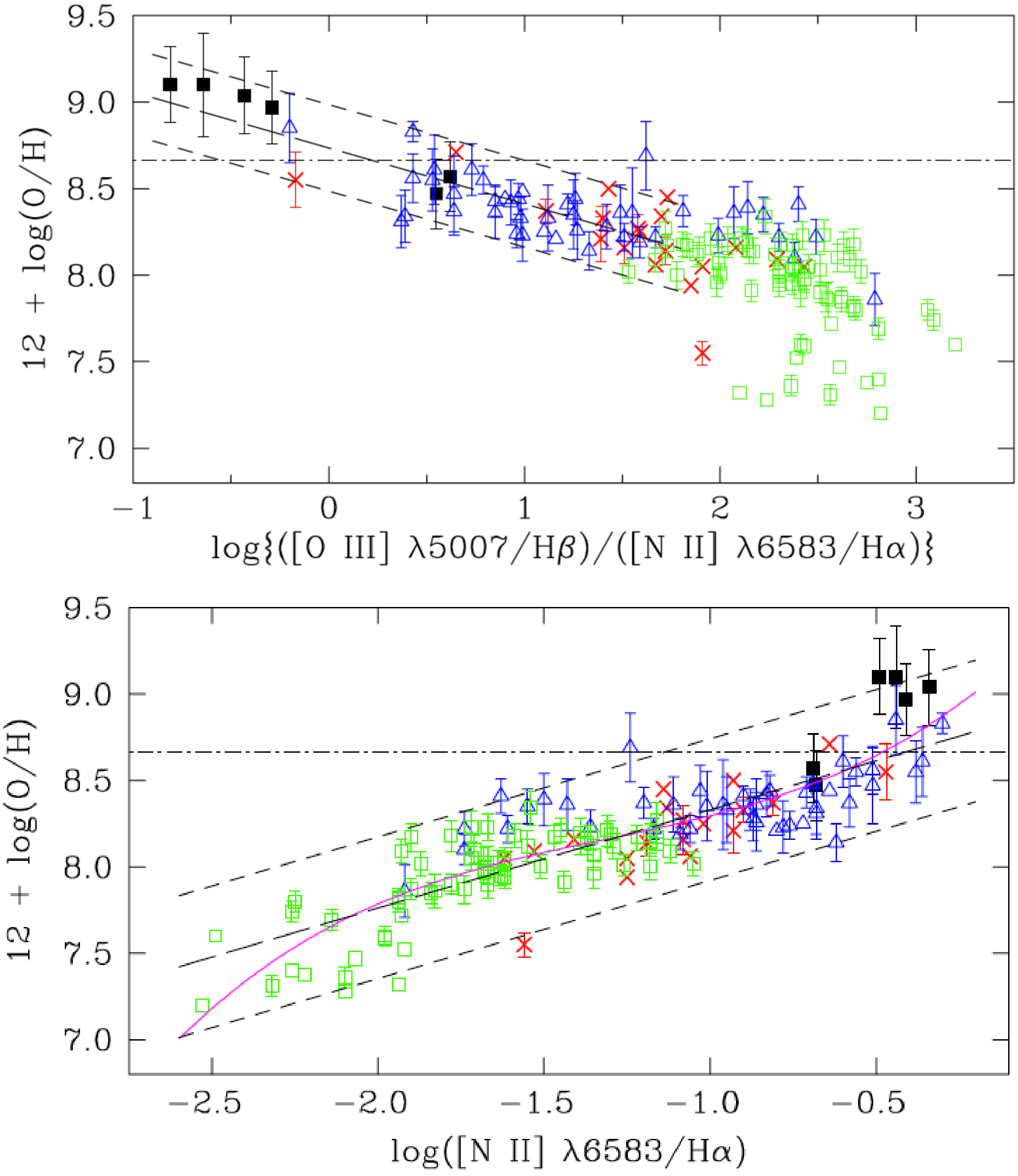

Figure 4.2: Oxygen abundance against the O3N2 (top panel) and N2 (bottom panel) indexes in extragalactic H II regions from PP04. The symbols are color code according the original work. The long-dashed line shows the best-fitting linear relationship while the short-dashed lines encompass 95 per cent of the measurements which satisfy this condition. The dot-dashed horizontal line shows the solar oxygen abundance (12+log(O/H)=8.66, Allende-Prieto et al. 2001; Asplund et al. 2004).

4.2 Marino et al. (2013) A&A, 559, A114

The O3N2 and N2 abundance indicators revisited: improved calibrations based on CALIFA and T_e-based literature data[⋆,⋆⋆]

R. A. Marino[1], F. F. Rosales-Ortega[2,3], S. F. Sánchez[4,5], A. Gil de Paz[1], J. Vílchez[4], D. Miralles-Caballero[2], C. Kehrig[4], E. Pérez-Montero[4], V. Stanishev[9], J. Iglesias-Páramo[4,5], A. I. Díaz[2], A. Castillo-Morales[1], R. Kennicutt[6], A. R. López-Sánchez[7,8], L. Galbany[9], R. García-Benito[4], D. Mast[4,5], J. Mendez-Abreu[10,11], A. Monreal-Ibero[4], B. Husemann[12], C. J. Walcher[12], B. García-Lorenzo[10,11], J. Masegosa[4], A. del Olmo Orozco[4], A. M. Mourão[9], B. Ziegler[13], M. Mollá[14], P. Papaderos[15], P. Sánchez-Blázquez[2], R. M. González Delgado[4], J. Falcón-Barroso[11,10], M. M. Roth[12], G. van de Ven[16], and the CALIFA team[4]

[1] CEI Campus Moncloa, UCM-UPM, Departamento de Astrofísica y CC. de la Atmósfera, Facultad de CC. Físicas, Universidad Complutense de Madrid, Avda. Complutense s/n, 28040 Madrid, Spain
e-mail: `ramarino@ucm.es`
[2] Departamento de Física Teórica, Universidad Autónoma de Madrid, 28049 Madrid, Spain
[3] Instituto Nacional de Astrofísica, Óptica y Electrónica, Luis E. Erro 1, 72840 Tonantzintla, Puebla, Mexico
[4] Instituto de Astrofísica de Andalucía (CSIC), Camino Bajo de Huétor s/n, Aptdo. 3004, 18080 Granada, Spain
[5] Centro Astronómico Hispano-Alemán, Calar Alto, (CSIC-MPG), C/Jesús Durbán Remón 2-2, 04004 Almeria, Spain
[6] University of Cambridge, Institute of Astronomy, Madingley Road, Cambridge, CB3 0HA, UK
[7] Australian Astronomical Observatory, PO Box 915, NSW 1670 North Ryde, Australia
[8] Department of Physics and Astronomy, Macquarie University, NSW 2109, Australia
[9] CENTRA – Instituto Superior Tecnico, Av. Rovisco Pais 1, 10 49-001 Lisbon, Portugal
[10] Depto. Astrofísica, Universidad de La Laguna (ULL), 38206 La Laguna, Tenerife, Spain
[11] Instituto de Astrofísica de Canarias (IAC), 38205 La Laguna, Tenerife, Spain
[12] Leibniz-Institut für Astrophysik Potsdam (AIP), An der Sternwarte 16, 14482 Potsdam, Germany
[13] University of Vienna, Department of Astrophysics, Türkenschanzstrasse 17, 1180 Vienna, Austria
[14] CIEMAT, Departamento de Investigación Básica, Avda. Complutense 40, 28040 Madrid, Spain
[15] Centro de Astrofísica and Faculdade de Ciencias, Universidade do Porto, rua das Estrelas, 4150-762 Porto, Portugal
[16] Max Planck Institute for Astronomy, Königstuhl 17, 69117 Heidelberg, Germany

Received 24 May 2013 / Accepted 19 July 2013

ABSTRACT

The use of integral field spectroscopy is since recently allowing to measure the emission line fluxes of an increasingly large number of star-forming galaxies, both locally and at high redshift. Many studies have used these fluxes to derive the gas-phase metallicity of the galaxies by applying the so-called strong-line methods. However, the metallicity indicators that these datasets use were empirically calibrated using few direct abundance data points (T_e-based measurements). Furthermore, a precise determination of the prediction intervals of these indicators is commonly lacking in these calibrations. Such limitations might lead to systematic errors in determining the gas-phase metallicity, especially at high redshift, which might have a strong impact on our understanding of the chemical evolution of the Universe. The main goal of this study is to review the most widely used empirical oxygen calibrations, O3N2 and N2, by using new direct abundance measurements. We pay special attention to (1) the expected uncertainty of these calibrations as a function of the index value or abundance derived and (2) the presence of possible systematic offsets. This is possible thanks to the analysis of the most ambitious compilation of T_e-based H II regions to date. This new dataset compiles the T_e-based abundances of 603 H II regions extracted from the literature but also includes new measurements from the CALIFA survey. Besides providing new and improved empirical calibrations for the gas abundance, we also present a comparison between our revisited calibrations with a total of 3423 additional CALIFA H II complexes with abundances derived using the ONS calibration from the literature. The combined analysis of T_e-based and ONS abundances allows us to derive their most accurate calibration to date for both the O3N2 and N2 single-ratio indicators, in terms of all statistical significance, quality, and coverage of the parameters space. In particular, we infer that these indicators show shallower abundance dependencies and statistically significant offsets compared to others'. The O3N2 and N2 indicators can be empirically applied to derive oxygen abundances calibrations from either direct abundance determinations with random errors of 0.18 and 0.16, respectively, or from indirect ones (but based on a large amount of data), reaching an average precision of 0.08 and 0.09 dex (random) and 0.02 and 0.08 dex (systematic; compared to the direct estimations), respectively.

Key words. Galaxy: abundances – Galaxy: evolution – ISM: abundances – HII regions – techniques: spectroscopic

1. Introduction

Studying H II regions offers a powerful tool for understanding the physical properties and chemical evolution of the interstellar medium (ISM) in galaxies. They also represent perfect laboratories for deriving chemical abundances of gaseous nebulae and stars clusters across the surface of nearby galaxies

---

[⋆] The compiled catalog is only available at the CDS via anonymous ftp to `cdsarc.u-strasbg.fr` (`130.79.128.5`) or via
`http://cdsarc.u-strasbg.fr/viz-bin/qcat?J/A+A/559/A114`

[⋆⋆] Based on observations collected at the German-Spanish Astronomical Center, Calar Alto, jointly operated by the Max-Planck-Institut für Astronomie Heidelberg and the Instituto de Astrofísica de Andalucía (CSIC).

5

Outer−disk reddening and gas−phase metallicities: The CALIFA connection

Resumen

A pesar de su popularidad (ver Capítulo §1) el escenario *inside-out* no es capaz de explicar las propiedades en las partes más alejadas de los discos de las galaxias. De hecho, sabemos que la mayor parte de las galaxias muestran perfiles truncados (o anti-truncados) donde la pendiente del perfil aumenta o bien se reduce, respectivamente.

Se han propuesto muchos mecanismos para intentar explicar estos truncamientos, principalmente un cambio en el umbral de formación estelar (Schaye 2004), procesos de evolución secular asociados a la migración de estrellas hacia las partes externas de los discos (Debattista et al. 2006). En el caso de los discos anti-truncados las posibles explicaciones incluyen una formación estelar reciente asociada con la formación de discos XUV (Gil de Paz et al. 2005), fusiones menores (Peñarrubia et al. 2006) u otros tipos de interacciones con el entorno (Kazantzidis et al. 2007; Minchev et al. 2012).

El trabajo de Bakos et al. (2008) sobre una muestra de únicamente 39 galaxias indica la presencia de un enrojecimiento de las partes externas a partir de la posición del *break* de los perfiles de brillo superficiál, con un mínimo de color $(g'$- $r')$= 0.47±0.02 mag.

En Marino et al. (2015) se ha llevado a cabo, por primera vez, un estudio sobre una muestra completa y bien caracterizada de más de 300 galaxias de la muestra CALIFA. Los principales resultados de este trabajo indican:

(I) El porcentaje de galaxias con los diferentes tipos perfiles de brillo y sus colores mínimos coinciden con los derivados en trabajos previos (Erwin et al. 2005; Pohlen & Trujillo 2006; Bakos et al. 2008).
(II) La mayor parte de las galaxias de CALIFA de tipo TII y TIII muestran un aplanamiento e incluso una inversión en sus colores (ver Bakos et al. 2008).
(III) La distribución de diferencias entre el gradiente externo e interno de los discos de galaxias tipo TII no muestra ninguna correlación con el cambio en el gradiente de color, mientras que una correlación positiva se encuentra en el caso de las galaxias de tipo TIII. Este resultado está de acuerdo con el trabajo de Bresolin et al. (2012) para cuatro discos UV extensos, que muy probablemente evolucionarán en discos de tipo TIII, y que según el cual sería debido a una pre-enriquecimiento de las partes externas y del IGM por vientos galácticos tempranos.

5.1 Introduction

Most of the detailed structural studies of nearby disk galaxies carried out to date have been concentrated on the (most easily accessible) inner parts of galaxies (Pohlen & Trujillo 2006, PT06 hereafter). However, the faintest regions of galactic disks, that are intimately linked to the mechanisms involved in their growing and shaping, are still poorly understood. It is well know that for many H II regions in the outskirts of late-type spirals, and in some dwarf irregular galaxies, the process of metal enrichment by stellar nucleosynthesis is still in its early stages, thus providing a window on the early chemical evolution of galaxies. The study of the H II regions observed in the outskirts of disks are of crucial importance because we presume that they have experienced only a small degree of alteration in their abundances due to star formation activity. Therefore, their present-day metal content should be nearly the same as the primordial value, providing valuable tests for cosmological theories. In order to address this aspect, I will present in this Chapter the combined analysis of the metallicity gradients obtained from CALIFA (based on the tools and calibrations presented in Marino et al. 2012, 2013) with their SDSS surface brightness (SB) and color profiles. Our analysis of the CALIFA outskirts has already confirmed the presence of U-shaped color profiles in the outer parts of the vast majority of the disk galaxies analyzed and allows the exploration of the so-called fossil evidence imprinted in their metallicity gradients by the galaxy formation and growth processes.

Since the pioneering works on surface photometry of nearby galaxies by Patterson (1940), de Vaucouleurs (1959), or Freeman (1970), it became accepted that galaxy disks follow an exponential light profile according to the *inside-out* scenario of galaxy formation. This simple description, however, has now been shown to fail at fainter SB. In fact, since van der Kruit (1979) we know that this decline does not continue to the last measured point, but is truncated after several radial scalelengths. Consequently, we now know that not all the disk galaxies (indeed, only the minority for late-types) are well described with a single exponential fitting function as shown in several recent studies (Erwin et al. 2005, hereafter E05; PT06; Florido et al.2006, 2007; Erwin et al. 2008, hereafter E08), where they have identified three basic classes of surface brightness profiles depending on an apparent break feature or lack of one: (i) TYPE I (TI) profiles that do follow a single exponential law beyond the bulge area all along the optical extension of the galaxies, (ii) TYPE II (TII) profiles that present a double exponential law with a *down-bending* beyond the break radius, and (iii) TYPE III (TIII) profiles that exhibit an *up-bending* in the outer part. As shown in Figure 5.1, E05 and PT06 proposed a more detailed classification of the different SB types according to the presence of a bar or/and to the relative position of the break respect to the bar. Thus, the TII class could be divided in different subgroups: TII types for no barred galaxies and TII.XX for weakly or barred disks. In addition, depending on the position of the break, the TII.XX class could be subdivided in two subgroups: TII.i (inside) or TII.o (outside). The TII.o class comprises profiles where the break radius coincides with an outer ring or occurs at 2−3 times the bar radius, these galaxies are classified as TII.o-OLR. If the break occurs well outside the bar length we will classify these galaxies as “Classical Truncations” or TII.o-CT. The up-bending TIII breaks are also subdivided according to the possible nature of the outer zone: if a spheroid-like outer region is observed they are classified as TIII-s types otherwise they are TIII-d (for a detailed explanation see the classification schema presented in Fig.4 of PT06).

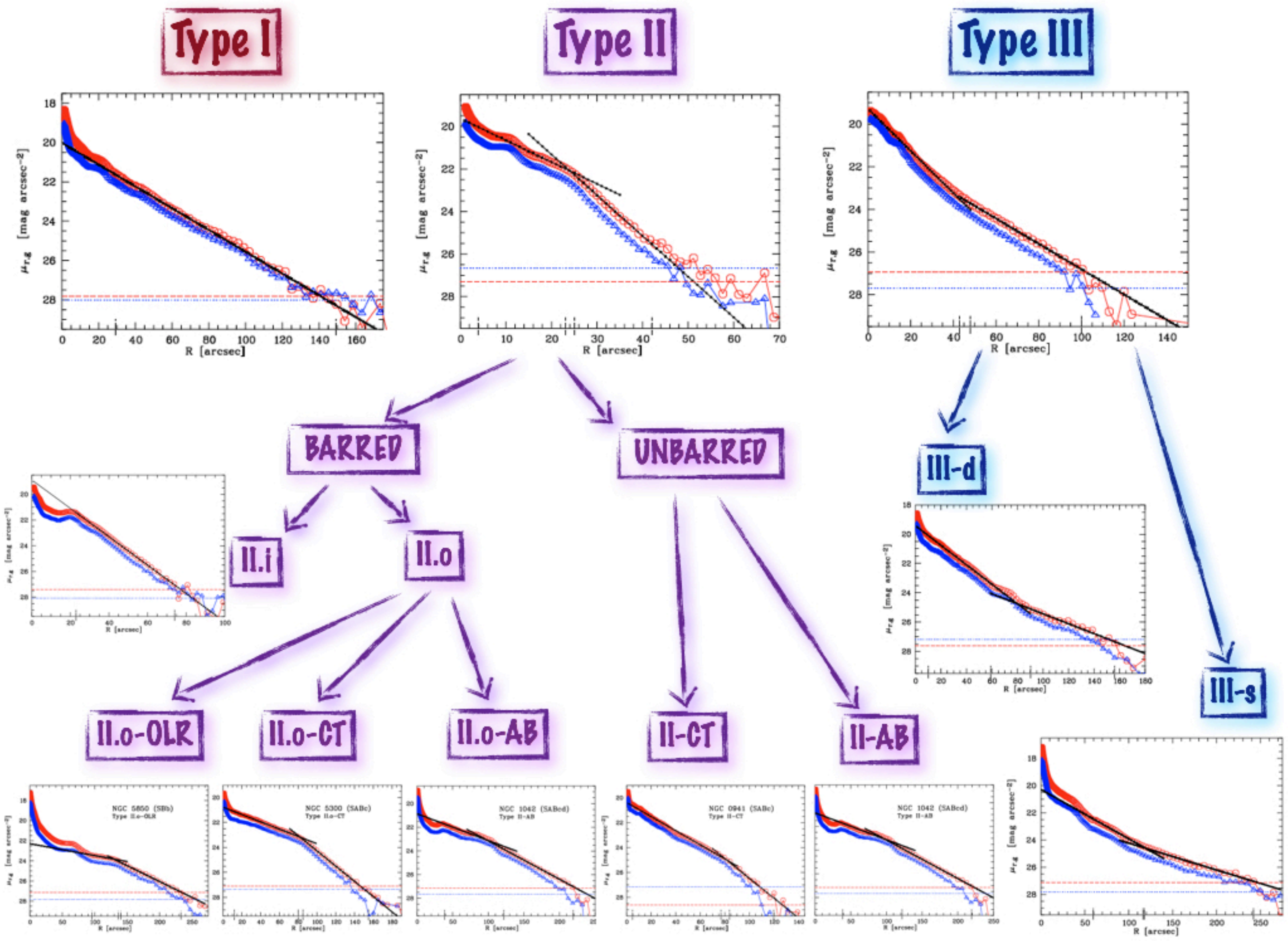

Figure 5.1: Classification schema (following Erwin et al. 2008): The three main disk types according to the characteristics of the break features found in their surface brightness profiles are TI (no break), TII (down-bending break), and TIII (up-bending break). Should the galaxy be barred the down-bending breaks (Type II) are subdivided according to the position of the break with respect to the bar: TII.i (inside) or TII.o (outside). An additional level of subclassification is applied for this class in order to connect the observed break to a physical mechanism. These are TII.o-AB, TII.o-OLR, and TII.o-CT (see text). For apparently unbarred galaxies, we use only TII-CT or TII-AB. The up-bending breaks (TIII) are subdivided according to the possible nature of the outer region: (d)isk or (s)pheroid.

Note that breaks and truncations are different phenomena as explained in Martín-Navarro et al. 2012 (MN12 hereafter). Breaks, first detected in face-on galaxies, could be caused by a threshold in the star formation in the galactic disk while truncations, commonly observed in edge-on galaxies, are more likely related with the maximum angular momentum of the proto-galactic cloud. In this study we will focus our attention on the breaks, meant as a significant variation in the slope of the galaxies' SB profiles.

Different mechanisms have been invoked to explain the origin of the breaks detected in the TII light profiles (see E08; PT06; MN12 and Marino et al.2015 for more details) including, among others, star formation threshold due to a critical gas density (Fall & Efstathiou 1980; Kennicutt 1989; Elmegreen & Parravano 1994; Schaye 2004); magnetic field (Battaner et al. 2002) or secular evolution processes as the distribution of the angular momentum through outward radial migration of stars, the presence of a bar or spiral structures (Debattista et al. 2006; Foyle et al. 2008; Roškar et al. 2008, R08 hereafter; Sánchez-Blázquez et al. 2009, SB09 hereafter; Martínez-Serrano et al. 2009). In the case of the TIII possible explanations for the breaks observed reside in the detection of an enhanced star formation in the extended UV disks (Gil de Paz et al. 2005; Thilker et al. 2005 and 2007; Zaritsky & Christlein 2007, Lemonias et al. 2011), minor mergers (Peñarrubia et al. 2006; Younger et al. 2007) or other types of interactions with the environment (e. g. dark matter subhalos (Kazantzidis et al. 2007) or smooth gas accretion (Minchev et al. 2012).

The recent findings of a reddening in the optical broad-band colors for 39 TII profiles (Bakos et al. 2008, B08 hereafter) as shown in Figure 5.2, has provided a fundamental piece of evidence to the *inside-out* scenario for the formation of galaxy disks and posed a challenge in many cases to these mechanisms. Using SDSS data, these authors have found a *U-shape* color profile for their TII galaxies with a minimum of *(g'- r')*= 0.47±0.02 mag at the break radius. They suggest that this result is related with a minimum in the luminosity-weighted age that results naturally from the theoretical predictions of the stellar migration scenario (R08; SB09; Sánchez-Blázquez et al. 2014). Despite the observational efforts based on several detailed structural studies of nearby disk galaxies (Muñoz-Mateos et al. 2013; Zheng et al. 2014, Pilyugin et al.2015, Ho et al.2015) the formation mechanisms responsible for the observed properties in the faintest part of the SB profile are still unknown as well as their connection to other physical properties as the breaks observed in the gas-abundance profiles. This diversity found in the properties of the disk light profiles is the result of different initial conditions and secular evolution processes that took place within a galaxy, therefore a detailed study of those regions beyond the break radius in different morphological types is mandatory.

In this context, in order to interpret the nature of SB breaks in nearby galaxies, we have investigated the relation between the outer-disk ionized-gas metallicity gradients and the presence of breaks in their surface brightness profiles and the changes in the color across these breaks. SDSS *g'*− and *r'*−band surface brightness, *(g'- r')* color, and CALIFA survey ionized-gas oxygen abundance profiles for 350 galaxies are used for this purpose. We perform a detailed light-profile classification of the CALIFA galaxies and from the analysis of the color gradients at both sides of this break we also found a *U-shape* profile for our TYPE II galaxies with a minimum (bluest) *(g'- r')* color of ∼0.5 mag that is in agreement with previous findings. Using the results from this analysis we compute, for

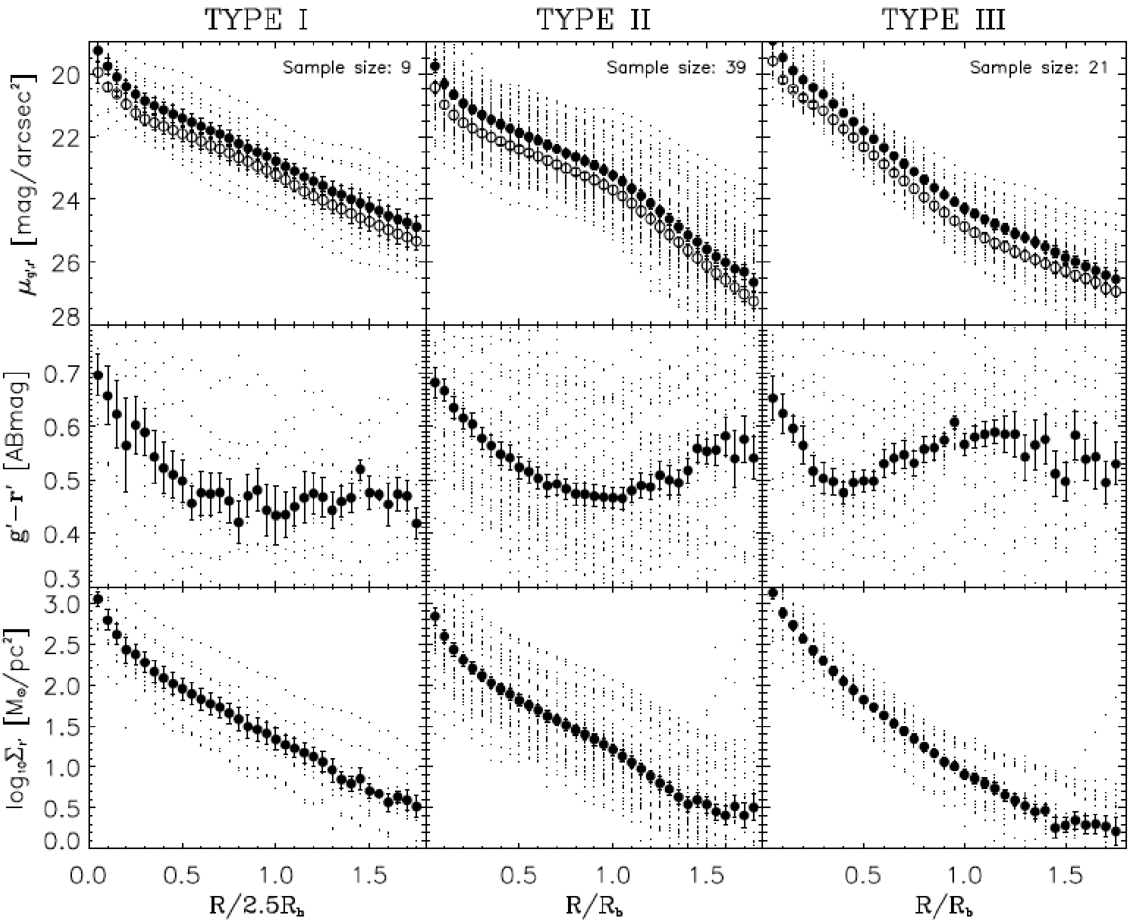

Figure 5.2: *Top row*: Averaged, scaled radial surface brightness profiles of 9 TI, 39 TII and 21 TIII galaxies. The filled circles correspond to the *r'*−band mean surface brightness, the open circles to the mean *g'*−band data. The small dots are the individual galaxy profiles in both bands. *Middle row*: *(g'- r')* color gradients. *Bottom row*: *r'*−band surface mass density profiles obtained using the color-to-M/L conversion of Bell et al. (2003).

the first time, in a statistically significant and well-defined sample, the behavior of the oxygen abundance in H II regions located at both sides of the break radius. The results presented in Marino et al. (2015) are a step forward in revealing which are the possible mechanism(s) that drive the formation and evolution of the galaxies' outskirts and, in particular, the reddening of the stellar colors found in these regions.

The main results from this paper are:

(I) The percentage of SB profiles and mean break colors found confirm those reported by previous works (Erwin et al. 2005; Pohlen & Trujillo 2006; Bakos et al. 2008), this time using the well-defined and large sample of nearby galaxies from the CALIFA IFS survey.
(II) Most of the CALIFA TII and TIII disk galaxies show a flattening and even a reverse in the color gradients (see also Bakos et al. 2008).

(III) The distribution of differences in the outer−inner (gas) metallicity gradient shows no correlation with the difference in color gradient in the case of the TII disks, while there is a positive correlation between them (i.e. a metallicity flattening) in the case of the TIII disks. This result agrees with the results of Bresolin et al. (2012) for the study of four extended-UV disks, systems that are likely to evolve into TIII disks with time. Such flattening in the oxygen abundance could be due to the presence of a polluted intergalactic medium (IGM) gas in the outskirts of these disks that was enriched by galactic winds and/or outflows during the early phase of galaxy evolution.

The complete atlas of the 324 CALIFA galaxies is presented in Appendix B along with the disk classification table and the derived properties at break radius from Marino et al. (2015).

5.2 Marino et al. (2015) submitted

Outer-disk reddening and gas-phase metallicities: The CALIFA connection

R. A. Marino[1], A. Gil de Paz[2], S. F. Sánchez[3], P. Sánchez-Blázquez[4], A. Castillo-Morales[2], N. Cardiel[2], S. Pascual[2], J. Vílchez[9], C. Kehrig[9], M. Mollá[5], J. Mendez-Abreu[6], C. Catalán-Torrecilla[2], E. Florido[7,8], I. Perez[7,8], T. Ruiz-Lara[7,8], S. Ellis[10], A. R. López-Sánchez[10,11], R. M. González-Delgado[9], A. de Lorenzo-Cáceres[6], R. García-Benito[9], L. Galbany[12,13], S. Zibetti[14], C. Cortijo[9], V. Kalinova[15], D. Mast[16], J. Iglesias-Páramo[9,17], P. Papaderos[18], C. J. Walcher[19], and the CALIFA Team[17,⋆]

[1] CEI Campus Moncloa, UCM-UPM, Departamento de Astrofísica y CC. de la Atmósfera, Facultad de CC. Físicas, Universidad Complutense de Madrid, Avda. Complutense s/n, 28040 Madrid, Spain, e-mail: `ramarino@ucm.es`
[2] Departamento de Astrofísica y CC. de la Atmósfera, Facultad de CC. Físicas, Universidad Complutense de Madrid, Avda. Complutense s/n, 28040 Madrid, Spain.
[3] Instituto de Astronomía, Universidad Nacional Autonóma de México, A.P. 70-264, 04510, México, D. F.
[4] Departamento de Física Teórica, Universidad Autónoma de Madrid, 28049 Madrid, Spain.
[5] CIEMAT, Departamento de Investigación Básica, Avda. Complutense 40, 28040 Madrid, Spain.
[6] School of Physics and Astronomy, University of St Andrews, North Haugh, St Andrews, KY16 9SS, U.K. (SUPA)
[7] Instituto Universitario Carlos I de Física Teórica y Computacional, Universidad de Granada, 18071 Granada, Spain
[8] Departamento de Física Teórica y del Cosmos, Facultad de Ciencias, Universidad de Granada, E-18071 Granada, Spain
[9] Instituto de Astrofísica de Andalucía (IAA/CSIC), Glorieta de la Astronomía s/n Aptdo. 3004, E-18080 Granada, Spain
[10] Australian Astronomical Observatory, PO Box 915, North Ryde, NSW 1670, Australia.
[11] Department of Physics and Astronomy, Macquarie University, NSW 2109, Australia.
[12] Millennium Institute of Astrophysics, Universidad de Chile, Santiago, Chile.
[13] Departamento de Astronomía, Universidad de Chile, Casilla 36-D, Santiago, Chile
[14] INAF-Osservatorio Astrofisico di Arcetri - Largo Enrico Fermi, 5 -I-50125 Firenze, Italy
[15] Department of Physics 4-181 CCIS, University of Alberta, Edmonton AB T6G 2E1, Canada
[16] Instituto de Cosmologia, Relatividade e Astrofísica, Centro Brasileiro de Pesquisas Físicas, CEP 22290-180, Rio de Janeiro, Brazil
[17] Centro Astronómico Hispano Alemán, Calar Alto, (CSIC-MPG), E-04004 Almeria, Spain
[18] Centro de Astrofísica and Faculdade de Ciencias, Universidade do Porto, Rua das Estrelas, 4150-762 Porto, Portugal.
[19] Leibniz-Institut für Astrophysik Potsdam (AIP), An der Sternwarte 16, D-14482 Potsdam, Germany

received; accepted

ABSTRACT

We investigate the relation between the outer-disk ionized-gas metallicity gradients and the presence of breaks in the surface brightness profiles of disk galaxies. SDSS *g'*- and *r'*-band surface brightness, *(g'- r')* color, and ionized-gas oxygen abundance profiles for 350 galaxies within the CALIFA survey are used for this purpose. We perform a detailed light-profile classification finding that 84% of our disks show *down*- or *up-bending* profiles (Type ii and Type iii, respectively) while the remaining 16% are well fitted by one single exponential (Type i). The analysis of the color gradients at both sides of this break shows a *U-shape* profile for the Type ii galaxies with a minimum *(g'- r')* color of ~0.5 mag, in agreement with previous findings. In this work we study, for the first time in a statistically significant and well-defined sample, the behavior of the oxygen abundance from H ii regions located within and beyond this break. This allows us to shed light on the possible mechanisms that drive the formation and evolution of the galaxy outskirts and, in particular, the reddening of their optical colors. In the case of the Type ii disks we find an ubiquitous outer-disk color reddening that has a metallicity flattening associated to it only for low-mass galaxies. Comparatively, more massive systems show a more monotonous metallicity gradient than less massive ones. The correlation between metallicity flattening and stellar mass yields *p*-values as low as 0.01. Thus, independently of the mechanism that shaped the outer profiles of these galaxies with stars, stellar migration or a previous episode of star formation in a shrinking star-forming disk, it is clear that the imprint in their ionized-gas metallicity was different for low- and high-mass Type ii galaxies. In the case of Type iii disks a positive correlation between the change in color and abundance gradient is found (the null hypothesis is ruled out with a *p*-value of 0.02), with the outer disks of Type iii galaxies with masses $\leq 10^{10}$ M$_{\odot}$ showing a weak color reddening or even a bluing. This is interpreted as a down-sizing effect on the population of Tiii galaxies capable of hosting enhanced inside-out growth, although the contribution from stellar migration to the shaping of the properties of massive Tiii galaxies cannot be quantified. Oxygen abundance measurements already provide important clues for futures studies of the chemical evolution of outer disks but deeper data from both the stellar and gas components should be definitively pursued.

Key words. Galaxies: abundances— Galaxies: evolution— Galaxies: photometry— ISM: abundances —(ISM): H ii regions — Techniques: spectroscopic

6

Future work: A multi−wavelength study of dust properties in spiral disks

Resumen

Los trabajos realizados hasta la fecha muestran la potencia de los datos IFU para el estudio de la formación y evolución de galaxias, confirmando además la importancia de las regiones H II en este tipo de análisis, especialmente cuando estos se combinan con datos de imágenes multi-frecuencia. En este capítulo presento las principales conclusiones (así como un sumario de las tareas pendientes) del estudio de mapas de espectroscopía 3D combinas con imágenes en el infrarrojo lejano de una muestra de galaxias extraídas del *Herschel Galaxy Reference Survey*.

El estudio de los efectos de emisión y absorción del polvo es fundamental para entender (I) los efectos del polvo sobre la luz ultravioleta y óptica emitida por las estrellas, (II) la distribución de las propiedades físicas del polvo (masa, temperatura, composición, tamaños de los granos) y (III) los posibles caminos de evolución (química) de las galaxias observadas que pudieran ser compatibles con dichas propiedades, especialmente con la masa del polvo y su composición química.

Con ese objetivo en mente se está llevando a cabo un estudio de una muestra de discos cercanos en espectroscopia 3D (mediante la IFU PPak en el telescopio de 3.5m de Calar Alto), lo que nos permitirá determinar la extinción del gas ionizado y su abundancia química en todo la superficie de estos objetos, y en imagen en el infrarrojo lejano (a partir de datos PACS y SPIRE del satélite Herschel de la ESA). Estos datos, combinados con las imágenes en el UV del satélite GALEX nos han permitido también deteminar la atenuación del continuo UV a partir de la medida del exceso infrarrojo. Por último, el análisis con el código CIGALE de los espectros ópticos obtenidos a partir de los cubos de la IFU PPak nos ha proporcionado una medida independiente de la atenuación del continuo estelar en longitudes de onda óptica. La combinación de todos estos datos es vital para desentrañar tanto los efectos del polvo sobre la luz estelar (curva de extinción), sus propiedades físico-químicas, así como la geometría relativa de estrellas, gas y polvo en el ISM de los discos de galaxias cercanas.

La relativamente pobre PSF de los datos infrarrojos obligó a elegir galaxias muy cercanas (todas ellas incluidas en el *Herschel Reference Galaxy Survey*) para las que fue necesario realizar mapas con la IFU PPak con multiples apuntados. Esto limitó el tamaño de la muestra de galaxias a analizar. Para compensar este hecho se analizaron objetos de disco que se localizaran en entornos distintos. De este modo se puede estudiar el efecto de dicho entorno sobre las propiedades y efectos del polvo.

En el trabajo que se presenta en este Capítulo (y pronto en Marino et al. 2015b) incluimos el análisis de las galaxia espiral aislada NGC 5668 y del par de galaxias en interacción NGC 3395 y NGC 3396. Los resultados preliminares de este trabajo indican la existencia de una diferencia entre la atenuación del gas ionizado y del continuo estelar en el UV similar a la derivada por Calzetti et al. (1994) para galaxias tipo *starburst*. Esa diferencia podría estar causada por variaciones en la composición química del polvo (y, por tanto, en su curva de extinción) respecto al polvo encontrado en nuestra Galaxia o a diferencias en la geometría de estrellas, gas y polvo. Así mismo, se encuentra una correlación entre la atenuación del gas ionizado y la abundancia de oxígeno que parece explicar que al menos parte de las diferencias entre las medidas de atenuación de estrellas y gas serían consecuencia de un cambio en la composición del polvo, aunque está aún por ver si esto es suficiente para explicar la diferencia observada.

The works done within this Thesis has shown the power and efficiency of using IFS data for the study of the formation and evolution of spiral galaxies. Once again this analysis has confirmed the importance of H II regions and their metallicities in shaping the present physical properties of disks. At the same time, this work has opened new windows of research that deserve further attention such as those based on the combined use of IFS and multi-wavelength imaging data. In this Chapter I will present an overview of the project started during my short stay at Laboratoire de Astrophysique de Marseille (LAM), France. The main goal of the collaboration with Dr. Alessandro Boselli and Dr. Mederic Boquien was to work on the comparative study of the bi-dimensional distribution of ionized-gas on one hand and the properties of the dust on the other using a sample of galaxies extracted from the Herschel Galaxy Reference Survey (HRS hereafter; Boselli et al. 2010) and that are been observed by our group at UCM using the PPak-IFU at the CAHA 3.5m telescope. The joint analysis of the stellar-continuum and ionized-gas attenuation allow us to investigate potential variations in the relative geometry of young stars, gas and dust or in the extinction curve within different environments. This work runs in parallel with other scientific objectives of my Ph.D. Thesis and will be soon submitted to the Astronomy & Astrophysics journal.

Combing PPAk Integral Field Spectroscopy and PACS-SPIRE Herschel data: a multi-wavelength study of dust properties in spiral disks. The cases of NGC 5668, NGC 3395 and NGC 3396.

R. A. Marino[1], A. Boselli[2], M. Boquien[2], A. Gil de Paz[1], S.F. Sánchez[3].

Departamento de Astrofísica y CC. de la Atmósfera, Facultad de CC. Físicas, Universidad Complutense de Madrid, Spain

Laboratoire dÁstrophysique de Marseille, OAMP, Université Aix-Marseille & CNRS, France

Instituto de Astronomía, Universidad Nacional Autonóma de México, México

6.1 Abstract

The analysis of the effects of dust emission and absorption on the Spectral Energy Distributions (SEDs) of galaxies provides fundamental clues to better understand the distribution and physical properties (e.g. temperature, composition, mass) of interstellar dust in galaxies and of the stellar populations whose light attenuates. Besides, the relation of these properties with the chemical composition of the ionized gas also reflects the chemical evolution of the ISM. The main strength of the work we presented here is the availability of both optical *3D* spectroscopy data obtained with the CAHA 3.5m telescope PMAS/PPak IFU data and FIR imaging data from the PACS/Herschel instrument for a subset of galaxies from the Herschel Reference Survey. We have focused our study on NGC 5668, an isolated spiral galaxy, and on the close galaxy pair NGC 3395/NGC 3396. These data allow us to also determine the attenuation (and oxygen abundance) of the ionized gas from the PPak data-cubes and compare it with that of the stellar continuum from the combined analysis of PACS/Herschel FIR and GALEX UV data. In particular, the availability of the (IRX-based) stellar-continuum and ionized-gas attenuation allow us to investigate potential variations in the relative geometry of young stars and dust and/or in the extinction curve. In this work we first focus on the study of the dependence of

the stellar-continuum to ionized-gas attenuation ratio with the amount of attenuation [as measured by A(Hα) and with the ionized-gas metallicity. We also analyze its dependence with the dust surface density and temperature and with the (population synthesis based) stellar mass density and continuum attenuation as given by the CIGALE code. Finally, we will also analyze the dependence of the dust-to-gas ratio with the metal abundance and the SFR.

6.2 Introduction

As claimed in Chapter §3 (and in Marino et al. 2012), the ISM is mixture of gas and dust particles whose properties are sensitive to several evolutionary processes that take place within a galaxy. Thus, the multi-wavelength analysis of the different components of the ISM might be key for understanding the star formation history and the chemical evolution both in locally and in high-redshift Universe. It is well known that, depending on the pressure and temperature conditions, the different phases of the ISM are identified: cold, warm and hot medium. In this Thesis we have analyzed in detail the ionized gas component (T$\sim 10^4$) within spiral galaxies and here we will add another piece to the puzzle by studying the properties of the dust.

There is a significant fraction of metals trapped into the dust grains that is injected in the ISM via winds and ejecta from massive stars, as for example, the supernova explosions (Clayton et al. 1997; Bianchi & Schneider 2007; Matsuura et al. 2011; Gomez et al. 2012) or the asymptotic giant branch winds (Gehrz 1989; Dwek 1998; Galliano et al. 2008). Several mechanisms in the literature has been proposed to explain the origin of the dust, such as those suggested by Sauvage & Thuan (1994) and Kewley et al. (2002). In particular, the large-scale diffuse dust emission could arise from cirrus (Helou 1986) heated by (a) energetic radiation escaping from individual star-forming regions (Sauvage et al. 1990; Xu 1990; Popescu et al. 2000, 2002, 2005; Misiriotis et al. 2001; Tabatabaei et al. 2007) and/or (b) the general radiation field of evolved stars (Helou 1986; Xu & Helou 1996; Li & Draine 2002; Boselli et al. 2004; Komugi et al. 2011). Also, hot grains in the photosphere or circumstellar atmosphere of mass-losing stars could contribute to the dust emission (Jura et al. 1987; Knapp et al. 1992; Mazzei & de Zotti 1994, for instance). Finally the presence of an embedded active galactic nuclei (AGN) could certainly affect the emission of the surrounding dust (de Grijp et al. 1985; Wu et al. 2007).

It is worth emphasizing that the presence of dust in a galaxy represents a strong barrier for a reliable measurement of several observables within a galaxy, such as the emission and absorption fluxes, colors, and the overall SEDs. Indeed, the effect of dust on the integrated light observed in a galaxy is two fold: from one side the dust effectively dims the light emitted by young massive stars (UV emission) and/or old stars (Optical-NIR emission) and, on the other hand, the light absorbed at short wavelengths by the dust grains is re-emitted to the longer ones (infrared and sub-millimeter domains). Due to their role as catalysts, the dust grains are good tracers of the different ISM phases because they drive the physical processes that transform the atomic hydrogen into the molecular one. They also contribute to the chemical enrichment of the ISM where new generation of stars will be born, shields the UV radiation field, therefore preventing the dissociation of molecular clouds, and to the cooling and heating of the ISM in photodissociation regions mainly through photoelectric effect in the latter case (Wolfire et al. 1995).

The study of the physical properties, the spatial distribution and effects of dust in a galaxy is based on the use of three indicators:

(i) the total infrared (TIR) to far-ultraviolet luminosity ratio method (LTIR/LFUV, i.e., Buat 1992; Xu & Buat 1995; Meurer et al. 1995, 1999), which is based on the assumption that a fraction of photons emitted by stars and gas are absorbed by the dust. This method is considered the most reliable estimator of the dust attenuation in star-forming galaxies because it is almost completely independent of the different dust extinction physical parameters (i.e., dust/star geometry, extinction law; see Buat & Xu 1996; Meurer et al. 1999; Gordon et al. 2000; Witt & Gordon 2000).

(ii) the ultraviolet spectral slope (determined from a power-law fit of the form $f_\lambda \sim \lambda^\beta$ to the UV continuum spectrum in the range between 1300 and 2600 (Calzetti et al. 1994).

(iii) the Balmer decrement, which gives an estimate of the attenuation of ionized gas, and not of the stellar continuum as in the previous two methods. It is based on the comparison of the observed Hα/Hβ ratio with its theoretically predicted value (2.86 for case B recombination, assuming an electronic density of 100 cm^{-3} and a temperature of 10^4 K, see e.g. Osterbrock 1989).

Since the pioneer work of Sauvage & Thuan (1994), including the most recent one by Boquien et al. (2013, 2014), Boselli et al. (2013, 2014), Cortese et al. (2012, 2014), claim substantial differences between the integrated high-redshift dust emission and its behavior at smaller physical scales locally but the physical parameters that drive those differences are still unclear. Despite major efforts, both observationally and theoretically, made in dissecting the interplay between dust and radiation in galaxies, dust introduces a considerable uncertainty in the measurements of the global properties of galaxies at different redshifts. A spatially-resolved multi-frequency analysis is mandatory to solve some of the open questions that we still have on dust, such as, for instance, whether the dust properties in starburst galaxies are also those of normal star-forming ones in the Local Universe. The notorious Calzetti attenuation law (Calzetti et al. 1994), widely used for the correction of dust effects, establishes an empirical relation between the ultraviolet spectral slope and the Balmer decrement Hα/Hβ, that is, a priori, valid only for starburst galaxies and not for normal star-forming systems. The key questions that drive this analysis are therefore: can we really get reliable attenuations using A(Hα) for the gas and A(FUV-TIR) for the dust/stellar content? If so, what are the values derived when analyzing integrated galaxies? Are they representative of the different substructures within a galaxy? In order to answer these questions we are studying, for the first time, with good spatial and spectral

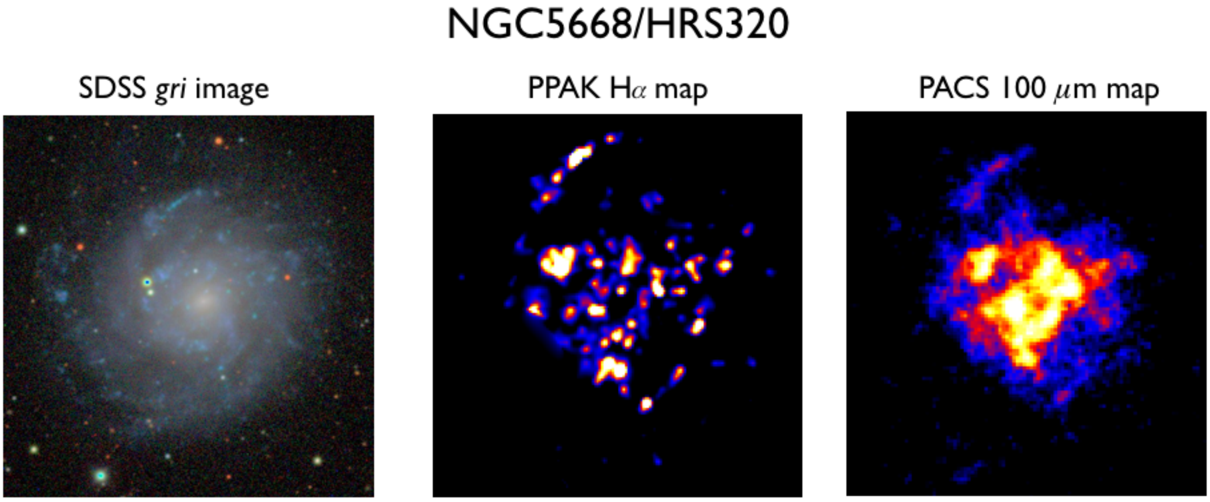

Figure 6.1: Left: SDSS optical *gri* image (from 4458 to 7706) of NGC 5668. Plate scale is 0.396 arcsec/pix. **Center:** Hα map obtained from the PPAK data cube. Plate scale is 1 arcsec/pix. **Right:** Herschel-PACS 100μm map. Plate scale is 3.2 arcsec/pix. North is up and East is to the left in all cases.

resolution, the attenuation values derived with these two different techniques. This analysis will allow us to understand which are the properties of the dust (content, extinction law, relative geometry compared to stars and gas) and provide further constrains on the present star formation and the star formation history of spiral galaxies.

6.3 Data and preliminary results

The main goal of this study is to combine the analysis of optical PPak spectroscopy data with the infrared imaging data from the PACS and SPIRE instruments, onboard the ESA/Herschel observatory, to determine some empirical relations for the dust and the gas at small scales. In this regard, we have focused our study on a subset of galaxies from the HRS: NGC 5668 an isolated spiral galaxy also described in Chapter §3; NGC 3395 and NGC 3396, a pair of spiral interacting galaxies for which we have data from the UV to submillimeter wavelengths. An example of how NGC 5668 looks at different wavelengths is given in Figure 6.1 where the composite SDSS, Hα and PACS 100μm images are shown. The main properties of the three galaxies analyzed are given in Table 7.1. They share the following properties (1) are spiral galaxies with no strong AGN; (2) are close enough to perform a pixel-by-pixel analysis even at the coarse spatial resolution defined by our longest wavelength (20" for PACS 160μm) so we can separate the different morphological components and (3) have maps available in all bands required for our analysis, namely FUV, NUV, Optical PPAk spectroscopy at least in the Hα, Hβ, [O III] λ 5007, [N II] λ 6584 regions, PACS 100μm and PACS 160μm. One of the most critical aspects of this analysis is the data processing. The combination of data from such a wide range of wavelengths and different facilities requires a detailed processing. Here we have followed a procedure similar to that described in Boquien et al. (2011). Briefly, the main steps of the procedure followed are: first we remove all background and contaminating sources and the Milky Way foreground attenuation correction was applied. Then, we process all images to a common point

Table 6.1: Sample global properties.

Galaxy		RA	Dec	D_L	Morphology	$\log(D_{25})$	Inclination	M_B
NGC#	HRS #	(J2000)^a	(J2000)^a	^{a}	Mpc^a	$'^b$	$^{\circ b}$	mag^b
3395	20	10h 49m 50.1s	+32° 58′ 58″	26.3	SAB(rs)cd pec: H II	· · ·	57.8	-20.24
3396	20	10h 49m 55.1s	+32° 59′ 27″	26.3	IBm pec: H II	1.49 ± 0.05	90.0	-20.46
5668	320	14h 33m 24.3s	+04° 27′ 02″	24.8	Sa(s)d	1.28 ± 0.04	33.0	-20.01

For each galaxy are listed in order the right ascension and declination coordinates for the 2000 equinox; the luminosity distance in unit of Mpc, the morphological type, the $\log(D_{25})$, the inclination and the B magnitudes.

^{a} Source: NASA/IPAC Extragalactic Database, `http://nedwww.ipac.caltech.edu/`

^{b} Source: HyperLEDA, `http://leda.univ-lyon1.fr`

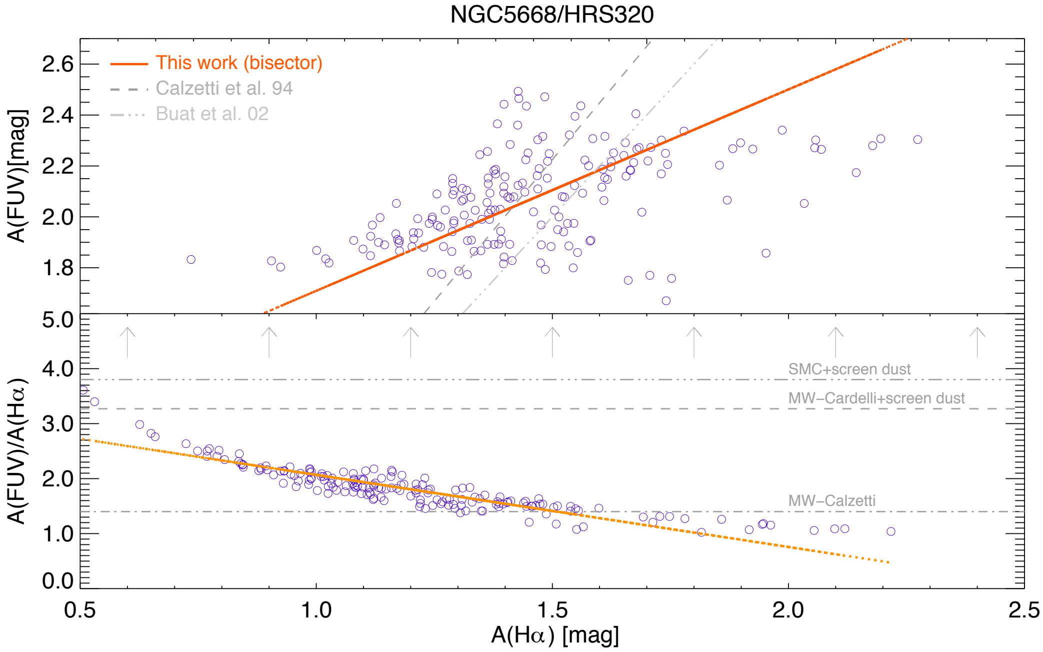

Figure 6.2: Behavior of the attenuation derived from the TIR and FUV bands (upper panel y axis) versus the gas attenuation (x-axis) obtained via the Balmer decrement for the galaxy NGC 5668. In the upper panel we also plot the Calzetti et al. (1994) law with a grey dashed line and the Buat et al. (2002) law with the grey 3dot-dashed line. Our bisector fit is drawn in orange. In the lower panel the y axis represents the A(FUV)/A(Hα) ratio. The grey horizontal lines represent the values for the A(FUV)-to-A(Hα) ratio in the case of three different extinction laws and dust geometries, namely MW-Cardelli+screen dust, MW-Calzetti and SMC+screen dust.

spread function (PSF) using the large set of convolution kernels presented in Aniano et al. (2011). Finally, all the sky-subtracted images are projected on the same grid to compute a direct pixel-by-pixel comparison as well to carry out a SED fitting with the code CIGALE[1] (Code Investigating GALaxy Emission, Noll et al. 2009).

In order to analyze the dependence of the dust content as a function of the diagnostic band used,

---

[1] `http://cigale.lam.fr/`

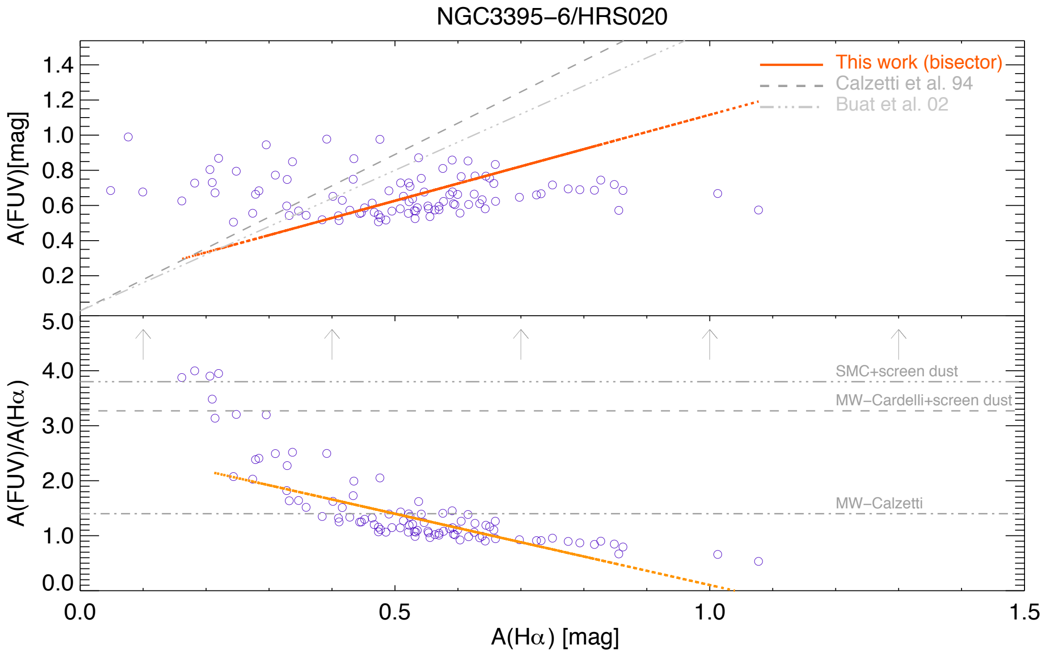

Figure 6.3: Behavior of the attenuation derived from the TIR and FUV bands (upper panel y axis) versus the gas attenuation (x axis) obtained via the Balmer decrement for galaxies NGC 3395 and NGC 3396. Symbols and lines are the same as in Fig 6.2.

we determine, on one hand, the attenuation of the gas from the PPak spectroscopic optical datacubes. In particular, we first compute the Balmer decrement attenuation *c*(Hβ) from the Hα and Hβ images and then we obtain the attenuation for the gas phase, A(Hα), as plotted in the x axis of Figure 6.2 and 6.3. On the other hand, using the Herschel PACS bands combined with the GALEX FUV image, we obtain the stellar attenuation, A(FUV-TIR), through the recipes explained in Boquien et . (2012) plotted in the y axis. The differences found between the attenuation of the ionized-gas and stellar continuum in the UV can be due to variations in the chemical composition of the dust and, therefore, in its extinction curve, or to changes in the relative geometry of stars, gas and dust as a function of star formation activity (or gas density) that could be also vary from galaxy to galaxy (Calzetti et al. 2001). Our analysis reveals that those changes are indeed present within our galaxies and when these galaxies are compared to each other, in the sense that regions with lower attenuations tend to show lower A(FUV)-to-A(Hα) ratios (similar to that produced by MW dust in screen geometry or dust in a more metal poor environment such as the Small Magellanic Cloud). Another preliminary result is that the correlation between A(Hα) and oxygen abundance suggests that part of that behavior might be due to a change in the composition of the dust although whether this is enough to explain the different attenuations of stars and gas remains to be analyzed.

We are currently analyzing the dependence of these local variations on the amount of dust attenuations of gas and stars with the dust surface density and temperature and with the (population synthesis based) stellar mass density and continuum attenuation given by the CIGALE code, the spectral energy distributions (SED) fitting algorithm written by Burgarella et al. (2005). CIGALE handles both the emission of the stars in the UV-optical domain, and the absorption and reemission of this radiation by the dust at longer wavelengths through an energy balance requirement. We are also testing the outputs of the tool CIGALE for this pixel-by-pixel analysis that has now being applied to our normal star-forming galaxies. The results summarized here will be soon submitted to the Astronomy & Astrophysical journal as Marino et al. (2015b).

Thanks to the increasing number of photometric data spanning the whole electromagnetic spectrum and to the high resolution spectroscopic observations available from the several ongoing IFS surveys, we anticipate a huge effort by the community to go deeper into the relation between the dust and the gas in galaxies in order to understand the interplay between stars, gas and dust in normal, MW-like galaxies and the connection between the properties of dust and the spectra-photometric and chemical evolution of galaxies.

7

Conclusiones

En esta tesis se ha llevado a cabo un análisis detallado y completo de la distribución espacial y composición química del gas ionizado en una amplia muestra de galaxias cercanas, utilizando datos de espectroscopía de campo integral (IFS, del inglés *Integral Field Spectroscopy*. El principal objetivo de este trabajo es mejorar nuestra comprensión sobre como evolucionan las galaxias, en particular, las galaxias espirales que, como la nuestra, representan sistemas intrínsecamente complejos aun en constante evolución en sus propiedades espectro-fotométricas. Hemos abordado este problema cuantificando las propiedades físicas de las regiones H II dentro de los discos galácticos en dos dimensiones con especial atención a la variación radial de su contenido en metales. El análisis detallado de la muestra de galaxias analizada en esta Tesis ha permitido inferir pistas importantes sobre los procesos que gobiernan la formación y la evolución de las galaxias espirales, así como para poner a prueba las predicciones teóricas del escenario *inside-out* de formación de los discos llegando a investigar las partes más exteriores de las galaxias espirales, donde las desviaciones de este escenario se esperan tengan efectos observacionales más notorios.

Con el fin de entender el cuadro completo de este escenario de formación *inside-out* para los discos de galaxias espirales, en primer lugar hemos llevado a cabo un estudio detallado de las propiedades fotométricas y químicas de la galaxia espiral cercana NGC 5668. Este análisis, que se ha discutido en detalle en el Capítulo §3 y que fue publicado en Marino et al. (2012), ha sido posible gracias al uso de datos IFS en el rango óptico combinados con imágenes de banda ancha multi-frecuencia de toda la galaxia, desde el UV hasta el infrarrojo. Las principales conclusiones de ese trabajo son las siguientes:

1. Se han obtenido los perfiles radiales de la atenuación del polvo utilizando diferentes métodos. La atenuación promedia del continuo es $A_V \sim 0.4$ mag. Hemos encontrado que la atenuación del gas ionizado es significativamente mayor de la del continuo. Ese resultado concuerda con las predicciones de Calzetti et al. (2001) sobre la mezcla de estrellas, polvo y gas.
2. Hemos medido los flujos de las líneas de emisión, corregidos por la atenuación del polvo, para un total de 62 regiones H II y 18 anillos concéntricos centrados en el núcleo de NGC 5668. Utilizando el método de líneas intensas propuesto por Kewley & Dopita (2002) para el cálculo de la abundancia de oxígeno en el gas ionizado, hemos medido metalicidades para el total de los 80 espectros extraídos. Encontramos una distribución bimodal en el gradiente de metalicidad,

con una pendiente negativa y más pronunciada (con una pendiente de -0.14±0.09 dex/kpc) hasta un radio de 36″ que empieza a aplanarse (o incluso a invertirse) más allá de ese punto (0.002 ± 0.002 dex/kpc).

3. También se han obtenido los perfiles de brillo superficial y de color desde UV hasta el infrarrojo cercano. Estos perfiles coinciden con las predicciones de los modelos espectrofotométricos y químicos para la evolución de los discos galácticos (Boissier & Prantzos 2000) para valores de la velocidad circular de $v_{\rm circ} = 167\,km\,s^{-1}$ y un parámetro de spin (momento angular específico del disco) de λ=0.053. Los parámetros de nuestro mejor ajuste también están de acuerdo con la forma del gradiente de metalicidad y con los valores de la curva de rotación aunque los modelos no pueden reproducir ni el cambio de pendiente de metalicidad ni el moderado azulamiento observado en algunos de los perfiles de color ($u - g$, $g - r$) para el mismo radio de break de la metalicidad. Esta discrepancia entre observaciones y modelos resaltan la limitación que comporta el escenario *inside-out* en el cual se basan los modelos de Boissier & Prantzos.

4. Entre los diferentes mecanismos, ajenos al escenario *inside-out*, propuestos en la literatura para explicar el cambio en la pendiente detectado en los perfiles de metalicidad y color de los discos espirales, sólo la presencia de un barra en su etapa de formación concilia bien todas las otras propiedades observacionales de NGC 5668: la posición, el cambio en las longitudes escala de disco en la metalicidad, los colores más azules en esa posición, el gran contenido de HI y de formación estelar, junto con la presencia de nubes de altas velocidad (HVC) y de los residuos de las velocidades de estas regiones respecto al campo de velocidad de la galaxia e incluso la detección de un exceso de luz con forma de óvalo en la región central de la galaxia.

El análisis presentado anteriormente de NGC 5668 responde en parte a la primera pregunta formulada en el Capítulo §1: ¿HAY UN GRADIENTE UNIVERSAL PARA TODAS LAS GALAXIAS DE DISCO? ¿ESTÁN CRECIENDO ESTAS *inside-out* TAL COMO NOS INDICAN LOS GRADIENTES DE COLOR Y METALICIDAD DE NUESTRA PROPIA VÍA LÁCTEA? Concluyendo, nuestros resultados indican que mientras que las propiedades observacionales generales de NGC 5668 son coherentes dentro de la predicciones del escenario *inside-out* de la formación de discos, hay observables (abundancias químicas y colores) y, especialmente, su variación con la distancia galactocentrica que nos indican la relevancia de otros fenómenos. En el caso de NGC 5668 sería la presencia de una barra en formación donde la formación estelar in-situ es significativa (o lo ha sido recientemente). Creemos que la formación de la barra sea debida a las inestabilidades del disco interior de NGC 5668, rico en gas, posiblemente causado por la interacción con una galaxia compañera. En otras palabras, el diablo (de la evolución de discos) está en los detalles[1].

Sin embargo, NGC 5668 es un único objeto y determinar si estas desviaciones del escenario *inside-out* son comunes o no requiere extender este análisis a una muestra más grande. Conscientes de esto y de las limitaciones que existían previas a esta Tesis para el estudio de las abundancias del gas ionizado en galaxias, nos propusimos el objetivo de entender las diferentes técnicas de diagnóstico utilizadas dentro de la comunidad científica para calcular la metalicidad del gas. El objetivo último

---

[1] N.T.: Traducción libre de la frase inglesa “the devil is in the details”.

de este trabajo siempre fue el de entender mejor la variedad de regiones H II dentro una amplia muestra de galaxias como las de la exploración CALIFA a fin de obtener unas medidas de abundancia metálica lo más precisa en cada caso. Así, en Marino et al. (2013) (véase el Capítulo §4) se presenta una revisión de los calibradores empíricos de abundancias más usados, O3N2 y N2, mediante la comparación de estos con medidas directas. Este trabajo representa la compilación más completa hasta la fecha de regiones H II con medidas de temperatura electronica, T_e. Se calcularon además abundancias de óxigeno utilizando múltiples líneas intensas (usando el método ONS de Pilyugin et al. 2010) para todas las regiones H II identificadas en las galaxias de disco de la muestra CALIFA. Gracias al uso de un conjunto sin precedentes de regiones H II (∼4.000) se pudo derivar la calibración de metalicidad más precisa y rigurosa hasta la fecha para los indicadores O3N2 y N2, en términos de su significancia estadística, calidad y cobertura del espacio de parámetros. Las conclusiones más relevantes de este análisis son las siguientes:

1. Hemos proporcionado a la comunidad científica las calibraciones empíricas para la abundancia de oxígeno en regiones H II más precisas hasta la fecha para los indicadores O3N2 y N2 obtenidos a través de método T_e (y conocidas también como las calibraciones M13-O3N2 y M13-N2). En particular, los ajustes lineales que hemos hecho a los valores de abundancia de oxígeno en función de los parámetros O3N2 y N2 nos proporcionan las siguiente relaciones lineales con un error aleatorio asociado de 0,18 dex y 0,16 dex, respectivamente.

$$12 + \log(\mathrm{O/H}), [\mathrm{M13 - O3N2 - Te}] = 8.533[\pm 0.012] - 0.214[\pm 0.012] \times \mathrm{O3N2}, \tag{7.1}$$

$$12 + \log(\mathrm{O/H}), [\mathrm{M13 - N2 - Te}] = 8.743[\pm 0.027] + 0.462[\pm 0.024] \times \mathrm{N2}. \tag{7.2}$$

   La buena estadística de nuestra muestra de regiones H II nos ha permitido ofrecer, por primera vez, intervalos de predicción en función del valor del indicador de líneas brillantes correspondiente.

2. Además de proporcionar nuevos y mejores calibraciones empíricas para el cálculo de la abundancia de metales en el gas ionizado, también se ha presentado una comparación entre nuestras calibraciones revisitadas con un total de 3423 complejos H II adicionales dentro de CALIFA para las cuales hemos derivado la abundancia usando la calibración ONS de la literatura. El análisis de este completo y homogéneo conjunto de regiones H II ha llevado a las siguientes relaciones:

$$12 + \log(\mathrm{O/H}), [\mathrm{M13 - O3N2 - ONS}] = 8.505[\pm 0.001] - 0.221[\pm 0.004 \times \mathrm{O3N2}, \tag{7.3}$$

$$12 + \log(\mathrm{O/H}), [\mathrm{M13 - N2 - ONS}] = 8.667[\pm 0.006] + [0.455 \pm 0.011] \times \mathrm{N2}. \tag{7.4}$$

3. Las diferencias encontradas entre estas calibraciones y las obtenidas por Pettini & Pagel 2004 (PP04), Nagao et al. 2006 (NAG06), y Pérez-Montero & Contini 2009 (PMC09) recomiendan la revisión de aquellos resultados obtenidos usando estas últimas calibraciones. Las diferencias encontradas son especialmente notables en el régimen de alta metalicidad (12 + log (O/H) $>$ 8,2). En el caso del primer trabajo citado esto es debido principalmente a la falta de observaciones de regiones H II con líneas aurorales en el regimen de alta metallicidad en la época de la publicación de la calibración PP04. Por otro lado, las grandes diferencias encontradas a alta metalicidad entre nuestra calibración y la de NAG06 se producen porque NAG06 en este rango de metalicidad utiliza una muestra de galaxias que no tiene abundancias medidas a partire de la T_e.
4. Nuestra nueva calibración también comporta implicaciones importantes para los estudios que investigan la evolución de la metalicidad de gas en galaxias hasta altos corrimientos al rojo. Por ejemplo, la relación masa-metalicidad (MZR), que se utiliza a menudo como referencia, se basó en la calibración N2 de PP04 resultando ahora obsoleta.

De esa manera, la segunda cuestión planteada en el Capítulo §1, ¿SON LAS DIFERENTES CALIBRACIONES EMPÍRICAS VÁLIDAS PARA UN AMPLIO RANGO (BAJO Y ALTO DESPLAZAMIENTO AL ROJO) DE REGIONES H II EXTRAGALÁCTICA O ESTAS DEPENDEN DEL MÉTODO DE DIAGNÓSTICO UTILIZADO?, tiene ahora una respuesta positiva. De hecho, nuestros resultados proporcionan ahora la derivación más precisa de la abundancia de oxígeno a partir de los indicadores O3N2 y N2 anclándolos al método T_e (o método *directo*) en todo el rango de metalicidades accesible. El método *indirecto* ONS para las abundancias de oxígeno (que está también anclado en último término al directo) pone de manifiesto que el resultado obtenido con CALIFA es particularmente útil para mappear un abanico más amplio de condiciones físicas respecto a la muestra T_e que, aunque determina las abundancias de manera más precisa, carece de una tan buena estadistica como la que proporciona la muestra de CALIFA. Podemos concluir que nuestros resultados están mejorando nuestra comprensión de la evolución química del Universo, aun cuando las mediciones de un solo parámetro de abundancia esté disponible y siempre que los intervalos de predicción derivados se tengan en cuenta en el computo de dicha abundancia metálica.

Finalmente, y una vez que hemos desarrollado las herramientas necesarias (tanto en términos del análisis de los datos de IFS como para la derivación de las abundancias de metales), hemos regresado al tema del crecimiento *inside-out* de las galaxias, objetivo científico último de este trabajo, para ahora extender dichas herramientas y metodología (desarrolladas en Marino et al. 2012, 2013) a una muestra mayor de discos espirales del Universo Local. Con ese objetivo, tal como se ha mostrado en el Capítulo §5, se ha estudiado por primera vez una muestra estadísticamente significativa y bien definida de galaxias desde el punto de vista de la derivación de las abundancias de oxígeno del gas ionizado. Así, se compararon los perfiles radiales de abundancia química de 350 galaxias CALIFA con sus perfiles de brillo superficial en las bandas g' y r' de SDSS, así como también sus perfiles de color $(g' - r')$ con el fin de interpretar la naturaleza y los mecanismos responsables de la evolución de las partes más externas de los discos dentro de los escenarios propuestos en la literatura. Los principales resultados derivados en ese trabajo (algunos de ellos ya encontrados por otros autores, otros no) son:

1. El porcentaje de galaxias con los diferentes tipos perfiles de brillo y sus colores mínimos coinciden con los derivados en trabajos previos (Erwin et al. 2005; Pohlen & Trujillo 2006; Bakos et al. 2008).

2. La mayor parte de las galaxias de CALIFA de tipo TII y TIII muestran un aplanamiento e incluso una inversión en sus colores (ver Bakos et al. 2008).

3. La distribución de diferencias entre el gradiente externo e interno de los discos de galaxias tipo TII no muestra ninguna correlación con el cambio en el gradiente de color, mientras que una correlación positiva se encuentra en el caso de las galaxias de tipo TIII. La variación del gradiente de metalicidad a ambos lados del radio de break en las galaxias TII varía con la masa estelar (valores $p{\sim}0.01$), de manera que para masas menores encontramos un aplanamiento en el gradiente de metalicidad más significativo respecto a las de mayor masa. Este resultado está de acuerdo con el trabajo de Bresolin et al. (2012) para cuatro discos UV extensos, que muy probablemente evolucione en discos de tipo TIII, y que según el cual sería debido a una per-enriquecimiento de las partes externas y del IGM por vientos galácticos tempranos.

4. Para masas menores de $\sim 10^{10}\,\mathrm{M}_{\odot}$, las galaxias TII y TIII se comportan de diferente manera en términos de enrojecimiento del color, en particular las galaxias TIII muestran poco enrojecimiento o incluso un azulamiento en sus perfiles de colores.

En particular, una pregunta surge naturalmente de nuestros resultados, ¿ES POSIBLE CONCILIAR LAS CARACTERÍSTICAS DE LA LUZ Y PERFILES QUÍMICOS DENTRO DE UN ESCENARIO AUTO CONSISTENTE? Varios estudios recientes confirman la presencia de cambios de pendiente (*breaks*) en sus perfiles de brillo superficial, pero todavía no está claro si existe una conexión entre estos y las propiedades de la abundancia de oxígeno de las regiones más allá de ese radio de *break*. Nuestros resultados muestran que las metalicidades de CALIFA por sí solas no son suficientes para explicar el claro cambio de color asociado a los cambios de pendiente en los perfiles. Serían necesarios datos más profundos (y en mayor número aún) de IFS para la determinación de los cambios de abundancia tanto estelar como del gas (ver el trabajo realizado en Sánchez et al. 2015 mediante el uso de datos de la IFU MUSE en el telescopio VLT; ver también Bresolin et al. 2012) hasta estas regiones tan externas será fundamental para mejorar nuestro conocimiento sobre la evolución de los bordes exteriores de los discos espirales. Por otro lado, una vez más, este tipo de estudios nos permitirán ahondar algo más sobre el posible mecanismo(s) que impulsan la formación y evolución de las partes externas de estas galaxias para ser capaz, entre otras cosas, de explicar el enrojecimiento de los colores de las poblaciones estelares en estas regiones.

Por último, pero no menos importante, además de los resultados puramente científicos de esta Tesis, también he detallado mi contribución personal a las fases técnicas de los procedimientos de reducción de datos y de control de calidad de los mayores proyectos IFU hasta a la fecha en los cuales estoy profundamente involucrada y que también han permitido una exploración científica de los datos de CALIFA en esta Tesis: PPak-CALIFA (*Calar Alto Legacy Integral Field Area Survey*) y MEGARA (*Multi-Espectrógrafo en GTC de Alta Resolución para Astronomía*).

Consideraciones finales

Los resultados de esta Tesis constituyen una contribución significativa a la corriente vision teórica detrás de la distribución de metales dentro de los discos espirales. No sólo hemos probado cuantitativamente muchas predicciones clave del escenario *inside-out* sino también hemos obtenido nuevas calibraciones empíricas para las abundancias de oxígeno que son hoy en día ampliamente aceptadas y utilizadas por la comunidad científica.

Hemos demostrado que la espectroscopía *3D* es el camino a seguir para el estudio de los objetos nebulosos extensos y que puede proporcionar nuevas importantes respuestas sobre muchos temas relacionados con el crecimiento y la evolución de las galaxias en el Universo. En esta Tesis, gracias a la uso de los datos CALIFA, hemos confirmado y extendido el cuerpo de resultados obtenidos anteriormente a partir de espectroscopía de rendija larga e imágenes basadas en muestras pequeñas gracias al uso de datos IFS para el estudio de los gradientes de abundancia en galaxias, abriendo una nueva frontera para el estudio de las propiedades físicas y químicas de los discos de galaxias espirales cercanas.

La principal motivación común a todos los resultados discutidos en esta Tesis es el deseo de obtener una vision detallada de la composición química de las galaxias de disco y entender su evolución (dentro y fuera del, hasta cierto punto ingenuo, paradigma *inside-out*) por medio de la caracterización de las propiedades espacialmente resueltas de las regiones H II en el Universo Local. Además se podrá utilizar esta información para encontrar una conexión con estudios similares a un mayor corrimiento al rojo y con ello comprender los procesos físicos que intervienen en la formación y evolución de las galaxias en su conjunto.

A pesar de la relevancia de todos estos resultados, aún queda mucho trabajo por hacer en la determinación de los detalles exactos que impulsan la evolución de los discos. Otros proyectos centrados en la evolución de galaxias en el Universo Local, utilizando la potencia de los datos IFS, han cogido el testigo de CALIFA. Estos incluyen la exploración *Sydney university AAO MOS* (SAMI), el proyecto *Mapping Nearby Galaxies at APO* (MaNGA; IP: Kevin Bundy), o el muestreo *MUSE Atlas of Disks* (MAD) con el instrumento MUSE (Bacon et al. 2004). Para mayores desplazamientos al rojo ya existen planes bien definidos para el uso del Telescopio Espacial James Webb (JWST), el Telescopio Gigante Magallanes (GMT), o el *European Extremely Large Telescope* (E-ELT). Todos estos proyectos revolucionaran la comprensión de las galaxias espirales ayudando a comprender mejor como estas han evolucionado con el tiempo.

7

Conclusions

In this thesis we have carried out a detailed and comprehensive analysis of the spatial distribution and chemical composition of the gas component in a large sample of nearby galaxies using integral field spectroscopy data. The main motivation of such work is to enhance our understanding of galaxy evolution, in particular, for spiral galaxies, that are intrinsically complex systems as they are still actively evolving in all their spectro-photometric. We have approached this problem by means of quantifying the bi-dimensional physical properties of H II regions across the galactic disks with special attention to the distribution of the metal content within disks. The analysis of the galaxy samples performed in this thesis has allowed us to infer important clues on the process driving the spiral galaxy assembly and evolution as well to test the theoretical prediction of the *inside-out* scenario of disk formation and dig into the outskirts of spirals to shed more light on the role of these poorly understood outer regions of disks.

In order to disentangle the whole picture of the *inside-out* formation of galaxy disks, we first have carried out an extensive and detailed study of the chemical and photometric properties of the nearby spiral galaxy NGC 5668. This detailed study, described in Chapter §3 and published in Marino et al. (2012), has been possible thanks to the combined use of IFS data in the optical and panchromatic broad-band imaging of the entire system. The main conclusions from that work are the following:

1. Dust-attenuation profiles have been obtained using a number of methods. The mean continuum attenuation is $A_V \sim 0.4$ mag. We find significantly larger ionized-gas attenuations than that of the continuum. This is in agreement with the predictions for the mixing of stars, dust and gas given by Calzetti et al. (2001).
2. We have derived dust-attenuation-corrected emission-line fluxes for a total of 62 individual H II complexes and 18 concentric annuli centered on the position of the nucleus of NGC 5668. Using the strong-line method of Kewley & Dopita (2002) oxygen-abundance measurements have been obtained for all these 80 extracted spectra. We find a bimodal radial distribution in metallicity with a steep negative gradient with slope -0.14±0.09(dex/kpc) within a galactocentric distance of $36''$and a shallower (or even positive) metallicity gradient beyond that point, 0.002±0.002 (dex/kpc).
3. Surface brightness and color profiles from the UV to the near-infrared have been also obtained. These profiles nicely match the predictions of the chemo-spectrophotometrical models for the evolution of galaxy disks (Boissier & Prantzos 2000) for a circular velocity of

$v_{\rm circ} = 167\, km\, s^{-1}$ and a spin parameter (specific angular momentum of the disk) of λ=0.053. This best-fitting model also agrees with the overall shape of the galaxy metallicity gradient and rotation curve although it cannot reproduce the steep-shallow metallicity break neither the moderate bluing in some of the color profiles ($u - g$, $g - r$) around the position of the metallicity break. This discrepancy highlight the limitation of the *inside-out* scenario on which the Boissier & Prantzos (2000) models are based.

4. Out of the different *beyond inside-out* mechanisms proposed in the literature to explain the change in the slope of the metallicity and color profiles in spiral disks, only the presence of a bar in its formative stages agrees well with the other observational properties of NGC 5668: the position of the metallicity break in disk-scale lengths, the bluing in the colors at that position, the large HI content and star formation rate of the galaxy, along with the presence of High Velocity Clouds and High-Residual-Velocity-Regions in the galaxy velocity field and even the detection of an oval excess of light in the central region of the galaxy.

The analysis presented above on NGC 5668 partly answers the first question addressed in Chapter §1: IS THERE AN UNIVERSAL GRADIENT FOR ALL DISK GALAXIES? ARE THEY GROWING *inside-out* AS PROPOSED TO EXPLAIN THE COLOR AND METALLICITY GRADIENTS IN OUR OWN MILKY WAY? All in all, our results indicate that while the overall observational properties of NGC 5668 are well fitted by the *inside-out* scenario of disk formation, there are observables (chemical abundances and colors) and, especially, radial intervals among them that need to be interpreted in the context of the presence of a nascent bar where significant in-situ star formation is (or have been recently) taking place. The formation of the bar is believed to be due to instabilities in the gas-rich inner disk of NGC 5668 possibly helped by the interaction with a companion. In other words, the devil is in the details.

However, NGC 5668 is a single object and determining if these deviations from the *inside-out* scenario are common or not requires of extending this analysis to a larger sample of objects. With this in mind, we then shifted our main subject of interest to the different gas metallicity diagnostic techniques used within the scientific community to better understand the variety of H II regions in a large sample of galaxies as the ones within the CALIFA Survey. In Marino et al . (2013) (see Chapter §4) the determination of the chemical abundances in galaxies is reviewed in detail. This work represents the most comprehensive compilation of both T_e-based and multiple strong-line (ONS-based) ionized-gas abundance measurements in external galaxies to date. I make use of an unprecedented set (∼4000) of H II regions and allow deriving the most accurate calibration of both the O3N2 and N2 single-ratio indicators, in terms of all statistical significance, quality, and coverage of the parameters space. The most relevant conclusions reached in that analysis are the following:

1. We provide revisited empirical calibrations for the oxygen abundances in H II regions based on the O3N2 and N2 indicators obtained via T_e-based method (known also as M13-O3N2 and M13-N2 calibrations). We find that the following linear relations provide a good fits to the oxygen abundance as a function of the O3N2 and N2 parameters with rms values of 0.18 dex

and 0.16 dex, respectively.

$$12 + \log(\mathrm{O/H}), [\mathrm{M13-O3N2-Te}] = 8.533[\pm 0.012] - 0.214[\pm 0.012] \times \mathrm{O3N2}, \tag{7.1}$$

$$12 + \log(\mathrm{O/H}), [\mathrm{M13-N2-Te}] = 8.743[\pm 0.027] + 0.462[\pm 0.024] \times \mathrm{N2}. \tag{7.2}$$

The large number of calibrating H II regions in this case allowed us to provide, for the first time, prediction intervals as a function of the value of the corresponding strong-line ratio.

2. Besides providing new and improved empirical calibrations for the gas abundance, we also present a comparison between our revisited calibrations with a total of 3423 additional CALIFA H II complexes with abundances derived using the ONS calibration from the literature. The analysis of these large and homogeneous set of H II regions yield to the following relations:

$$12 + \log(\mathrm{O/H}), [\mathrm{M13-O3N2-ONS}] = 8.505[\pm 0.001] - 0.221[\pm 0.004 \times \mathrm{O3N2}, \tag{7.3}$$

$$12 + \log(\mathrm{O/H}), [\mathrm{M13-N2-ONS}] = 8.667[\pm 0.006] + [0.455 \pm 0.011] \times \mathrm{N2}. \tag{7.4}$$

3. The differences found between our calibrations and those obtained by Pettini & Pagel 2004 (PP04), Nagao et al. 2006 (NAG06), and Pérez-Montero & Contini (2009) recommend revising the results obtained using these latter calibrations. These differences are particularly noticeable in the high-metallicity regime (12+log(O/H) $>$ 8.2), on one hand mainly due to the lack of high-quality observations of H II regions with auroral lines at the high-metallicity end at the time of the publication of the PP04 calibration. Hence they by themselves justify the need for updating their calibrations. On the other hand, the large differences found at high metallicity between our calibration and the one of NAG06 occur because NAG06 in this metallicity range uses a sample of galaxies that has no simply T_e-based abundances measured.

4. Our new calibration also has important implications for studies that investigate the gas metallicity evolution of galaxies up to high redshifts. For example, the mass-metallicity relation (MZR), which is often used as a reference sample, was based on the N2 calibration of PP04.

Thus, the second question raised in Chapter §1, namely Are the different empirical calibrations valid for a wide range (low and high redshift) of extragalactic H II regions or are they dependent on the diagnostic method used? has a positive answer. We demonstrate that the T_e-based (*direct*) method represent the most accurate derivation of the oxygen abundance from the single-ratio indicators O3N2 and N2 anchored. The *indirect* ONS derivations of the oxygen abundances (that are also T_e-anchored) of the CALIFA sample result particularly useful to map a larger Universe of physical conditions with respect to our T_e sample and to determine in a precise way the uncertainty associated to this method as a function of the strong-line ratio used. We conclude that our results will improve our understanding of the chemical evolution of the Universe, even when only single-parameter abundance measurements are available and as long as the predicting intervals derived are taken into account.

Finally, and once we have the necessary tools in hand (both in terms of the analysis of the IFS data and on the derivation of reliable metal abundances), we returned to the topic of galactic *inside-out* growth extending the tools and methodology developed in Marino et al. (2012) and (2013), to a larger sample of nearby spiral disks. To that aim, as explained in Chapter §5, in addition to the ionized-gas oxygen abundances we study the stellar light profiles of 350 CALIFA galaxies using the SDSS *g'*- and *r'*-bands together with the *(g'- r')* color profiles for the first time in a statistically-significant and well-defined galaxy sample. In order to interpret the nature of surface brightness (SB) profile breaks in nearby galaxies we investigate what are the mechanism(s) responsible for such breaks. These should also be able to explain the diversity of morphologies, colors and metallicity gradients found in these, otherwise poorly understood outskirts of disk galaxies. Moreover, any theoretical interpretation should also explain the main results derived from that work (some of them already found by other authors), namely:

1. The percentage of SB profiles and mean break colors found confirm those reported by previous works (Erwin et al. 2005; Pohlen & Trujillo 2006; Bakos et al. 2008), this time using the well-defined and large sample of nearby galaxies from the CALIFA IFS survey.

2. Most of the CALIFA TII and TIII disk galaxies show a flattening and even a reverse in the color gradients (see also B08).

3. The distribution of differences in the outer−inner (gas) metallicity gradient shows no correlation with the difference in color gradient in the case of the TII disks, while there is a positive correlation between them (i.e. a metallicity flattening) in the case of the TIII disks.

4. The change in the ionized-gas metallicity gradient at both sides of the SB breaks in TII disk galaxies varies with the galaxy stellar mass (p-value$\sim$0.01) in the sense that the low-mass galaxies show a more significant metallicity flattening than more massive systems.

5. At stellar masses below $\sim 10^{10}\,M_{\odot}$, TII and TIII galaxies behave differently in terms of outer-disk reddening, with the latter showing little reddening or even bluing in their color profiles.

In particular, a question naturally arises from our results, IS IT POSSIBLE TO CONCILIATE THE LIGHT AND CHEMICAL PROFILES FEATURES WITHIN A SELF-CONSISTENT SCENARIO? Several recent studies confirms the presence of breaks in their surface brightness profiles but is still unclear if a connection exists between these and the oxygen properties of the regions beyond that break radius. Our results show that the CALIFA metallicities alone are not enough to tackle these aspects, further deeper IFU data both for the stellar and the gas components as (see the work done in Sánchez et al. 2015 using MUSE data) will improve our knowledgment on the evolution of the outer edges of spiral disks. On the other hand, they again allow us to shed some light on the possible mechanism(s) that drive the formation and evolution of the galaxies' outskirts and, in particular, the reddening of the stellar colors found in these regions.

Last but not least, besides the purely scientific outcome of this thesis, I have also discussed my personal contribution to those technical phases of the data reduction and quality-control procedures of the largest IFU projects up-to-date in which I am deeply involved, that has also allowed for a timely scientific exploration of the CALIFA survey data included in this Thesis: PPak-CALIFA (*Calar Alto Legacy Integral Field Area Survey*) and MEGARA (*Multi-Espectrógrafo en GTC de Alta Resolución para Astronomía*).

Concluding remarks

The results of this Thesis constitute a significant contribution to the current theoretical picture behind the distribution of metals within spiral disks. Not only we have quantitatively tested many key predictions of the *inside-out* scenario, but have also obtained new empirical metallicity calibrations that are nowadays widely accepted and used by the scientific community.

We have demonstrated that *3D* spectroscopy is the way to go for the study of extended nebular objects and it provides new insights into many topics regarding the growth and evolution of galaxies in the Universe. In this dissertation, thanks to the use of the CALIFA data in testing, confirming, and extending the previous body of results from small-sample studies based on imaging and long-slit spectroscopy, along with our IFS approach in studying abundance gradients we open up a new frontier for the physical and chemical properties of disks in nearby spiral galaxies.

The primary motivation common to all the results discussed in this thesis is the desire of get insight into the chemical composition of disk galaxies as a probe of the evolution of these systems (within and beyond the somewhat naive *inside-out* paradigm) by means of characterizing the spatially resolved properties of the H II regions in the local Universe. Additionally one could use this information to find a link with similar studies at higher redshift and thereby understand the physical processes at play in the formation and evolution of galaxies as a whole.

Despite the power and importance of all these results, much work remains to be done on determining the exact details that drive the evolution of disks. Other surveys, using the power of IFS data, include new generation surveys in the local Universe, such as the Sydney university AAO MOS IFU (SAMI), Mapping Nearby Galaxies at APO, (MaNGA, PI: Kevin Bundy), or the MAD (Muse Atlas of Disks) survey with the Multi Unit Spectroscopic Explorer (MUSE, Bacon et al. 2004) at VLT and at high redshift using the James Webb Space Telescope (JWST), the Giant Magellan Telescope (GMT), or the European Extremely Large Telescope (E-ELT). Projects all that will revolutionize the understanding of spiral galaxies like our own have evolved with time.

A

Appendix A: H II regions catalog

In this Appendix we provide the most ambitious compilation of T$_e$-based H II regions to date. The emission lines present here were used to obtain the new empirical metallicity calibration for the O3N2 and N2 indicators, as exhaustively discussed in Chapter §4. In Marino et al. (2013), we performed a comprehensive search in the literature for H II regions within spiral and irregular galaxies in order to compile our T$_e$-based sample. We looked for those targets in previous works that included measurements in bright emission lines (typically [O III]λ5007 and [N II]λ6584) and at least one of the auroral emission lines [O III] λ4363, [N II] λ5755, and [S III] λ6312, in order to recalculate all the temperatures and the indices in an homogeneous way. The compilation consists of a set of 603 calibrating H II regions from 17 different works in the literature whose references are given in this table. In our compilation we removed H II regions that were found to be duplicated among different works but that actually came from the same original observational dataset. Is worth to emphasize that here we also present for the first time measurements for the CALIFA H II regions with [O III] λ4363 detections. For each T$_e$-H II region (*ID*) in the first column, the bibliographic references to the original works for the compiled T$_e$-sample (*Source*) are given in the second column. The meaning of the reference short names is the following:

CAL for the CALIFA T$_e$-based H II regions, **BER12** for Berg et al. (2012) data, **BRE12** for Bresolin et al. (2012) data, **CrB09** for Crowther & Bibby (2009) data, **Cro09** for Croxall et al. (2009) data, **Est13** for Esteban et al. (2013) data, **Gbe10** for García-Benito et al. (2010) data, **Gus12** for Guseva et al. (2012) data, **Had07** for Hadfield & Crowther (2007) data, **Keh11** for Kehrig et al. (2011) data, **Mon12** for Monreal-Ibero et al. (2012a) data, **PMC09r** for Pérez−Montero & Contini (2009) data, **P12** for Pilyugin et al. (2012) data, **San12** for Sanders et al. (2012) data, **Sta13** for Stasińska et al. (2013) data, **Wes13** for Westmoquette et al. (2013) data, **ZaB11** for Zahid & Bresolin (2011) data and **ZB12** for Zurita & Bresolin (2012) data.

From the third to the 13rd column in the table the dereddened emission line ratios relative to Hβ fluxes of the T$_e$ sample are listed. Fluxes are measured in units of $10^{-16}\,\mathrm{erg\,cm^{-2}\,s^{-1}}$ and are sorted by wavelength. The observed lines are dereddened with a Cardelli et al. (1989) extinction law. The dust extinction A$_V$ is calculated from the Balmer decrement (Hα/Hβ=2.86) adopting the same extinction law (A$_V$/A$_{H_\beta}$ =1.164). Regarding the errors associated with the individual emission line fluxes the reader is referred to the original works.

Then follows two indexes *iDoub* and *iTemp* that indicates what doublets ([OII], [SII]) were resolved in the original source and which line was used to calculate the electron temperature. The meaning of the *iDoub* index is: **0**=[OII], [SII] are resolved; **1**= only [SII] is resolved and we assume

[OII]3729/[OII]3726=1.5; **2**= none is resolved, we assume [OII]3729/[OII]3726=1.5 and [SII]6717/[SII]6731=1.5. The index *iTemp* is **1** when the electron temperature is derived from the auroral and nebular lines of [O III], is **2** for the lines of [N II], and **3** for [S III]. The last two columns represent the T_e electron temperature (in units of 10^4 K) and the derived oxygen abundance. These results are obtained using the equations proposed in Sec.2.2 of Pilyugin et al. (2010) and of Pilyugin et al. (2012).

ID	Source	[O II] λ 3726	[O II] λ 3729	[O III] λ 4363	[O III] λ 4959	[O III] λ 5007	[N II] λ 5755	[N II] λ 6548	[N II] λ 6584	[S III] λ 6312	[S II] λ 6717	[S II] λ 6731	iDoub	iTemp	T_3 10^4 K	12+log(O/H) dex
M51CCM10	P12	0.50357	0.75536	···	0.04027	0.12080	0.00500	0.37234	1.11702	0.00300	0.27615	0.18410	2	2	0.55000	8.56100
M51CCM53	P12	0.51649	0.77473	···	0.11065	0.33194	0.00540	0.39897	1.19691	0.00310	0.24612	0.16408	2	3	0.55600	8.66100
M51CCM54	P12	0.46032	0.69048	···	0.13802	0.41406	0.00650	0.40545	1.21636	0.00440	0.37770	0.25180	2	2	0.60000	8.53000
M51CCM55	P12	0.31193	0.46790	···	0.06323	0.18970	0.00430	0.38899	1.16697	0.00310	0.24612	0.16408	2	2	0.50000	8.63400
M51CCM72	P12	0.25180	0.37770	···	0.02193	0.06578	0.00280	0.33261	0.99784	0.00160	0.27615	0.18410	2	2	0.43800	8.66900
M51CCM84A	P12	0.50010	0.75016	···	0.28245	0.84735	0.00920	0.47856	1.43569	···	0.20378	0.13585	2	2	0.65700	8.52800
NGC1232no0	P12	0.82806	1.24208	···	1.33334	4.00001	···	0.07310	0.21931	0.01470	0.13809	0.09206	2	3	1.08100	8.23000
NGC1232no0	P12	0.84345	1.26518	···	0.16632	0.49895	0.00660	0.29919	0.89756	···	0.44994	0.29996	2	2	0.70500	8.46700
NGC1232no0	P12	0.65172	0.97758	···	0.07310	0.21931	0.00390	0.39897	1.19691	0.00360	0.37166	0.24778	2	3	0.60200	8.55300
NGC1232no1	P12	1.21916	1.82874	···	0.26604	0.79811	0.00840	0.30899	0.92696	0.00800	0.46790	0.31193	2	3	0.80100	8.44300
NGC1365no0	P12	0.67618	1.01426	···	0.08316	0.24949	0.00450	0.33569	1.00707	0.00320	0.39642	0.26428	2	3	0.58900	8.61300
NGC1365no1	P12	0.83572	1.25358	···	0.12970	0.38910	···	0.30265	0.90795	0.00380	0.36572	0.24381	2	3	0.64600	8.57700
NGC1365no1	P12	0.88320	1.32480	···	0.24600	0.73801	0.00920	0.42554	1.27662	0.01000	0.33585	0.22390	2	2	0.69800	8.54600
NGC1365no1	P12	0.97512	1.46269	···	0.30899	0.92696	···	0.22281	0.66844	0.00780	0.25772	0.17181	2	3	0.79200	8.40900
NGC2997no0	P12	0.85913	1.28870	···	0.26912	0.80735	0.00580	0.27922	0.83765	0.00960	0.21585	0.14390	2	3	0.71100	8.52100
NGC2997no0	P12	0.81107	1.21661	···	0.14620	0.43859	0.00640	0.32280	0.96841	0.00610	0.33585	0.22390	2	2	0.66800	8.52600
NGC5236no0	P12	0.83188	1.24782	···	0.39259	1.17777	0.00740	0.32579	0.97738	0.00720	0.25772	0.17181	2	2	0.71600	8.56500
NGC5236no1	P12	0.17181	0.25772	···	0.02992	0.08976	0.00400	0.53820	1.61459	0.00230	0.35412	0.23608	2	2	0.41300	8.75700
NGC5236no1	P12	0.57552	0.86328	···	0.07655	0.22965	0.00600	0.44868	1.34605	0.00350	0.30630	0.20420	2	2	0.54800	8.67000
M101H1013	P12	0.88320	1.32480	0.00240	0.33880	1.01639	0.00590	0.23602	0.70805	0.00770	0.17871	0.11914	2	2	0.75200	8.47500
M83no29	P12	1.01639	1.52458	0.00700	0.63818	1.91453	···	0.19631	0.58893	···	0.17995	0.11997	2	1	0.84900	8.43700
NGC300no2	P12	0.66383	0.99575	0.05590	1.67471	5.02413	0.00180	0.02558	0.07675	0.01850	0.10451	0.06967	2	3	1.21100	8.12500
NGC300no4	P12	1.14304	1.71455	0.02140	0.84128	2.52384	···	0.06775	0.20326	0.01730	0.19914	0.13276	2	1	1.08700	8.16800
NGC300no6	P12	1.09916	1.64874	0.01600	0.81835	2.45505	···	0.09035	0.27106	0.01380	0.23182	0.15455	2	3	1.00900	8.25400
NGC300no8	P12	1.22761	1.84141	0.00770	0.47856	1.43569	0.00500	0.11349	0.34046	0.01320	0.26494	0.17663	2	1	0.94300	8.28200
NGC300no9	P12	0.68875	1.03312	0.00890	0.78152	2.34456	···	0.10813	0.32439	0.01090	0.19868	0.13245	2	1	0.85800	8.39100
NGC300no10	P12	0.71955	1.07932	0.00910	0.78513	2.35538	0.00230	0.06382	0.19145	0.01110	0.09776	0.06517	2	1	0.86200	8.39200
NGC300no11	P12	1.03290	1.54936	0.01110	0.66825	2.00475	···	0.09749	0.29246	0.01340	0.25070	0.16713	2	1	0.95200	8.28100
NGC300no12	P12	1.04727	1.57091	···	0.09976	0.29927	0.00370	0.17986	0.53959	0.00730	0.43466	0.28977	2	3	0.72200	8.46500
NGC300no13	P12	0.98415	1.47622	···	0.39531	1.18594	0.00630	0.13364	0.40092	0.01040	0.22498	0.14999	2	3	0.85900	8.32500
NGC300no14	P12	0.99097	1.48645	0.00750	0.60248	1.80743	0.00400	0.13675	0.41026	0.01400	0.24955	0.16636	2	1	0.87800	8.36800
NGC300no15	P12	0.73971	1.10956	···	0.30615	0.91846	0.00570	0.19317	0.57951	0.01100	0.28784	0.19189	2	3	0.77500	8.36200
NGC300no16	P12	1.05696	1.58545	···	0.31618	0.94855	0.00690	0.17986	0.53959	0.00990	0.31780	0.21187	2	3	0.78900	8.44000
NGC300no17	P12	0.85126	1.27688	0.00590	0.63818	1.91453	0.00340	0.09182	0.27546	0.01320	0.16374	0.10916	2	3	0.85300	8.39000
NGC300no18	P12	1.03529	1.55293	···	0.39259	1.17777	0.00410	0.15558	0.46673	0.01260	0.34289	0.22859	2	3	0.85600	8.34400
NGC300no19	P12	0.76747	1.15120	0.00610	0.54820	1.64460	0.00250	0.07744	0.23231	0.00950	0.18372	0.12248	2	2	0.86200	8.31800
NGC300no20	P12	0.58353	0.87529	0.00710	0.75499	2.26496	0.00280	0.07942	0.23827	0.01150	0.11999	0.07999	2	1	0.81700	8.43300
NGC300no21	P12	0.86708	1.30062	···	0.34272	1.02816	0.00630	0.24151	0.72454	0.01090	0.33278	0.22185	2	2	0.76900	8.43600
NGC300no22	P12	1.07910	1.61864	···	0.25582	0.76747	0.00470	0.20462	0.61385	0.00820	0.42969	0.28646	2	3	0.75400	8.49000
NGC300no23	P12	0.70479	1.05719	0.00570	0.65908	1.97725	0.00280	0.09246	0.27737	0.00990	0.16794	0.11196	2	2	0.83300	8.39600
NGC300no24	P12	0.78715	1.18073	0.00620	0.59833	1.79499	0.00370	0.10763	0.32289	···	0.18161	0.12108	2	1	0.83700	8.38900
NGC300no25	P12	1.14831	1.72247	···	0.44253	1.32758	0.00600	0.14620	0.43859	0.01070	0.26987	0.17991	2	3	0.81300	8.46800
NGC300no26	P12	0.63982	0.95973	0.01190	0.86087	2.58262	0.00270	0.06744	0.20233	0.01430	0.13248	0.08832	2	1	0.90300	8.32600
NGC300no27	P12	1.42909	2.14364	0.01590	0.59148	1.77444	0.00540	0.10567	0.31700	0.01500	0.48995	0.32663	2	1	1.10700	8.13900
NGC300no28	P12	1.25620	1.88431	0.01890	0.81085	2.43255	0.00430	0.07078	0.21235	0.01510	0.22344	0.14896	2	1	1.05600	8.22100
Tol1004-29	P12	0.59301	0.88951	0.04000	1.47550	4.42651	···	0.03890	0.11670	···	0.11276	0.07517	2	1	1.11000	8.18400
Tol1004-29	P12	0.88932	1.33399	0.04100	1.29402	3.88205	···	0.04819	0.14456	···	0.17344	0.11563	2	1	1.17300	8.12400

Mi462	P12	0.58218	0.87328	0.09600	1.84901	5.54704	···	0.01963	0.05889	···	0.11999	0.07999	2	1	1.42700	7.94800
Tol0633-41	P12	0.69512	1.04268	0.07700	1.99499	5.98496	···	0.03953	0.11859	···	0.14627	0.09751	2	1	1.26300	8.13400
F30	P12	0.43457	0.65186	0.10100	1.81526	5.44580	···	0.02162	0.06487	···	0.11276	0.07517	2	1	1.47200	7.88300
Tol1324-27	P12	0.60403	0.90605	0.06100	1.80692	5.42077	···	0.03062	0.09185	···	0.12887	0.08591	2	1	1.20100	8.15100
Tol1304-38	P12	0.40744	0.61115	0.10200	2.02740	6.08221	···	0.02890	0.08671	···	0.13557	0.09038	2	1	1.40700	7.97100
IIZw40	P12	0.18158	0.27236	0.10500	2.36559	7.09678	···	0.01828	0.05484	···	0.06240	0.04160	2	1	1.33500	8.05800
Mi439	P12	0.30624	0.45936	0.12900	2.52895	7.58685	···	0.01197	0.03590	···	0.06717	0.04478	2	1	1.41600	8.03400
Tol1334-32	P12	0.33042	0.49562	0.11400	2.41513	7.24538	···	0.01096	0.03289	···	0.05335	0.03557	2	1	1.37000	8.05700
C1148-203	P12	0.33501	0.50252	0.10900	1.80692	5.42077	···	0.01563	0.04689	···	0.08094	0.05396	2	1	1.52800	7.82400
Tol1457-26	P12	0.81670	1.22504	0.05200	1.59934	4.79801	···	0.04092	0.12276	···	0.16075	0.10717	2	1	1.18400	8.16400
Mrk36	P12	0.31193	0.46790	0.09700	1.72958	5.18873	···	0.01164	0.03492	···	0.12478	0.08319	2	1	1.47700	7.84000
Tol1008-28	P12	0.44675	0.67012	0.11500	2.65424	7.96272	···	0.03162	0.09486	···	0.09664	0.06443	2	1	1.32200	8.15000
NGC628H13	P12	1.18320	1.77481	0.00100	0.51397	1.54192	0.00500	0.16479	0.49438	0.01200	0.21289	0.14193	2	2	0.83400	8.46300
NGC1232CDT	P12	1.27075	1.90612	···	0.27986	0.83958	0.00800	0.29644	0.88933	0.00800	0.36320	0.24214	2	2	0.78300	8.49600
U5005(2-2)	P12	1.03053	1.54579	0.03300	1.10902	3.32706	···	0.06854	0.20562	···	0.32670	0.21780	2	1	1.14700	8.13800
M101NGC546	P12	0.41215	0.61823	0.01100	1.00448	3.01343	0.00340	0.09637	0.28911	0.01160	0.12710	0.08473	2	2	0.90600	8.31300
M101H1013	P12	0.53959	0.80938	0.00190	0.32280	0.96841	0.00430	0.19631	0.58893	0.00720	0.15529	0.10353	2	2	0.70300	8.45700
M31K9323	P12	0.57156	0.85734	0.00950	0.94176	2.82528	0.00390	0.10640	0.31920	0.01110	0.09487	0.06325	2	1	0.83100	8.46600
M33NGC0595	P12	0.82046	1.23070	0.00190	0.30615	0.91846	0.00390	0.15168	0.45505	···	0.13006	0.08671	2	1	0.74000	8.46300
M33NGC0604	P12	0.45926	0.68889	0.00630	0.70136	2.10408	0.00270	0.08809	0.26428	···	0.15246	0.10164	2	2	0.83800	8.33400
NGC1741Zon	P12	0.53218	0.79827	0.01100	1.01377	3.04131	0.00340	0.08668	0.26005	0.01090	0.21486	0.14324	2	2	0.96100	8.25500
NGC2366NGC	P12	0.10071	0.15106	0.13700	1.90082	5.70245	0.00050	0.00565	0.01695	0.01240	0.04085	0.02723	2	2	1.62000	7.74100
NGC2403VS2	P12	0.57156	0.85734	0.00430	0.48188	1.44564	0.00350	0.12970	0.38910	0.00860	0.15071	0.10048	2	2	0.78300	8.38000
NGC2403VS3	P12	0.42664	0.63996	0.00600	0.50227	1.50682	0.00230	0.09140	0.27420	0.00550	0.11096	0.07397	2	2	0.75500	8.40200
NGC2403VS4	P12	0.53464	0.80196	0.00620	0.64112	1.92336	0.00330	0.10138	0.30413	0.00960	0.17344	0.11563	2	1	0.82200	8.36300
NGC4861bri	P12	0.34361	0.51541	0.08200	2.01809	6.05426	0.00100	0.01462	0.04386	0.02040	0.09776	0.06517	2	2	1.35200	8.00500
NGC2403no5	P12	1.20798	1.81197	0.02570	1.15329	3.45988	···	0.06053	0.18158	···	0.16075	0.10717	2	1	1.04100	8.30800
IIZw70	P12	0.72788	1.09182	0.05300	1.45191	4.35573	···	0.05187	0.15562	···	0.19822	0.13215	2	1	1.23600	8.06500
IZw122	P12	0.50823	0.76234	0.12500	2.33314	6.99941	···	0.02094	0.06281	···	0.10621	0.07080	2	1	1.44800	8.00400
PHL293B	P12	0.28318	0.42477	0.15300	2.03676	6.11028	···	0.00665	0.01996	···	0.06182	0.04122	2	1	1.70100	7.74900
Tol1214-27	P12	0.09751	0.14627	0.17310	1.69410	5.08231	···	0.00299	0.00898	···	0.01858	0.01239	2	1	2.02600	7.47700
NHC2403VS4	P12	1.11959	1.67939	···	0.40266	1.20798	···	0.12881	0.38642	0.01100	0.23505	0.15670	2	3	0.80000	8.47100
NHC2403VS3	P12	0.90377	1.35566	0.01000	0.48858	1.46575	···	0.10938	0.32814	0.01200	0.19505	0.13003	2	3	0.84900	8.35700
M51CCM10	P12	0.64872	0.97309	···	0.06652	0.19955	0.00600	0.36219	1.08658	0.00400	0.26372	0.17582	2	2	0.61000	8.52200
NGC2363A2	P12	0.17261	0.25891	0.16500	2.48279	7.44837	···	0.01130	0.03389	0.01000	0.04019	0.02680	2	3	1.41300	8.01100
NGC2363WR1	P12	0.28383	0.42575	0.14800	2.09382	6.28147	···	0.00798	0.02394	···	0.05823	0.03882	2	1	1.64900	7.79200
NGC2363D2	P12	0.33578	0.50368	0.12600	1.92726	5.78178	···	0.00964	0.02891	···	0.07676	0.05118	2	1	1.58700	7.80800
NGC2363D3	P12	0.30765	0.46148	0.12300	2.11320	6.33959	···	0.00798	0.02394	···	0.06297	0.04198	2	1	1.50200	7.89800
NGC2363B2	P12	0.35568	0.53352	0.12500	2.09382	6.28147	···	0.00998	0.02993	···	0.07554	0.05036	2	1	1.52100	7.88800
NGC2363B3	P12	0.23992	0.35987	0.13000	2.25912	6.77737	···	0.00731	0.02193	···	0.05523	0.03682	2	1	1.49400	7.92000
NGC2363B4	P12	0.16790	0.25186	0.14000	2.29583	6.88749	···	0.00598	0.01795	···	0.04679	0.03119	2	1	1.53600	7.88600
NGC2363B5	P12	0.20001	0.30002	0.13000	2.25912	6.77737	···	0.00665	0.01996	···	0.05037	0.03358	2	1	1.49400	7.91500
NGC2363WR1	P12	0.33578	0.50368	0.13300	2.11807	6.35421	···	0.00798	0.02394	···	0.05877	0.03918	2	1	1.55700	7.86400
IIZw40	P12	0.33578	0.50368	0.10900	2.46570	7.39710	···	0.02094	0.06281	···	0.07264	0.04842	2	1	1.33400	8.09700
Mrk1236	P12	0.60542	0.90814	0.04300	1.37385	4.12156	···	0.04591	0.13774	···	0.19282	0.12855	2	1	1.16800	8.09700
Mrk178	P12	0.50589	0.75884	0.11900	1.81945	5.45835	···	0.01896	0.05689	···	0.16794	0.11196	2	1	1.58800	7.81200
SBS0940+54	P12	0.18839	0.28259	0.12800	1.39939	4.19818	···	0.00399	0.01197	···	0.03777	0.02518	2	1	1.89700	7.47800
SBS0940+54	P12	0.23500	0.35249	0.14200	1.40262	4.20786	···	0.00532	0.01596	···	0.03838	0.02559	2	1	2.01500	7.43400
HS1442+425	P12	0.21383	0.32074	0.13800	1.65554	4.96662	···	0.00765	0.02296	···	0.04257	0.02838	2	1	1.80000	7.60000
HS1442+425	P12	0.55088	0.82633	0.05500	0.77080	2.31239	···	0.02193	0.06578	···	0.13494	0.08996	2	1	1.65800	7.50500

SBS1415+43	P12	0.37937	0.56905	0.08400	1.17744	3.53233	· · ·	0.01064	0.03192	· · ·	0.09187	0.06124	2	1	1.65700	7.59200
SBS1415+43	P12	0.43357	0.65036	0.07000	1.05424	3.16272	· · ·	0.01396	0.04189	· · ·	0.11045	0.07363	2	1	1.60000	7.60500
Pox186	P12	0.11170	0.16755	0.14300	2.03208	6.09623	· · ·	0.00532	0.01596	· · ·	0.04562	0.03041	2	1	1.64600	7.75400
J0014-0044	P12	0.39633	0.59450	0.08870	2.06509	6.19528	· · ·	0.01896	0.05689	· · ·	0.08282	0.05522	2	1	1.31700	8.05300
J0301-0059	P12	1.32452	1.98679	0.03460	0.91399	2.74196	· · ·	0.06822	0.20467	· · ·	0.42969	0.28646	2	1	1.25300	8.03700
G0405-3648	P12	0.51768	0.77652	0.04020	0.68697	2.06092	· · ·	0.01794	0.05383	· · ·	0.12828	0.08552	2	1	1.50600	7.56700
J2324-0006	P12	0.60962	0.91443	0.09470	1.80692	5.42077	· · ·	0.01629	0.04887	· · ·	0.12307	0.08205	2	1	1.43300	7.94000
UM283D	P12	1.17777	1.76665	0.04100	1.11928	3.35785	· · ·	0.06652	0.19955	0.01810	0.30071	0.20047	2	3	1.15800	8.15500
UM133H	P12	0.42861	0.64291	0.07720	1.22445	3.67334	· · ·	0.01030	0.03091	0.01540	0.09776	0.06517	2	1	1.56000	7.68000
UM133O	P12	0.36063	0.54094	0.08830	1.33641	4.00923	· · ·	0.00998	0.02993	0.01520	0.09597	0.06398	2	1	1.59500	7.67300
UM408	P12	0.42273	0.63409	0.08090	1.73756	5.21268	· · ·	0.01762	0.05285	0.01620	0.11406	0.07604	2	1	1.36200	7.95400
UM417	P12	0.24607	0.36911	0.12960	1.69410	5.08231	· · ·	0.00832	0.02495	0.01450	0.06356	0.04237	2	1	1.71900	7.66000
MRK600	P12	0.15455	0.23182	0.12510	2.15248	6.45745	· · ·	0.00798	0.02394	0.01600	0.05877	0.03918	2	1	1.50100	7.88300
HE2-10E	P12	0.77279	1.15918	0.00260	0.42067	1.26201	· · ·	0.24263	0.72788	0.00720	0.17995	0.11997	2	1	0.73900	8.50800
MRK1259	P12	0.68401	1.02601	0.01080	0.53820	1.61459	0.00650	0.28245	0.84735	0.00770	0.20331	0.13554	2	2	0.72100	8.58000
MRK1271	P12	0.41885	0.62828	0.08310	1.84901	5.54704	· · ·	0.01563	0.04689	0.01270	0.09357	0.06238	2	1	1.34200	7.99300
POX4	P12	0.32513	0.48770	0.09120	2.16740	6.50221	· · ·	0.01164	0.03492	0.01640	0.08094	0.05396	2	3	1.51500	7.90100
TOL1214-27	P12	0.12333	0.18499	0.17290	1.70192	5.10577	· · ·	0.00266	0.00798	0.00830	0.02158	0.01439	2	1	2.01800	7.48700
NGC5253C2	P12	0.59437	0.89156	0.03090	1.48231	4.44694	0.00240	0.04159	0.12476	0.01980	0.16186	0.10791	2	2	1.21200	8.07100
NGC5253P1	P12	0.70155	1.05233	· · ·	1.67857	5.03572	· · ·	0.03162	0.09486	0.01850	0.11328	0.07552	2	3	1.16000	8.18700
TOL89no1	P12	0.60682	0.91023	0.03380	1.62907	4.88721	0.00230	0.04425	0.13276	0.01690	0.12421	0.08281	2	2	1.13600	8.18900
NGC5408no1	P12	0.46565	0.69848	0.19770	3.08276	9.24829	0.00080	0.00897	0.02692	0.02000	0.07147	0.04765	2	1	1.57200	8.01400
TOL1457-26	P12	1.03529	1.55293	0.06800	2.08901	6.26702	0.00100	0.02729	0.08186	0.01510	0.12536	0.08357	2	3	1.32000	8.14000
TOL1924-41	P12	0.37762	0.56644	0.05360	1.45191	4.35573	· · ·	0.02393	0.07179	0.01330	0.10143	0.06762	2	1	1.24200	7.99200
TOL1924-41	P12	0.45610	0.68415	0.06230	1.76579	5.29738	· · ·	0.01828	0.05484	0.01710	0.11699	0.07799	2	3	1.43300	7.90700
PHL293B	P12	0.20094	0.30141	0.14550	1.94062	5.82185	· · ·	0.00598	0.01795	0.01600	0.05226	0.03484	2	1	1.69900	7.71800
TOL0513-39	P12	0.19101	0.28652	0.14760	2.48279	7.44837	· · ·	0.01096	0.03289	0.01230	0.05523	0.03682	2	1	1.51600	7.93500
J154054+56	P12	0.87108	1.30663	0.02910	1.02787	3.08362	· · ·	0.07046	0.21138	· · ·	0.27174	0.18116	2	1	1.12700	8.11200
J161623+47	P12	0.33967	0.50951	0.08510	2.04616	6.13849	· · ·	0.01429	0.04286	0.01860	0.08094	0.05396	2	3	1.35200	8.01000
J172906+56	P12	0.70479	1.05719	0.06600	1.71372	5.14116	0.00600	0.07277	0.21830	0.01760	0.13809	0.09206	2	3	1.13400	8.22400
M101NGC545	P12	0.83188	1.24782	0.02700	1.26456	3.79368	· · ·	0.09549	0.28646	· · ·	0.18287	0.12192	2	1	1.02700	8.28600
WLMno7	P12	0.57951	0.86926	0.09000	1.23010	3.69030	· · ·	0.01330	0.03991	· · ·	0.10793	0.07195	2	1	1.67900	7.63700
WLMno9	P12	0.41597	0.62395	0.05000	1.43529	4.30587	· · ·	0.04325	0.12974	· · ·	0.20378	0.13585	2	1	1.21400	8.02500
0832+699	P12	0.42175	0.63263	0.06700	0.93743	2.81230	· · ·	0.00964	0.02891	· · ·	0.06717	0.04478	2	1	1.65900	7.52600
0946+558	P12	0.59437	0.89156	0.08200	1.81526	5.44580	· · ·	0.02128	0.06384	· · ·	0.11753	0.07835	2	1	1.34500	8.01100
1135+581	P12	0.53834	0.80752	0.06900	1.58467	4.75402	0.00100	0.02228	0.06684	· · ·	0.11999	0.07999	2	1	1.32500	7.97400
1159+545	P12	0.27106	0.40658	0.10900	1.15064	3.45192	0.00300	0.00731	0.02193	· · ·	0.05756	0.03838	2	1	1.93500	7.40500
1211+540	P12	0.25826	0.38739	0.11600	1.54504	4.63512	· · ·	0.00665	0.01996	· · ·	0.05704	0.03802	2	1	1.70100	7.63800
1331+493N	P12	0.35405	0.53107	0.12100	1.81526	5.44580	· · ·	0.01064	0.03192	· · ·	0.07197	0.04798	2	1	1.60200	7.77800
1437+370	P12	0.55983	0.83975	0.08800	1.74961	5.24882	· · ·	0.01963	0.05889	· · ·	0.13682	0.09121	2	1	1.40700	7.94200
0723+692A	P12	0.24494	0.36741	0.14300	2.19250	6.57751	· · ·	0.00798	0.02394	· · ·	0.05154	0.03436	2	1	1.58600	7.84400
0723+692B	P12	0.63104	0.94657	0.08200	1.43199	4.29597	· · ·	0.01828	0.05484	· · ·	0.11753	0.07835	2	1	1.49200	7.82100
0741+535	P12	1.16429	1.74643	0.06800	1.46535	4.39604	· · ·	0.04055	0.12164	· · ·	0.25654	0.17103	2	1	1.36000	8.02000
0749+568	P12	0.66690	1.00035	0.09800	1.62159	4.86476	· · ·	0.02529	0.07587	· · ·	0.17505	0.11670	2	1	1.52800	7.84100
0749+582	P12	0.50473	0.75710	0.11500	2.62386	7.87157	· · ·	0.02594	0.07781	· · ·	0.10073	0.06715	2	1	1.32900	8.14600
0907+543	P12	0.37589	0.56383	0.12100	2.27478	6.82435	· · ·	0.01096	0.03289	· · ·	0.06905	0.04603	2	1	1.44300	7.98100
0917+527	P12	0.75520	1.13279	0.09200	1.55575	4.66725	· · ·	0.01927	0.05782	· · ·	0.16678	0.11119	2	1	1.51300	7.85300
0926+606	P12	0.71460	1.07189	0.08300	1.58833	4.76498	· · ·	0.02760	0.08281	· · ·	0.19686	0.13124	2	1	1.43200	7.91500
0930+554	P12	0.16333	0.24499	0.06000	0.63378	1.90135	· · ·	0.00399	0.01197	· · ·	0.03063	0.02042	2	1	1.93400	7.15300
0940+544N	P12	0.22807	0.34210	0.13500	1.32416	3.97248	· · ·	0.00532	0.01596	· · ·	0.04317	0.02878	2	1	2.02300	7.40700

1030+583	P12	0.38731	0.58097	0.10400	1.67086	5.01258	...	0.01030	0.03091	...	0.09776	0.06517	2	1	1.55000	7.78900
1054+365	P12	0.42664	0.63996	0.09500	1.97670	5.93009	...	0.01596	0.04787	...	0.09531	0.06354	2	1	1.38000	7.98600
1116+583B	P12	0.23554	0.35331	0.11700	1.61042	4.83127	...	0.00897	0.02692	...	0.07983	0.05322	2	1	1.67300	7.66600
1124+792	P12	0.53341	0.80011	0.07100	1.14799	3.44398	...	0.01663	0.04990	...	0.10670	0.07113	2	1	1.54500	7.69400
1128+573	P12	0.34919	0.52378	0.14300	1.92726	5.78178	...	0.01096	0.03289	...	0.08038	0.05359	2	1	1.69000	7.74500
1222+614	P12	0.46780	0.70170	0.10200	1.98125	5.94376	...	0.01265	0.03794	...	0.09293	0.06195	2	1	1.42200	7.95900
1223+487	P12	0.28778	0.43167	0.12700	1.84476	5.53428	...	0.00964	0.02891	...	0.06356	0.04237	2	1	1.62900	7.75500
1256+351	P12	0.44062	0.66092	0.08900	1.92726	5.78178	...	0.01531	0.04593	...	0.09958	0.06638	2	1	1.35700	7.99900
1319+579B	P12	0.97737	1.46606	0.05000	1.09129	3.27387	...	0.05357	0.16072	...	0.38829	0.25886	2	1	1.35300	7.92100
1441+294	P12	0.60126	0.90189	0.06900	1.63659	4.90977	...	0.02760	0.08281	...	0.20519	0.13679	2	1	1.30700	8.01300
1535+554	P12	0.87712	1.31568	0.06000	1.55934	4.67801	...	0.03357	0.10071	...	0.21735	0.14490	2	1	1.26100	8.08500
IZw18NW	P12	0.11483	0.17225	0.06400	0.64854	1.94563	...	0.00299	0.00898	...	0.02219	0.01479	2	1	1.98200	7.11700
IZw18SE	P12	0.23662	0.35494	0.04830	0.53081	1.59243	...	0.00665	0.01996	...	0.04199	0.02799	2	1	1.89000	7.14900
Mrk600	P12	0.52127	0.78190	0.11800	1.82364	5.47093	...	0.01164	0.03492	...	0.10143	0.06762	2	1	1.57900	7.82200
Mrk5	P12	0.85126	1.27688	0.04400	1.26748	3.80243	...	0.04591	0.13774	...	0.23941	0.15961	2	1	1.21300	8.07000
Mrk1271	P12	0.64278	0.96416	0.10200	2.02274	6.06822	...	0.03026	0.09079	...	0.15854	0.10570	2	1	1.40900	8.00300
Mrk36	P12	0.51768	0.77652	0.09600	1.60672	4.82016	...	0.01762	0.05285	...	0.12055	0.08036	2	1	1.52000	7.81900
Mrk162	P12	1.31844	1.97766	0.04000	1.22445	3.67334	...	0.06713	0.20140	...	0.30985	0.20657	2	1	1.18600	8.16700
UM461	P12	0.21089	0.31634	0.13600	2.00419	6.01258	...	0.00698	0.02094	...	0.05638	0.03759	2	1	1.61700	7.78300
UM462SW	P12	0.69672	1.04508	0.07800	1.64036	4.92109	...	0.02426	0.07279	...	0.16794	0.11196	2	1	1.37500	7.96900
SBS1159+54	P12	0.27106	0.40658	0.10900	1.23863	3.71588	...	0.00698	0.02094	...	0.05756	0.03838	2	1	1.85500	7.47200
SBS1249+49	P12	0.50010	0.75016	0.10800	1.53088	4.59263	...	0.01297	0.03891	...	0.07382	0.04921	2	1	1.64800	7.71300
SBS1415+43	P12	0.44984	0.67476	0.08600	1.14009	3.42028	...	0.01164	0.03492	...	0.09531	0.06354	2	1	1.70500	7.56900
Mrk930	P12	0.94855	1.42282	0.05000	1.38656	4.15969	...	0.04753	0.14258	...	0.28000	0.18666	2	1	1.23000	8.09400
IZw18South	P12	0.20094	0.30141	0.05420	0.58202	1.74607	...	0.00499	0.01496	...	0.04141	0.02761	2	1	1.91700	7.14800
Tol65	P12	0.26981	0.40472	0.09500	1.20765	3.62294	...	0.00598	0.01795	...	0.06594	0.04396	2	1	1.74500	7.52200
Tol65no1	P12	0.17950	0.26925	0.12200	1.34567	4.03702	...	0.00432	0.01297	...	0.04562	0.03041	2	1	1.88700	7.46600
Tol65no2	P12	0.27356	0.41035	0.09400	1.08878	3.26634	...	0.00798	0.02394	...	0.06953	0.04635	2	1	1.83400	7.43700
HS0122+074	P12	0.28778	0.43167	0.12200	1.49259	4.47777	...	0.00765	0.02296	...	0.06779	0.04519	2	1	1.78100	7.58400
HS0128+283	P12	0.31554	0.47332	0.08960	2.37651	7.12954	...	0.02360	0.07080	...	0.09597	0.06398	2	1	1.25200	8.15700
HS0134+341	P12	0.26065	0.39098	0.17230	2.46570	7.39710	...	0.00931	0.02793	...	0.07928	0.05285	2	1	1.64100	7.85800
UM133	P12	0.72287	1.08430	0.09090	1.24721	3.74163	...	0.01364	0.04093	...	0.12166	0.08111	2	1	1.67600	7.67200
Mrk1063	P12	0.92909	1.39364	0.02000	0.96814	2.90443	...	0.08510	0.25531	...	0.24387	0.16258	2	1	1.01700	8.24800
HS0811+491	P12	0.46888	0.70332	0.11630	2.17741	6.53223	...	0.01828	0.05484	...	0.10260	0.06840	2	1	1.44500	7.97500
CGCG007-02	P12	0.43758	0.65637	0.12980	1.83206	5.49618	...	0.01064	0.03192	...	0.07502	0.05001	2	1	1.65100	7.76400
CGCG007-02	P12	0.62526	0.93789	0.10820	1.51684	4.55052	...	0.01496	0.04488	...	0.11459	0.07639	2	1	1.65800	7.72600
Mrk1236	P12	0.58353	0.87529	0.07140	2.02740	6.08221	0.00270	0.03388	0.10164	...	0.14933	0.09955	2	1	1.22000	8.16800
Mrk724	P12	0.59987	0.89981	0.07280	1.78213	5.34640	...	0.01963	0.05889	...	0.11328	0.07552	2	1	1.29100	8.05600
UM439	P12	0.42273	0.63409	0.13430	2.67264	8.01791	...	0.01462	0.04386	...	0.08398	0.05598	2	1	1.40600	8.07800
Pox36	P12	1.10678	1.66016	0.04980	1.33027	3.99081	0.00380	0.03523	0.10570	...	0.19550	0.13033	2	1	1.24800	8.09100
Mrk1315	P12	0.43357	0.65036	0.05220	2.00882	6.02645	0.00130	0.01896	0.05689	...	0.07433	0.04955	2	2	1.35600	8.01400
HS1213+363	P12	1.24756	1.87133	0.02560	1.06155	3.18465	0.00450	0.05820	0.17461	...	0.18499	0.12333	2	1	1.06800	8.26100
HS1214+380	P12	0.56242	0.84363	0.08520	1.92726	5.78178	...	0.01927	0.05782	...	0.09889	0.06593	2	1	1.33300	8.03800
Mrk1329	P12	0.49666	0.74499	0.04430	1.82785	5.48354	0.00130	0.02296	0.06887	...	0.08753	0.05835	2	2	1.19800	8.14200
Mrk450no1	P12	0.70804	1.06207	0.05240	1.69021	5.07062	0.00210	0.03758	0.11274	...	0.15891	0.10594	2	2	1.18800	8.15900
Mrk450no2	P12	0.69034	1.03550	0.06470	1.73756	5.21268	...	0.03427	0.10282	...	0.18414	0.12276	2	1	1.24600	8.10500
Mrk67	P12	0.72621	1.08931	0.08020	1.87906	5.63717	...	0.02296	0.06887	...	0.15176	0.10117	2	1	1.31500	8.07000
HS2236+134	P12	0.24325	0.36488	0.17680	1.59566	4.78698	...	0.00565	0.01695	...	0.03599	0.02399	2	1	2.13200	7.43500
M101no1	P12	0.48872	0.73308	0.10070	2.14259	6.42778	...	0.01995	0.05985	...	0.10868	0.07245	2	1	1.36800	8.03500
M101no2	P12	0.97737	1.46606	0.07300	1.54149	4.62446	...	0.04886	0.14658	...	0.24107	0.16072	2	1	1.37200	7.99700

M101no3	P12	0.91635	1.37452	0.02430	1.27626	3.82879	· · ·	0.08952	0.26857	· · ·	0.18161	0.12108	2	1	0.99100	8.35500
M101no4	P12	1.04727	1.57091	0.02440	1.12964	3.38892	· · ·	0.08870	0.26611	· · ·	0.22088	0.14725	2	1	1.03100	8.29000
0335-052En	P12	0.09399	0.14098	0.11220	1.04698	3.14095	· · ·	0.00299	0.00898	0.00610	0.01982	0.01321	2	1	2.08500	7.25300
0335-052En	P12	0.08711	0.13066	0.11330	1.00911	3.02734	0.00060	0.00333	0.00998	0.00590	0.02100	0.01400	2	1	2.15100	7.20800
0335-052En	P12	0.09910	0.14865	0.06880	0.66060	1.98181	· · ·	0.00333	0.00998	· · ·	0.03063	0.02042	2	1	2.04800	7.08700
0335-052En	P12	0.10001	0.15002	0.06150	0.64705	1.94116	· · ·	0.00266	0.00798	0.00510	0.02762	0.01841	2	1	1.94000	7.12900
0335-052Wn	P12	0.30065	0.45097	0.03330	0.43245	1.29736	· · ·	0.01130	0.03389	· · ·	0.06594	0.04396	2	1	1.72300	7.21100
PHL293B	P12	0.20467	0.30701	0.13190	1.80277	5.40831	· · ·	0.00565	0.01695	0.01270	0.04615	0.03077	2	1	1.67900	7.70200
UM306	P12	1.11445	1.67167	0.05120	1.52736	4.58207	· · ·	0.07144	0.21432	· · ·	0.29727	0.19818	2	1	1.19700	8.18100
Tol0140-42	P12	1.12476	1.68714	0.05900	1.38019	4.14058	· · ·	0.04819	0.14456	· · ·	0.21535	0.14357	2	1	1.31400	8.04000
UM396	P12	0.60822	0.91233	0.08500	2.21789	6.65367	· · ·	0.02162	0.06487	· · ·	0.08094	0.05396	2	1	1.26000	8.16300
UM408	P12	0.75694	1.13541	0.08250	1.72958	5.18873	· · ·	0.03162	0.09486	· · ·	0.22654	0.15103	2	1	1.37600	7.99400
Tol0341-40	P12	0.85913	1.28870	0.07340	1.57015	4.71044	· · ·	0.03357	0.10071	· · ·	0.23505	0.15670	2	1	1.36400	7.99100
Tol0528-38	P12	1.00244	1.50367	0.07060	1.47890	4.43671	· · ·	0.04285	0.12855	· · ·	0.25419	0.16946	2	1	1.37600	7.98600
Tol0528-38	P12	1.79912	2.69868	0.06490	1.46872	4.40617	· · ·	0.05956	0.17867	· · ·	0.28586	0.19057	2	1	1.33200	8.13100
IIZw40	P12	0.33347	0.50021	0.10510	2.26433	6.79299	0.00400	0.02729	0.08186	· · ·	0.10572	0.07048	2	1	1.36100	8.04000
Tol0633-41	P12	1.04246	1.56369	0.07370	2.02740	6.08221	· · ·	0.04591	0.13774	· · ·	0.20756	0.13838	2	1	1.23400	8.21500
Cam0840+10	P12	0.31409	0.47114	0.10910	1.52034	4.56101	· · ·	0.00897	0.02692	· · ·	0.11045	0.07363	2	1	1.66200	7.66700
Tol0957-27	P12	1.00014	1.50021	0.04740	1.18288	3.54863	· · ·	0.04285	0.12855	· · ·	0.24499	0.16333	2	1	1.28100	8.01000
Tol1004-29	P12	0.77994	1.16991	0.03700	1.44524	4.33572	· · ·	0.05093	0.15278	· · ·	0.17028	0.11352	2	1	1.08900	8.23700
Tol1004-29	P12	0.82425	1.23638	0.03620	1.37069	4.11208	· · ·	0.05457	0.16370	· · ·	0.18161	0.12108	2	1	1.10100	8.21300
CTS1011	P12	0.94855	1.42282	0.09550	2.24874	6.74623	· · ·	0.03228	0.09684	· · ·	0.17748	0.11832	2	1	1.31100	8.16100
CTS1020	P12	0.96175	1.44262	0.05210	1.75768	5.27304	· · ·	0.06515	0.19546	· · ·	0.19371	0.12914	2	1	1.14600	8.25500
CTS1022	P12	1.13256	1.69884	0.06100	1.50640	4.51920	· · ·	0.03388	0.10164	· · ·	0.24612	0.16408	2	1	1.28600	8.09000
Fairall30	P12	0.63250	0.94875	0.11000	2.06035	6.18104	· · ·	0.02691	0.08073	· · ·	0.14865	0.09910	2	1	1.44400	7.98000
Mkr36	P12	0.63835	0.95753	0.07260	1.37702	4.13106	· · ·	0.01896	0.05689	· · ·	0.16038	0.10692	2	1	1.43700	7.85200
UM439	P12	0.71624	1.07436	0.10140	1.89208	5.67625	· · ·	0.02328	0.06983	· · ·	0.18670	0.12447	2	1	1.44800	7.95900
UM439SE	P12	0.55726	0.83589	0.11120	2.19250	6.57751	· · ·	0.01862	0.05585	· · ·	0.28718	0.19145	2	1	1.41300	8.01600
UM448	P12	1.30035	1.95052	0.02490	0.93959	2.81878	· · ·	0.13272	0.39816	· · ·	0.39369	0.26246	2	1	1.10200	8.20200
UM455NW	P12	0.47870	0.71804	0.09660	1.79862	5.39587	· · ·	0.01828	0.05484	· · ·	0.17225	0.11483	2	1	1.44900	7.90400
UM456	P12	0.81858	1.22787	0.08540	1.56653	4.69960	· · ·	0.02624	0.07872	· · ·	0.19017	0.12678	2	1	1.45900	7.90600
UM456NE	P12	0.61243	0.91865	0.09170	1.72958	5.18873	· · ·	0.02328	0.06983	· · ·	0.14593	0.09729	2	1	1.44000	7.91900
UM456Cent	P12	0.88932	1.33399	0.06230	1.46872	4.40617	· · ·	0.02857	0.08572	· · ·	0.21486	0.14324	2	1	1.31100	8.02300
UM461	P12	0.31554	0.47332	0.14800	1.92283	5.76848	· · ·	0.00598	0.01795	· · ·	0.07314	0.04876	2	1	1.72300	7.71900
UM461E	P12	0.27737	0.41606	0.15800	2.06509	6.19528	· · ·	0.00731	0.02193	· · ·	0.07197	0.04798	2	1	1.71800	7.74400
UM462	P12	0.92270	1.38405	0.07200	1.38019	4.14058	0.00900	0.02660	0.07981	· · ·	0.20144	0.13430	2	1	1.43000	7.90900
UM462NE	P12	0.88320	1.32480	0.06600	1.36439	4.09318	· · ·	0.02193	0.06578	· · ·	0.17954	0.11969	2	1	1.38500	7.93600
UM483	P12	1.07167	1.60750	0.07830	1.82364	5.47093	· · ·	0.03758	0.11274	· · ·	0.21289	0.14193	2	1	1.31800	8.10600
DDO155	P12	0.92909	1.39364	0.04100	0.69014	2.07043	· · ·	0.03126	0.09377	· · ·	0.21289	0.14193	2	1	1.51600	7.67700
CTS1033	P12	0.42566	0.63849	0.12920	2.30643	6.91929	· · ·	0.01730	0.05189	· · ·	0.12710	0.08473	2	1	1.47700	7.96700
Tol1457-26	P12	0.87712	1.31568	0.06970	1.61786	4.85357	· · ·	0.03026	0.09079	· · ·	0.21486	0.14324	2	1	1.32000	8.04100
Tol1457-26	P12	1.42580	2.13871	0.04020	1.12186	3.36559	· · ·	0.06652	0.19955	· · ·	0.37945	0.25296	2	1	1.22800	8.12200
Tol1457-26	P12	1.47591	2.21387	0.03720	1.08128	3.24385	· · ·	0.07708	0.23124	· · ·	0.37166	0.24778	2	1	1.20900	8.14100
Tol1457-26	P12	1.42253	2.13379	0.04310	1.10139	3.30416	· · ·	0.06652	0.19955	· · ·	0.37684	0.25122	2	1	1.26900	8.07600
Tol1924-41	P12	0.60682	0.91023	0.09100	1.83628	5.50885	· · ·	0.02660	0.07981	· · ·	0.14294	0.09529	2	1	1.39900	7.97200
Tol1924-41	P12	0.60264	0.90396	0.08380	1.76986	5.30959	· · ·	0.02857	0.08572	· · ·	0.14327	0.09551	2	1	1.37100	7.98300
Tol1924-41	P12	0.60822	0.91233	0.09800	1.91840	5.75521	· · ·	0.02328	0.06983	· · ·	0.13969	0.09312	2	1	1.41700	7.97200
M33MA1	P12	0.21580	0.32371	0.09000	1.99959	5.99876	· · ·	0.01995	0.05985	· · ·	0.07801	0.05201	2	1	1.34200	7.99000
M33BCLMP65	P12	0.85913	1.28870	0.04700	1.46198	4.38593	· · ·	0.07979	0.23937	· · ·	0.25186	0.16790	2	1	1.17900	8.14900
DDO154no2	P12	0.64426	0.96639	0.04000	0.73780	2.21341	· · ·	0.02494	0.07483	· · ·	0.14593	0.09729	2	1	1.45400	7.66300

DDO154no2	P12	0.64426	0.96639	0.04000	0.73780	2.21341	· · ·	0.02494	0.07483	· · ·	0.14593	0.09729	2	1	1.45400	7.66300
M101H1013	P12	0.75173	1.12759	· · ·	0.34272	1.02816	0.00500	0.21475	0.64426	0.00800	0.17264	0.11510	2	2	0.72500	8.49400
M101H1105	P12	0.73971	1.10956	0.01400	1.05182	3.15545	0.00400	0.11116	0.33347	0.01300	0.14459	0.09640	2	2	0.91600	8.38200
M101H1159	P12	0.79261	1.18892	0.01900	1.05424	3.16272	· · ·	0.07851	0.23554	0.01600	0.17871	0.11914	2	1	0.97500	8.30200
M101H1176	P12	0.63982	0.95973	0.02400	1.22727	3.68181	· · ·	0.07046	0.21138	0.01500	0.13809	0.09206	2	1	1.00000	8.28000
M101H1216	P12	0.60403	0.90605	0.04700	1.57377	4.72130	· · ·	0.03689	0.11068	0.01600	0.09664	0.06443	2	1	1.14900	8.16200
M101H128	P12	0.57951	0.86926	0.01700	1.29999	3.89997	0.00300	0.06917	0.20752	0.01300	0.13969	0.09312	2	2	1.01900	8.25900
M101H149	P12	0.84734	1.27102	0.01800	1.05667	3.17001	0.00900	0.11938	0.35815	0.01400	0.22344	0.14896	2	1	0.95900	8.33900
M101H336	P12	0.71131	1.06697	· · ·	0.07655	0.22965	0.00500	0.31911	0.95733	0.00600	0.34053	0.22702	2	2	0.59300	8.61000
M101H409	P12	0.87108	1.30663	0.02300	1.23010	3.69030	0.00400	0.09077	0.27231	0.01700	0.18713	0.12476	2	2	1.02900	8.28400
M101H70	P12	1.24469	1.86703	0.02500	0.88703	2.66110	· · ·	0.07851	0.23554	0.01400	0.28324	0.18883	2	1	1.12500	8.15300
M101NGC547	P12	0.42370	0.63555	0.09500	2.14259	6.42778	· · ·	0.02259	0.06777	0.01600	0.09487	0.06325	2	1	1.33500	8.05400
M101NGC547	P12	0.54835	0.82253	0.08000	1.92283	5.76848	· · ·	0.02824	0.08473	0.01700	0.12364	0.08243	2	1	1.30100	8.06400
M101SDH323	P12	0.77635	1.16453	0.05500	0.75499	2.26496	· · ·	0.02624	0.07872	· · ·	0.12478	0.08319	2	1	1.67600	7.55000
M101Searle	P12	0.73971	1.10956	· · ·	0.06652	0.19955	0.00490	0.32579	0.97738	0.00320	0.40846	0.27231	2	2	0.58100	8.64600
HS0822+354	P12	0.13245	0.19868	0.12300	1.17744	3.53233	· · ·	0.00499	0.01496	· · ·	0.02762	0.01841	2	1	2.05300	7.32500
NGC5253H II	P12	0.78897	1.18345	0.04100	1.47890	4.43671	· · ·	0.14189	0.42566	0.02900	0.28784	0.19189	2	1	1.11900	8.20800
NGC5253UV-	P12	0.52007	0.78010	0.04700	1.61786	4.85357	· · ·	0.03427	0.10282	· · ·	0.10868	0.07245	2	1	1.13800	8.17000
POX36	P12	1.06920	1.60380	0.04670	1.45861	4.37584	· · ·	0.03890	0.11670	· · ·	0.15601	0.10401	2	1	1.17700	8.18300
POX108	P12	0.35080	0.52620	0.11600	2.30643	6.91929	· · ·	0.02027	0.06082	· · ·	0.07747	0.05165	2	1	1.40700	8.01100
POX139	P12	0.58757	0.88136	0.09600	1.89644	5.68933	· · ·	0.02060	0.06181	· · ·	0.11645	0.07764	2	1	1.41100	7.97100
Tol2	P12	0.77994	1.16991	0.05900	1.46872	4.40617	· · ·	0.02958	0.08873	· · ·	0.13066	0.08711	2	1	1.28200	8.03100
Tol35	P12	0.82425	1.23638	0.07000	1.78213	5.34640	· · ·	0.02624	0.07872	· · ·	0.09250	0.06167	2	1	1.27200	8.10800
IIZw40	P12	0.25767	0.38650	0.10900	2.57597	7.72790	· · ·	0.01794	0.05383	· · ·	0.05574	0.03716	2	1	1.31000	8.12600
M33MA3	P12	0.69512	1.04268	0.02190	1.38656	4.15969	· · ·	0.05649	0.16946	· · ·	0.07928	0.05285	2	1	0.93800	8.42200
M33NGC604	P12	1.05211	1.57816	0.01820	0.69493	2.08478	0.00330	0.09374	0.28123	· · ·	0.15071	0.10048	2	2	0.90500	8.36700
M33IC132	P12	0.42861	0.64291	0.07240	1.87042	5.61127	· · ·	0.02360	0.07080	· · ·	0.06953	0.04635	2	1	1.26500	8.07100
WLMHM9(ap2	P12	0.83572	1.25358	0.06300	1.30900	3.92700	· · ·	0.02494	0.07483	· · ·	0.25128	0.16752	2	1	1.38100	7.92000
WLMHM9(ap3	P12	0.81670	1.22504	0.05400	1.24434	3.73303	· · ·	0.02760	0.08281	· · ·	0.23941	0.15961	2	1	1.32300	7.95100
VCC0848-1	P12	1.01639	1.52458	0.04550	1.16934	3.50801	· · ·	0.06222	0.18666	· · ·	0.31416	0.20944	2	1	1.26600	8.02500
A1243-335A	P12	1.65982	2.48972	0.02340	0.90770	2.72309	· · ·	0.08452	0.25355	· · ·	0.25186	0.16790	2	1	1.09200	8.26700
KISSB23	P12	0.98869	1.48303	0.02600	0.46659	1.39978	· · ·	0.03288	0.09864	· · ·	0.25128	0.16752	2	1	1.47300	7.65200
KISSR73	P12	1.04486	1.56730	0.05600	1.20487	3.61461	· · ·	0.02792	0.08376	· · ·	0.18843	0.12562	2	1	1.36100	7.95100
NGC6822V	P12	0.57818	0.86726	0.05250	1.78624	5.35872	· · ·	0.02060	0.06181	· · ·	0.06474	0.04316	2	1	1.14200	8.20800
IC10no2	P12	0.57818	0.86726	0.04370	1.78624	5.35872	· · ·	0.03828	0.11483	· · ·	0.09250	0.06167	2	1	1.07300	8.29200
IIZw70	P12	1.23612	1.85418	0.05620	1.38656	4.15969	· · ·	0.04385	0.13154	· · ·	0.20997	0.13998	2	1	1.28700	8.08300
HGC31E	P12	1.39335	2.09002	0.02440	0.91188	2.73565	· · ·	0.08510	0.25531	0.01300	0.43068	0.28712	2	1	1.10600	8.20700
HGC31F1	P12	0.64426	0.96639	0.06960	1.81526	5.44580	· · ·	0.03258	0.09774	0.01800	0.17344	0.11563	2	1	1.26000	8.09900
HGC31F2	P12	0.84151	1.26227	0.04900	1.37385	4.12156	· · ·	0.03388	0.10164	0.01500	0.19914	0.13276	2	1	1.22600	8.07800
HGC31G	P12	1.64460	2.46690	0.03100	1.01845	3.05535	· · ·	0.10045	0.30134	0.02200	0.48434	0.32289	2	1	1.15700	8.21000
NGC5253A	P12	0.54835	0.82253	0.06460	1.92726	5.78178	0.00500	0.09704	0.29111	0.02510	0.15494	0.10329	2	2	1.12900	8.24500
NGC5253B	P12	0.53959	0.80938	0.06700	1.98582	5.95746	0.00440	0.08184	0.24551	0.02430	0.13494	0.08996	2	2	1.16000	8.21900
NGC5253C	P12	0.72956	1.09434	0.03950	1.53088	4.59263	0.00180	0.03926	0.11778	0.01700	0.15673	0.10449	2	1	1.09300	8.24100
NGC5253D	P12	1.41273	2.11910	0.02610	0.99756	2.99269	0.00320	0.07481	0.22442	0.01530	0.39008	0.26005	2	3	1.14300	8.18600
Mrk5A-INT-	P12	0.76394	1.14591	0.05140	1.40585	4.21756	· · ·	0.04886	0.14658	0.02310	0.22241	0.14827	2	1	1.23700	8.06000
Mrk5A-INT-	P12	0.85126	1.27688	0.05290	1.42870	4.28609	· · ·	0.04655	0.13966	0.01920	0.22917	0.15278	2	1	1.24300	8.07400
IRAS08208-	P12	0.58757	0.88136	0.03120	1.56293	4.68880	· · ·	0.12273	0.36818	0.01460	0.23182	0.15455	2	1	1.00600	8.34000
IRAS08208-	P12	1.11702	1.67553	0.01660	0.75847	2.27542	· · ·	0.13030	0.39090	0.01130	0.41224	0.27483	2	1	1.03500	8.20700
IRAS08208-	P12	1.00475	1.50713	0.02260	1.01377	3.04131	· · ·	0.12559	0.37676	· · ·	0.52499	0.34999	2	1	1.04100	8.24100
Pox4	P12	0.40000	0.60000	0.11890	2.43187	7.29560	0.00080	0.01396	0.04189	0.01600	0.08282	0.05522	2	1	1.39100	8.05100

SBS1054+36	P12	0.40092	0.60138	0.09700	2.06986	6.20957	· · ·	0.01862	0.05585	0.01360	0.10260	0.06840	2	1	1.36500	8.01200
SBS1211+54	P12	0.31121	0.46682	0.12200	1.59934	4.79801	· · ·	0.00731	0.02193	0.02800	0.06297	0.04198	2	1	1.71600	7.65300
IIIZw107A	P12	0.85126	1.27688	0.03140	1.24721	3.74163	· · ·	0.09549	0.28646	0.01020	0.21289	0.14193	2	1	1.08300	8.21300
IIIZw107B	P12	1.22479	1.83718	0.01970	0.97486	2.92457	· · ·	0.12301	0.36903	· · ·	0.38384	0.25589	2	1	1.01000	8.31500
Tol1457-26	P12	0.89549	1.34323	0.08680	1.86183	5.58549	· · ·	0.03090	0.09270	0.01340	0.18542	0.12361	2	1	1.36300	8.04900
Tol1457-26	P12	0.74827	1.12241	0.10600	1.73756	5.21268	· · ·	0.01896	0.05689	0.01760	0.18542	0.12361	2	1	1.53600	7.87000
Tol1457-26	P12	1.07910	1.61864	0.06800	1.51335	4.54006	· · ·	0.03459	0.10377	· · ·	0.28520	0.19013	2	1	1.34200	8.03300
ESO566-8	P12	1.02343	1.53515	· · ·	0.67755	2.03264	0.01230	0.39350	1.18049	0.00230	0.41224	0.27483	2	2	0.84800	8.45300
IC10HL90	P12	1.04006	1.56010	0.02420	1.03978	3.11933	· · ·	0.06822	0.20467	· · ·	0.16871	0.11248	2	1	1.05500	8.23600
IC10AP1	P12	0.68401	1.02601	0.02400	1.24148	3.72444	· · ·	0.04159	0.12476	· · ·	0.08998	0.05999	2	1	0.99600	8.29700
IC10AP2	P12	0.89137	1.33706	0.02000	0.96148	2.88444	· · ·	0.05754	0.17261	· · ·	0.19686	0.13124	2	1	1.01900	8.23600
IC10AP3	P12	0.82046	1.23070	0.03000	1.22163	3.66489	· · ·	0.05457	0.16370	· · ·	0.13745	0.09163	2	1	1.07500	8.21200
IC10AP4	P12	0.63250	0.94875	0.02500	1.14272	3.42816	· · ·	0.05714	0.17142	· · ·	0.10189	0.06793	2	1	1.03500	8.20800
IC10Fib90	P12	0.56762	0.85143	0.02700	1.27333	3.81998	· · ·	0.03258	0.09774	· · ·	0.07314	0.04876	2	1	1.02500	8.24200
IC10Fib92	P12	0.50823	0.76234	0.02900	1.33027	3.99081	· · ·	0.03026	0.09079	· · ·	0.07147	0.04765	2	1	1.03400	8.23200
M101NGC547	P12	0.40838	0.61256	0.09350	2.24874	6.74623	0.00320	0.02494	0.07483	0.01620	0.11406	0.07604	2	1	1.30100	8.10200
IC10no120	P12	0.19367	0.29050	0.01810	1.23010	3.69030	· · ·	0.05780	0.17340	· · ·	0.10073	0.06715	2	1	0.91900	8.31000
NGC2403-13	P12	0.71131	1.06697	0.03720	1.18288	3.54863	· · ·	0.05623	0.16868	· · ·	0.18414	0.12276	2	1	1.17000	8.06900
KISSR396	P12	0.99554	1.49331	0.06900	1.38656	4.15969	· · ·	0.02729	0.08186	0.01900	0.20997	0.13998	2	1	1.40100	7.94600
KISSR675	P12	0.50706	0.76059	0.11000	1.87906	5.63717	· · ·	0.01828	0.05484	· · ·	0.14593	0.09729	2	1	1.50600	7.88200
KISSR1194	P12	0.81858	1.22787	0.09200	1.71372	5.14116	· · ·	0.02890	0.08671	0.02100	0.20237	0.13491	2	1	1.44800	7.94200
KISSR1752	P12	0.43658	0.65486	0.09100	1.18834	3.56501	· · ·	0.01164	0.03492	0.01700	0.11173	0.07448	2	1	1.71900	7.57100
KISSR1778	P12	1.11959	1.67939	0.04000	0.95927	2.87780	· · ·	0.04655	0.13966	0.03500	0.33508	0.22339	2	1	1.30100	7.96400
KISSR1845	P12	0.97064	1.45597	0.07600	1.75768	5.27304	· · ·	0.03556	0.10667	0.01700	0.21936	0.14624	2	1	1.32100	8.07800
SBS0335-05	P12	0.10211	0.15316	0.11100	1.16129	3.48386	· · ·	0.00399	0.01197	· · ·	0.02158	0.01439	2	1	1.94500	7.36000
NGC6822X	P12	0.88728	1.33092	0.05000	1.44192	4.32575	· · ·	0.03326	0.09978	· · ·	0.13187	0.08791	2	1	1.21200	8.11400
Mrk59no1	P12	0.43457	0.65186	0.09160	2.02740	6.08221	· · ·	0.01629	0.04887	· · ·	0.10073	0.06715	2	1	1.34600	8.02600
Mrk59no2	P12	0.83188	1.24782	0.05500	1.29402	3.88205	· · ·	0.04591	0.13774	· · ·	0.20804	0.13869	2	1	1.31200	7.97600
NGC1313no7	P12	1.45231	2.17847	0.03890	1.18016	3.54047	· · ·	0.05915	0.17744	· · ·	0.21045	0.14030	2	1	1.19000	8.17500
IIZw40ld86	P12	0.21580	0.32371	0.11150	2.55823	7.67470	· · ·	0.01396	0.04189	· · ·	0.04679	0.03119	2	1	1.32600	8.10300
NGC3310C	P12	1.26491	1.89737	0.02500	0.81459	2.44378	· · ·	0.18278	0.54835	0.01400	0.32972	0.21982	2	3	0.93400	8.39500
NGC2366NGC	P12	0.23018	0.34526	0.13490	2.35472	7.06417	· · ·	0.00765	0.02296	· · ·	0.04562	0.03041	2	1	1.49200	7.93700
NGC3109no1	P12	0.91635	1.37452	0.05000	0.82213	2.46639	· · ·	0.03655	0.10966	· · ·	0.20378	0.13585	2	1	1.53400	7.69800
NGC3109no1	P12	0.65172	0.97758	0.06000	1.14272	3.42816	· · ·	0.04325	0.12974	· · ·	0.28784	0.19189	2	1	1.43300	7.80100
IIZw71B	P12	1.64839	2.47259	0.03000	0.79605	2.38815	· · ·	0.07779	0.23338	· · ·	0.39008	0.26005	2	1	1.25200	8.07000
HS1312+350	P12	1.04486	1.56730	0.07000	1.63659	4.90977	· · ·	0.03655	0.10966	· · ·	0.17995	0.11997	2	1	1.31600	8.07300
HS1330+365	P12	0.74483	1.11725	0.09000	1.62907	4.88721	· · ·	0.02992	0.08976	· · ·	0.20997	0.13998	2	1	1.46700	7.90000
A1228+12	P12	0.37073	0.55610	0.10280	1.52034	4.56101	· · ·	0.00998	0.02993	· · ·	0.09250	0.06167	2	1	1.61300	7.70800
VV131(a)	P12	0.55726	0.83589	0.13500	2.00882	6.02645	· · ·	0.01396	0.04189	· · ·	0.08693	0.05795	2	1	1.60900	7.84200
VV531(e)	P12	1.23612	1.85418	0.03700	1.27040	3.81120	· · ·	0.07412	0.22236	· · ·	0.27049	0.18033	2	1	1.13900	8.21600
HS0822+354	P12	0.12248	0.18372	0.10260	1.18834	3.56501	· · ·	0.00333	0.00998	· · ·	0.02637	0.01758	2	1	1.83400	7.43000
DDO68knot1	P12	0.21780	0.32670	0.05700	0.62365	1.87095	· · ·	0.00532	0.01596	· · ·	0.03063	0.02042	2	1	1.89500	7.19100
HS2134+040	P12	0.20944	0.31416	0.13100	1.31807	3.95422	· · ·	0.00632	0.01897	· · ·	0.04799	0.03199	2	1	1.99100	7.41500
M101NGC545	P12	0.57818	0.86726	0.08710	2.24874	6.74623	0.00130	0.02460	0.07380	0.01260	0.08693	0.05795	2	1	1.26500	8.15900
M101NGC546	P12	0.98188	1.47283	0.01410	1.07632	3.22895	0.00300	0.10279	0.30836	0.01020	0.11753	0.07835	2	1	0.89000	8.47800
ESO245-G00	P12	1.10678	1.66016	0.05500	1.07137	3.21411	· · ·	0.02296	0.06887	· · ·	0.25713	0.17142	2	1	1.42000	7.88400
M101NGC544	P12	0.77994	1.16991	0.02300	1.16397	3.49190	· · ·	0.07744	0.23231	· · ·	0.17830	0.11887	2	1	1.00300	8.28700
M101NGC545	P12	1.30335	1.95502	0.02200	1.11928	3.35785	0.00300	0.07815	0.23446	· · ·	0.18414	0.12276	2	1	1.00100	8.37200
M101NGC546	P12	1.18320	1.77481	0.02800	1.08128	3.24385	· · ·	0.09374	0.28123	· · ·	0.20472	0.13648	2	1	1.09400	8.22200
M101NGC547	P12	0.46351	0.69527	0.09300	2.25912	6.77737	0.00300	0.02128	0.06384	· · ·	0.09123	0.06082	2	1	1.29500	8.11700

M101Searle	P12	0.65172	0.97758	0.03600	1.53088	4.59263	· · ·	0.03793	0.11378	· · ·	0.12946	0.08631	2	1	1.06000	8.27000
M101NGC547	P12	0.52852	0.79278	0.10000	2.31707	6.95122	· · ·	0.02027	0.06082	· · ·	0.08456	0.05637	2	1	1.32000	8.11100
M101NGC547	P12	1.19966	1.79950	0.06200	1.30299	3.90896	· · ·	0.04325	0.12974	· · ·	0.28784	0.19189	2	1	1.37400	7.98500
M101NGC547	P12	0.81670	1.22504	0.05400	1.53088	4.59263	· · ·	0.05320	0.15961	· · ·	0.16186	0.10791	2	1	1.22100	8.11000
M101NGC547	P12	0.64426	0.96639	0.06400	1.97670	5.93009	· · ·	0.03026	0.09079	· · ·	0.09844	0.06562	2	1	1.18200	8.20800
IZw18SE	P12	0.18623	0.27935	0.04400	0.57140	1.71420	· · ·	0.00432	0.01297	· · ·	0.04199	0.02799	2	1	1.72500	7.23800
IZw18NW	P12	0.10570	0.15854	0.06200	0.64854	1.94563	· · ·	0.00266	0.00798	· · ·	0.02158	0.01439	2	1	1.94600	7.13000
ESO471-G06	P12	0.82806	1.24208	0.05000	0.88296	2.64887	· · ·	0.03258	0.09774	· · ·	0.18414	0.12276	2	1	1.48400	7.73100
ESO473-G24	P12	0.44367	0.66550	0.05800	0.76197	2.28592	· · ·	0.01531	0.04593	· · ·	0.07197	0.04798	2	1	1.71400	7.43500
M81no81	P12	1.68291	2.52436	0.01500	0.36808	1.10423	0.01000	0.31546	0.94637	· · ·	0.35412	0.23608	2	2	0.85400	8.48900
M81no123	P12	1.49989	2.24984	· · ·	0.32280	0.96841	0.00800	0.26604	0.79811	0.01300	0.18078	0.12052	2	2	0.82900	8.48000
Tol0341-40	P12	0.69512	1.04268	0.10670	2.20770	6.62310	· · ·	0.01828	0.05484	· · ·	0.12250	0.08167	2	1	1.38400	8.06000
IIZw40	P12	0.17663	0.26494	0.09400	2.58786	7.76357	· · ·	0.01794	0.05383	· · ·	0.06240	0.04160	2	1	1.23400	8.19000
Tol0633-41	P12	0.83572	1.25358	0.06580	1.94062	5.82185	· · ·	0.04255	0.12766	· · ·	0.15601	0.10401	2	1	1.20200	8.20700
Tol1004-29	P12	0.91424	1.37136	0.04830	1.70192	5.10577	· · ·	0.03758	0.11274	· · ·	0.11459	0.07639	2	1	1.12800	8.25900
Tol1008-28	P12	0.38642	0.57963	0.11000	2.66036	7.98107	· · ·	0.02729	0.08186	· · ·	0.10572	0.07048	2	1	1.29800	8.16600
Fairall30	P12	0.52127	0.78190	0.09100	2.13767	6.41300	· · ·	0.02460	0.07380	· · ·	0.12250	0.08167	2	1	1.31200	8.08800
Tol1116-32	P12	0.83572	1.25358	0.03740	1.69410	5.08231	· · ·	0.03062	0.09185	· · ·	0.06717	0.04478	2	1	1.03800	8.35900
UM439	P12	0.33967	0.50951	0.12520	2.57004	7.71012	· · ·	0.01265	0.03794	· · ·	0.09250	0.06167	2	1	1.38800	8.06700
UM461	P12	0.18200	0.27299	0.15700	2.13767	6.41300	· · ·	0.00632	0.01897	· · ·	0.04317	0.02878	2	1	1.68200	7.76500
UM462SW	P12	0.65172	0.97758	0.10100	1.88339	5.65017	· · ·	0.01963	0.05889	· · ·	0.10572	0.07048	2	1	1.44800	7.94800
Tol1156-34	P12	0.31409	0.47114	0.12390	2.69737	8.09210	· · ·	0.01828	0.05484	· · ·	0.06953	0.04635	2	1	1.35400	8.11200
Tol1304-38	P12	0.52609	0.78913	0.10020	2.24874	6.74623	· · ·	0.02529	0.07587	· · ·	0.11699	0.07799	2	1	1.33800	8.08400
Tol1400-41	P12	0.38642	0.57963	0.12100	2.28003	6.84008	· · ·	0.01429	0.04286	· · ·	0.07554	0.05036	2	1	1.44100	7.98500
1249+493	P12	0.42762	0.64143	0.10600	1.45191	4.35573	· · ·	0.01096	0.03289	· · ·	0.07433	0.04955	2	1	1.67800	7.66200
1331+493S	P12	0.94202	1.41303	0.04500	0.99070	2.97209	· · ·	0.03459	0.10377	· · ·	0.27871	0.18581	2	1	1.34800	7.89400
1415+437	P12	0.42370	0.63555	0.08600	0.99070	2.97209	· · ·	0.01096	0.03289	· · ·	0.08998	0.05999	2	1	1.84100	7.44000
1533+469	P12	0.89962	1.34943	0.07700	1.61414	4.84241	0.01000	0.05116	0.15348	· · ·	0.31200	0.20800	2	1	1.37600	7.99500
S1415+4371	P12	0.42175	0.63263	0.08800	1.17203	3.51610	· · ·	0.01230	0.03690	· · ·	0.09123	0.06082	2	1	1.70200	7.57300
S1415+4371	P12	0.33271	0.49906	0.08700	1.22163	3.66489	· · ·	0.00964	0.02891	· · ·	0.07382	0.04921	2	1	1.65700	7.59400
M101NGC546	P12	0.85518	1.28278	0.01480	1.00448	3.01343	0.00370	0.12076	0.36229	· · ·	0.13494	0.08996	2	1	0.92000	8.38700
M101NGC547	P12	0.52730	0.79095	0.09120	2.09865	6.29595	0.00170	0.02958	0.08873	· · ·	0.10572	0.07048	2	2	1.20800	8.18400
NGC55	P12	0.75173	1.12759	0.04000	1.39939	4.19818	0.00200	0.03655	0.10966	· · ·	0.15002	0.10001	2	2	1.17200	8.12500
UGC191-1	P12	1.19415	1.79123	0.04800	1.35189	4.05566	· · ·	0.04560	0.13679	· · ·	0.22190	0.14793	2	1	1.22400	8.13300
UGC191-2	P12	1.27956	1.91934	0.03500	1.06155	3.18465	· · ·	0.07708	0.23124	· · ·	0.35494	0.23662	2	1	1.19000	8.12500
UGC5716-2	P12	1.21356	1.82033	0.02900	0.69975	2.09924	· · ·	0.04560	0.13679	· · ·	0.41035	0.27356	2	1	1.29800	7.92300
UGCA357-1	P12	0.99554	1.49331	0.04100	1.18016	3.54047	· · ·	0.03357	0.10071	· · ·	0.17954	0.11969	2	1	1.21400	8.07600
NGC1232+13	P12	0.75520	1.13279	0.03100	1.31202	3.93606	· · ·	0.07851	0.23554	· · ·	0.15002	0.10001	2	1	1.06100	8.23900
NGC2805-06	P12	1.45566	2.18349	0.03350	1.13747	3.41241	· · ·	0.08749	0.26246	· · ·	0.31561	0.21041	2	1	1.14300	8.22000
NGC	P12	1.24469	1.86703	0.03000	1.16934	3.50801	· · ·	0.06744	0.20233	· · ·	0.26801	0.17867	2	1	1.09000	8.25600
IC2458+002	P12	0.98869	1.48303	0.06790	1.61414	4.84241	· · ·	0.04159	0.12476	· · ·	0.17830	0.11887	2	1	1.30700	8.06900
IC2458-033	P12	0.49211	0.73816	0.06820	1.58467	4.75402	· · ·	0.01896	0.05689	· · ·	0.09889	0.06593	2	1	1.31900	7.97200
NGC5457-45	P12	1.19966	1.79950	0.02200	0.99986	2.99959	· · ·	0.06713	0.20140	· · ·	0.20804	0.13869	2	1	1.03700	8.27900
UGCA292no1	P12	0.33347	0.50021	0.03800	0.47967	1.43900	· · ·	0.00998	0.02993	· · ·	0.05523	0.03682	2	1	1.75200	7.23800
UGC685/A+0	P12	0.81107	1.21661	0.08900	1.80692	5.42077	· · ·	0.03228	0.09684	· · ·	0.22864	0.15243	2	1	1.39500	8.00100
UGC685/B+0	P12	0.82236	1.23353	0.08400	1.80277	5.40831	· · ·	0.03655	0.10966	· · ·	0.22602	0.15068	2	1	1.36200	8.03000
UGC1104/B+	P12	1.11189	1.66783	0.05300	1.14272	3.42816	· · ·	0.02328	0.06983	· · ·	0.19282	0.12855	2	1	1.36000	7.95000
UGC1104/B+	P12	1.27368	1.91052	0.04500	0.94611	2.83832	· · ·	0.03162	0.09486	· · ·	0.27049	0.18033	2	1	1.37400	7.92400
UGC2023/B-	P12	1.14831	1.72247	0.03900	0.99527	2.98580	· · ·	0.05714	0.17142	· · ·	0.28389	0.18926	2	1	1.27100	8.00600
UGC2023/C-	P12	0.78715	1.18073	0.05000	1.33027	3.99081	· · ·	0.04092	0.12276	· · ·	0.15891	0.10594	2	1	1.25000	8.03500

UGC3647/A-	P12	0.68716	1.03075	0.05100	1.48573	4.45719	· · ·	0.04187	0.12562	· · ·	0.14526	0.09684	2	1	1.20800	8.09200
C007-025/A	P12	0.48313	0.72469	0.08100	1.44857	4.34572	· · ·	0.01629	0.04887	· · ·	0.11645	0.07764	2	1	1.47400	7.81100
C007-025/A	P12	0.49666	0.74499	0.06500	1.33641	4.00923	· · ·	0.01862	0.05585	· · ·	0.10260	0.06840	2	1	1.38800	7.85400
UGCA292/C+	P12	0.36480	0.54721	0.02900	0.44253	1.32758	· · ·	0.01364	0.04093	· · ·	0.06182	0.04122	2	1	1.58800	7.33400
UGC9992/A+	P12	0.77635	1.16453	0.03800	0.93959	2.81878	· · ·	0.04988	0.14964	· · ·	0.34686	0.23124	2	1	1.28700	7.90100
UGC12713/A	P12	0.84930	1.27395	0.03900	0.81835	2.45505	· · ·	0.02460	0.07380	· · ·	0.17995	0.11997	2	1	1.37500	7.80500
GR8-019-01	P12	0.81294	1.21941	0.04500	0.69975	2.09924	· · ·	0.02594	0.07781	0.01600	0.15316	0.10211	2	1	1.57500	7.60700
GR8+008-01	P12	0.86310	1.29465	0.03800	0.64260	1.92780	· · ·	0.03126	0.09377	0.01400	0.16755	0.11170	2	1	1.51300	7.64700
M33NGC604	P12	0.86111	1.29167	0.00750	0.69014	2.07043	· · ·	0.11141	0.33424	· · ·	0.17028	0.11352	2	1	0.84700	8.42100
VCC1313	P12	0.44062	0.66092	0.09500	1.54149	4.62446	· · ·	0.01030	0.03091	· · ·	0.12055	0.08036	2	1	1.54300	7.77400
VCC848	P12	1.36477	2.04716	0.04100	1.06645	3.19935	· · ·	0.06515	0.19546	· · ·	0.36826	0.24550	2	1	1.26000	8.06900
NGC300no15	P12	1.15894	1.73841	0.04400	1.42870	4.28609	· · ·	0.04120	0.12361	· · ·	0.18078	0.12052	2	1	1.16100	8.20900
NGC5253no3	P12	0.49211	0.73816	0.07500	2.09865	6.29595	· · ·	0.08316	0.24949	· · ·	0.16149	0.10766	2	1	1.22600	8.16000
NGC5253no4	P12	0.59574	0.89362	0.06700	1.93170	5.79510	· · ·	0.06323	0.18970	· · ·	0.13432	0.08955	2	1	1.21300	8.16100
NGC5253no5	P12	1.37107	2.05661	0.03600	1.15595	3.46786	· · ·	0.07655	0.22965	· · ·	0.40940	0.27294	2	1	1.16500	8.18500
NGC3359no3	P12	0.82046	1.23070	0.02800	1.34878	4.04633	· · ·	0.03326	0.09978	· · ·	0.09664	0.06443	2	1	1.01800	8.31600
NGC3359no1	P12	1.07910	1.61864	0.02700	0.89730	2.69191	· · ·	0.06652	0.19955	· · ·	0.27615	0.18410	2	1	1.15100	8.09400
NGC4449	PMC09r23	1.20800	1.81200	0.01700	1.21033	3.63100	· · ·	0.15233	0.45700	0.0	0.14500	0.10500	1	1	0.90809	8.51507
H40	PMC09r21	1.07680	1.61520	0.00300	0.27733	0.83200	0.00600	0.21033	0.63100	0.0	0.14500	0.10700	1	1	0.84663	8.32522
NGC7714	PMC09r28	0.91200	1.36800	0.01600	0.54000	1.62000	· · ·	0.35000	1.05000	0.0	0.27000	0.27700	1	1	1.14641	7.95750
N160A2	PMC09r37	0.98400	1.47600	0.01800	1.27367	3.82100	· · ·	0.06100	0.18300	0.0	0.11700	0.09300	1	1	0.90965	8.49051
HS1728+5655	PMC09r29	0.84400	1.26600	0.03000	1.66667	5.00000	· · ·	0.08333	0.25000	0.0	· · ·	0.23000	1	1	0.97541	8.44425
TO1327-380	PMC09r27	1.37200	2.05800	0.03500	1.97900	5.93700	· · ·	0.01767	0.05300	0.0	0.06100	0.04000	1	1	0.97029	8.56952
Tol0104-388	PMC09r41	1.68120	2.52180	0.07500	1.19300	3.57900	· · ·	0.07367	0.22100	0.0	0.29700	0.21900	1	1	1.55932	7.89269
UM238	PMC09r41	0.84680	1.27020	0.11500	1.66200	4.98600	· · ·	0.02867	0.08600	0.0	0.17200	0.13400	1	1	1.63424	7.80490
Mrk35	PMC09r53	1.00360	1.50540	0.02700	1.35200	4.05600	0.00400	0.06533	0.19600	0.0	0.15300	0.12400	1	1	1.00671	8.36191
HS1203+3636A	PMC09r53	1.24720	1.87080	0.02600	1.06533	3.19600	0.00500	0.05833	0.17500	0.0	0.17900	0.12900	1	1	1.07316	8.25465
VS51	PMC09r10	0.91200	1.36800	0.00500	0.58000	1.74000	0.00800	0.09667	0.29000	0.0	0.20000	0.14000	1	1	0.79965	8.48462
RCW16-1	PMC09r11	0.93760	1.40640	0.01100	0.96133	2.88400	0.00500	0.15233	0.45700	0.0	0.16200	0.12600	1	1	0.85913	8.49521
30Dor	PMC09r11	0.44800	0.67200	0.03600	1.96267	5.88800	· · ·	0.02167	0.06500	0.0	0.05000	0.04000	1	1	0.98094	8.43369
Orion	PMC09r11	0.40000	0.60000	0.01300	1.15567	3.46700	0.00500	0.13267	0.39800	0.0	0.01900	0.03400	1	1	0.85530	8.44782
VCC1374	PMC09r35	1.20280	1.80420	0.01500	0.99833	2.99500	· · ·	0.08067	0.24200	0.0	0.41300	0.29400	1	1	0.92544	8.44040
VS35	PMC09r10	0.98400	1.47600	0.00400	0.45667	1.37000	0.00900	0.19267	0.57800	0.0	0.28000	0.19800	1	1	0.80277	8.45084
NGC3690	PMC09r28	1.04000	1.56000	0.02200	0.42333	1.27000	· · ·	0.32267	0.96800	0.0	0.28800	0.21600	1	1	1.42913	7.68616
N160A1	PMC09r37	0.66200	0.99300	0.02400	1.41200	4.23600	0.00300	0.06233	0.18700	0.0	0.12700	0.10100	1	1	0.95899	8.38803
IC131	PMC09r25	0.83600	1.25400	0.02100	1.29400	3.88200	· · ·	0.11933	0.35800	0.0	0.20500	0.16600	1	1	0.94613	8.41155
KISSR87	PMC09r52	0.75800	1.13700	0.02800	1.49000	4.47000	· · ·	0.07567	0.22700	0.0	0.18900	0.14000	1	1	0.98814	8.37731
N3310E	PMC09r5	1.25200	1.87800	0.01200	0.67333	2.02000	· · ·	0.19667	0.59000	0.0	0.35000	0.27000	1	1	0.97254	8.29888
UM311	PMC09r27	0.59640	0.89460	0.02400	1.36333	4.09000	· · ·	0.05133	0.15400	0.0	0.13100	0.08800	1	1	0.96897	8.34971
Tol0306-405	PMC09r41	0.95400	1.43100	0.07300	1.74167	5.22500	· · ·	0.04700	0.14100	0.0	0.24300	0.20900	1	1	1.30591	8.08664
VCC1437	PMC09r35	1.92640	2.88960	0.01400	0.82733	2.48200	· · ·	0.17167	0.51500	0.0	0.36100	0.27600	1	1	0.95774	8.47007
VCC1699	PMC09r35	0.50400	0.75600	0.04100	1.84367	5.53100	· · ·	0.02633	0.07900	0.0	0.10400	0.07700	1	1	1.04128	8.33314
KISSR286	PMC09r52	0.82120	1.23180	0.03700	1.42100	4.26300	· · ·	0.05100	0.15300	0.0	0.21300	0.15300	1	1	1.09655	8.22814
N4A	PMC09r37	0.60880	0.91320	0.02600	1.43333	4.30000	0.00400	0.04433	0.13300	0.0	0.09100	0.06900	1	1	0.97768	8.35511
UM311	PMC09r2	0.72000	1.08000	0.02300	1.32500	3.97500	· · ·	0.06000	0.18000	0.0	0.16700	0.12400	1	1	0.96495	8.36926
NGC588	PMC09r25	0.59280	0.88920	0.03100	1.54900	4.64700	· · ·	0.02667	0.08000	0.0	0.09000	0.07000	1	1	1.00735	8.33457
N7793-W11	PMC09r9	1.26480	1.89720	0.01000	0.83733	2.51200	· · ·	0.06800	0.20400	0.0	0.14800	0.10000	1	1	0.86891	8.50686
J1509	PMC09r57	0.61280	0.91920	0.04200	1.66467	4.99400	· · ·	0.04633	0.13900	0.0	0.19700	0.14900	1	1	1.08503	8.25788
N604	PMC09r4	0.86080	1.29120	0.00500	0.69233	2.07700	· · ·	0.11167	0.33500	0.0	0.16600	0.11800	1	1	0.76650	8.58060
VS24	PMC09r10	0.96800	1.45200	0.00400	0.42000	1.26000	0.00500	0.14567	0.43700	0.0	0.20200	0.14500	1	1	0.81960	8.40036

N5461	PMC09r21	0.98200	1.47300	0.01400	1.07867	3.23600	0.00300	0.10300	0.30900	0.0	0.10700	0.08900	1	1	0.88857	8.48127
H40	PMC09r21	1.07680	1.61520	0.00300	0.27733	0.83200	0.00600	0.21033	0.63100	0.0	0.14500	0.10700	1	1	0.84663	8.32522
NGC4449	PMC09r23	1.20800	1.81200	0.01700	1.21033	3.63100	· · ·	0.15233	0.45700	0.0	0.14500	0.10500	1	1	0.90809	8.51508
NGC7714	PMC09r28	0.91200	1.36800	0.01600	0.54000	1.62000	· · ·	0.35000	1.05000	0.0	0.27000	0.27700	1	1	1.14642	7.95750
H1013	PMC09r56	0.88400	1.32600	0.00200	0.34000	1.02000	0.00600	0.23667	0.71000	0.0	0.17800	0.12000	1	1	0.73139	8.51917
N5236-16	PMC09r39	0.57600	0.86400	· · ·	0.04000	0.12000	0.00600	0.45000	1.35000	0.0	0.28000	0.23000	1	2	0.54841	8.61282
N1232-05	PMC09r39	1.01200	1.51800	· · ·	0.33333	1.00000	0.00500	0.27667	0.83000	0.0	0.34000	0.25000	1	2	0.63772	8.78036
H40	PMC09r21	1.07680	1.61520	0.00300	0.27733	0.83200	0.00600	0.21033	0.63100	0.0	0.14500	0.10700	1	2	0.80779	8.39448
CCM57A	PMC09r38	0.41600	0.62400	· · ·	0.56200	1.68600	0.00500	0.23333	0.70000	0.0	0.20000	0.14000	1	2	0.69538	8.57515
N2997-05	PMC09r39	0.85200	1.27800	· · ·	0.27333	0.82000	0.00500	0.29000	0.87000	0.0	0.38000	0.27000	1	2	0.62284	8.74217
N1232CDT1	PMC09r14	0.59600	0.89400	· · ·	0.07633	0.22900	0.00400	0.34667	1.04000	0.0	0.35700	0.27400	1	2	0.51106	8.80506
CCM71A	PMC09r38	0.58800	0.88200	· · ·	0.15367	0.46100	0.00800	0.38667	1.16000	0.0	0.41000	0.28000	1	2	0.68298	8.39445
CCM57	PMC09r38	0.45600	0.68400	· · ·	0.05300	0.15900	0.00700	0.41333	1.24000	0.0	0.26000	0.19000	1	2	0.61731	8.35904
CCM57A	PMC09r38	0.41600	0.62400	· · ·	0.56200	1.68600	0.00500	0.23333	0.70000	0.0	0.20000	0.14000	1	2	0.69537	8.57517
Mrk35	PMC09r53	1.00360	1.50540	0.02700	1.35200	4.05600	0.00400	0.06533	0.19600	0.0	0.15300	0.12400	1	2	1.26031	8.06552
HS1203+3636A	PMC09r53	1.24720	1.87080	0.02600	1.06533	3.19600	0.00500	0.05833	0.17500	0.0	0.17900	0.12900	1	2	1.58595	7.78390
N1365-08	PMC09r39	0.68800	1.03200	· · ·	0.20000	0.60000	0.00700	0.28667	0.86000	0.0	0.30000	0.22000	1	2	0.74406	8.34074
VS51	PMC09r10	0.91200	1.36800	0.00500	0.58000	1.74000	0.00800	0.09667	0.29000	0.0	0.20000	0.14000	1	2	1.54628	7.61482
RCW16-1	PMC09r11	0.93760	1.40640	0.01100	0.96133	2.88400	0.00500	0.15233	0.45700	0.0	0.16200	0.12600	1	2	0.87171	8.47279
Orion	PMC09r11	0.40000	0.60000	0.01300	1.15567	3.46700	0.00500	0.13267	0.39800	0.0	0.01900	0.03400	1	2	0.94148	8.29744
VS35	PMC09r10	0.98400	1.47600	0.00400	0.45667	1.37000	0.00900	0.19267	0.57800	0.0	0.28000	0.19800	1	2	1.06624	8.04386
N160A1	PMC09r37	0.66200	0.99300	0.02400	1.41200	4.23600	0.00300	0.06233	0.18700	0.0	0.12700	0.10100	1	2	1.08544	8.21227
N4A	PMC09r37	0.60880	0.91320	0.02600	1.43333	4.30000	0.00400	0.04433	0.13300	0.0	0.09100	0.06900	1	2	1.64688	7.71085
VS24	PMC09r10	0.96800	1.45200	0.00400	0.42000	1.26000	0.00500	0.14567	0.43700	0.0	0.20200	0.14500	1	2	0.89343	8.27207
N1232CDT1	PMC09r14	0.59600	0.89400	· · ·	0.07633	0.22900	0.00400	0.34667	1.04000	0.0	0.35700	0.27400	1	2	0.51107	8.80503
N5461	PMC09r21	0.98200	1.47300	0.01400	1.07867	3.23600	0.00300	0.10300	0.30900	0.0	0.10700	0.08900	1	2	0.81685	8.61298
H40	PMC09r21	1.07680	1.61520	0.00300	0.27733	0.83200	0.00600	0.21033	0.63100	0.0	0.14500	0.10700	1	2	0.80781	8.39443
CCM10	PMC09r36	0.64800	0.97200	· · ·	0.06667	0.20000	0.00600	0.34667	1.04000	0.0	0.25600	0.18400	1	2	0.62405	8.48469
CCM10	PMC09r38	0.50400	0.75600	· · ·	0.04033	0.12100	0.00500	0.37333	1.12000	0.0	0.27000	0.19000	1	2	0.54961	8.56133
CCM53	PMC09r38	0.51600	0.77400	· · ·	0.11100	0.33300	0.00500	0.40000	1.20000	0.0	0.24000	0.17000	1	2	0.53140	8.74522
CCM54	PMC09r38	0.46000	0.69000	· · ·	0.13833	0.41500	0.00700	0.40667	1.22000	0.0	0.36000	0.27000	1	2	0.62233	8.46507
CCM57A	PMC09r38	0.41600	0.62400	· · ·	0.56200	1.68600	0.00500	0.23333	0.70000	0.0	0.20000	0.14000	1	2	0.69536	8.57520
CCM84A	PMC09r38	0.50000	0.75000	· · ·	0.28300	0.84900	0.00900	0.48000	1.44000	0.0	0.19000	0.15000	1	2	0.64966	8.54819
N1232-05	PMC09r39	1.01200	1.51800	· · ·	0.33333	1.00000	0.00500	0.27667	0.83000	0.0	0.34000	0.25000	1	2	0.63772	8.78038
N2997-05	PMC09r39	0.85200	1.27800	· · ·	0.27333	0.82000	0.00500	0.29000	0.87000	0.0	0.38000	0.27000	1	2	0.62283	8.74220
N5236-03	PMC09r39	0.83200	1.24800	· · ·	0.39333	1.18000	0.00700	0.32667	0.98000	0.0	0.25000	0.18000	1	2	0.69537	8.61324
N5236-16	PMC09r39	0.57600	0.86400	· · ·	0.04000	0.12000	0.00600	0.45000	1.35000	0.0	0.28000	0.23000	1	2	0.54842	8.61278
H1013	PMC09r56	0.88400	1.32600	0.00200	0.34000	1.02000	0.00600	0.23667	0.71000	0.0	0.17800	0.12000	1	2	0.75878	8.46060
MCG-01-54-016-001	CAL	1.53173	2.29760	0.04097	1.03736	3.11207	· · ·	0.04043	0.12129	· · ·	0.33503	0.23420	1	1	1.27553	8.09111
UGC00312-001	CAL	1.40396	2.10594	0.01528	0.97721	2.93163	· · ·	0.07796	0.23388	· · ·	0.36575	0.26859	1	1	0.93600	8.46614
UGC00312-004	CAL	1.22898	1.84347	0.01559	0.89272	2.67816	· · ·	0.08202	0.24606	· · ·	0.37432	0.26483	1	1	0.96658	8.37134
UGC00312-005	CAL	1.58914	2.38371	0.01781	0.79284	2.37851	· · ·	0.08554	0.25662	· · ·	0.46526	0.32776	1	1	1.04466	8.30821
UGC00312-008	CAL	1.20168	1.80252	0.03437	1.03935	3.11805	· · ·	0.06443	0.19330	· · ·	0.39190	0.27905	1	1	1.19253	8.11814
UGC00312-013	CAL	1.73077	2.59616	0.03342	0.63861	1.91582	· · ·	0.09667	0.29002	· · ·	0.45487	0.37560	1	1	1.43361	7.91154
UGC10796-001	CAL	1.25679	1.88518	0.03206	0.63696	1.91088	· · ·	0.10694	0.32083	· · ·	0.44233	0.30122	1	1	1.40933	7.83736
UGC12494-001	CAL	1.00259	1.50389	0.06407	1.55529	4.66588	· · ·	0.03996	0.11989	· · ·	0.24384	0.16724	1	1	1.29698	8.07975
NGC3991-001	CAL	1.15138	1.72707	0.01821	0.91130	2.73390	· · ·	0.07900	0.23701	· · ·	0.29469	0.21499	1	1	1.00692	8.30381
NGC3991-002	CAL	1.59239	2.38859	0.01625	0.72710	2.18129	· · ·	0.09883	0.29648	· · ·	0.43034	0.30260	1	1	1.04296	8.29743
UGC08733-004	CAL	0.97687	1.46531	0.02059	0.75023	2.25068	· · ·	0.08770	0.26310	· · ·	0.40730	0.26871	1	1	1.11637	8.08782
NGC7489-002	CAL	1.34193	2.01289	0.04331	1.06176	3.18529	· · ·	0.08812	0.26436	· · ·	0.36676	0.18392	1	1	1.29185	8.04886

NGC3991-007	CAL	2.07341	3.11012	0.01283	0.58895	1.76685	· · ·	0.12281	0.36843	· · ·	0.54291	0.38690	1	1	1.03439	8.36138
UGC00312-007	CAL	1.46099	2.19148	0.01800	0.93961	2.81882	· · ·	0.07905	0.23716	· · ·	0.43961	0.31596	1	1	0.99386	8.38373
UGC10331-004	CAL	2.31397	3.47095	0.01854	0.70699	2.12098	· · ·	0.12849	0.38547	· · ·	0.51040	0.35946	1	1	1.09921	8.33786
NGC7489-007	CAL	1.54979	2.32468	0.07980	1.28991	3.86974	· · ·	0.08813	0.26440	· · ·	0.31458	0.12548	1	1	1.54745	7.91477
17	ZB12	0.57200	0.85800	0.00400	0.40000	1.14000	· · ·	0.20000	0.63000	· · ·	0.46832	0.32738	1	1	0.83735	8.22262
25	ZB12	0.63200	0.94800	0.01300	0.86000	2.51000	· · ·	0.10700	0.32000	· · ·	1.87625	1.37780	1	1	0.93181	8.27101
26	ZB12	0.92000	1.38000	0.01200	0.75000	2.20000	· · ·	0.16300	0.48000	· · ·	1.11037	0.78558	1	1	0.94613	8.28456
35	ZB12	0.60000	0.90000	0.01350	1.04000	3.20000	· · ·	0.11000	0.34000	· · ·	0.72211	0.50871	1	1	0.88343	8.41185
2	ZB12	0.84000	1.26000	· · ·	0.22000	0.58000	0.00500	0.26000	0.81000	· · ·	0.46832	0.32738	1	2	0.64785	8.62368
3	ZB12	0.68000	1.02000	· · ·	0.15600	0.44000	0.00690	0.26700	0.80000	· · ·	1.87625	1.37780	1	2	0.76585	8.25687
17	ZB12	0.57200	0.85800	· · ·	0.40000	1.14000	0.00430	0.20000	0.63000	· · ·	1.11037	0.78558	1	2	0.68268	8.55882
19	ZB12	0.63600	0.95400	· · ·	0.11700	0.34000	0.00510	0.32000	0.97000	· · ·	0.72211	0.50871	1	2	0.59584	8.60688
25	ZB12	0.63200	0.94800	· · ·	0.86000	2.51000	0.00400	0.10700	0.32000	· · ·	0.23475	0.16715	1	2	0.93705	8.26267
26	ZB12	0.92000	1.38000	· · ·	0.75000	2.20000	0.00660	0.16300	0.48000	· · ·	0.17980	0.14847	1	2	0.98722	8.22389
33	ZB12	0.88000	1.32000	· · ·	0.20500	0.59000	0.00700	0.24000	0.71000	· · ·	0.41818	0.28478	1	2	0.82100	8.26831
34	ZB12	1.15600	1.73400	· · ·	0.59000	1.80000	0.01600	0.32000	0.98000	· · ·	0.18076	0.12397	1	2	1.09866	8.09232
35	ZB12	0.60000	0.90000	· · ·	1.04000	3.20000	0.00450	0.11000	0.34000	· · ·	5.47916	3.99724	1	2	0.97254	8.26696
2	ZB12	2.10000	1.26000	· · ·	0.22000	0.58000	· · ·	0.26000	0.81000	0.00600	0.46832	0.32738	1	3	0.76127	8.36716
17	ZB12	1.43000	0.85800	· · ·	0.40000	1.14000	· · ·	0.20000	0.63000	0.00970	1.87625	1.37780	1	3	0.86330	8.17598
25	ZB12	1.58000	0.94800	· · ·	0.86000	2.51000	· · ·	0.10700	0.32000	0.01210	1.11037	0.78558	1	3	0.95063	8.24146
26	ZB12	2.30000	1.38000	· · ·	0.75000	2.20000	· · ·	0.16300	0.48000	0.01370	0.72211	0.50871	1	3	0.97593	8.24016
35	ZB12	1.50000	0.90000	· · ·	1.04000	3.20000	· · ·	0.11000	0.34000	0.01450	0.23475	0.16715	1	3	1.21823	7.96176
1a	BRE12	1.04000	1.56000	0.05900	1.71667	5.15000	· · ·	0.06667	0.20000	· · ·	0.28000	0.18667	3	1	1.20961	8.18895
12a	BRE12	0.76400	1.14600	0.05800	1.71667	5.15000	· · ·	0.04667	0.14000	· · ·	0.18000	0.12000	3	1	1.20200	8.15681
55a	BRE12	1.37600	2.06400	0.02300	0.77000	2.31000	· · ·	0.08667	0.26000	· · ·	0.35000	0.23333	3	1	1.14970	8.12230
57a	BRE12	1.14400	1.71600	0.02400	0.97000	2.91000	· · ·	0.09333	0.28000	· · ·	0.38000	0.25333	3	1	1.07804	8.20941
1b	BRE12	1.04400	1.56600	0.15200	3.05000	9.15000	· · ·	0.06000	0.18000	· · ·	0.42000	0.28000	3	1	1.40336	8.19124
16b	BRE12	1.18800	1.78200	0.01700	0.77000	2.31000	· · ·	0.06333	0.19000	· · ·	0.30000	0.20000	3	1	1.03889	8.21968
20b	BRE12	1.15600	1.73400	0.01700	0.83667	2.51000	· · ·	0.12333	0.37000	· · ·	0.69000	0.46000	3	1	1.01213	8.26585
46b	BRE12	0.64800	0.97200	0.02000	1.33000	3.99000	· · ·	0.06000	0.18000	· · ·	0.17000	0.11333	3	1	0.92566	8.41950
49b	BRE12	1.10400	1.65600	0.03300	1.13333	3.40000	· · ·	0.05000	0.15000	· · ·	0.25000	0.16667	3	1	1.13943	8.16516
51b	BRE12	0.66400	0.99600	0.02500	1.19000	3.57000	· · ·	0.05000	0.15000	· · ·	0.22000	0.14667	3	1	1.02270	8.24242
52b	BRE12	0.96400	1.44600	0.01800	1.03333	3.10000	· · ·	0.04667	0.14000	· · ·	0.22000	0.14667	3	1	0.96595	8.34331
53b	BRE12	0.64000	0.96000	0.02800	1.48333	4.45000	· · ·	0.03667	0.11000	· · ·	0.17000	0.11333	3	1	0.98945	8.35425
60b	BRE12	1.12800	1.69200	0.03100	1.32667	3.98000	· · ·	0.07000	0.21000	· · ·	0.46000	0.30667	3	1	1.05801	8.30741
62b	BRE12	1.26800	1.90200	0.02100	0.89333	2.68000	· · ·	0.07667	0.23000	· · ·	0.40000	0.26667	3	1	1.06008	8.23724
63b	BRE12	1.17600	1.76400	0.03500	1.24000	3.72000	· · ·	0.05333	0.16000	· · ·	0.30000	0.20000	3	1	1.12717	8.21326
64b	BRE12	1.09200	1.63800	0.03500	1.17333	3.52000	· · ·	0.05333	0.16000	· · ·	0.27000	0.18000	3	1	1.14912	8.16054
NGC3359-2	ZaB11	0.98000	1.47000	0.01700	1.30000	3.89000	· · ·	0.06000	0.18000	· · ·	0.20000	0.16000	1	1	0.89026	8.52847
NGC3359-3	ZaB11	0.82000	1.23000	0.02800	1.38000	4.06000	· · ·	0.03333	0.10000	· · ·	0.09300	0.06800	1	1	1.01545	8.32177
NGC3359-13	ZaB11	1.08000	1.62000	0.02700	0.91000	2.70000	· · ·	0.06667	0.20000	· · ·	0.27000	0.19000	1	1	1.14931	8.09746
NGC1313-14	Had07	0.68640	1.02960	0.03000	1.46400	4.20000	· · ·	0.03900	0.11700	· · ·	0.10700	0.08000	1	1	1.02457	8.29830
NGC1313-85	Had07	0.57560	0.86340	0.03400	1.65900	4.88700	· · ·	0.03200	0.09600	· · ·	0.11100	0.08300	1	1	1.01835	8.33550
NGC1313-H1	Had07	1.22800	1.84200	0.03300	1.04100	3.17000	· · ·	0.07633	0.22900	· · ·	0.22500	0.17100	1	1	1.16857	8.13752
NGC1313-H2	Had07	1.01880	1.52820	0.05200	1.23100	3.66600	· · ·	0.04533	0.13600	· · ·	0.14000	0.10600	1	1	1.31160	7.99416
NGC1313-H3	Had07	1.00680	1.51020	0.02900	1.27600	3.72400	· · ·	0.10933	0.32800	· · ·	0.47900	0.33100	1	1	1.05471	8.27713
NGC1313-H4	Had07	0.45760	0.68640	0.04500	1.86600	5.77500	· · ·	0.04567	0.13700	· · ·	0.14500	0.11100	1	1	1.05994	8.31477
MA1inner	Keh11	0.21862	0.32138	0.09000	2.07000	6.02000	· · ·	0.03000	0.06000	· · ·	0.08000	0.05000	1	1	1.33666	7.99911
HBW673	Keh11	1.36437	2.00563	0.18000	5.54000	16.63000	· · ·	0.26000	0.86000	· · ·	0.37000	0.23000	1	1	1.18362	8.63023
BCLMP651	Keh11	0.87045	1.27955	0.04700	1.47000	4.40000	· · ·	0.08500	0.24000	· · ·	0.17000	0.09000	1	1	1.17766	8.15094

IC4662-01	CrB09	0.33520	0.50280	0.07900	2.06300	6.04000	· · ·	0.02860	0.08580	· · ·	· · ·	· · ·	1	1	1.26796	8.08253
IC4662-02	CrB09	0.45560	0.68340	0.07400	1.98500	5.90600	· · ·	0.02860	0.08580	· · ·	· · ·	· · ·	1	1	1.24909	8.10972
IC4662-03	CrB09	0.69920	1.04880	0.07000	1.80400	5.28600	· · ·	0.02860	0.08580	· · ·	· · ·	· · ·	1	1	1.27420	8.08527
IC4662-04	CrB09	0.65440	0.98160	0.07400	2.02000	6.07800	· · ·	0.02860	0.08580	· · ·	· · ·	· · ·	1	1	1.23678	8.16020
NGC2537A	Ber12	1.36800	2.05200	0.01200	0.71000	2.14000	· · ·	0.15000	0.48000	0.01600	0.36000	0.27000	1	1	0.95570	8.35673
NGC4449A	Ber12	0.95600	1.43400	0.01900	1.15000	3.46000	· · ·	0.04800	0.16300	0.01400	0.18000	0.13000	1	1	0.94976	8.39531
KDG61-9	Cro09	0.51480	0.77220	0.06500	2.42200	7.29500	· · ·	0.07300	0.22100	· · ·	0.16600	0.10700	1	1	1.10576	8.35271
Garland-5	Cro09	0.82680	1.24020	0.06900	2.54800	7.57300	· · ·	0.13600	0.33600	· · ·	0.28700	0.19700	1	1	1.11293	8.39483
Haro11B	Gus12	0.51716	0.77574	0.01980	1.24430	3.94680	· · ·	0.28910	0.86960	· · ·	0.28860	0.18990	1	1	1.00261	8.32276
Haro11C	Gus12	0.78808	1.18212	0.02800	1.02660	3.31110	· · ·	0.22860	0.72570	· · ·	0.37160	0.17080	1	1	1.12584	8.13129
ESO338-IG004	Gus12	0.44260	0.66390	0.08800	1.71170	5.31050	· · ·	0.02910	0.09040	· · ·	0.14070	0.10990	1	1	1.47283	7.88239
H II045	San12	0.55200	0.82800	0.01400	1.06000	3.17000	· · ·	0.13200	0.37000	· · ·	0.11700	0.08710	1	1	0.90204	8.37443
H II064	San12	1.03200	1.54800	0.02600	0.46300	1.42000	· · ·	0.29900	0.89400	· · ·	0.29300	0.21100	1	1	1.51710	7.66762
H II209	San12	0.53600	0.80400	0.00600	0.71000	2.13000	· · ·	0.32400	1.01000	· · ·	0.21400	0.18100	1	1	0.81677	8.42707
H II247	San12	0.52800	0.79200	0.01300	1.01700	3.03000	· · ·	0.12500	0.37600	· · ·	0.09650	0.07870	1	1	0.89496	8.36754
H II251	San12	0.75600	1.13400	0.00900	0.82300	2.50000	· · ·	0.21700	0.65000	· · ·	0.20700	0.15500	1	1	0.86509	8.43194
CHR2	Sta13	1.80160	2.70240	0.01500	0.52900	1.52500	· · ·	0.11200	0.33400	0.01200	0.24400	0.17700	1	1	1.13971	8.15415
CHR5	Sta13	0.99400	1.49100	0.01100	0.75400	2.21400	· · ·	0.09900	0.29600	0.01600	0.17300	0.13300	1	1	0.92129	8.34122
CHR8	Sta13	1.15280	1.72920	0.00800	0.43700	1.30800	· · ·	0.10600	0.31600	0.01100	0.18100	0.12600	1	1	0.98013	8.19646
CHR39	Sta13	0.46720	0.70080	0.01500	0.92800	2.84000	· · ·	0.18200	0.57100	0.07000	0.34800	0.24500	1	1	0.94026	8.24901
CHR57	Sta13	1.31160	1.96740	0.02600	1.60300	4.78000	· · ·	0.27000	0.79900	0.02900	0.64900	0.46100	1	1	0.94651	8.54012
CHR87	Sta13	1.29760	1.94640	0.01900	0.68900	2.02900	· · ·	0.12300	0.36300	0.02500	0.17100	0.13600	1	1	1.12254	8.11663
CHR90a	Sta13	1.16760	1.75140	0.02000	0.87100	2.54800	· · ·	0.09400	0.26800	0.02000	0.14100	0.12000	1	1	1.05762	8.21293
CHR90b	Sta13	1.19920	1.79880	0.01700	0.82000	2.41900	· · ·	0.08100	0.20700	NaN	0.07200	0.08600	1	1	1.02167	8.25519
CHR102	Sta13	1.41760	2.12640	0.01700	0.63000	1.84000	· · ·	0.08000	0.24000	0.01400	0.22800	0.16100	1	1	1.11656	8.13233
CHR2	Sta13	1.80160	2.70240	0.01500	0.52900	1.52500	· · ·	0.11200	0.33400	0.01200	0.24400	0.17700	1	3	0.90488	8.46517
CHR5	Sta13	0.99400	1.49100	0.01100	0.75400	2.21400	· · ·	0.09900	0.29600	0.01600	0.17300	0.13300	1	3	1.00541	8.21654
CHR8	Sta13	1.15280	1.72920	0.00800	0.43700	1.30800	· · ·	0.10600	0.31600	0.01100	0.18100	0.12600	1	3	0.82716	8.44094
CHR57	Sta13	1.31160	1.96740	0.02600	1.60300	4.78000	· · ·	0.27000	0.79900	0.02900	0.64900	0.46100	1	3	1.10644	8.32201
CHR87	Sta13	1.29760	1.94640	0.01900	0.68900	2.02900	· · ·	0.12300	0.36300	0.02500	0.17100	0.13600	1	3	1.02731	8.23450
CHR90a	Sta13	1.16760	1.75140	0.02000	0.87100	2.54800	· · ·	0.09400	0.26800	0.02000	0.14100	0.12000	1	3	0.95225	8.35905
CHR102	Sta13	1.41760	2.12640	0.01700	0.63000	1.84000	· · ·	0.08000	0.24000	0.01400	0.22800	0.16100	1	3	1.02211	8.24969
NGC5253-001	Wes13	1.47436	2.21154	· · ·	1.76761	5.10840	0.00260	0.05223	0.15670	· · ·	0.24600	0.18640	1	2	1.12833	8.34487
NGC5253-002	Wes13	1.61540	2.42310	· · ·	1.20304	3.47680	0.00420	0.06943	0.20830	· · ·	0.30640	0.24000	1	2	1.27629	8.12451
NGC5253-003	Wes13	1.65588	2.48382	· · ·	1.24156	3.58810	0.00620	0.07460	0.22380	· · ·	0.41830	0.30860	1	2	1.58697	7.88731
NGC5253-dr1	Wes13	1.50420	2.25630	· · ·	1.13197	3.27140	0.00460	0.07953	0.23860	· · ·	0.40660	0.30050	1	2	1.23990	8.13089
NGC5253-005	Wes13	1.34172	2.01258	· · ·	1.46900	4.24540	0.00250	0.06053	0.18160	· · ·	0.26510	0.21740	1	2	1.00852	8.43312
NGC5253-006	Wes13	1.34488	2.01732	· · ·	1.27692	3.69030	0.00280	0.04690	0.14070	· · ·	0.17260	0.12720	1	2	1.26547	8.10566
NGC5253-dr2	Wes13	1.42908	2.14362	· · ·	1.14381	3.30560	0.00320	0.07567	0.22700	· · ·	0.38850	0.28470	1	2	1.02273	8.37078
NGC6946A	GBe10	1.15320	1.72980	0.00600	0.51700	1.55600	· · ·	0.13600	0.49700	0.00600	0.23000	0.16900	1	1	0.86123	8.40819
NGC6946B	GBe10	2.03400	3.05100	0.00300	0.31300	0.87400	· · ·	0.24700	0.76000	· · ·	0.39800	0.28200	1	1	0.83152	8.57438
NGC6946C	GBe10	1.47040	2.20560	0.00200	0.18900	0.58100	· · ·	0.25200	0.80400	· · ·	0.41100	0.29500	1	1	0.83734	8.41576
NGC6946A	GBe10	1.15320	1.72980	0.00600	0.51700	1.55600	· · ·	0.13600	0.49700	0.00600	0.23000	0.16900	1	3	1.14555	8.01438
NGC2579	Est13	0.46228	0.69342	0.01880	1.22800	3.56200	· · ·	0.07680	0.23790	0.01610	0.03490	0.04100	1	1	0.93643	8.33218
Knot1	Mon12	0.46207	0.48875	0.07736	2.25723	7.00879	· · ·	0.10724	0.32598	· · ·	0.13675	0.12614	0	1	1.19572	8.21416
Knot2	Mon12	0.79203	0.98657	0.03685	1.58338	4.88191	· · ·	0.05892	0.17923	· · ·	0.20151	0.16194	0	1	1.04876	8.31177
Knot3	Mon12	1.08026	1.53090	0.02627	1.10586	3.41039	· · ·	0.11358	0.34965	· · ·	0.54040	0.39729	0	1	1.05570	8.25619

NOTE: See the description of the columns in the text of this Appendix.

B

Appendix B: CALIFA Galaxies Atlas

In this appendix we provide radial ionized-gas metallicity, surface brightness and color profiles of the 324 CALIFA disks analyzed in Chapter §5. For each galaxy we provide a specific panel whose content is the following. *Left:* the radial oxygen abundance profile is shown in the top row: filled purple stars represent the metallicity values obtained for each H II region using the *M13-O3N2* calibration (Marino et al. 2013) while the filled orange stars show the ones obtained via the *M13-N2* calibration. The single fits to both profiles are drawn with grey solid lines. The double fits are plotted in red (inner part) and pink (outer part) for the *M13-N2* case and blue (inner part) and cyan (outer part) for the *M13-O3N2* one. The error bars plotted include both random and typical systematic errors associated to these calibrations. The SDSS surface brightness profile is shown in the second row: the $r'-$band profile is plotted with yellow circles and the $g'-$band one with cyan circles. The double fit performed to the $r'-$band is indicated with a green solid line. The third row shows the $(g'-r')$ color gradient with violet squares and the double-linear fit is plotted with blue solid lines. The top x axis shows the galactocentric radius in kiloparsecs while the bottom shows the galactocentric radius normalized to $R_{\rm eff}$. The vertical dashed (in color only in the second panel) mark the inner radius (green), the break radius (red) and the outer radius (green) used in each surface brightness double fit. *Right:* The physical properties derived for each galaxy, including the surface brightness type, are listed at right$-$top while the SDSS 3'$\times$ 3' $r'-$band post-stamp image is shown at the right-bottom. The overplotted ellipses correspond to the same radii used for the SB double fit. SB profiles are in units of mag/$^{\square}$ and are corrected for Galactic extinction using the Milky Way extinction curve of Cardelli et al.(1998).

This dataset (that shall be provided in electronic form on request) can be useful to purse scientific objectives that go beyond those presented throughout this Ph.D. Thesis. Given its legacy value I decide to include as an appendix to this work. Here are shown the first 10 CALIFA galaxies analyzed, the complete CALIFA ATLAS is available in the following webpage `http://guaix.fis.ucm.es/~raffaella/Thesis_ATLAS/`.

2MASXJ01331766

$z = 0.0093$

$R_{eff} = 3.35$ [kpc]

$M_* = 9.19$ [log $M_\odot$]

$M_R = -18.82$ [mag]

MorphT = ScAB

PhotT = II.o-OLR

$\mu_{r,\,break} = 22.07$ [mag/''^{2}]

$(g'-r')_{break} = 0.46$ [mag]

$12+\log(O/H)_{break} = 8.39$ [dex]

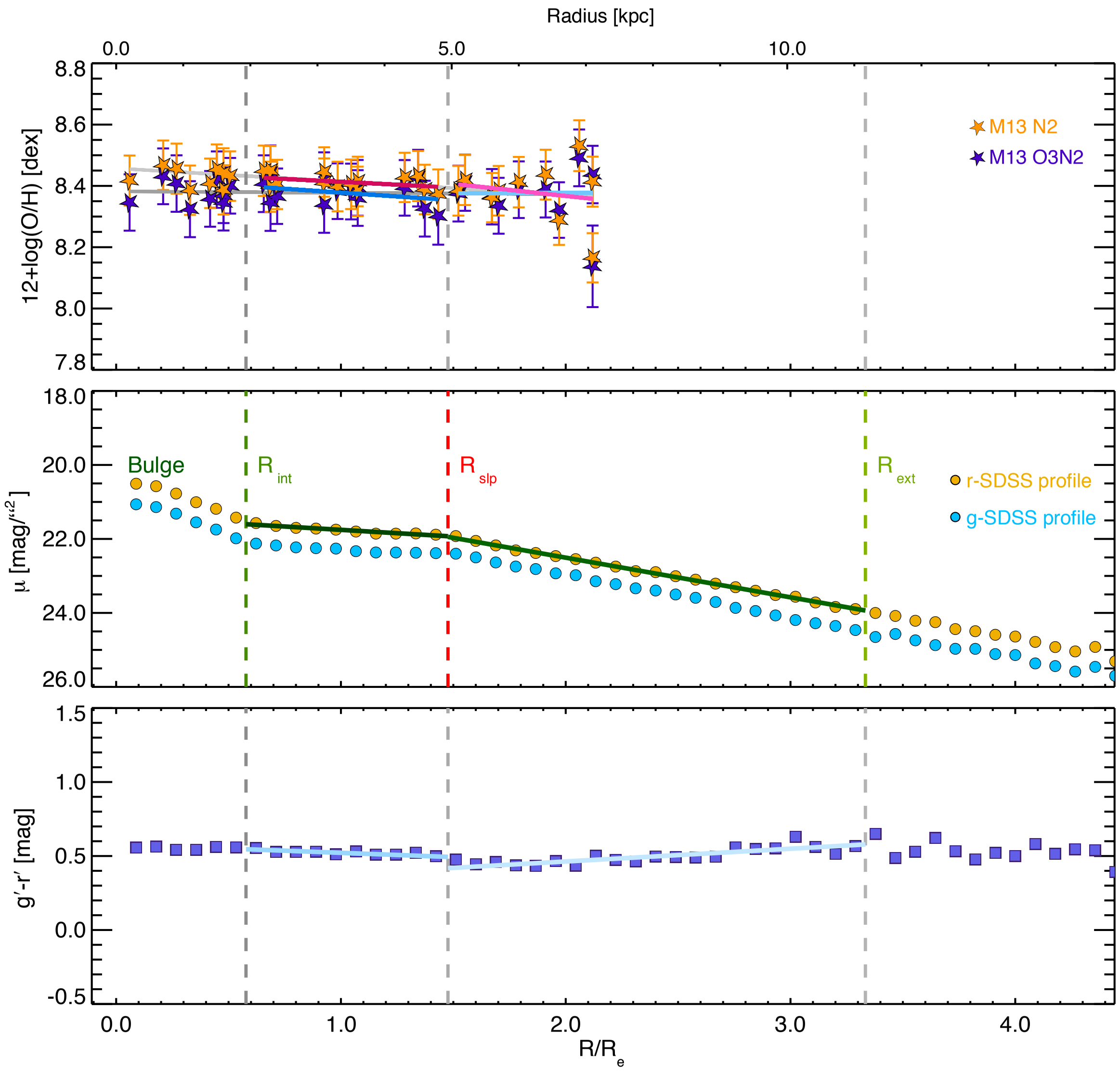

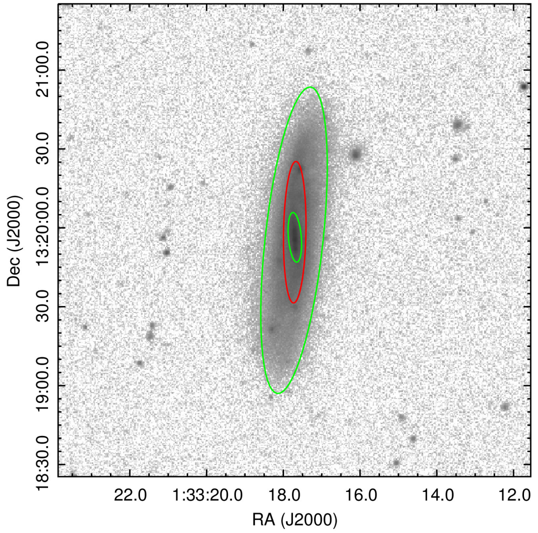

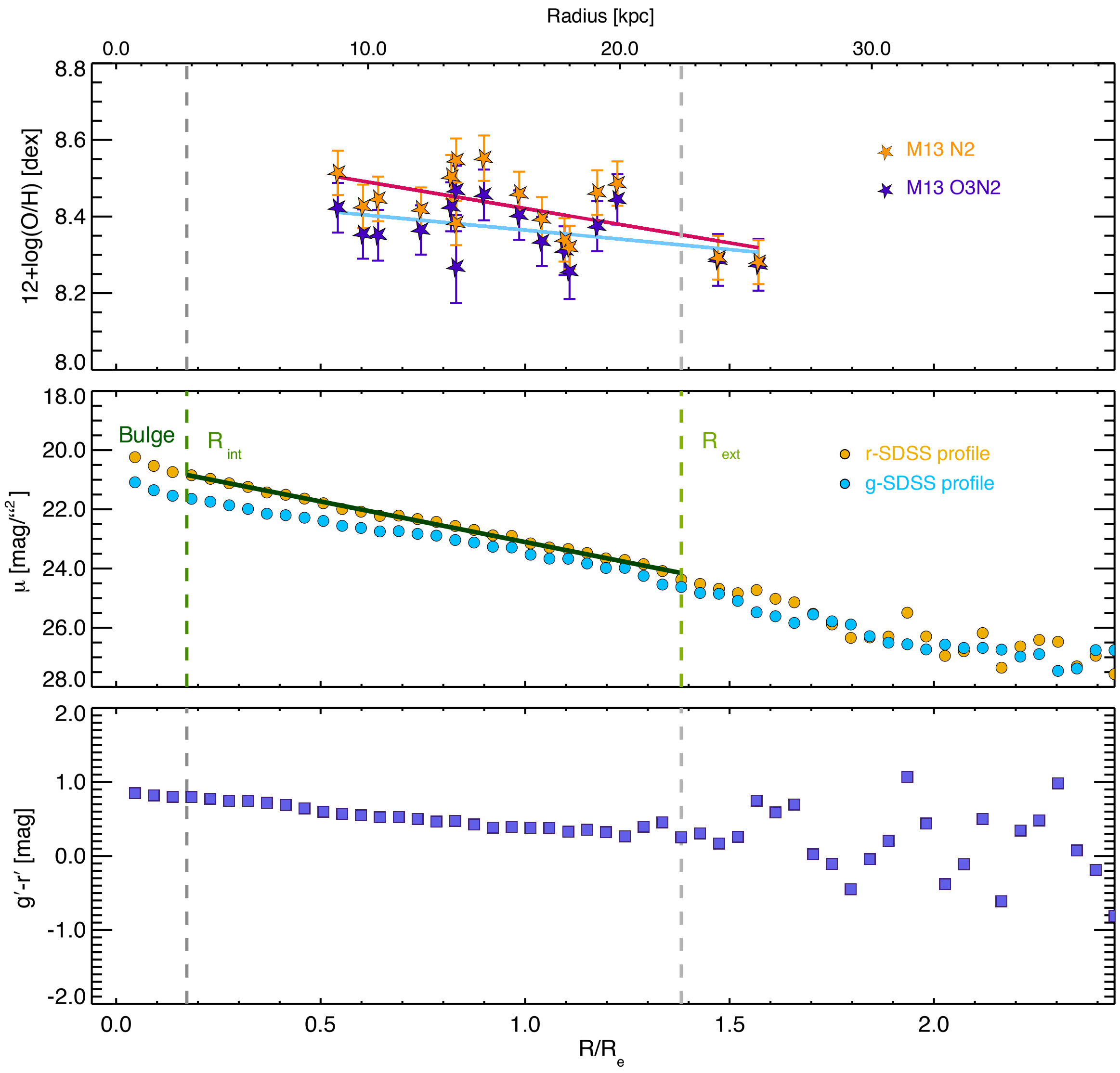

ESO539–G014

$z = 0.0233$

$R_{\rm eff} = 16.23$ [kpc]

$M_* = 9.91$ [log $M_\odot$]

$M_R = -20.20$ [mag]

MorphT = ScdA

PhotT = I

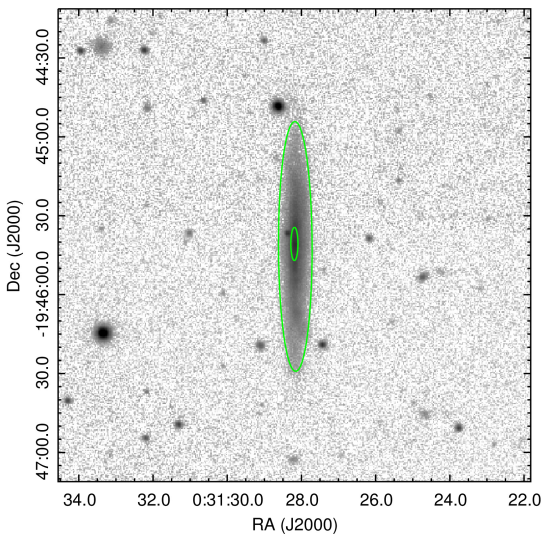

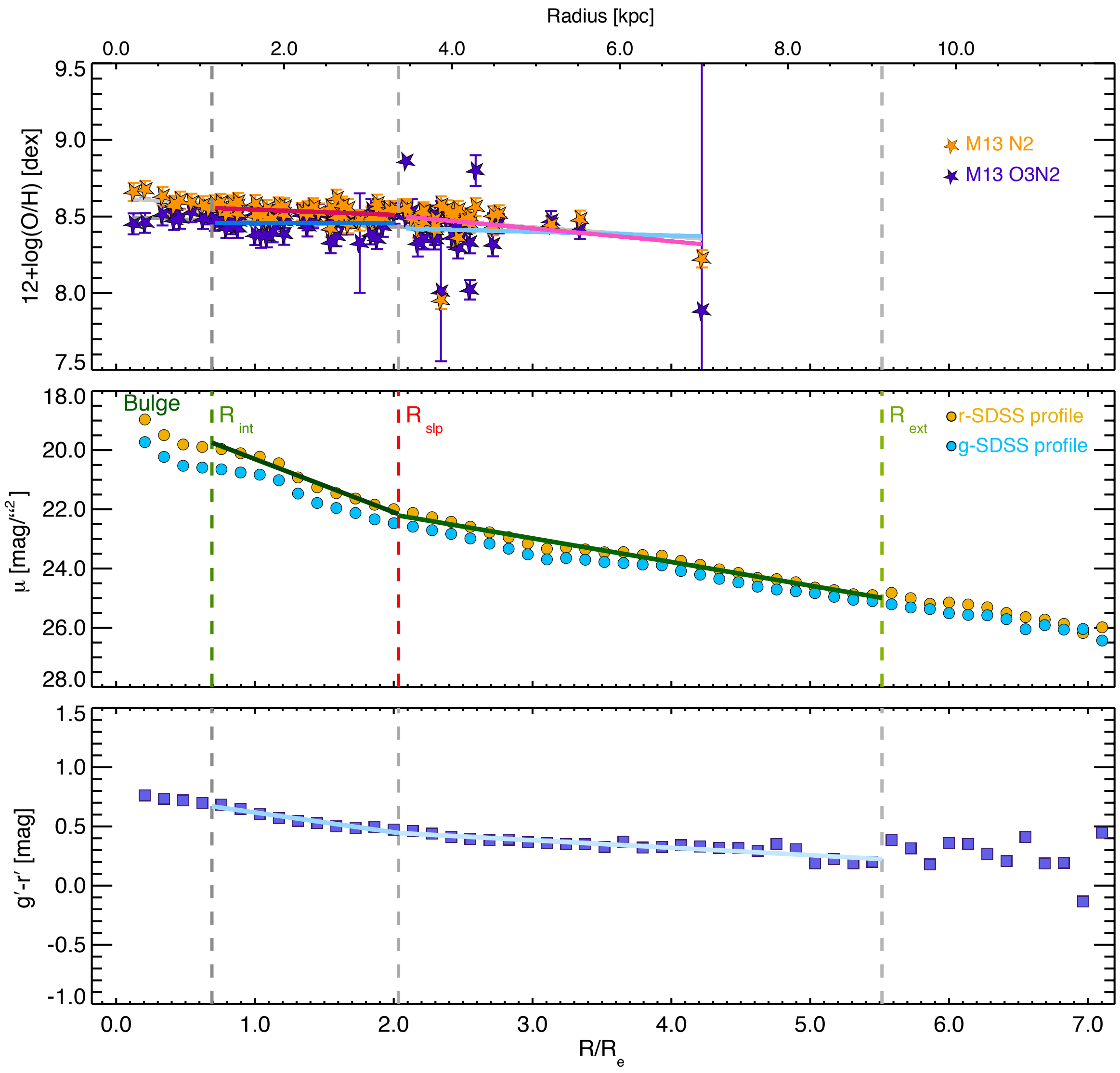

ESO540−G003

$z = 0.0108$

$R_{\mathrm{eff}} = 2.39$ [kpc]

$M_* = 9.84$ [log $M_{\odot}$]

$M_R = -20.45$ [mag]

MorphT = SbAB

PhotT = III

$\mu_{r,\,\mathrm{break}} = 22.27$ [mag/"^{2}]

$(g'-r')_{\mathrm{break}} = 0.44$ [mag]

$12+\log(\mathrm{O/H})_{\mathrm{break}} = 8.53$ [dex]

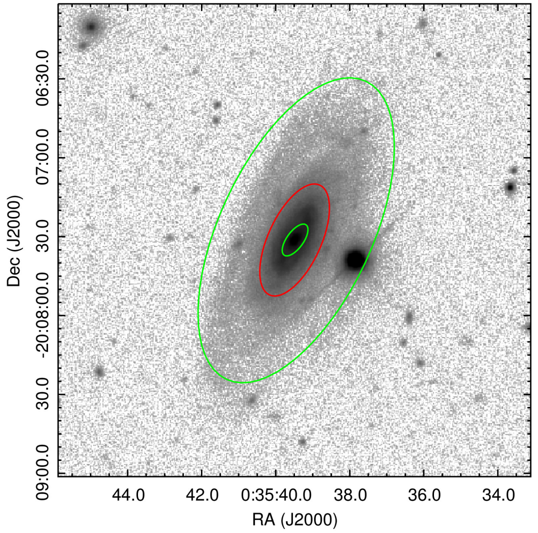

IC0159

$z = 0.0126$

$R_{eff} = 5.57$ [kpc]

$M_* = 9.47$ [log $M_\odot$]

$M_R = -20.35$ [mag]

MorphT = SdmB

PhotT = I

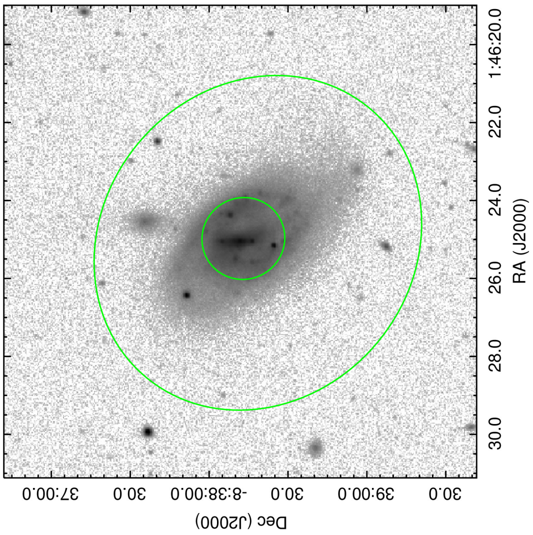

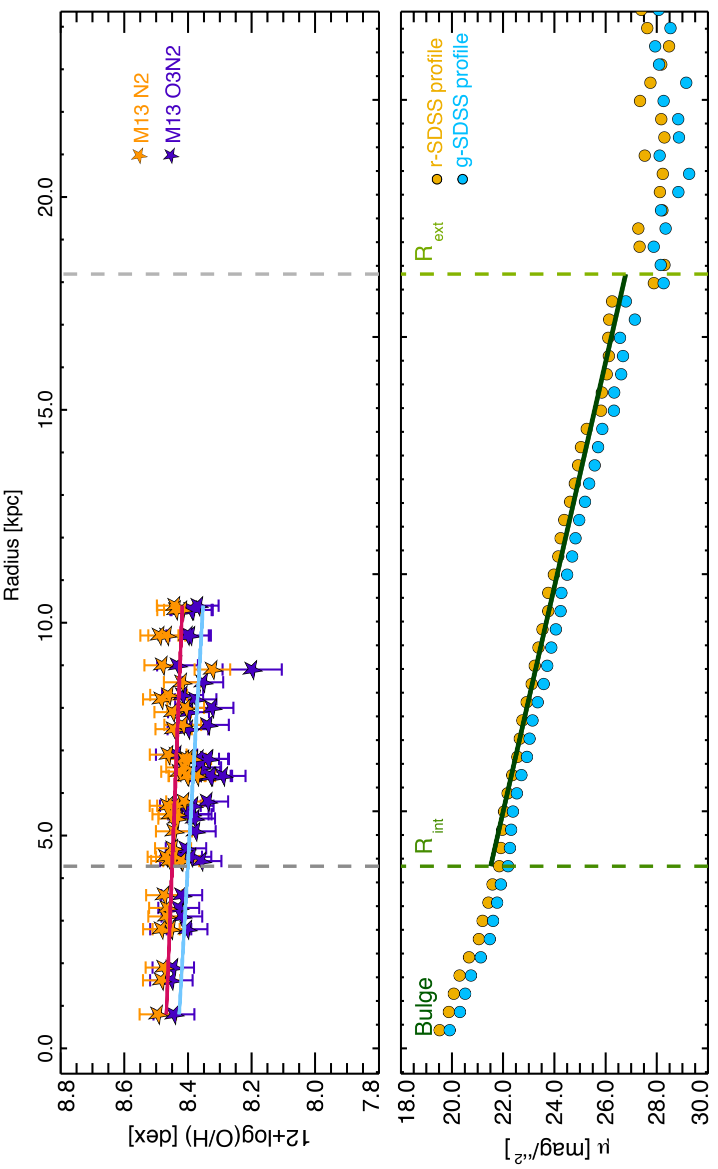

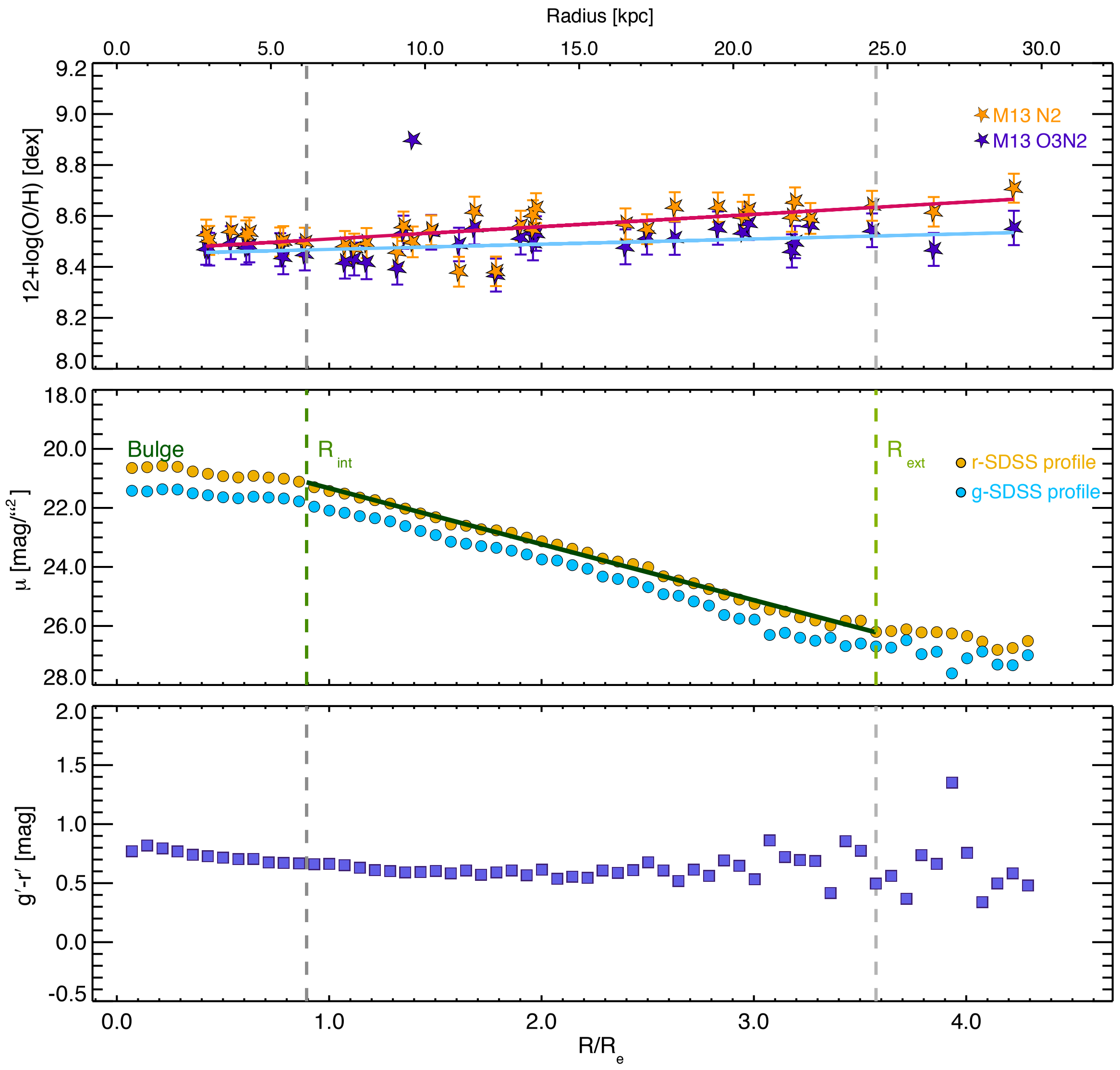

IC0480

$z = 0.0158$

$R_{eff} = 6.89$ [kpc]

$M_* = 9.83$ [log $M_{\odot}$]

$M_R = -20.37$ [mag]

MorphT = ScAB

PhotT = I

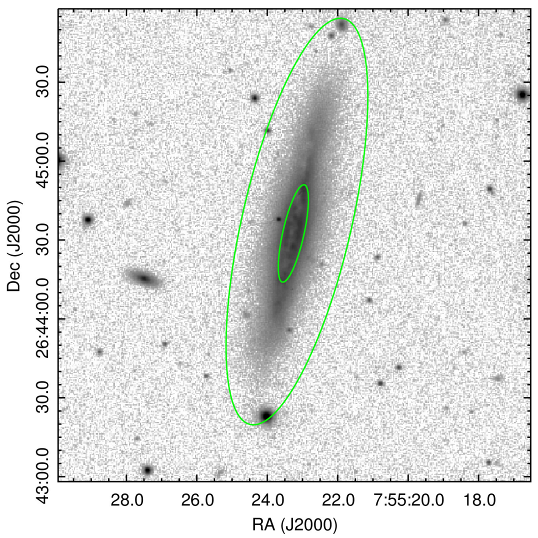

IC0674

z = 0.0264

R_{eff} = 10.35 [kpc]

M_* = 10.75 [log $M_\odot$]

M_R = -22.07 [mag]

MorphT = SabB

PhotT = II.o-OLR

$\mu_{r,\,break}$ = 22.99 [mag/''^{2}]

$(g'-r')_{break}$ = 0.52 [mag]

$12+\log(O/H)_{break}$ = 8.52 [dex]

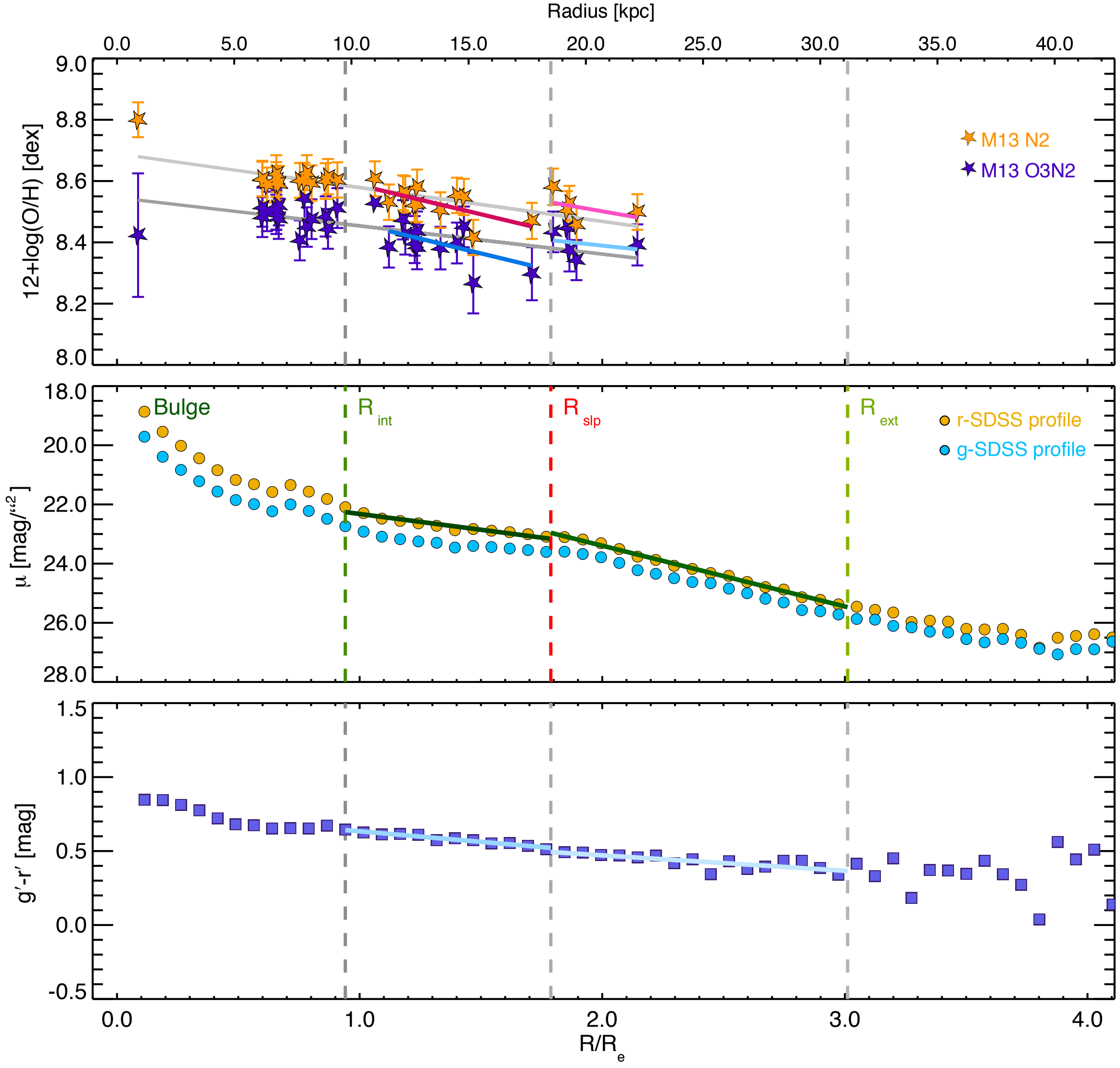

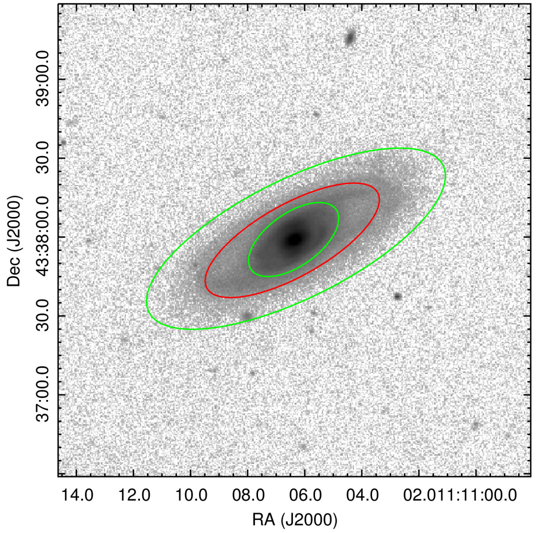

IC0776

$z = 0.0098$

$R_{eff} = 6.91$ [kpc]

$M_* = 9.16$ [log $M_\odot$]

$M_R = -19.34$ [mag]

MorphT = SdmA

PhotT = I

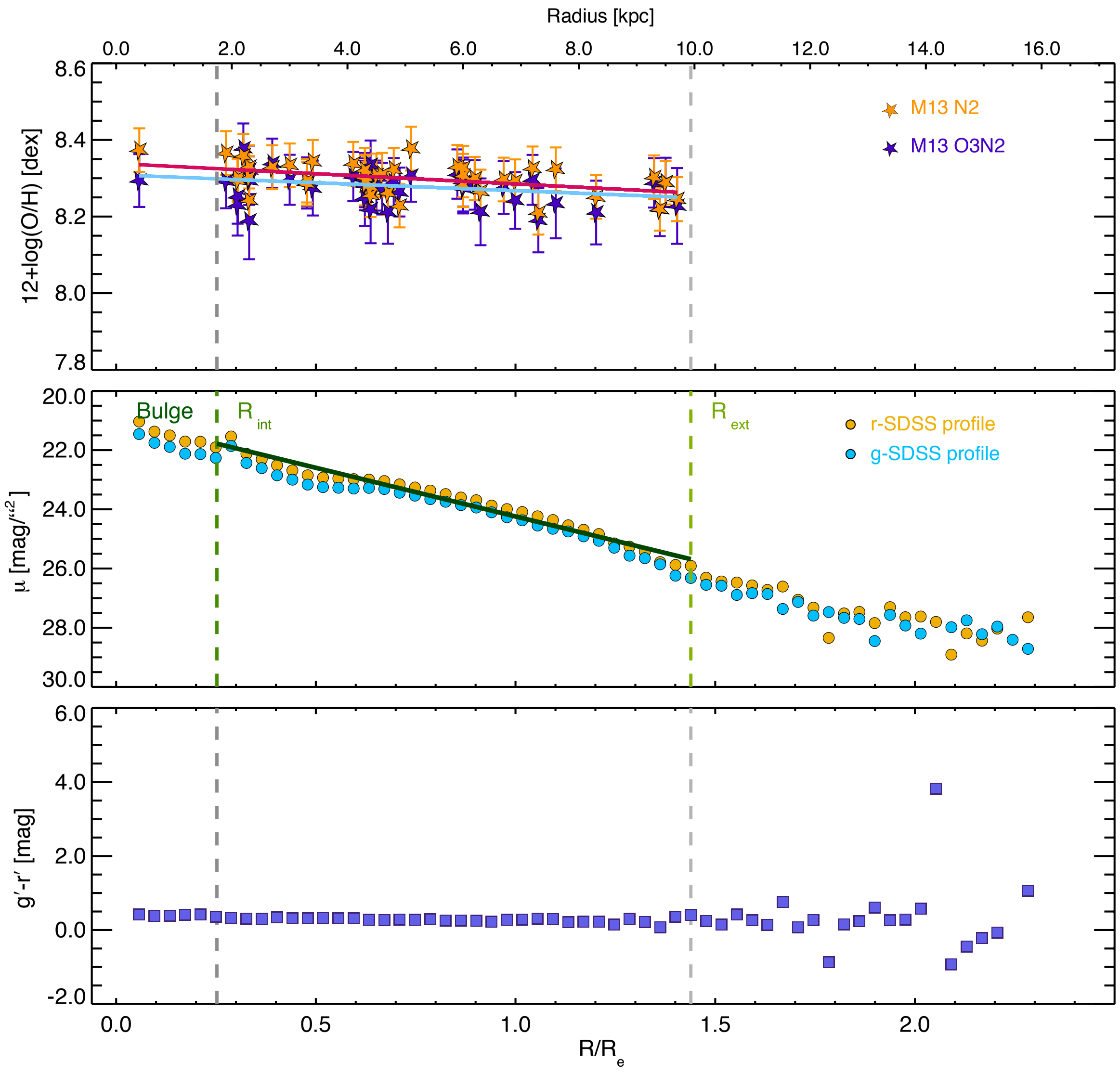

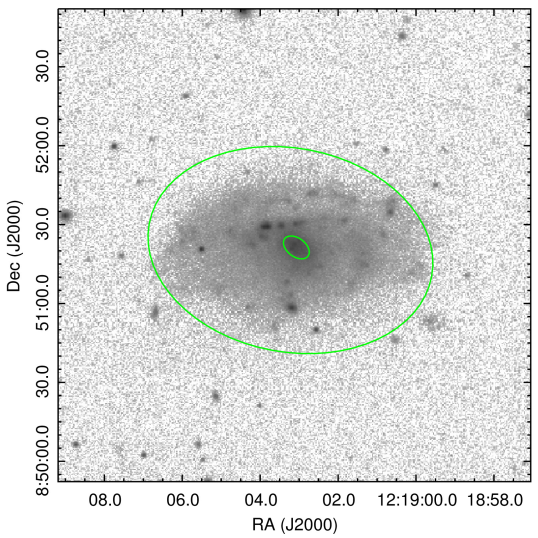

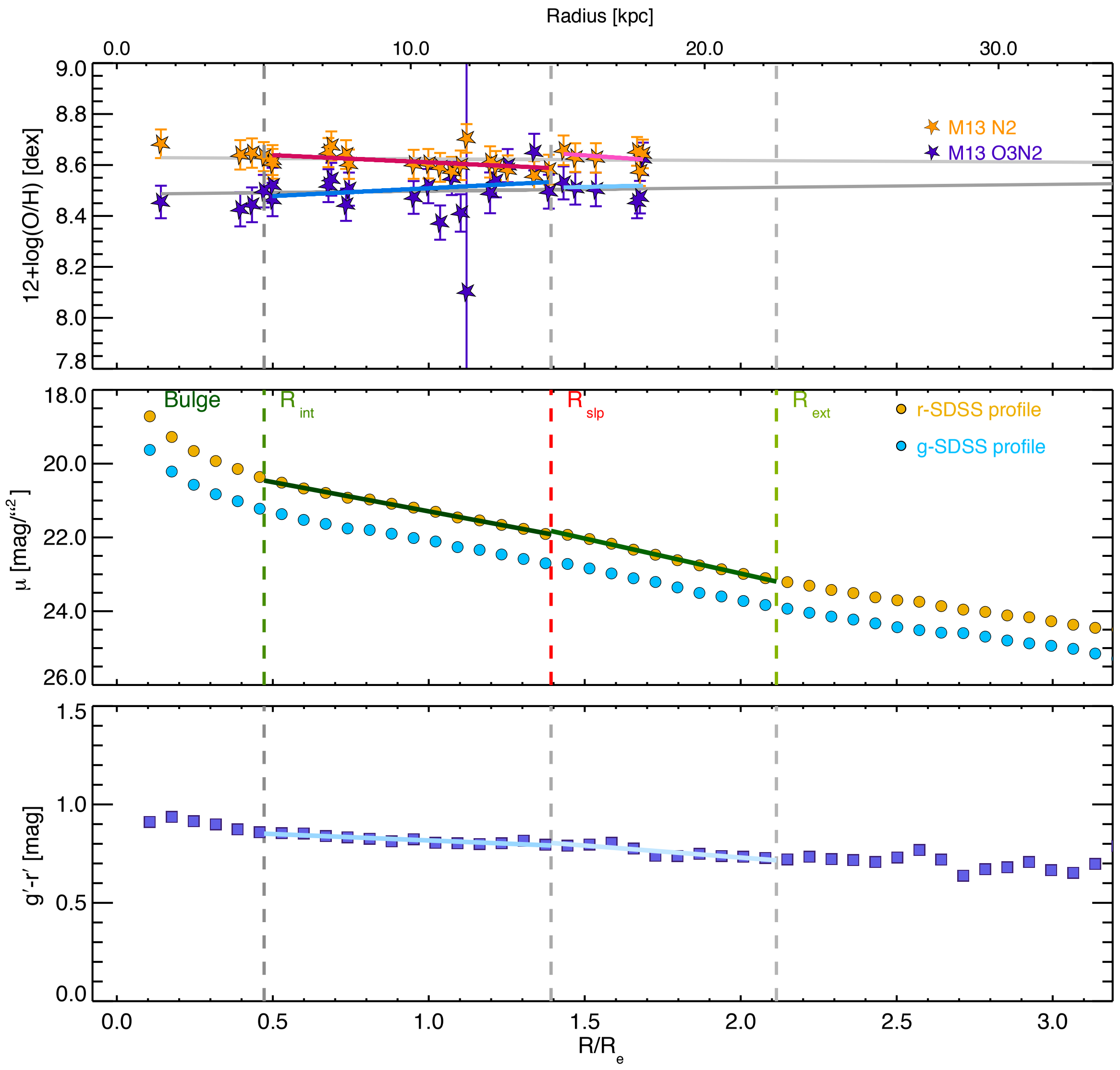

IC0944

$z = 0.0255$

$R_{eff} = 10.61$ [kpc]

$M_* = 11.23$ [log $M_\odot$]

$M_R = -22.36$ [mag]

MorphT = SabA

PhotT = II-CT

$\mu_{r,\,break} = 21.88$ [mag/''^{2}]

$(g'-r')_{break} = 0.79$ [mag]

$12+\log(O/H)_{break} = 8.61$ [dex]

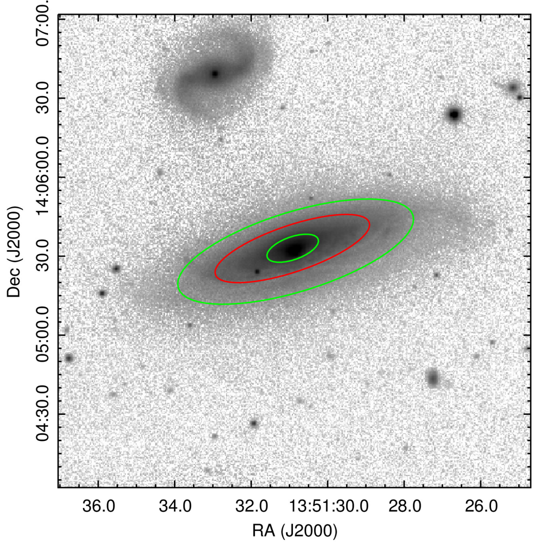

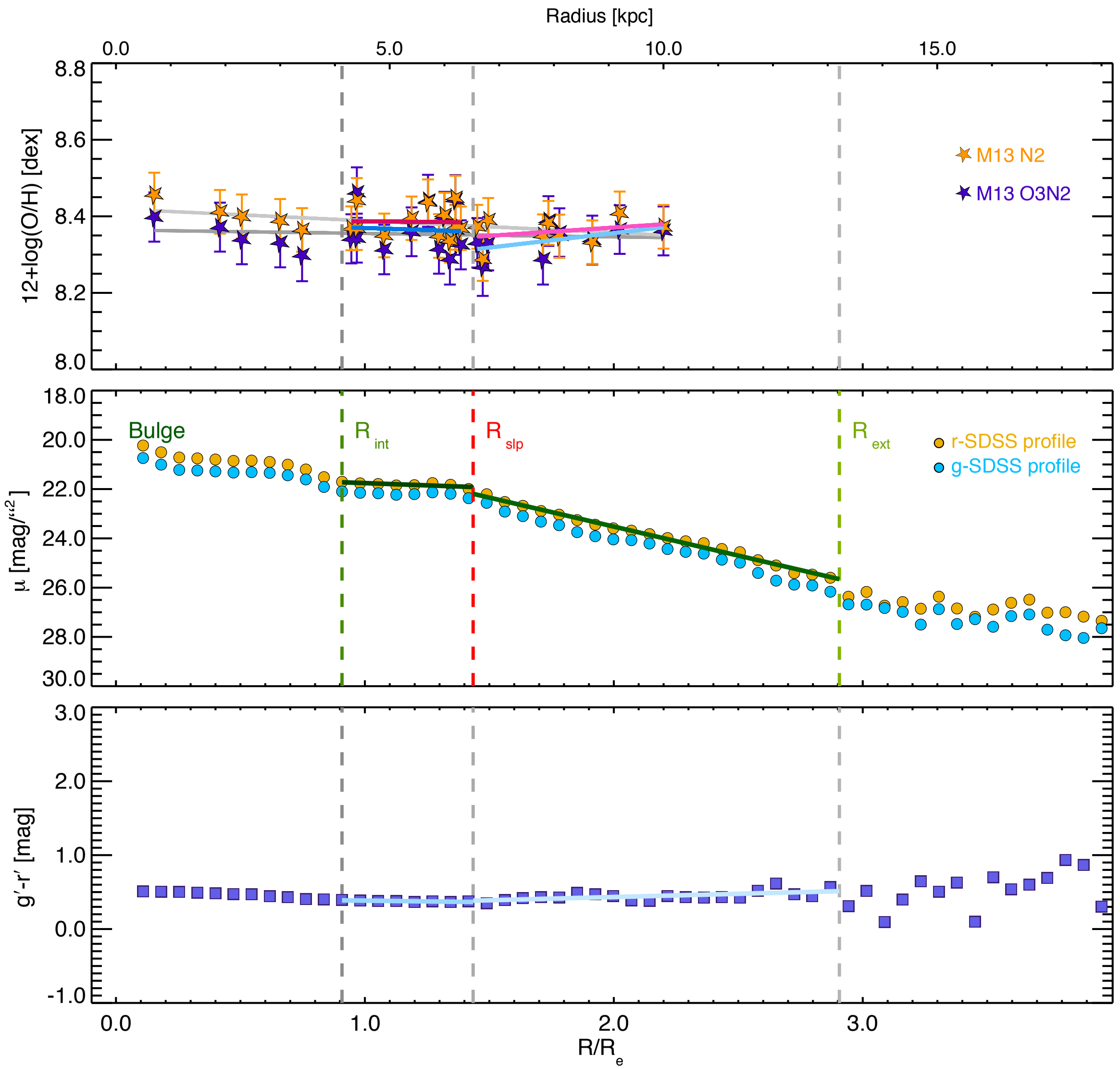

IC0995

$z = 0.0120$

$R_{eff} = 4.55$ [kpc]

$M_* = 9.44$ [log $M_\odot$]

$M_R = -19.72$ [mag]

MorphT = ScdAB

PhotT = II.o-CT

$\mu_{r,\, break} = 22.22$ [mag/''^{2}]

$(g'-r')_{break} = 0.37$ [mag]

$12+\log(O/H)_{break} = 8.37$ [dex]

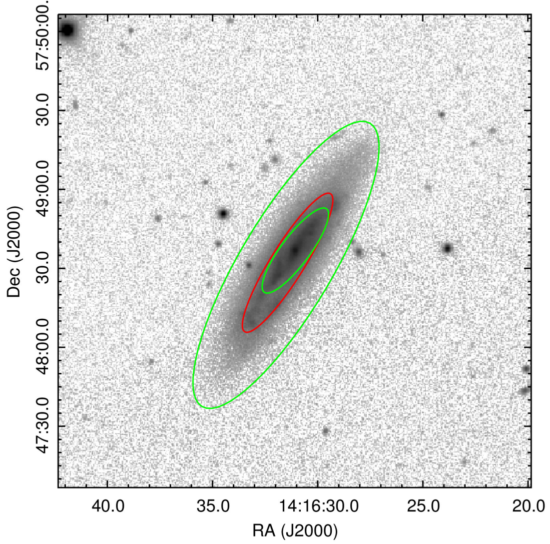

IC1151

$z = 0.0091$

$R_{eff} = 4.62$ [kpc]

$M_{*} = 9.49$ [log $M_{\odot}$]

$M_{R} = -20.20$ [mag]

MorphT = ScdB

PhotT = II.o-CT

$\mu_{r,\,break} = 22.22$ [mag/''^{2}]

$(g'-r')_{break} = 0.34$ [mag]

$12+\log(O/H)_{break} = 8.43$ [dex]

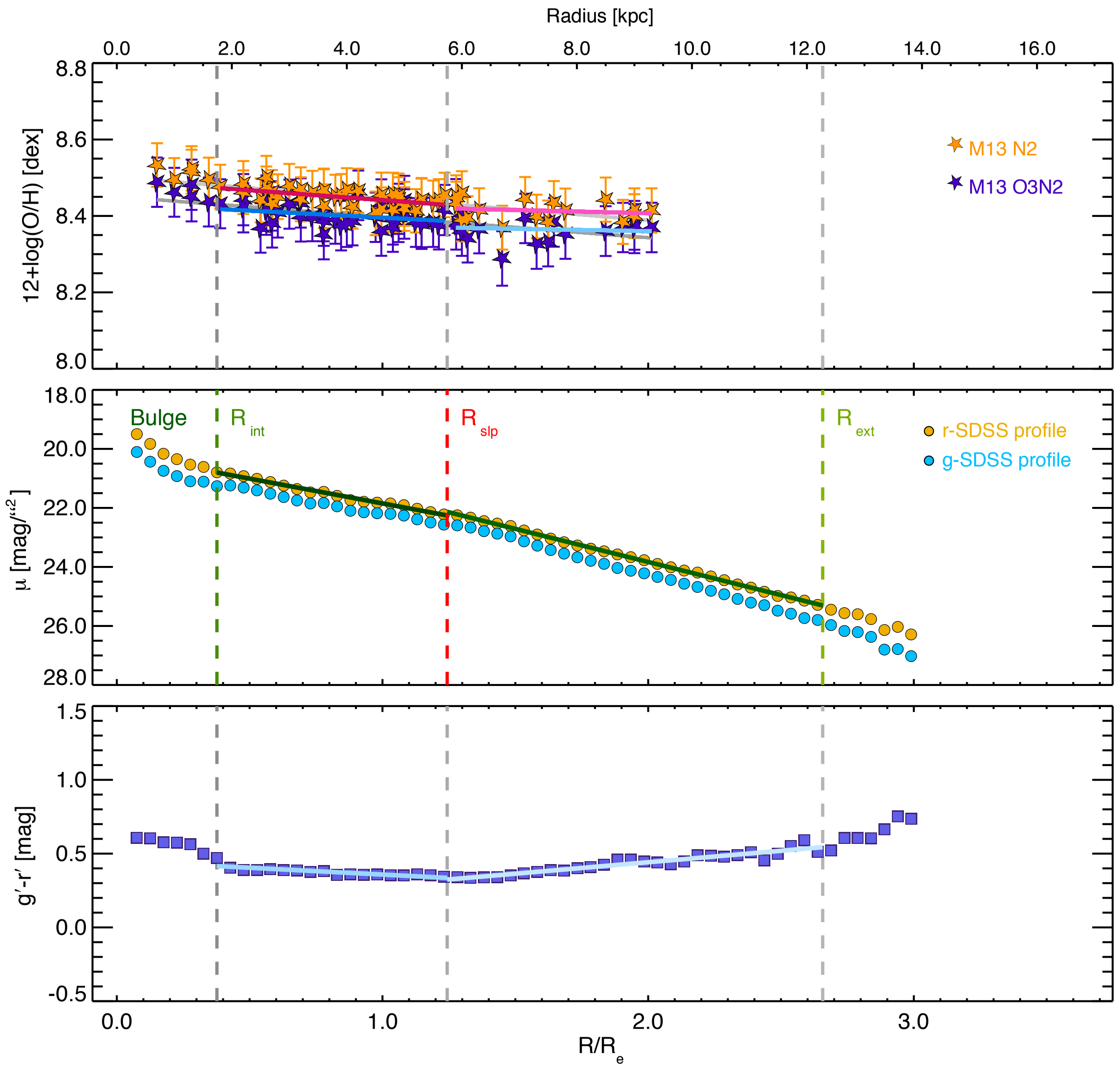

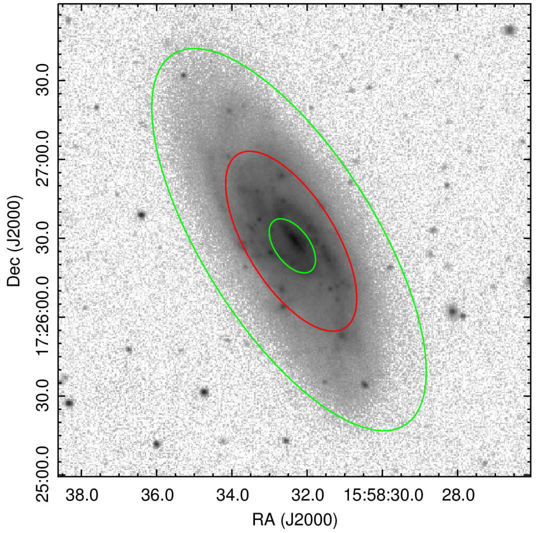

B.1 Disk classification and physical properties of the CALIFA galaxies

In the following table, the surface brightness classification performed in Marino et al. (2015) is provided. For each galaxy we provide in the fist column the galaxy name. In the subsequent columns we list the following properties in order as they appear: the heliocentric redshift z distance obtained from the NED database; *Phot Type* is the photometrical type obtained from our analysis of the SDSS *r'*-band profiles; the morphological type (*Morph Type*), the stellar mass (M_*) and R-band absolute magnitude (M_R) values as obtained by the CALIFA collaboration (Walcher et al. 2014), follows to the effective radius, R_{eff}, values expressed in units of kiloparsec (Sánchez et al. 2014). Finally, the last two columns correspond to R_{rbreak}, the break radii obtained as the minimum of the double bootstrapping fit to the SDSS *g'*− and *r'*−band data in units of their $\mathrm{R}_{\mathrm{eff}}$ along with their errors.

Name	z	Phot Type	Morph Type	M_*	M_R	R_{eff}	$R_{g',break}$	$R_{r',break}$
2MASXJ01331766	0.0093	II.o-OLR	ScAB	9.19	-18.82	3.35	1.4761 ± 0.0367	1.5471 ± 0.0238
ESO540-G003	0.0108	III	SbAB	9.87	-20.45	2.39	2.1202 ± 0.2192	2.1478 ± 0.2435
IC0674	0.0264	II.o-OLR	Sab B	10.80	-22.07	10.35	1.9300 ± 0.0309	1.9448 ± 0.0453
IC0944	0.0255	II-CT	Sab A	11.23	-22.36	10.61	1.5427 ± 0.0516	1.5483 ± 0.0577
IC0995	0.0120	II.o-CT	ScdAB	9.55	-19.72	4.55	1.3029 ± 0.0377	1.3058 ± 0.0350
IC1151	0.0091	II.o-CT	Scd B	9.49	-20.20	4.62	1.4112 ± 0.0320	1.3827 ± 0.0261
IC1199	0.0179	II.o-OLR	SbAB	10.53	-21.73	11.00	0.7988 ± 0.0379	0.7391 ± 0.0500
IC1528	0.0125	II.o-CT	SbcAB	10.06	-20.93	6.79	2.0091 ± 0.0704	1.9584 ± 0.5677
IC1683	0.0159	III	SbAB	10.46	-21.06	4.79	1.7631 ± 0.0898	1.6586 ± 0.1110
IC1755	0.0257	II-CT	Sb A	10.84	-21.69	9.69	1.7299 ± 0.0828	1.6965 ± 0.0997
IC2095	0.0093	II.o-CT	ScAB	8.54	-17.84	4.92	1.1836 ± 0.0453	1.1503 ± 0.0480
IC2247	0.0150	II-CT	Sab A	10.45	-20.76	6.97	1.5958 ± 0.0411	1.5784 ± 0.0533
IC2487	0.0156	II.o-OLR	ScAB	10.24	-21.03	7.21	1.5657 ± 0.0549	1.6503 ± 0.0393
IC3598	0.0274	II.o-OLR	S0AB	10.89	-21.81	11.29	1.6455 ± 0.0584	1.7124 ± 0.0873
IC4215	0.0150	III	Sb A	10.41	-20.56	4.46	1.3802 ± 0.0356	1.3899 ± 0.0314
IC4566	0.0210	III	Sb B	10.82	-21.91	8.78	1.3082 ± 0.0284	1.3743 ± 0.0488
IC5309	0.0140	III	ScAB	10.22	-20.59	3.38	2.2867 ± 0.1003	2.3365 ± 0.0902
IC5376	0.0166	II-CT	Sb A	10.50	-21.07	7.38	1.5711 ± 0.0539	1.5727 ± 0.0521
MCG-01-54-016	0.0104	II-CT	Scd A	8.79	-18.32	2.60	2.5610 ± 0.0544	2.5387 ± 0.0453
MCG-02-02-030	0.0115	II.o-OLR	SbAB	10.30	-20.92	4.06	1.1900 ± 0.0575	1.1956 ± 0.0574
MCG-02-02-040	0.0117	II.o-CT	ScdAB	9.97	-20.20	3.48	2.2344 ± 0.0637	2.2043 ± 0.0673
MCG-02-03-015	0.0188	II.o-OLR	SabAB	10.63	-21.42	10.49	1.5386 ± 0.0084	1.5304 ± 0.0101
MCG-02-51-004	0.0199	II-CT	Sb A	10.67	-21.59	10.07	1.0193 ± 0.0677	1.0558 ± 0.0684
NGC0001	0.0150	III	Sbc A	10.63	-21.70	5.98	2.3990 ± 0.1989	2.6323 ± 0.2330
NGC0023	0.0150	III	Sb B	10.98	-22.44	8.46	1.4986 ± 0.0362	1.4833 ± 0.0437
NGC0036	0.0197	II.o-OLR	Sb B	10.82	-22.34	14.66	1.1576 ± 0.1444	1.1579 ± 0.3299
NGC0171	0.0129	II.o-OLR	Sb B	10.45	-21.79	6.53	1.9621 ± 0.1200	1.9579 ± 0.1237
NGC0177	0.0126	II-CT	Sab A	10.35	-20.69	7.60	1.2184 ± 0.0476	1.2242 ± 0.0600
NGC0180	0.0172	II.o-OLR	Sb B	10.66	-22.27	12.62	1.3455 ± 0.0237	1.3179 ± 0.0322
NGC0192	0.0135	II.o-CT	SabAB	10.85	-21.62	5.61	0.9532 ± 0.0156	0.9528 ± 0.0144
NGC0214	0.0148	II.o-OLR	SbcAB	10.47	-22.11	6.73	1.9455 ± 0.0250	1.9843 ± 0.0410
NGC0216	0.0051	III	Sd A	9.11	-18.90	2.03	1.8726 ± 0.0781	1.8861 ± 0.0962
NGC0234	0.0145	II.o-CT	ScAB	10.63	-21.92	6.14	1.3841 ± 0.0468	1.3396 ± 0.0541
NGC0237	0.0136	III	Sc B	10.20	-21.15	4.09	1.6295 ± 0.0370	1.6235 ± 0.0270
NGC0257	0.0171	II-CT	Sc A	10.81	-22.11	8.57	1.2135 ± 0.0303	1.2422 ± 0.0220
NGC0444	0.0158	II-CT	Scd A	9.80	-20.21	9.07	1.5290 ± 0.0444	1.5200 ± 0.0584
NGC0477	0.0193	II.o-CT	SbcAB	10.41	-21.67	13.97	1.0857 ± 0.0342	1.0981 ± 0.0340
NGC0496	0.0196	II-CT	Scd A	10.30	-21.36	11.00	1.5131 ± 0.3454	1.5131 ± 0.2520

NGC0551	0.0170	II.o-OLR	SbcAB	10.57	-21.53	7.35	1.4900 ± 0.0801	1.4382 ± 0.0446
NGC0681	0.0057	III-s	SaAB	10.18	-20.69	3.64	0.9584 ± 0.1154	0.9133 ± 0.4993
NGC0693	0.0051	III	E7AB	9.86	-19.89	4.10	1.0200 ± 0.0408	1.0120 ± 0.0411
NGC0716	0.0147	II.o-CT	SbAB	10.59	-21.35	5.65	1.5636 ± 0.0272	1.5592 ± 0.0259
NGC0755	0.0053	III	Scd B	9.26	-19.38	3.30	1.6114 ± 0.0384	1.6114 ± 0.0386
NGC0768	0.0227	II.o-OLR	Sc B	10.36	-21.75	10.42	1.7437 ± 0.0398	1.7496 ± 0.0397
NGC0776	0.0159	II.o-OLR	Sb B	10.60	-21.84	6.90	1.1795 ± 0.0439	1.1797 ± 0.0124
NGC0932	0.0132	II-CT	S0a A	10.94	-22.11	7.39	1.1081 ± 0.0328	1.0990 ± 0.0416
NGC1056	0.0052	III-s	Sa A	9.97	-19.95	3.40	0.9716 ± 0.0396	0.9640 ± 0.0381
NGC1093	0.0172	III	Sbc B	10.47	-21.36	7.15	1.4703 ± 0.7340	1.4739 ± 0.3502
NGC1167	0.0161	III-s	S0 A	11.30	-22.97	8.99	1.4958 ± 0.0457	1.5185 ± 0.0441
NGC1349	0.0214	III-s	E6 A	10.80	-22.56	8.12	1.2225 ± 0.0367	2.7401 ± 1.1819
NGC1677	0.0090	III	ScdAB	9.32	-19.35	3.19	1.3919 ± 0.1343	1.3849 ± 0.1086
NGC2253	0.0125	III	Sbc B	10.57	-21.60	2.23	5.1625 ± 0.1021	5.1502 ± 0.1054
NGC2347	0.0153	III	SbcAB	10.54	-22.14	5.75	2.6814 ± 0.2423	3.1285 ± 0.0851
NGC2410	0.0161	II.o-CT	SbAB	10.80	-21.85	8.44	2.0725 ± 0.0854	1.2550 ± 0.5895
NGC2449	0.0169	II.o-CT	SabAB	10.81	-21.72	5.53	1.8494 ± 0.0468	1.8824 ± 0.0523
NGC2639	0.0121	III	Sa A	11.12	-22.25	4.06	2.4625 ± 0.0634	2.5027 ± 0.0640
NGC2730	0.0138	II.o-OLR	Scd B	10.01	-20.92	6.82	1.4785 ± 0.0189	1.4522 ± 0.0300
NGC2805	0.0069	III	Sc A	9.73	-20.76	5.71	0.4698 ± 0.0458	0.4499 ± 0.0420
NGC3106	0.0219	III	Sab A	11.03	-22.76	12.04	1.7898 ± 0.0409	1.8205 ± 0.0360
NGC3381	0.0070	III	Sd B	9.56	-20.10	2.21	1.9026 ± 0.1292	1.9537 ± 0.0414
NGC3614	0.0093	II.o-OLR	SbcAB	9.97	-21.08	7.21	0.9885 ± 0.3214	0.9844 ± 0.3119
NGC3619	0.0067	III-s	S0a A	10.30	-21.00	4.55	0.8388 ± 0.0145	0.8456 ± 0.0230
NGC3687	0.0100	II.o-OLR	Sb B	10.16	-20.93	3.80	1.8009 ± 0.0528	1.8579 ± 0.1447
NGC3811	0.0119	III	Sbc B	10.32	-21.42	4.54	1.8552 ± 0.2237	2.0300 ± 0.2747
NGC3994	0.0120	III	SbcAB	10.20	-21.21	3.37	1.8521 ± 0.0176	1.8485 ± 0.0174
NGC4047	0.0130	III	Sbc A	10.65	-21.93	4.30	2.3394 ± 0.0550	2.3832 ± 0.0833
NGC4149	0.0117	II.o-OLR	SaAB	10.34	-20.62	2.21	2.2025 ± 0.0802	2.1912 ± 0.0853
NGC4210	0.0105	II.o-OLR	Sb B	10.28	-21.01	3.81	1.7599 ± 0.0986	1.7836 ± 0.1331
NGC4470	0.0093	III	Sc A	9.94	-20.72	2.61	1.9272 ± 0.2506	1.7782 ± 0.2503
NGC4711	0.0154	II-CT	Sbc A	10.26	-21.06	4.08	1.7437 ± 0.0297	1.7461 ± 0.0280
NGC4961	0.0103	II.o-OLR	Scd B	9.57	-20.21	3.01	1.6405 ± 0.0303	1.6575 ± 0.0321
NGC5000	0.0207	III	Sbc B	10.48	-21.78	7.07	1.4252 ± 0.0308	1.4617 ± 0.0287
NGC5056	0.0206	II.o-CT	ScAB	10.61	-21.90	7.52	2.2243 ± 0.0577	2.2107 ± 0.0577
NGC5205	0.0075	III	Sbc B	9.94	-20.17	2.54	2.1258 ± 0.0404	2.1058 ± 0.0405
NGC5267	0.0216	II.o-OLR	Sab B	10.86	-22.09	7.77	1.8566 ± 0.0887	1.8384 ± 0.0596
NGC5289	0.0103	II.o-CT	Sab A	10.22	-20.70	4.79	1.4354 ± 0.0155	1.4335 ± 0.0173
NGC5320	0.0106	III	SbcAB	10.16	-21.09	6.20	1.5022 ± 0.0312	1.5164 ± 0.0348
NGC5376	0.0086	I	SbAB	0.05	-20.86	2.65	2.7071 ± 0.1495	2.7068 ± 0.1298

NGC5378	0.0121	II.o-OLR	Sb B	10.32	-21.22	5.52	2.1619 ± 0.1516	2.0759 ± 0.0725
NGC5379	0.0071	III	SabAB	9.83	-19.43	2.42	1.4214 ± 0.0407	1.4389 ± 0.0397
NGC5406	0.0192	II.o-OLR	Sb B	11.02	-22.56	8.55	1.5502 ± 0.0536	1.6273 ± 0.0385
NGC5425	0.0087	II.o-OLR	ScdAB	9.45	-19.54	2.93	1.8040 ± 0.0370	1.8006 ± 0.0275
NGC5443	0.0078	III	Sab A	10.32	-20.78	4.36	1.6658 ± 0.0378	1.6988 ± 0.0302
NGC5519	0.0271	III	Sb B	10.66	-21.91	16.92	0.7797 ± 0.0156	0.7796 ± 0.0143
NGC5522	0.0174	II.o-OLR	SbAB	10.69	-21.55	7.96	1.5589 ± 0.0178	1.5513 ± 0.0190
NGC5533	0.0148	III	Sab A	11.04	-22.63	11.46	0.9619 ± 0.0590	1.0073 ± 0.0639
NGC5559	0.0193	II.o-OLR	Sb B	10.53	-21.26	6.62	1.9552 ± 0.0296	1.8753 ± 0.0340
NGC5587	0.0095	II-CT	Sa A	10.33	-20.56	4.13	0.5978 ± 0.0174	0.5951 ± 0.0221
NGC5610	0.0190	II.o-OLR	Sb B	10.63	-21.84	15.43	1.0775 ± 0.0340	1.0818 ± 0.0304
NGC5616	0.0300	II.o-CT	ScAB	11.09	-22.52	17.78	1.2034 ± 0.1153	1.2512 ± 0.0357
NGC5622	0.0147	II-CT	Sbc A	10.23	-20.89	5.36	1.5292 ± 0.6857	1.4938 ± 0.6116
NGC5623	0.0132	III-s	E7 A	10.79	-21.70	5.01	1.4031 ± 0.0389	1.3898 ± 0.0296
NGC5630	0.0108	II.o-OLR	Sdm B	9.51	-20.31	4.20	1.1566 ± 0.0316	1.1712 ± 0.0272
NGC5631	0.0083	III	S0 A	10.54	-21.50	4.54	1.3260 ± 0.1212	1.3326 ± 0.0774
NGC5633	0.0096	III	Sbc A	10.25	-20.98	1.83	3.1312 ± 0.0581	3.1263 ± 0.0466
NGC5635	0.0164	II-CT	Sa A	11.04	-22.33	8.64	1.2040 ± 0.0519	1.4745 ± 0.2401
NGC5657	0.0151	II.o-OLR	Sbc B	10.34	-21.05	6.00	1.8181 ± 0.0365	1.8898 ± 0.0454
NGC5659	0.0170	II-CT	Sb A	10.45	-21.14	7.60	1.7313 ± 0.0291	1.7031 ± 0.0167
NGC5675	0.0152	III-s	SaAB	10.62	-21.84	7.77	0.6464 ± 0.0415	0.6015 ± 0.0858
NGC5684	0.0156	III-s	E3 A	10.70	-21.77	6.57	2.0968 ± 0.0550	2.1596 ± 0.0696
NGC5714	0.0093	II-CT	Sb A	10.06	-20.05	4.70	1.2834 ± 0.0295	1.3127 ± 0.0194
NGC5720	0.0275	III	Sbc B	10.85	-22.30	11.03	1.9490 ± 0.0533	1.9490 ± 0.0532
NGC5731	0.0103	III	SdAB	8.98	-19.56	3.11	1.3986 ± 0.0598	1.4064 ± 0.0753
NGC5732	0.0144	II-CT	Sbc A	9.89	-20.49	5.43	1.6921 ± 0.0420	1.6311 ± 0.0248
NGC5735	0.0145	II.o-OLR	Sbc B	10.13	-21.37	6.67	1.7380 ± 0.0271	1.6893 ± 0.0537
NGC5739	0.0198	III	S0aAB	11.14	-22.91	9.65	1.7317 ± 0.0474	1.7632 ± 0.0517
NGC5772	0.0182	III	Sab A	10.79	-22.15	8.23	2.1118 ± 0.0372	2.1164 ± 0.0387
NGC5784	0.0197	III	S0 A	11.16	-22.62	8.43	1.9021 ± 0.2856	2.1070 ± 0.2982
NGC5829	0.0209	II-CT	Sc A	10.59	-21.81	9.22	1.8829 ± 0.0291	1.8826 ± 0.0189
NGC5876	0.0126	II.o-OLR	S0a B	10.68	-21.35	8.36	1.3150 ± 0.0455	1.2942 ± 0.0575
NGC5888	0.0308	II.o-OLR	Sb B	11.15	-22.77	10.21	1.6848 ± 0.0227	1.6185 ± 0.0721
NGC5908	0.0127	III-s	Sa A	11.25	-22.16	4.70	2.5907 ± 0.0861	2.5889 ± 0.1006
NGC5947	0.0214	II.o-OLR	Sbc B	10.54	-21.41	6.79	1.7525 ± 0.0313	1.7388 ± 0.0276
NGC5957	0.0078	III	Sb B	9.99	-20.79	3.04	1.7020 ± 0.0150	1.7175 ± 0.0282
NGC5971	0.0159	II.o-CT	SbAB	10.22	-20.83	5.50	1.5803 ± 0.0210	1.5802 ± 0.0239
NGC5980	0.0157	II-CT	Sbc A	10.73	-21.81	4.93	1.9841 ± 0.0226	2.0121 ± 0.0227
NGC6004	0.0148	II.o-OLR	Sbc B	10.66	-21.88	6.46	1.5001 ± 0.0134	1.4931 ± 0.0148
NGC6032	0.0163	II.o-OLR	Sbc B	10.26	-21.21	5.94	1.6877 ± 0.0822	1.7016 ± 0.0923

NGC6060	0.0168	II-CT	Sb A	10.83	-22.27	10.73	0.8722 ± 0.0166	0.9010 ± 0.0128
NGC6063	0.0114	II-CT	Sbc A	9.94	-20.54	5.05	1.2008 ± 0.0188	1.1963 ± 0.0241
NGC6081	0.0194	II-CT	S0a A	10.97	-21.94	6.67	1.5846 ± 0.0299	1.5715 ± 0.0298
NGC6154	0.0216	III	Sab B	10.77	-22.21	8.23	1.9648 ± 0.0590	1.9392 ± 0.0618
NGC6155	0.0098	II-CT	Sc A	10.13	-20.79	2.85	2.1482 ± 0.0685	2.1188 ± 0.0681
NGC6168	0.0103	II.o-OLR	ScAB	9.78	-20.00	3.17	1.8883 ± 0.0566	1.8851 ± 0.0481
NGC6186	0.0117	II.o-OLR	Sb B	10.49	-21.21	2.86	2.1890 ± 0.0326	2.1820 ± 0.0360
NGC6301	0.0293	II-CT	Sbc A	10.78	-22.66	14.25	1.2115 ± 0.0552	1.2426 ± 0.0845
NGC6310	0.0128	II-CT	Sb A	10.49	-20.99	4.78	1.2065 ± 0.0429	1.2118 ± 0.0435
NGC6361	0.0141	II-CT	Sab A	10.89	-21.51	6.40	1.3225 ± 0.0524	1.3605 ± 0.0738
NGC6394	0.0294	II.o-OLR	Sbc B	10.76	-21.88	14.60	1.8524 ± 0.5450	1.8744 ± 0.1591
NGC6478	0.0239	II-CT	Sc A	10.97	-22.59	9.32	1.1671 ± 0.0608	1.2176 ± 0.0264
NGC6497	0.0217	II.o-OLR	Sab B	10.93	-22.08	20.05	0.7380 ± 0.0118	0.7444 ± 0.0105
NGC7047	0.0199	II.o-OLR	Sbc B	10.70	-21.82	5.59	2.6924 ± 0.0807	2.6822 ± 0.2942
NGC7311	0.0153	III	Sa A	10.97	-22.48	5.55	2.7295 ± 0.5309	1.9428 ± 1.0860
NGC7321	0.0238	II.o-OLR	Sbc B	10.89	-22.48	9.15	1.6047 ± 0.0664	1.5953 ± 0.0513
NGC7364	0.0163	III	Sab A	10.81	-22.03	5.78	1.3978 ± 0.3478	1.3646 ± 0.3904
NGC7466	0.0249	II-CT	Sbc A	10.62	-21.91	11.72	1.6175 ± 0.0412	1.6018 ± 0.0354
NGC7489	0.0207	II-CT	Sbc A	10.34	-22.05	10.15	1.7673 ± 0.0341	1.7637 ± 0.0313
NGC7549	0.0158	III	Sbc B	10.22	-21.39	8.49	1.2469 ± 0.0392	1.2464 ± 0.0309
NGC7591	0.0164	II.o-OLR	Sbc B	10.67	-21.93	8.17	1.3972 ± 0.0533	1.4095 ± 0.0468
NGC7625	0.0058	III	Sa A	9.89	-20.31	1.75	3.0677 ± 0.0761	3.0453 ± 0.0940
NGC7631	0.0125	II-CT	Sb A	10.39	-21.10	6.82	1.7357 ± 0.0258	1.6968 ± 0.0205
NGC7653	0.0142	II-CT	Sb A	10.48	-21.62	6.09	2.0509 ± 0.0438	2.0168 ± 0.0413
NGC7684	0.0170	II-CT	S0 A	10.93	-21.68	5.25	2.3845 ± 0.0536	2.3868 ± 0.0655
NGC7691	0.0134	II.o-CT	Sbc B	10.18	-21.30	8.67	1.5071 ± 0.0349	1.4580 ± 0.0170
NGC7716	0.0087	III	Sb A	10.29	-20.98	4.14	1.1831 ± 0.3328	1.5154 ± 0.1099
NGC7738	0.0222	III	Sb B	10.88	-22.17	9.09	1.4136 ± 0.0990	1.4745 ± 0.0539
NGC7782	0.0177	II-CT	Sb A	11.08	-22.64	10.37	0.9940 ± 0.0323	0.9942 ± 0.0361
NGC7787	0.0219	III	SabAB	10.43	-21.11	8.40	1.2977 ± 0.0679	1.2457 ± 0.0642
NGC7800	0.0060	III	IrAB	9.21	-19.58	2.44	1.5866 ± 0.1718	1.6188 ± 0.0636
NGC7819	0.0164	II-CT	Sc A	10.09	-21.05	8.16	1.4266 ± 0.0494	1.4336 ± 0.0411
NGC7824	0.0201	II-CT	Sab A	11.15	-22.24	11.47	1.5688 ± 0.0277	1.5591 ± 0.0318
SDSSJ100141	0.0066	II.o-CT	SmAB	8.73	-18.26	3.29	1.6757 ± 0.0391	1.7059 ± 0.0408
UGC00005	0.0238	II-CT	Sbc A	10.76	-22.09	9.51	1.6806 ± 0.0797	1.6314 ± 0.0934
UGC00139	0.0130	III	Scd A	9.61	-20.37	6.57	1.3911 ± 0.0590	1.4361 ± 0.0539
UGC00148	0.0138	II-CT	Sc A	10.01	-20.75	5.11	1.5290 ± 0.0657	1.5583 ± 0.0546
UGC00312	0.0142	II.o-OLR	Sd B	9.69	-20.67	6.33	1.7867 ± 0.1282	1.7157 ± 0.1462
UGC00809	0.0138	II-CT	Scd A	9.58	-19.72	5.09	1.6908 ± 0.0327	1.7020 ± 0.0362
UGC00841	0.0182	II-CT	Sbc A	9.93	-20.22	7.31	1.2645 ± 0.0322	1.3716 ± 0.0883

UGC00987	0.0152	III	SaAB	10.55	-21.24	6.39	1.1408 ± 0.0416	1.1376 ± 0.0526
UGC01057	0.0206	II.o-OLR	ScAB	10.11	-20.88	8.63	1.7293 ± 0.0576	1.7289 ± 0.0392
UGC01274	0.0255	II-CT	Sa A	10.78	-21.81	9.49	1.4293 ± 0.0420	1.4241 ± 0.0878
UGC01368	0.0262	II-CT	Sab A	10.79	-21.71	8.91	1.5586 ± 0.0420	1.5060 ± 0.0682
UGC01659	0.0267	II.o-OLR	Sc B	10.50	-21.69	13.88	1.3119 ± 0.0333	1.2649 ± 0.0420
UGC01749	0.0261	II.o-OLR	SabAB	10.68	-21.44	15.24	1.0138 ± 0.0144	1.0128 ± 0.0197
UGC01918	0.0165	II.o-OLR	Sb B	10.55	-21.14	7.70	1.4280 ± 0.0319	1.4313 ± 0.0374
UGC01938	0.0206	II.o-OLR	SbcAB	10.28	-20.94	8.02	1.9052 ± 0.1632	1.7498 ± 0.1163
UGC02403	0.0133	III	Sb B	10.48	-20.80	4.15	2.2143 ± 0.0441	2.2162 ± 0.0475
UGC02405	0.0249	II-CT	Sbc A	10.41	-21.72	11.71	1.0725 ± 0.0461	1.0809 ± 0.0498
UGC03038	0.0264	II-CT	Sab A	10.71	-21.54	10.11	1.3684 ± 0.0339	1.3954 ± 0.0260
UGC03107	0.0273	II-CT	Sb A	10.65	-21.54	10.90	1.4485 ± 0.1768	1.4310 ± 0.2009
UGC03151	0.0143	II.o-CT	SaAB	10.59	-21.62	4.68	1.3883 ± 0.1013	1.3500 ± 0.0796
UGC03253	0.0145	II.o-OLR	Sb B	10.43	-21.06	5.87	1.7592 ± 0.0539	1.7839 ± 0.4846
UGC03539	0.0117	III	ScAB	9.83	-19.67	7.41	0.9370 ± 0.0400	0.8470 ± 0.0656
UGC03899	0.0135	II-CT	Sd A	9.00	-19.22	3.99	1.7823 ± 0.0474	1.8021 ± 0.0452
UGC03944	0.0136	II.o-CT	SbcAB	9.89	-20.47	5.94	2.0594 ± 0.0428	2.0515 ± 0.0376
UGC03969	0.0275	II-CT	Sb A	10.68	-21.16	8.69	1.6218 ± 0.0332	1.6436 ± 0.0248
UGC04132	0.0180	II.o-CT	SbcAB	10.71	-21.78	7.69	1.3182 ± 0.0424	1.3216 ± 0.0421
UGC04280	0.0125	II.o-CT	SbAB	10.09	-20.32	3.56	2.1887 ± 0.0595	2.2086 ± 0.0651
UGC04461	0.0174	II-CT	Sbc A	10.05	-20.85	7.59	0.8745 ± 0.0272	0.8815 ± 0.0250
UGC04659	0.0070	II-CT	Sdm A	8.83	-18.00	3.62	1.3835 ± 0.0391	1.3434 ± 0.0264
UGC05108	0.0280	II.o-OLR	Sb B	10.84	-22.12	16.27	1.0894 ± 0.0327	1.1437 ± 0.0774
UGC05111	0.0234	II.o-CT	SbAB	10.91	-21.64	8.13	1.1960 ± 0.0296	1.1925 ± 0.0318
UGC05358	0.0109	II.o-OLR	Sd B	9.26	-19.11	4.57	1.4081 ± 0.0453	1.4212 ± 0.0365
UGC05359	0.0295	II.o-OLR	Sb B	10.56	-21.66	11.08	1.0524 ± 0.0595	1.1014 ± 0.0384
UGC05396	0.0194	II.o-CT	SbcAB	10.22	-20.98	11.76	0.7763 ± 0.0356	0.7844 ± 0.0397
UGC05598	0.0202	II-CT	Sb A	10.19	-20.77	8.22	1.6524 ± 0.0529	1.6819 ± 0.0535
UGC05990	0.0068	III	Sc A	9.17	-18.31	1.61	0.8919 ± 0.0437	0.9148 ± 0.0369
UGC06036	0.0231	II-CT	Sa A	11.03	-21.92	8.04	1.9642 ± 0.0628	1.9920 ± 0.0717
UGC06256	0.0126	II-CT	Sbc A	9.78	-18.99	5.49	1.3001 ± 0.0683	1.2867 ± 0.0544
UGC07012	0.0120	III	ScdAB	9.11	-19.86	4.41	1.2077 ± 0.1914	1.1970 ± 0.1725
UGC07145	0.0238	II-CT	Sbc A	10.31	-21.16	9.22	1.7951 ± 0.0332	1.7900 ± 0.0410
UGC08004	0.0225	II.o-CT	ScdAB	9.93	-20.71	12.32	1.4406 ± 0.0372	1.4315 ± 0.0258
UGC08231	0.0099	II.o-OLR	SdAB	9.04	-19.27	4.05	1.3158 ± 0.0453	1.3212 ± 0.0348
UGC08250	0.0196	II-CT	Sc A	9.79	-20.12	8.08	1.2335 ± 0.0723	1.2175 ± 0.0672
UGC08781	0.0274	II.o-OLR	Sb B	10.96	-22.34	15.82	0.9140 ± 0.0629	0.9737 ± 0.0479
UGC09067	0.0283	III	SbcAB	10.51	-21.96	8.40	1.7151 ± 0.7951	3.0375 ± 0.2283
UGC09071	0.0079	II-CT	Scd A	8.92	-18.58	4.02	0.8437 ± 0.0420	0.8481 ± 0.0438
UGC09080	0.0119	II-CT	Sc A	8.95	-18.80	3.40	1.6483 ± 0.1056	1.6282 ± 0.0763

UGC09113	0.0126	III	SbAB	9.83	-19.75	5.08	1.2151 ± 0.1061	1.2643 ± 0.3464
UGC09165	0.0196	II-CT	Sa A	10.63	-21.06	5.67	1.3138 ± 0.0546	1.2983 ± 0.0471
UGC09253	0.0151	II.o-CT	ScAB	9.94	-20.41	4.07	2.1752 ± 0.0622	2.1598 ± 0.0412
UGC09448	0.0092	II-CT	Sb A	9.45	-18.84	3.00	1.3951 ± 0.0885	1.7689 ± 0.1596
UGC09476	0.0127	II-CT	Sbc A	10.18	-20.99	4.64	1.6335 ± 0.0420	1.6175 ± 0.0264
UGC09492	0.0299	III	SabAB	11.09	-22.34	9.87	1.3736 ± 0.0376	1.3857 ± 0.0411
UGC09537	0.0313	I	Sb A	11.12	-22.60	17.62	2.0676 ± 0.0390	2.0723 ± 0.0388
UGC09542	0.0200	II-CT	Sc A	10.30	-20.95	8.28	1.1978 ± 0.1457	1.3400 ± 0.1382
UGC09598	0.0204	II.o-CT	SbcAB	10.50	-21.23	8.17	1.5801 ± 0.0153	1.5811 ± 0.0197
UGC09665	0.0103	II-CT	Sb A	10.04	-19.99	2.81	2.2076 ± 0.0837	2.2776 ± 0.0686
UGC09759	0.0131	III	Sab A	10.14	-20.21	5.51	0.9441 ± 0.0182	0.9440 ± 0.0266
UGC09777	0.0178	II-CT	Sbc A	10.20	-20.97	6.46	2.1407 ± 0.1098	2.1490 ± 0.0517
UGC09873	0.0205	II-CT	Sb A	10.02	-20.36	9.64	1.2723 ± 0.1381	1.2273 ± 0.1189
UGC09892	0.0207	II-CT	Sbc A	10.30	-20.72	9.22	1.0650 ± 0.0385	1.0674 ± 0.0290
UGC09919	0.0126	II-CT	Sc A	9.54	-19.52	3.81	2.0477 ± 0.0632	2.0538 ± 0.0590
UGC10043	0.0091	III	SabAB	9.80	-19.30	7.79	0.2570 ± 0.0135	0.6559 ± 0.5920
UGC10123	0.0142	II-CT	Sab A	10.51	-20.55	3.84	3.1948 ± 1.5399	1.2081 ± 1.5326
UGC10257	0.0146	II-CT	Sbc A	10.00	-20.44	3.36	2.2700 ± 0.0652	2.1754 ± 0.0359
UGC10297	0.0095	III	Sc A	9.22	-19.12	4.17	1.8583 ± 0.0988	2.0298 ± 0.0699
UGC10384	0.0186	III	Sb A	10.31	-20.73	5.07	1.6045 ± 0.5386	1.6037 ± 0.4616
UGC10650	0.0117	III	Scd A	9.32	-19.37	3.36	2.9686 ± 0.1196	2.0536 ± 0.5676
UGC10811	0.0303	II.o-OLR	Sb B	10.77	-21.93	12.73	1.0068 ± 0.0452	1.1208 ± 0.0721
UGC10972	0.0172	III	Sbc A	10.33	-21.20	4.93	2.9478 ± 0.0969	2.9517 ± 0.1032
UGC11262	0.0200	II-CT	Sc A	9.87	-20.21	9.93	1.2480 ± 0.1533	1.1748 ± 0.0933
UGC11680NED01	0.0264	III	Sb B	10.70	-22.48	13.05	0.9778 ± 0.5334	1.4605 ± 0.5925
UGC11694	0.0175	III-s	S0a A	11.01	-22.04	9.11	2.2397 ± 0.0528	2.2474 ± 0.0586
UGC11717	0.0215	III	Sab A	10.63	-21.73	29.45	0.8204 ± 0.0474	0.7765 ± 0.0779
UGC11740	0.0220	II-CT	Sbc A	10.26	-21.25	4.96	2.2758 ± 0.2051	2.1389 ± 0.1306
UGC12054	0.0073	II-CT	Sc A	8.95	-18.34	2.41	2.0199 ± 0.0504	1.8872 ± 0.2555
UGC12185	0.0222	II.o-OLR	Sb B	10.54	-21.46	7.90	1.9773 ± 0.0660	1.9852 ± 0.0805
UGC12224	0.0119	II-CT	Sc A	9.92	-20.80	7.28	0.8840 ± 0.0780	0.9166 ± 0.0502
UGC12308	0.0077	III	Scd A	8.96	-18.87	5.41	0.8372 ± 0.0131	0.8379 ± 0.0133
UGC12519	0.0146	II.o-CT	ScAB	10.07	-20.55	4.57	1.9236 ± 0.0478	1.9506 ± 0.0412
UGC12633	0.0140	III	SabAB	10.19	-20.93	6.59	1.1130 ± 0.0215	1.1085 ± 0.0179
UGC12653	0.0134	II-CT	Sc A	9.79	-20.24	2.52	1.8875 ± 0.0555	1.8967 ± 0.0784
UGC12767	0.0173	II.o-OLR	Sb B	10.77	-22.32	11.92	1.6566 ± 0.0167	1.6567 ± 0.0145
UGC12810	0.0266	II.o-OLR	Sbc B	10.67	-22.01	14.89	1.7309 ± 0.0427	1.7071 ± 0.0283
UGC12857	0.0083	II-CT	Sbc A	9.77	-19.50	2.19	3.1356 ± 0.0821	3.1335 ± 0.0702
UGC12864	0.0155	III	Sc B	9.97	-20.66	7.91	2.6607 ± 0.0400	2.6164 ± 0.0446
ESO539-G014	0.0233	I	Scd A	9.98	-20.20	16.23	· · ·	· · ·

IC0159	0.0126	I	Sdm B	9.62	-20.35	5.57	···	···
IC0480	0.0158	I	ScAB	9.87	-20.37	6.89	···	···
IC0776	0.0098	I	Sdm A	9.28	-19.34	6.91	···	···
IC1256	0.0175	I	SbAB	10.25	-21.32	5.82	···	···
IC2101	0.0148	I	ScdAB	10.18	-20.90	6.56	···	···
NGC0165	0.0192	I	Sb B	10.52	-21.64	12.81	···	···
NGC0447	0.0183	I	Sa B	10.95	-22.27	13.35	···	···
NGC1645	0.0160	I	S0a B	10.75	-21.72	9.51	···	···
NGC2487	0.0168	I	Sb B	10.71	-22.19	11.45	···	···
NGC2604	0.0079	I	Sd B	9.60	-20.22	3.67	···	···
NGC2906	0.0081	I	Sbc A	10.41	-20.78	2.95	···	···
NGC2916	0.0136	I	Sbc A	10.51	-22.11	7.13	···	···
NGC3057	0.0063	I	Sdm B	9.02	-19.25	4.83	···	···
NGC3815	0.0141	I	Sbc A	10.27	-21.02	4.19	···	···
NGC3991	0.0124	I	Sm A	9.26	-20.08	3.23	···	···
NGC4185	0.0148	I	SbcAB	10.60	-21.96	9.04	···	···
NGC5016	0.0106	I	Sbc A	10.20	-21.07	3.53	···	···
NGC5157	0.0263	I	Sab B	11.06	-22.48	9.06	···	···
NGC5376	0.0086	I	SbAB	0.05	-20.86	2.65	···	···
NGC5402	0.0117	I	Sc A	9.70	-19.96	2.33	···	···
NGC5439	0.0082	I	Sb A	9.52	-19.26	1.69	···	···
NGC5520	0.0081	I	Sbc A	9.79	-20.24	2.54	···	···
NGC5549	0.0279	I	S0 A	11.31	-23.05	11.58	···	···
NGC5656	0.0125	I	Sb A	0.05	-21.66	3.44	···	···
NGC5665	0.0091	I	ScAB	10.02	-21.09	3.67	···	···
NGC5682	0.0094	I	Scd B	9.31	-19.43	4.22	···	···
NGC5730	0.0103	I	Scd A	9.67	-19.76	4.40	···	···
NGC5951	0.0077	I	ScdAB	9.68	-20.12	5.14	···	···
NGC6132	0.0186	I	Sbc A	10.14	-21.10	6.67	···	···
NGC6941	0.0216	I	Sb B	10.92	-22.39	11.13	···	···
NGC7536	0.0156	I	ScAB	10.25	-21.13	7.31	···	···
NGC7722	0.0133	I	Sab A	10.95	-22.02	8.89	···	···
UGC02465	0.0165	I	S0 A	10.64	-21.28	10.79	···	···
UGC03973	0.0226	I	Sbc B	10.58	-22.25	7.36	···	···
UGC03995	0.0164	I	Sb B	10.77	-22.08	12.37	···	···
UGC04054	0.0078	I	Scd A	9.19	-19.03	3.75	···	···
UGC04722	0.0070	I	Sdm A	8.71	-18.20	37.47	···	···
UGC05244	0.0112	I	Sbc A	9.29	-19.18	4.82	···	···
UGC08322	0.0275	I	S0aAB	11.05	-22.24	7.21	···	···
UGC08733	0.0097	I	Sdm B	9.31	-19.75	4.48	···	···

UGC09199	0.0280	I	SbAB	10.65	-21.31	4.26	···	···
UGC09291	0.0116	I	Scd A	9.80	-20.83	5.98	···	···
UGC09401	0.0209	I	SaAB	10.89	-22.00	7.27	···	···
UGC09537	0.0313	I	Sb A	11.12	-22.60	17.62	···	···
UGC09842	0.0315	I	Sbc B	10.62	-21.80	12.91	···	···
UGC09849	0.0133	I	Sd A	9.44	-19.31	6.05	···	···
UGC09901	0.0125	I	Sc A	9.37	-19.37	3.58	···	···
UGC10710	0.0294	I	Sb A	10.89	-22.13	12.64	···	···
UGC10796	0.0117	I	ScdAB	9.28	-19.49	4.75	···	···
UGC11649	0.0135	I	Sab B	10.39	-21.29	5.56	···	···
UGC12816	0.0175	I	Sc A	9.38	-20.55	8.28	···	···
UGCA021	0.0064	I	Sdm B	9.01	-19.74	4.83	···	···

B.2 Derived physical properties at break radius for the CALIFA galaxies

In this Appendix are provided the best-fitting parameters obtained for the breaks in the surface brightness profile of the CALIFA galaxies' outer disks. The results obtained are summarized in the following table.

The derived properties of each galaxies listed after are:

1. galaxy name,
2. the photometrical type obtained from our analysis of the SDSS *r'*-band profiles,
3. $R_{r',break}$, the break radius obtained as the minimum of the double bootstrapping fit to the SDSS *r'*$-$band data in units of their $\mathrm{R_{eff}}$ along with their errors,
4. $\Delta\,\alpha_{\mathrm{(O/H)}}$ represents the difference between the outer-to-the-inner slopes as measured in the oxygen profiles,
5. $\Delta\,\alpha_{\mathrm{color}}$ represents the difference between the outer-to-the-inner slopes as measured in the (*g'*$-$*r'*) color profiles,
6. mu$_{r',break}$, *r'*-band surface brightness computed at the break radius in unit of magnitudes/$''^2$,
7. (*g'*$-$*r'*)$_{r',break}$, color value computed at the break radius in unit of magnitudes,
8. (O/H)$_{r',break}$, oxygen abundance value computed at the break radius and expressed in dex

Name	PhotT	$R_{r',break}$	$\Delta\,\alpha_{(O/H)}$	$\Delta\,\alpha_{color}$	$mu_{r',break}$	$(g'-r')_{r',break}$	$(O/H)_{r',break}$
2MASXJ01331766	II.o-OLR	1.4761 ± 0.0367	0.0311 ± 0.0137	0.1233 ± 0.0196	21.9443	0.4645	8.3922
ESO540-G003	III	2.1202 ± 0.2192	0.0250 ± 0.0073	0.1039 ± 0.0273	22.2779	0.4621	8.5081
IC0995	II.o-CT	1.3029 ± 0.0377	0.0436 ± 0.0236	0.1516 ± 0.0383	21.8803	0.3828	8.3875
IC1151	II.o-CT	1.4112 ± 0.0320	0.0278 ± 0.0152	0.2408 ± 0.0247	22.5108	0.3826	8.3934
IC1199	II.o-OLR	0.7988 ± 0.0379	0.1033 ± 0.0916	0.5204 ± 0.0931	21.5814	0.6187	8.5825
IC1528	II.o-CT	2.0091 ± 0.0704	0.1765 ± 0.0753	0.0471 ± 0.0759	23.5494	0.3657	8.4267
IC2095	II.o-CT	1.1836 ± 0.0453	0.1241 ± 0.0782	0.0963 ± 0.0874	23.1223	0.3954	8.1490
MCG-02-02-030	II.o-OLR	1.1900 ± 0.0575	0.0142 ± 0.0066	0.1353 ± 0.0110	20.9136	0.6622	8.5650
MCG-02-02-040	II.o-CT	2.2344 ± 0.0637	0.4204 ± 0.1658	0.0549 ± 0.1662	22.4190	0.5627	8.4410
MCG-02-51-004	II-CT	1.0193 ± 0.0677	0.1038 ± 0.0709	0.4136 ± 0.0736	21.7452	0.5489	8.5411
NGC0001	III	2.3990 ± 0.1989	0.0445 ± 0.0148	0.0274 ± 0.0193	23.9403	0.6315	8.5613
NGC0023	III	1.4986 ± 0.0362	0.0193 ± 0.0091	0.0639 ± 0.0307	22.9655	0.6511	8.6450
NGC0036	II.o-OLR	1.1576 ± 0.1444	0.0455 ± 0.0318	0.0257 ± 0.0429	22.5453	0.6249	8.5431
NGC0171	II.o-OLR	1.9621 ± 0.1200	0.0571 ± 0.0249	0.0186 ± 0.0284	23.1604	0.5349	8.5885
NGC0177	II-CT	1.2184 ± 0.0476	0.0296 ± 0.0176	0.0349 ± 0.0266	21.7609	0.5540	8.5641
NGC0180	II.o-OLR	1.3455 ± 0.0237	0.0553 ± 0.0332	0.0703 ± 0.0371	22.5772	0.5605	8.5493
NGC0192	II.o-CT	0.9532 ± 0.0156	0.0124 ± 0.0072	0.0762 ± 0.0165	20.3120	0.7596	8.6410
NGC0216	III	1.8726 ± 0.0781	0.0458 ± 0.0172	0.1157 ± 0.0192	22.5519	0.5507	8.3604
NGC0234	II.o-CT	1.3841 ± 0.0468	0.0186 ± 0.0096	0.1407 ± 0.0161	21.8476	0.6339	8.5563
NGC0237	III	1.6295 ± 0.0370	0.0427 ± 0.0159	0.2050 ± 0.0332	22.3930	0.4613	8.5195
NGC0257	II-CT	1.2135 ± 0.0303	0.0356 ± 0.0187	0.2551 ± 0.0252	21.4468	0.5558	8.5686
NGC0444	II-CT	1.5290 ± 0.0444	0.0727 ± 0.0395	0.0125 ± 0.0447	22.7991	0.5124	8.4263
NGC0477	II.o-CT	1.0857 ± 0.0342	0.0221 ± 0.0166	0.1149 ± 0.0462	22.7822	0.4341	8.5100
NGC0551	II.o-OLR	1.4900 ± 0.0801	0.0521 ± 0.0301	0.1523 ± 0.0405	21.8906	0.5984	8.5713
NGC0681	III-s	0.9584 ± 0.1154	0.0607 ± 0.0487	0.1526 ± 0.0494	21.5312	0.7305	8.5038
NGC0693	III	1.0200 ± 0.0408	0.0259 ± 0.0187	0.0717 ± 0.0230	22.4233	0.6720	8.5520
NGC0716	II.o-CT	1.5636 ± 0.0272	0.0382 ± 0.0197	0.1508 ± 0.0392	21.5638	0.5614	8.5717
NGC0768	II.o-OLR	1.7437 ± 0.0398	0.1192 ± 0.0590	0.0184 ± 0.0633	22.8962	0.4023	8.4940
NGC0776	II.o-OLR	1.1795 ± 0.0439	0.0275 ± 0.0118	0.3186 ± 0.0549	21.7079	0.5962	8.6038
NGC0932	II-CT	1.1081 ± 0.0328	0.0312 ± 0.0195	0.2188 ± 0.0294	21.8986	0.8547	8.5458
NGC1056	III-s	0.9716 ± 0.0396	0.0199 ± 0.0126	0.0919 ± 0.0226	22.4664	0.7892	8.5204

NGC1093	III	1.4703 ± 0.7340	0.0743 ± 0.0564	0.3297 ± 0.1744	23.0920	0.5000	8.5674
NGC1677	III	1.3919 ± 0.1343	0.0500 ± 0.0259	0.2729 ± 0.0400	22.5778	0.6220	8.4583
NGC2730	II.o-OLR	1.4785 ± 0.0189	0.1273 ± 0.0754	0.3035 ± 0.0842	23.0287	0.4359	8.4813
NGC2805	III	0.4698 ± 0.0458	0.0165 ± 0.0236	0.1493 ± 0.0444	22.0101	0.5347	8.5327
NGC3381	III	1.9026 ± 0.1292	0.0245 ± 0.0099	0.0936 ± 0.0351	22.9745	0.4336	8.5009
NGC3614	II.o-OLR	0.9885 ± 0.3214	0.0826 ± 0.0650	0.1602 ± 0.0711	22.6938	0.3986	8.4852
NGC3687	II.o-OLR	1.8009 ± 0.0528	0.1952 ± 0.0879	0.0772 ± 0.0882	23.1171	0.4410	8.5062
NGC3811	III	1.8552 ± 0.2237	0.0493 ± 0.0199	0.0865 ± 0.0322	23.2928	0.4354	8.5459
NGC3994	III	1.8521 ± 0.0176	0.0296 ± 0.0103	0.0899 ± 0.0199	23.1548	0.5789	8.6350
NGC4149	II.o-OLR	2.2025 ± 0.0802	0.0152 ± 0.0045	0.0792 ± 0.0085	20.6926	0.6405	8.5893
NGC4210	II.o-OLR	1.7599 ± 0.0986	0.0867 ± 0.0354	0.3218 ± 0.0460	22.0749	0.4458	8.5691
NGC4711	II-CT	1.7437 ± 0.0297	0.0712 ± 0.0312	0.1526 ± 0.0373	21.6948	0.4841	8.5573
NGC4961	II.o-OLR	1.6405 ± 0.0303	0.0580 ± 0.0255	0.2623 ± 0.0345	22.4703	0.2530	8.4078
NGC5000	III	1.4252 ± 0.0308	0.0230 ± 0.0099	0.1216 ± 0.0388	22.6819	0.5808	8.5781
NGC5267	II.o-OLR	1.8566 ± 0.0887	0.1966 ± 0.0942	0.0147 ± 0.0949	22.0734	0.6565	8.6318
NGC5289	II.o-CT	1.4354 ± 0.0155	0.0386 ± 0.0203	0.0821 ± 0.0217	21.7146	0.5491	8.5456
NGC5406	II.o-OLR	1.5502 ± 0.0536	0.0436 ± 0.0177	0.1540 ± 0.0228	22.3001	0.4853	8.5911
NGC5443	III	1.6658 ± 0.0378	0.0361 ± 0.0183	0.0609 ± 0.0199	22.3751	0.6730	8.5721
NGC5522	II.o-OLR	1.5589 ± 0.0178	0.0719 ± 0.0396	0.3314 ± 0.0423	21.9747	0.4966	8.5810
NGC5533	III	0.9619 ± 0.0590	0.0218 ± 0.0173	0.1175 ± 0.0361	22.3573	0.6742	8.5761
NGC5587	II-CT	0.5978 ± 0.0174	0.0041 ± 0.0034	0.1362 ± 0.0099	20.3161	0.7939	8.6298
NGC5610	II.o-OLR	1.0775 ± 0.0340	0.6333 ± 0.5208	1.0974 ± 0.5351	23.3642	0.4466	8.5562
NGC5616	II.o-CT	1.2034 ± 0.1153	0.0464 ± 0.0249	0.0993 ± 0.0653	22.0481	0.5623	8.5762
NGC5622	II-CT	1.5292 ± 0.6857	0.0773 ± 0.0384	0.1321 ± 0.0724	22.6505	0.4417	8.5062
NGC5630	II.o-OLR	1.1566 ± 0.0316	0.0457 ± 0.0264	0.1216 ± 0.0353	21.4752	0.2654	8.3468
NGC5635	II-CT	1.2040 ± 0.0519	0.0248 ± 0.0141	0.1515 ± 0.0234	21.5062	0.7073	8.5666
NGC5657	II.o-OLR	1.8181 ± 0.0365	0.0783 ± 0.0324	0.1047 ± 0.0351	22.9777	0.4604	8.4656
NGC5714	II-CT	1.2834 ± 0.0295	0.0265 ± 0.0146	0.1293 ± 0.0175	21.5869	0.5628	8.5202
NGC5731	III	1.3986 ± 0.0598	0.0259 ± 0.0137	0.1835 ± 0.0248	22.3412	0.2855	8.3648
NGC5735	II.o-OLR	1.7380 ± 0.0271	0.1057 ± 0.0497	0.1154 ± 0.0523	23.1385	0.4507	8.5201
NGC5829	II-CT	1.8829 ± 0.0291	0.0973 ± 0.0457	0.3147 ± 0.0468	23.5771	0.3528	8.4235
NGC5908	III-s	2.5907 ± 0.0861	0.0157 ± 0.0048	0.0947 ± 0.0066	22.0215	0.7362	8.7320
NGC5947	II.o-OLR	1.7525 ± 0.0313	0.0710 ± 0.0338	0.0034 ± 0.0383	22.7007	0.4226	8.5135

NGC5980	II-CT	1.9841 ± 0.0226	0.0767 ± 0.0321	0.3709 ± 0.0340	21.9156	0.4288	8.5613
NGC6004	II.o-OLR	1.5001 ± 0.0134	0.0265 ± 0.0140	0.1978 ± 0.0176	22.1011	0.6129	8.5756
NGC6032	II.o-OLR	1.6877 ± 0.0822	0.0236 ± 0.0103	0.0262 ± 0.0243	22.6953	0.6487	8.5407
NGC6060	II-CT	0.8722 ± 0.0166	0.0387 ± 0.0285	0.2010 ± 0.0327	21.2152	0.6829	8.5733
NGC6063	II-CT	1.2008 ± 0.0188	0.0274 ± 0.0189	0.1189 ± 0.0270	22.0787	0.4831	8.5145
NGC6155	II-CT	2.1482 ± 0.0685	0.0368 ± 0.0152	0.1761 ± 0.0191	22.6385	0.5406	8.5457
NGC6168	II.o-OLR	1.8883 ± 0.0566	0.0379 ± 0.0168	0.0590 ± 0.0176	21.7263	0.5988	8.4016
NGC6186	II.o-OLR	2.1890 ± 0.0326	0.0407 ± 0.0165	0.1861 ± 0.0170	21.4848	0.6433	8.6275
NGC6301	II-CT	1.2115 ± 0.0552	0.0221 ± 0.0128	0.0372 ± 0.0170	22.0241	0.5269	8.5365
NGC6310	II-CT	1.2065 ± 0.0429	0.0095 ± 0.0045	0.0244 ± 0.0157	20.9412	0.7308	8.5873
NGC6478	II-CT	1.1671 ± 0.0608	0.0351 ± 0.0156	0.1680 ± 0.0422	20.9371	0.5456	8.5698
NGC6497	II.o-OLR	0.7380 ± 0.0118	0.1506 ± 0.1777	0.4406 ± 0.1812	22.4704	0.6111	8.6137
NGC7321	II.o-OLR	1.6047 ± 0.0664	0.0319 ± 0.0140	0.0943 ± 0.0165	22.4925	0.4973	8.5514
NGC7364	III	1.3978 ± 0.3478	0.0149 ± 0.0071	0.0270 ± 0.0128	22.0679	0.7015	8.5968
NGC7489	II-CT	1.7673 ± 0.0341	0.1257 ± 0.0670	0.5392 ± 0.0674	23.0400	0.4615	8.3203
NGC7549	III	1.2469 ± 0.0392	0.0330 ± 0.0213	0.0697 ± 0.0359	22.5154	0.7149	8.5557
NGC7591	II.o-OLR	1.3972 ± 0.0533	0.0471 ± 0.0256	0.2346 ± 0.0391	22.3105	0.6585	8.6003
NGC7691	II.o-CT	1.5071 ± 0.0349	0.1668 ± 0.0993	0.1832 ± 0.1012	23.3423	0.4827	8.4083
NGC7716	III	1.1831 ± 0.3328	0.0888 ± 0.0432	0.0913 ± 0.1239	21.6834	0.4936	8.5490
NGC7782	II-CT	0.9940 ± 0.0323	0.0092 ± 0.0051	0.1958 ± 0.0199	21.3228	0.6876	8.5795
NGC7800	III	1.5866 ± 0.1718	0.0579 ± 0.0249	0.0666 ± 0.0649	22.5799	0.3805	8.3417
NGC7819	II-CT	1.4266 ± 0.0494	0.0332 ± 0.0156	0.2225 ± 0.0192	22.8648	0.4172	8.4950
SDSSJ100141	II.o-CT	1.6757 ± 0.0391	0.2664 ± 0.1383	0.0587 ± 0.1388	24.1090	0.1821	8.1108
UGC00139	III	1.3911 ± 0.0590	0.0346 ± 0.0181	0.1979 ± 0.0423	23.0474	0.3295	8.4187
UGC00148	II-CT	1.5290 ± 0.0657	0.0169 ± 0.0064	0.1202 ± 0.0111	21.3740	0.5056	8.4393
UGC00312	II.o-OLR	1.7867 ± 0.1282	0.1158 ± 0.0543	0.1337 ± 0.0614	23.2612	0.3012	8.3443
UGC00809	II-CT	1.6908 ± 0.0327	0.1245 ± 0.0567	0.2657 ± 0.0579	22.3242	0.5287	8.3542
UGC00841	II-CT	1.2645 ± 0.0322	0.0691 ± 0.0375	0.0324 ± 0.0404	22.0943	0.5598	8.4811
UGC00987	III	1.1408 ± 0.0416	0.0138 ± 0.0072	0.0870 ± 0.0137	21.8566	0.7113	8.6331
UGC01057	II.o-OLR	1.7293 ± 0.0576	0.0781 ± 0.0343	0.6681 ± 0.0439	23.2597	0.3424	8.4055
UGC01659	II.o-OLR	1.3119 ± 0.0333	0.1254 ± 0.0712	0.0105 ± 0.0787	22.4374	0.6283	8.5032
UGC01749	II.o-OLR	1.0138 ± 0.0144	0.1937 ± 0.1572	0.0627 ± 0.1576	22.2254	0.7855	8.5728
UGC02403	III	2.2143 ± 0.0441	0.0392 ± 0.0126	0.1059 ± 0.0236	23.0036	0.7346	8.6383

UGC02405	II-CT	1.0725 ± 0.0461	0.0466 ± 0.0279	0.3443 ± 0.0820	21.8839	0.5037	8.5155
UGC03253	II.o-OLR	1.7592 ± 0.0539	0.1266 ± 0.0607	0.1712 ± 0.0621	23.1580	0.5381	8.5423
UGC03539	III	0.9370 ± 0.0400	0.0853 ± 0.0676	0.4401 ± 0.0712	22.4952	0.4209	8.4751
UGC03899	II-CT	1.7823 ± 0.0474	0.0919 ± 0.0448	0.2593 ± 0.0486	23.2729	0.2744	8.2331
UGC04132	II.o-CT	1.3182 ± 0.0424	0.0283 ± 0.0138	0.1341 ± 0.0216	21.4140	0.6716	8.5673
UGC05108	II.o-OLR	1.0894 ± 0.0327	0.1672 ± 0.1191	0.2673 ± 0.1220	23.0755	0.5331	8.5851
UGC05111	II.o-CT	1.1960 ± 0.0296	0.0298 ± 0.0162	0.0577 ± 0.0285	21.3205	0.8661	8.5572
UGC05358	II.o-OLR	1.4081 ± 0.0453	0.0566 ± 0.0302	0.1757 ± 0.0371	23.5825	0.2881	8.3499
UGC05359	II.o-OLR	1.0524 ± 0.0595	0.0396 ± 0.0230	0.1202 ± 0.0310	22.0802	0.5417	8.5371
UGC05396	II.o-CT	0.7763 ± 0.0356	0.0391 ± 0.0285	0.3451 ± 0.0415	21.7213	0.4895	8.5037
UGC07012	III	1.2077 ± 0.1914	0.0194 ± 0.0097	0.0242 ± 0.0472	23.2451	0.2921	8.4002
UGC07145	II-CT	1.7951 ± 0.0332	0.1357 ± 0.0645	0.2028 ± 0.0655	23.1649	0.4602	8.4625
UGC08231	II.o-OLR	1.3158 ± 0.0453	0.0757 ± 0.0427	0.4464 ± 0.0456	22.5212	0.1366	8.2508
UGC08250	II-CT	1.2335 ± 0.0723	0.2576 ± 0.1568	0.1680 ± 0.1574	22.4006	0.4702	8.3792
UGC08781	II.o-OLR	0.9140 ± 0.0629	0.1438 ± 0.1006	0.1518 ± 0.1048	22.3946	0.4697	8.5896
UGC09067	III	1.7151 ± 0.7951	0.1146 ± 0.0306	0.2153 ± 0.0832	22.9252	0.4035	8.4633
UGC09071	II-CT	0.8437 ± 0.0420	0.0228 ± 0.0185	0.0663 ± 0.0495	22.1546	0.4349	8.3845
UGC09598	II.o-CT	1.5801 ± 0.0153	0.0926 ± 0.0464	0.1486 ± 0.0483	22.4715	0.5251	8.4982
UGC09665	II-CT	2.2076 ± 0.0837	0.1304 ± 0.0465	0.2495 ± 0.0468	22.4083	0.3744	8.5890
UGC09759	III	0.9441 ± 0.0182	0.0219 ± 0.0153	0.1220 ± 0.0293	22.3046	0.6414	8.4923
UGC09777	II-CT	2.1407 ± 0.1098	0.6101 ± 0.2514	0.1333 ± 0.2523	24.5863	0.2621	8.4851
UGC09873	II-CT	1.2723 ± 0.1381	0.2507 ± 0.1704	0.1644 ± 0.1719	22.5546	0.5463	8.4752
UGC09892	II-CT	1.0650 ± 0.0385	0.0409 ± 0.0285	0.2674 ± 0.0309	22.1741	0.5287	8.5142
UGC10257	II-CT	2.2700 ± 0.0652	0.0328 ± 0.0126	0.0650 ± 0.0173	22.0132	0.4698	8.4336
UGC10384	III	1.6045 ± 0.5386	0.1101 ± 0.0453	0.2309 ± 0.0779	22.3213	0.4425	8.4823
UGC10811	II.o-OLR	1.0068 ± 0.0452	0.0464 ± 0.0284	0.0453 ± 0.0690	21.9359	0.6094	8.5764
UGC11262	II-CT	1.2480 ± 0.1533	0.1705 ± 0.1205	0.0714 ± 0.1233	23.5880	0.4264	8.4449
UGC11740	II-CT	2.2758 ± 0.2051	0.0756 ± 0.0195	0.1548 ± 0.0212	22.4081	0.5504	8.5091
UGC12224	II-CT	0.8840 ± 0.0780	0.0332 ± 0.0244	0.0897 ± 0.1436	22.2285	0.5188	8.5215
UGC12308	III	0.8372 ± 0.0131	0.0266 ± 0.0208	0.0252 ± 0.0659	22.3933	0.3840	8.3213
UGC12519	II.o-CT	1.9236 ± 0.0478	0.1325 ± 0.0560	0.2981 ± 0.0566	21.5957	0.5128	8.4800
UGC12767	II.o-OLR	1.6566 ± 0.0167	0.1240 ± 0.0652	0.2901 ± 0.0659	23.4284	0.6607	8.5822
UGC12810	II.o-OLR	1.7309 ± 0.0427	0.3052 ± 0.1548	0.1027 ± 0.1575	23.6597	0.4496	8.5057

UGC12864	III	2.6607 ± 0.0400	0.1354 ± 0.0455	0.0879 ± 0.0485	25.1057	0.3601	8.4083

C

Appendix C: List of publications

In this Appendix its provided a full list of all publications in which I was involved during my Ph.D. Thesis and that are related to the topic of this Ph.D. (IFU spectroscopy of galaxies in the nearby Universe). 50 papers in total, 35 of these refereed, 3 as first author, 2 as third author. These papers have been cited 623 in total, among these 51 as first author. These works have been presented in 50 national and international meetings.

C.1 List of Publications

C.1.1 Refereed (First Author)

- OUTER–DISK REDDENING AND GAS-PHASE METALLICITIES: THE CALIFA CONNECTION
  Marino, R.A.; Gil de Paz, A.; Sánchez, S.F.; Sánchez-Blázquez, P.; Castillo-Morales, A.; Cardiel, N.; Pascual, S.; Mollá, M.; Vílchez, J.; Kehrig, C.; Méndez-Abreu, J.; Catalán-Torrecilla, C.; Florido, E.; Pérez, I.; Ruiz-Lara, T.; Ellis, S.; López-Sánchez, A.R.; González Delgado, R.; de Lorenzo-Cáceres, A.; García-Benito, R.; Galbany, L.; Zibetti, S.; Cortijo-Ferrero, C.; Kalinova, V.; Mast, D.; Iglesias-Páramo, J.; Papaderos, P.; Walcher, J. C. and the CALIFA team. *Astronomy & Astrophysics, 2015, submitted*

- THE O3N2 AND N2 ABUNDANCE INDICATORS REVISITED: IMPROVED CALIBRATIONS BASED ON CALIFA AND TE-BASED LITERATURE DATA
  Marino, R.A.; Rosales-Ortega, F. F.; Sánchez, S.F.; Gil de Paz, A.; Vílchez, J.; Miralles-Caballero, D.; Kehrig, C.; Pérez-Montero, E.; Iglesias-Páramo, J.; Díaz, A.I.; Castillo-Morales, A.; Kennicutt, R.; López-Sánchez, A.R.; Galbany, L.; García-Benito, R.; Mast, D.; Méndez-Abreu, J.; Stanishev,V.; Monreal-Ibero, A.; Husemann, B.; Walcher, J. C.; García-Lorenzo, B.; Masegosa, J.; del Olmo Orozco, A.; Mourao, A.M.; Ziegler, B.; Mollá, M.; Sánchez-Blázquez, P.; González Delgado, R.; Falcón-Barroso, J.; Roth, M.M.; Papaderos, P.; van Glenn, G. and the CALIFA team. *Astronomy & Astrophysics, Volume 559, id.A114, 12 pp., 2013*

- INTEGRAL FIELD SPECTROSCOPY AND MULTI-WAVELENGTH IMAGING OF THE NEARBY SPIRAL GALAXY NGC 5668: AN UNUSUAL FLATTENING IN METALLICITY GRADIENT
  Marino, R.A.; Gil de Paz, A.; Castillo-Morales, A.; Muñoz-Mateos, J. C.; Sánchez, S. F.; Pérez-González, P. G.; Gallego, J.; Zamorano, J.; Alonso-Herrero, A.; Boissier, S. *The Astrophysical Journal, Volume 754, Issue 1, article id. 61, 24 pp., 2012*

C.1.2 Refereed (Co-Author)

- CENTRAL STAR FORMATION AND METALLICITY IN CALIFA INTERACTING GALAXIES
  Barrera-Ballesteros, J. K.; Sánchez, S. F.; García-Lorenzo, B.; Falcón-Barroso, J.; Mast, D.; García-Benito, R.; Husemann, B.; van de Ven, G.; Iglesias-Páramo, J.; Rosales-Ortega, F. F.; Pérez-Torres, M. A.; Márquez, I.; Kehrig, C.; **Marino, R. A.**; and 4 coauthors *Astronomy & Astrophysics, Volume 576, id.A45, 9 pp., 2015*

- THE CALIFA SURVEY ACROSS THE HUBBLE SEQUENCE: SPATIALLY RESOLVED STELLAR POPULATION PROPERTIES IN GALAXIES
  González Delgado, R. M.; García-Benito, R.; Pérez, E.; Cid Fernandes, R.; de Amorim, A. L.; Cortijo-Ferrero, C.; Lacerda, E. A. D.; López Fernández, R.; Vale-Asari, N.; Sánchez, S. F.; Mollá, M.; Ruiz-Lara, T.; Sánchez-Blázquez, P.; Walcher, C. J.; Alves, J.; Aguerri, J. A. L.; Bekeraité, S.; Bland-Hawthorn, J.; Galbany, L.; Gallazzi, A.; Husemann, B.; Iglesias-Páramo, J.; Kalinova, V.; López-Sánchez, A. R.; **Marino, R. A.**; and 6 coauthors *eprint arXiv:1506.04157*

- TRACING KINEMATIC (MIS)ALIGNMENTS IN CALIFA MERGING GALAXIES: STELLAR AND IONIZED GAS KINEMATIC ORIENTATIONS AT EVERY MERGER STAGE
  Barrera-Ballesteros, J. K.; García-Lorenzo, B.; Falcón-Barroso, J.; van de Ven, G.; Sánchez, S. F.; Marquez, I.; Masegosa, J.; Monreal-Ibero, A.; Ziegler, B.; del Olmo, A.; Verdes-Montenegro, L.; García-Benito, R.; Husemann, B.; Mast, D.; Kehrig, C.; Iglesias-Páramo, J.; **Marino, R. A.**; and 10 coauthors *eprint arXiv:1506.03819*

- THE INCIDENCE OF BAR-LIKE KINEMATIC FLOWS IN CALIFA GALAXIES
  Holmes, L.; Spekkens, K.; Sánchez, S. F.; Walcher, C. J.; García Benito, R.; Mast, D.; Cortijo-Ferrero, C.; Kalinova, V.; **Marino, R. A.**; Méndez-Abreu, J.; Barrera-Ballesteros, J. K. *eprint arXiv:1506.01378*

- STAR FORMATION IN THE LOCAL UNIVERSE FROM THE CALIFA SAMPLE. I. CALIBRATING THE SFR USING IFS DATA
  Catalán-Torrecilla, C.; Gil de Paz, A.; Castillo-Morales, A.; Iglesias-Páramo, J.; Sánchez, S. F.; Kennicutt, R.; Pérez-González, P. G.; **Marino, R. A.**; and 18 coauthors *Astronomy & Astrophysics, 2015, submitted*

- BAR PATTERN SPEEDS IN CALIFA GALAXIES: I. FAST BARS ACROSS THE HUBBLE SEQUENCE
  Aguerri, J. A. L.; Méndez-Abreu, J.; Falcón-Barroso, J.; Amorin, A.; Barrera-Ballesteros, J. K.; García Benito, R.; González Delgado, R.; Cid Fernandes, R.; Husemann, B.; Kalinova, V.; Lyubenova, M.; **Marino, R. A.**; and 15 coauthors *Astronomy & Astrophysics, Volume 576, id.A102, 17 pp., 2015*

- IMPRINTS OF GALAXY EVOLUTION ON H II REGIONS MEMORY OF THE PAST UNCOVERED BY THE CALIFA SURVEY
  Sánchez, S. F.; Pérez, E.; Rosales-Ortega, F. F.; Miralles-Caballero, D.; López-Sánchez, A. R.; Iglesias-Páramo, J.; **Marino, R. A.**; and 22 coauthors *Astronomy & Astrophysics, Volume 574, id.A47, 17 pp., 2015*

- CENSUS OF HII REGIONS IN NGC 6754 DERIVED WITH MUSE: CONSTRAINTS ON THE METAL MIXING SCALE

Sánchez, S. F.; Galbany, L.; Pérez, E.; Sánchez-Blázquez, P.; Falcón-Barroso, J.; Rosales-Ortega, F. F.; Sánchez-Menguiano, L.; **Marino, R. A.**; and 6 coauthors *Astronomy & Astrophysics, Volume 573, id.A105, 13 pp., 2015*

- IONIZED GAS KINEMATICS OF GALAXIES IN THE CALIFA SURVEY I: VELOCITY FIELDS, KINEMATIC PARAMETERS OF THE DOMINANT COMPONENT, AND PRESENCE OF KINEMATICALLY DISTINCT GASEOUS SYSTEMS
  García-Lorenzo, B.; Márquez, I.; Barrera-Ballesteros, J. K.; Masegosa, J.; Husemann, B.; Falcón-Barroso, J.; Lyubenova, M.; Sánchez, S. F.; Walcher, J.; Mast, D.; García-Benito, R.; Méndez-Abreu, J.; van de Ven, G.; Spekkens, K.; Holmes, L.; Monreal-Ibero, A.; del Olmo, A.; Ziegler, B.; Bland-Hawthorn, J.; Sánchez-Blázquez, P.; Iglesias-Páramo, J.; Aguerri, J. A. L.; Papaderos, P.; Gomes, J. M.; **Marino, R. A.**; and 6 coauthors *Astronomy & Astrophysics, Volume 573, id.A59, 43 pp., 2015*

- NEARBY SUPERNOVA HOST GALAXIES FROM THE CALIFA SURVEY: I. SAMPLE, DATA ANALYSIS, AND CORRELATION TO STAR-FORMING REGIONS
  Galbany, L.; Stanishev, V.; Mourão, A. M.; Rodrigues, M.; Flores, H.; García-Benito, R.; Mast, D.; Mendoza, M. A.; Sánchez, S. F.; Badenes, C.; Barrera-Ballesteros, J.; Bland-Hawthorn, J.; Falcón-Barroso, J.; García-Lorenzo, B.; Gomes, J. M.; González Delgado, R. M.; Kehrig, C.; Lyubenova, M.; López-Sánchez, A. R.; de Lorenzo-Cáceres, A.; **Marino, R. A.**; and 6 coauthors *Astronomy & Astrophysics, Volume 572, id.A38, 24 pp., 2014*

- STELLAR POPULATION GRADIENTS IN GALAXY DISCS FROM THE CALIFA SURVEY. THE INFLUENCE OF BARS
  Sánchez-Blázquez, P.; Rosales-Ortega, F. F.; Méndez-Abreu, J.; Pérez, I.; Sánchez, S. F.; Zibetti, S.; Aguerri, J. A. L.; Bland-Hawthorn, J.; Catalán-Torrecilla, C.; Cid Fernandes, R.; de Amorim, A.; de Lorenzo-Caceres, A.; Falcón-Barroso, J.; Galazzi, A.; García Benito, R.; Gil de Paz, A.; González Delgado, R.; Husemann, B.; Iglesias-Páramo, Jorge; Jungwiert, B.; **Marino, R. A.**; and 9 coauthors *Astronomy & Astrophysics, Volume 570, id.A6, 85 pp. 2014*

- CALIFA, THE CALAR ALTO LEGACY INTEGRAL FIELD AREA SURVEY. III. SECOND PUBLIC DATA RELEASE
  García-Benito, R.; Zibetti, S.; Sánchez, S. F.; Husemann, B.; de Amorim, A. L.; Castillo-Morales, A.; Cid Fernandes, R.; . Ellis, S. C; Falcón-Barroso, J.; Galbany, L.; Gil de Paz, A.; González Delgado, R. M.; Lacerda, E. A. D.; López-Fernandez, R.; de Lorenzo-Cáceres, A.; Lyubenova, M.; **Marino, R. A.**; and 54 coauthors *Astronomy & Astrophysics, Vol. 576, id.A135, 30 pp. 2015*

- CALIFA: A DIAMETER-SELECTED SAMPLE FOR AN INTEGRAL FIELD SPECTROSCOPY GALAXY SURVEY
  Walcher, C. J.; Wisotzki, L.; Bekeraité, S.; Husemann, B.; Iglesias-Páramo, J.; Backsmann, N.; Barrera Ballesteros, J.; Catalán-Torrecilla, C.; Cortijo, C.; del Olmo, A.; García Lorenzo, B.; Falcón-Barroso, J.; Jilkova, L.; Kalinova, V.; Mast, D.; **Marino, R. A.**; and 35 coauthors *Astronomy & Astrophysics, Volume 569, id.A1, 18 pp., 2014*

- INSIGHTS ON THE STELLAR MASS-METALLICITY RELATION FROM THE CALIFA SURVEY
  González Delgado, R. M.; Cid Fernandes, R.; García-Benito, R.; Pérez, E.; de Amorim, A. L.; Cortijo-Ferrero, C.; Lacerda, E. A. D.; López Fernández, R.; Sánchez, S. F.; Vale Asari, N.; Alves, J.; Bland-Hawthorn, J.; Galbany, L.; Gallazzi, A.; Husemann, B.; Bekeraité, S.; Jungwiert, B.; López-Sánchez, A. R.; de Lorenzo-Cáceres, A.; **Marino, R. A.**; and 9 coauthors *The Astrophysical Journal Letters, Volume 791, Issue 1, article id. L16, 5 pp., 2014*

- KINEMATIC ALIGNMENT OF NON-INTERACTING CALIFA GALAXIES. QUANTIFYING THE IMPACT OF BARS ON STELLAR AND IONISED GAS VELOCITY FIELD ORIENTATIONS
  Barrera-Ballesteros, J. K.; Falcón-Barroso, J.; García-Lorenzo, B.; van de Ven, G.; Aguerri, J. A. L.; Méndez-Abreu, J.; Spekkens, K.; Lyubenova, M.; Sánchez, S. F.; Husemann, B.; Mast, D.; García-Benito, R.; Iglesias-Páramo, J.; Del Olmo, A.; Márquez, I.; Masegosa, J.; Kehrig, C.; **Marino, R. A.**; and 5 coauthors *Astronomy & Astrophysics, Volume 568, id.A70, 30 pp., 2014*

- THE MICE AT PLAY IN THE CALIFA SURVEY. A CASE STUDY OF A GAS-RICH MAJOR MERGER BETWEEN FIRST PASSAGE AND COALESCENCE
  Wild, V.; Rosales-Ortega, F.; Falcón-Barroso, J.; García-Benito, R.; Gallazzi, A.; González Delgado, R.; Bekeraité, S.; Pasquali, A.; Johansson, P.; García Lorenzo, B.; van de Ven, G.; Pawlik, M.; Peréz, E.; Monreal-Ibero, A.; Lyubenova, M.; Cid Fernandes, R.; Méndez-Abreu, J.; Barrera-Ballesteros, J.; Kehrig, C.; Iglesias-Páramo, J.; Bomans, D.; Márquez, I.; Johnson, B.; Kennicutt, R. C.; Husemann, B.; Mast, D.; Sánchez, S. F.; Walcher, C. J.; Alves, J.; Aguerri, A. L.; Alonso Herrero, A.; Bland-Hawthorn, J.; Catalán-Torrecilla, C.; Florido, E.; Gomes, J.; Jahnke, K.; López-Sánchez, A. R.; de Lorenzo-Cáceres, A.; **Marino, R. A.**; and 7 coauthors *Astronomy & Astrophysics, Volume 567, id.A132, 21 pp., 2014*

- CALIFA: A DIAMETER-SELECTED SAMPLE FOR AN INTEGRAL FIELD SPECTROSCOPY GALAXY SURVEY
  Walcher, C. J.; Wisotzki, L.; Bekeraité, S.; Husemann, B.; Iglesias-Páramo, J.; Backsmann, N.; Barrera Ballesteros, J.; Catalán-Torrecilla, C.; Cortijo, C.; del Olmo, A.; García Lorenzo, B.; Falcón-Barroso, J.; Jilkova, L.; Kalinova, V.; Mast, D.; **Marino, R. A.**; and 35 coauthors *Astronomy & Astrophysics, Volume 569, id.A1, 18 pp., 2014*

- A CHARACTERISTIC OXYGEN ABUNDANCE GRADIENT IN GALAXY DISKS UNVEILED WITH CALIFA
  Sánchez, S. F.; Rosales-Ortega, F. F.; Iglesias-Páramo, J.; Mollá, M.; Barrera-Ballesteros, J.; **Marino, R. A.**; and 31 coauthors *Astronomy & Astrophysics, Volume 563, id.A49, 25 pp., 2014*

- THE STAR FORMATION HISTORY OF CALIFA GALAXIES: RADIAL STRUCTURES
  González Delgado, R. M.; Pérez, E.; Cid Fernandes, R.; García-Benito, R.; de Amorim, A. L.; Sánchez, S. F.; Husemann, B.; Cortijo-Ferrero, C.; López Fernández, R.; Sánchez-Blázquez, P.; Bekeraite, S.; Walcher, C. J.; Falcón-Barroso, J.; Gallazzi, A.; van de Ven, G.; Alves, J.; Bland-Hawthorn, J.; Kennicutt, R. C.; Kupko, D.; Lyubenova, M.; Mast, D.; Mollá, M.; **Marino, R. A.**; and 3 coauthors *Astronomy & Astrophysics, Volume 562, id.A47, 25 pp., 2014*

- THE EFFECTS OF SPATIAL RESOLUTION ON INTEGRAL FIELD SPECTROGRAPH SURVEYS AT DIFFERENT REDSHIFTS - THE CALIFA PERSPECTIVE
  Mast, D.; Rosales-Ortega, F. F.; Sánchez, S. F.; Vílchez, J. M.; Iglesias-Paramo, J.; Walcher, C. J.; Husemann, B.; Márquez, I.; **Marino, R. A.**; Kennicutt, R. C.; and 20 coauthors *Astronomy & Astrophysics, Volume 561, id.A129, 19 pp., 2014*

- THE NATURE OF LINER GALAXIES:. UBIQUITOUS HOT OLD STARS AND RARE ACCRETING BLACK HOLES
  Singh, R.; van de Ven, G.; Jahnke, K.; Lyubenova, M.; Falcón-Barroso, J.; Alves, J.; Cid Fernandes, R.; Galbany, L.; García-Benito, R.; Husemann, B.; Kennicutt, R. C.; **Marino, R. A.**; and 9 coauthors *Astronomy & Astrophysics, Volume 558, id.A43, 8 pp., 2013*

- MASS-METALLICITY RELATION EXPLORED WITH CALIFA. I. IS THERE A DEPENDENCE ON THE STAR-FORMATION RATE?

Sánchez, S. F.; Rosales-Ortega, F. F.; Jungwiert, B.; Iglesias-Páramo, J.; Vílchez, J. M.; **Marino, R. A.**; Walcher, C. J.; and 35 coauthors *Astronomy & Astrophysics, Volume 554, id.A58, 8 pp., 2013*

- APERTURE CORRECTIONS FOR DISK GALAXY PROPERTIES DERIVED FROM THE CALIFA SURVEY. BALMER EMISSION LINES IN SPIRAL GALAXIES
  Iglesias-Páramo, J.; Vílchez, J. M.; Galbany, L.; Sánchez, S. F.; Rosales-Ortega, F. F.; Mast, D.; García-Benito, R.; Husemann, B.; Aguerri, J. A. L.; Alves, J.; Bekeraité, S.; Bland-Hawthorn, J.; Catalán-Torrecilla, C.; de Amorim, A. L.; de Lorenzo-Cáceres, A.; Ellis, S.; Falcón-Barroso, J.; Flores, H.; Florido, E.; Gallazzi, A.; Gomes, J. M.; González Delgado, R. M.; Haines, T.; Hernández-Fernández, J. D.; Kehrig, C.; López-Sánchez, A. R.; Lyubenova, M.; **Marino, R. A.**; Mollá, M.; and 12 coauthors *Astronomy & Astrophysics, Volume 553, id.L7, 5 pp., 2013*

- CALIFA, THE CALAR ALTO LEGACY INTEGRAL FIELD AREA SURVEY. II. FIRST PUBLIC DATA RELEASE
  Husemann, B.; Jahnke, K.; Sánchez, S. F.; Barrado, D.; Bekeraité, S.; Bomans, D. J.; Castillo-Morales, A.; Catalán-Torrecilla, C.; Cid Fernandes, R.; Falcón-Barroso, J.; García-Benito, R.; González Delgado, R. M.; Iglesias-Páramo, J.; Johnson, B. D.; Kupko, D.; López-Fernandez, R.; Lyubenova, M.; **Marino, R. A.**; and 58 coauthors *Astronomy & Astrophysics, Volume 549, id.A87, 25 pp., 2013*

- INTEGRAL FIELD SPECTROSCOPY OF A SAMPLE OF NEARBY GALAXIES. II. PROPERTIES OF THE HII REGIONS
  Sánchez, S. F.; Rosales-Ortega, F. F.; **Marino, R. A.**; Iglesias-Páramo, J.; Vílchez, J. M.; Kennicutt, R. C.; Díaz, A. I.; Mast, D.; Monreal-Ibero, A.; García-Benito, R.; Bland-Hawthorn, J.; Pérez, E.; González Delgado, R.; Husemann, B.; López-Sánchez, A. R.; Cid Fernandes, R.; Kehrig, C.; Walcher, C. J.; Gil de Paz, A.; Ellis, S. *Astronomy & Astrophysics, Volume 546, id.A2, 28 pp., 2012*

- THE IONIZED GAS IN THE CALIFA EARLY-TYPE GALAXIES. I. MAPPING TWO REPRESENTATIVE CASES: NGC 6762 AND NGC 5966
  Kehrig, C.; Monreal-Ibero, A.; Papaderos, P.; Vílchez, J. M.; Gomes, J. M.; Masegosa, J.; Sánchez, S. F.; Lehnert, M. D.; Cid Fernandes, R.; Bland-Hawthorn, J.; Bomans, D. J.; Marquez, I.; Mast, D.; Aguerri, J. A. L.; López-Sánchez, A. R.; **Marino, R. A.**; and 5 coauthors *Astronomy & Astrophysics, Volume 540, id.A11, 15 pp., 2012*

- SPATIALLY RESOLVED PROPERTIES OF THE GRAND-DESIGN SPIRAL GALAXY UGC 9837: A CASE FOR HIGH-REDSHIFT 2-D OBSERVATIONS
  Viironen, K.; Sánchez, S. F.; Marmol-Queraltó, E.; Iglesias-Páramo, J.; Mast, D.; **Marino, R. A.**; and 5 coauthors *Astronomy & Astrophysics, Volume 538, id.A144, 12 pp., 2012*

- CALIFA, THE CALAR ALTO LEGACY INTEGRAL FIELD AREA SURVEY. I. SURVEY PRESENTATION
  Sánchez, S. F.; Kennicutt, R. C.; Gil de Paz, A.; van de Ven, G.; Vílchez, J. M.; Wisotzki, L.; Walcher, C. J.; Mast, D.; Aguerri, J. A. L.; Albiol-Pérez, S.; Alonso-Herrero, A.; Alves, J.; Bakos, J.; Bartáková, T.; Bland-Hawthorn, J.; Boselli, A.; Bomans, D. J.; Castillo-Morales, A.; Cortijo-Ferrero, C.; de Lorenzo-Cáceres, A.; Del Olmo, A.; Dettmar, R.-J.; Díaz, A.; Ellis, S.; Falcón-Barroso, J.; Flores, H.; Gallazzi, A.; García-Lorenzo, B.; González Delgado, R.; Gruel, N.; Haines, T.; Hao, C.; Husemann, B.; Iglésias-Páramo, J.; Jahnke, K.; Johnson, B.; Jungwiert, B.; Kalinova, V.; Kehrig, C.; Kupko, D.; López-Sánchez, A. R.; Lyubenova, M.; **Marino, R. A.**; and 29 coauthors *Astronomy & Astrophysics, Volume 538, id.A8, 31 pp., 2012*

- INTEGRAL FIELD SPECTROSCOPY OF A SAMPLE OF NEARBY GALAXIES. I. SAMPLE, OBSERVATIONS, AND DATA REDUCTION
  Mármol-Queraltó, E.; Sánchez, S. F.; **Marino, R. A.**; Mast, D.; Viironen, K.; Gil de Paz, A.; Iglesias-Páramo, J.; Rosales-Ortega, F. F.; Vilchez, J. M. *Astronomy & Astrophysics, Volume 534, id.A8, 17 pp., 2011*

C.1.3 Technical (Co-Author)

- MEGARA: A NEW GENERATION OPTICAL SPECTROGRAPH FOR GTC
  Gil de Paz, A.; Gallego, J.; Carrasco, E.; Iglesias-Páramo, J.; Cedazo, R.; Vílchez, J. M.; García-Vargas, M. L.; Arrillaga, X.; Carrera, M. A.; Castillo-Morales, A.; Castillo-Domínguez, E.; Eliche-Moral, M. C.; Ferrusca, D.; González-Guardia, E.; Lefort, B.; Maldonado, M.; **Marino, R. A.**; and 57 coauthors *Proceedings of the SPIE, Volume 9147, id. 91470O 16 pp., 2014*

- MEGARA: THE FUTURE OPTICAL IFU AND MULTI-OBJECT SPECTROGRAPH FOR THE 10.4M GTC TELESCOPE
  Gil de Paz, A.; Carrasco, E.; Gallego, J.; Sánchez, F. M.; Vílchez Medina, J. M.; Garc'ia-Vargas, M. L.; Arrillaga, X.; Carrera, M. A.; Castillo-Morales, A.; Castillo-Domínguez, E.; Cedazo, R.; Eliche-Moral, C.; Ferrusca, D.; González-Guardia, E.; Maldonado, M.; **Marino, R. A.**; and 48 coauthors *Proceedings of the SPIE, Volume 8446, article id. 84464Q, 9 pp., 2012*

C.1.4 Non-Refereed (First author only)

- COMBING PPAK INTEGRAL FIELD SPECTROSCOPY AND PACS-HERSCHEL DATA: A MULTI-WAVELENGTH STUDY OF DUST PROPERTIES IN SPIRAL DISKS
  Marino, R.A.; Boselli, A., Boquien, M.; Gil de Paz, A.; Sánchez, S. F.; Castillo-Morales, A.; Muñoz-Mateos, J. C. *Highlights of Spanish Astrophysics VIII, Proceedings of the XI Scientific Meeting of the Spanish Astronomical Society, p. 374, 2015*

- NEW EMPIRICAL METALLICITY CALIBRATIONS: JOINT ANALYSIS OF CALIFA DATA AND LITERATURE T_e−BASED MEASUREMENTS
  Marino, R.A.; Rosales-Ortega, F.F; Sánchez, S.; Gil de Paz, A. *Highlights of Spanish Astrophysics VIII, Proceedings of the XI Scientific Meeting of the Spanish Astronomical Society, p. 374, 2015*

- NEW EMPIRICAL METALLICITY CALIBRATIONS: JOINT ANALYSIS OF CALIFA DATA AND LITERATURE T_e−BASED MEASUREMENTS
  Marino, R.A.; Rosales-Ortega, F.F; Sánchez, S.; Gil de Paz, A. Vílchez, J.; CALIFA Team *Galaxies in 3D across the Universe, Proceedings of the International Astronomical Union, IAU Symposium, Vol. 309, pp. 328-328, 2015*

- INTEGRAL FIELD SPECTROSCOPY AND AND MULTI-WAVELENGTH IMAGING OF NEARBY SPIRAL GALAXIES: NGC 5668 AS A PILOT CASE FOR MEGARA
  Marino, R.A.; Gil de Paz, A.; Castillo-Morales, A.; and 13 coauthors *Revista Mexicana de Astronomía y Astroísica, Vol. 42, pp. 112-112, 2013*

- STUDYING NEARBY DISK GALAXIES:NGC 3982 A CASE FOR THE CALIFA SURVEY
  Marino, R.A.; Gil de Paz, A.; Castillo-Morales, A.; and 6 coauthors *Highlights of Spanish Astrophysics VII, pp.447-447, 2013*

- INTEGRAL FIELD SPECTROSCOPY AND AND MULTI-WAVELENGTH IMAGING OF NEARBY SPIRAL GALAXIES
  Marino, R.A.; Gil de Paz, A.; Castillo-Morales, A.; and 7 coauthors *Highlights of Spanish Astrophysics VII, pp.262-268, 2013*

- STUDYING NEARBY DISK GALAXIES WITH THE CALIFA SURVEY
  Marino, R.A.; Gil de Paz, A.; Sánchez,S.; Castillo-Morales, A. *Memorie della Societa Astronomica Italiana Supplement, v.19, p.290, 2012*

- INTEGRAL FIELD SPECTROSCOPY OF THE NEARBY SPIRAL GALAXY NGC 5668
  Marino, R.A.; Gil de Paz, A.; and 3 coauthors *Highlights of Spanish Astrophysics VI, pp.238-244, 2011*

- INTEGRAL FIELD SPECTROSCOPY OF THE NEARBY SPIRAL GALAXY NGC 5668
  Marino, R.A.; and 4 coauthors *Memorie della Societa Astronomica Italiana Supplement, v.14, p.271, 2010*

Bibliography

Abazajian, K., Adelman-McCarthy, J., Agüeros, M. et al. 2009, ApJS, 182, 543

Afflerbach, A., Churchwell, E., Werner, M. W. 1997, ApJ, 478, 190

Aguerri, J., Méndez-Abreu, J., Falcón-Barroso, J, et al. 2015, A&A, 576, 102

Allende-Prieto, C., Lambert, D. L. & Asplund, M. 2001, ApJ, 556, L63

Aller, L.H. 1942, ApJ, 95, 52

Alloin, D., Collin-Souffrin, S., Joly, M., & Vigroux, L. 1979, A&A, 78, 200

Arribas, S., Colina, L., Monreal-Ibero, A. et al. 2008, A&A, 479, 687

Arribas, S., Mediavilla, E., García-Lorenzo, B., del Burgo, C. & Fuensalida, J. 1999, A&AS, 136, 189

Asplund, M., Grevesse, N., Jacques Sauval, A., & Scott, P. 2009, ARA&A, 47, 481

Bacon, R. et al. 1995, A&ASS, 113, 347

Bacon, R. et al. 2001a, MNRAS, 326, 23

Bacon, R. et al. 2001b, A&A, 371, 409

Bacon, R. et al. 2004, SPIE, 5492, 1145

Barnes, L., Garel, T. & Kacprzak, G. 2014, PASP, 126, 969

Barwig, H., Schoembs, R., Buckenmayer, C. 1987, A&A, 175, 327

Barrera-Ballesteros, J., Falcón-Barroso, J., García-Lorenzo, B. et al. 2014, A&A, 568, A70

Barrera-Ballesteros, J. K., Sánchez, S. F., García-Lorenzo, B. 2015, arXiv150503153B

Bakos, J., Trujillo, I. & Pohlen, M. 2008, ApJ, 683, L103

Battaner, E.; Florido, E.; Jiménez-Vicente, J. 2002, A&A, 388, 213

Bell, E. F., McIntosh, D. H., Katz, N., & Weinberg, M. D. 2003, ApJS, 149, 289

Bershady, M., Verheijen, M, Swaters, R. et al. 2010, ApJ, 716, 198

Bianchi S. & Schneider R. 2007, MNRAS, 378, 973

Binney , J.& Tremaine, S. 1987, *Galactic Dynamics*

Blanc, G. A., Schruba, A., Evans, N. J. et al. 2013, ApJ, 764, 117

Boeche, C. et al, 2014, A&A, 568, 71

Boissier, S., & Prantzos, N. 1999, MNRAS, 307, 857

Boissier, S., & Prantzos, N. 2000, MNRAS, 312, 398

Boselli, A., Lequeux, J., & Gavazzi, G. 2002, A&A, 384, 33

Boselli, A., Gavazzi, G., & Sanvito, G. 2003, A&A, 402, 37

Boselli, A., Lequeux, J., & Gavazzi, G. 2004, A&A, 428, 409

Boselli, A., Eales, S., Cortese, L. et al. 2010, PASP, 122, 261

Boselli, A., Hughes, T. M., Cortese, L., Gavazzi, G., & Buat, V. 2013, A&A,550, A114

Boselli, A., Cortese, L., & Boquien, M. 2014a, A&A, 564, AA65

Boselli, A., Cortese, L., Boquien, M., et al. 2014b, A&A, 564, 66

Boselli, A., Cortese, L., Boquien, M. et al. 2014c, A&A, 564, 67

Boselli, A., Voyer, E., Boissier, S. et al. 2014d, A&A, 570, 69

Boquien, M., Calzetti, D., Combes, F., et al. 2011, AJ, 142, 111

Boquien, M., Boselli, A., Buat, V. et al. 2013, A&A, 554, 14B

Boquien, M., Buat, V., & Perret, V. 2014, A&A, 571, AA72

Bovy, J. et al. 2014, ApJ, 790, 127

Bresolin, F., Gieren, W., Kudritzki, R.P., et al. 2009a, ApJ, 700, 309

Bresolin, F., Ryan-Weber, E., Kennicutt, R. C., & Goddard, Q. 2009b, ApJ, 695, 580

Bresolin, F., Kennicutt, R. C., & Ryan-Weber, E. 2012, ApJ, 750, 122

Buat, V. 1992 A&A, 264, 444

Buat, V., & Xu, C. 1996, A&A, 306, 61

Buat, V., Donas, J., Milliard, B., Xu, C. 1999, A&A, 352, 371

Buat, V. et al. 2005, ApJ, 619, 51

Burgarella, D., Buat, V., Donas, J., Milliard, B., & Chapelon, S. 2001, A&A, 369, 421

Burgarella et al. 2005, MNRAS 360, 1411

Calzetti, D. 2001, PASP, 113, 1449

Calzetti, D., Kinney, A. L., & Storchi-Bergmann, T. 1994, ApJ, 429, 582

Cappellari M. & Copin, Y. 2003, MNRAS, 342, 345

Cappellari, M., Emsellem, E., Krajnovic, D. et al. 2011, MNRAS, 416, 1680

Caputo, F., Marconi, M., Musella, I., Pont, F. 2001, A&A, 372, 544

Cardelli, J. A., Clayton, G. C., & Mathis, J. S. 1989, ApJ, 345, 245

Catalán-Torrecilla, A. Gil de Paz, A. Castillo-Morales et al. 2015, A&A, accepted

Chabrier G. 2003, ApJL, 586, L133

Chiappini, C., Matteucci, F., & Gratton, R. 1997, ApJ, 477, 765

Christensen, L., Møller, P., Fynbo, J. P. U. et al. 2014, MNRAS, 445, 225

Cid Fernandes, R., Pérez, E., García-Benito, R. et al. 2013, A&A, 557A, 86

Cid Fernandes, R., González-Delgado, R. M., García-Benito et al. 2014, A&A, 561, 130

Clayton, G., Wolff, M. et al. 1997, AJ, 114, 1132

Croom, S., Lawrence, J., Bland-Hawthorn, J. et al. 2012, MNRAS, 421, 872

Cooke, R., Pettini, M., Steidel, C. C. et al. 2011, MNRAS, 417, 1534

Cortese, L., Boissier, S., Boselli, A. et al. 2012a, A&A, 544, 101

Cortese, L., Ciesla, L., Boselli, A. et al. 2012b, A&A, 540, 52

Cortese, L., Fritz, J., Bianchi, S. et al. 2014, MNRAS, 440, 942

Cowie, L. L., & Hu, E. M. 1998, AJ, 115, 1319

Cowsik, R. & McClelland, J. 1973, ApJ, 180, 7

Curtis, H. D. 1918, *Publications of Lick Observatory*, 13, 9

Daflon, S., & Cunha, K. 2004, ApJ, 617, 1115

Davies, R. & Birkinshaw, M. 1988, ApJS, 68, 409

Debattista, V. P., Mayer, L., Carollo, C. M., et al. 2006, ApJ, 645, 209

Deharveng, L., Peña, M., Caplan, J. & Costero, R. 2000, MNRAS, 311, 329

Denicoló, G., Terlevich, R., & Terlevich, E. 2002, MNRAS, 330, 69

de Grijp, M. H. K., Miley, G. K., Lub, J., & de Jong, T. 1985, Nature, 314, 240

de Vaucouleurs, G. 1959, *Handbuch der Physik*, 53, 275

de Vaucouleurs, G., de Vaucouleurs, A., Corwin, H. G., Buta, R. J., Paturel, G., & Fouqué, P. 1991, *Third Reference Catalogue of Bright Galaxies* (RC3) (Springer-Verlag)

de Zeeuw, P. T., Bureau, M., Emsellem, E. et al. 2002, MNRAS, 329, 513

Dinerstein, H. 1990, ASSL, 161, 257

Dopita, M. A. & Evans, I. N. 1986, ApJ, 307, 431

Dopita, M. A., Kewley, L. J., Heisler, C., Sutherland, R. 2000, ApJ, 542, 224

Dopita, M. A., Sutherland, R., Nicholls, D. et al. 2013, ApJS, 208, 10

Dweck, E. 1998, ApJ, 501, 643

Eggen, O. J., Lynden-Bell, D., & Sandage, A. R. 1962, ApJ, 136, 748

Elmegreen, B. G., Elmegreen, D. M. 1983, ApJ, 267, 31

Elmegreen, B. G. & Parravano, A. 1994, ApJ, 435, L121

Emsellem, E. et al. 1996, A&A, 312, 777

Ercolano, B., Bastian, N., Stasinska, G. 2007 MNRAS, 379, 945

Ercolano, B., Bastian, N., Spezzi, L. 2011, MNRAS, 416. 439

Erwin, P., Beckman, J., Pohlen, M. 2005, ApJ, 626, 81

Erwin, P., Pohlen, M., & Beckman, J. E. 2008, AJ, 135, 20

Esteban, C., Bresolin, F., Peimbert, M. et al. 2009, ApJ, 700, 654

Esteban, C., Carigi, L., Copetti, M. et al. 2013, MNRAS, 433, 382

Fall, S. M., & Efstathiou, G. 1980, MNRAS, 193, 189

Ferguson, A. & Clarke, C. J. 2001, MNRAS, 325, 781

Ferrini F., Penco U., Palla F. 1990, A&A, 231, 391

Fich, M., & Silkey, M. 1991, ApJ, 366, 107

Filippenko, A. V. 1982, PASP, 94, 715

Florido, E., Battaner, E., Guijarro, A., Garzón, F., Castillo-Morales, A. 2006, A&A, 455, 467

Florido, E., Battaner, E., Zurita, A., Guijarro, A. 2007, A&A, 472, 39

Freeman, K. C. 1970, ApJ, 160, 811

Friel, E. D., Janes, K. A., Tavarez, M. 2002, AJ, 124, 2693

Fitzsimmons, A., Brown, P. J. F., Dufton, P. L. & Lennon, D. J. 1990, A&A, 232, 437

Frinchaboy, P. M. 2013, ApJ, 777, 1

Foyle, K., Courteau, S., & Thacker, R. 2008, MNRAS, 386, 1821

Forman, W. & Jones, C. 1982, A&A, 20, 574

Förster Schreiber, N., Genzel, R., Lehnert, M. et al. 2006, ApJ, 645, 1062

Fukugita, M., Shimasaku, K., & Ichikawa, T. 1995, PASP, 107, 945

Galbany, L., Stanishev, V., Mourão, A. M. et al. 2014, A&A, 572, 38

Galliano, F., Dwek, E. & Chanial, P. 2008, ApJ, 672, 214

García-Benito, R., Zibetti, S., Sánchez, S. F. et al. 2015, A&A, 576, A135

Gawiser, E., Francke, H., Lai, K. et al. 2007, ApJ, 671, 278

Gehrz R. 1989, *Interstellar Dust*, IAU Symposium 1335, 445

Giammanco, C., Beckman, J. E. & Cedérs, B. 2005, A&A, 438, 599

Gil de Paz, A. et al. 2007a, ApJS, 173, 185

Gil de Paz, A. et al. 2007b, ApJ, 661, 115

Gil de Paz, A. et al. 2012, SPIE Conference Series, Vol. 8446

Gil de Paz, A. et al. 2014, SPIE Conference Series, Vol. 9147

Gomez H.L., Krause O., Barlow M.J., et al. 2012, ApJ, 760, 96

González-Delgado, R. M., Cid Fernandes, R., García-Benito, R. et al. 2014a, ApJ, 791, L16

González-Delgado, R. M., Pérez, E., Cid Fernandes, R. et al. 2014b, A&A, 562,A47

Gordon, Karl D., Witt, Adolf N., et al. 2000, ApJ, 544, 859

Guaita, L., Francke, H., Gawiser, E. et al. 2013, A&A, 551, 93

Hayden, M. R. et al. 2013, AJ, 147, 116

Helou, G. 1986, ApJ, 311, L33

Henry, R. & Worthey, G. 1999, PASP, 111, 919

Hill, J. M., Angel, J. R. P., Scott, J. S., Lindley, D., & Hintzen, P. 1980, ApJ, 242, L69

Ho, I.-T., Kudritzki, R.-P., Kewley, L. J., et al. 2015, MNRAS, 448, 2030

Hubble, E. P. 1925, ApJ, 62, 409

Hubble, E. P. 1926a, ApJ, 63, 236

Hubble, E. P. 1926b, ApJ, 64, 321

Hubble, E. P. 1929, ApJ, 69, 103

Hubble, E. P. 1936, *The Realm of the Nebulae* (New Haven: Yale University Press)

Husemann, B., Jahnke, K., Sánchez, S. F. et al. 2013, A&A, 549, A87

Iglesias-Páramo, J., Vílchez, J. M., Galbany, L. et al. 2013, A&A, 553, L7

Israelian, G. & Meynet, G. 2008, *The Metal Rich Universe*, Cambridge University Press

Jacoby, G. H. & Kaler, J. B., 1993, ApJ, 417, 209

Janes, K. A. 1979, ApJS, 39, 135

Jura, M., Kim, D. W., Knapp, G. R. & Guhathakurta, P. 1987, ApJ, 312, L11

Karman, W., Caputi, K. I., Grillo, C. et al. 2015, A&A, 574, 11

Kehrig, C., Monreal-Ibero, A., Papaderos, P. et al. 2012, A&A, 540, A11

Kennicutt, R. C., Keel, W. & Blaha C. 1989, AJ, 97, 1022

Kennicutt, R. C. 1998, ARA&A, 36, 189

Kennicutt, Jr., R. C., Bresolin, F., & Garnett, D. R. 2003, ApJ, 591, 801

Kennicutt, Jr., R. C., Calzetti, D., Aniano, G. 2011, PASP, 123, 1347

Kewley, L. J., & Dopita, M. A. 2002, ApJS, 142, 35

Kewley, L. J., & Ellison, S. L. 2008, ApJ, 681, 1183

Kobulnicky, H. A., & Kewley, L. J. 2004, ApJ, 617, 240

Kormendy, J. 1977, ApJ, 217, 406

Kormendy, J. 1982, ApJ, 257, 75

Kormendy, J. & Kennicutt, R. C. 2004 ARA&A, 42, 603

Korotin, S. A., Andrievsky, S. M., Luck, R. et al. 2014, arXiv408.6103

Knapp, G., Gunn, J. E., & Wynn-Williams, C. G. 1992, ApJ, 399, 76

Kroupa, P. 2001, MNRAS, 322, 231

Kroupa P., 2002, Sci, 295, 82

LeFévre et al. 2003, SPIE, 4841, 1670

Lemasle, B., François, P., Piersimoni, A., 2008, A&A, 490, 613

Lemonias, J., Schiminovich, D., Thilker, D., et al. 2011, ApJ, 733, 74

Li, A. & Draine, B. T. 2002, ApJ, 572, 232

Li, C., & White, S. 2009, MNRAS, 398, 2177

Lian, J. H., Li, J. R., Yan, W. et al. 2015, MNRAS, 446, 1449

Lin, C. C. & Shu, F. H., 1964, ApJ, 140, 646

Lin, D. & Pringle, J. E. 1987, ApJ, 320, L87

Lindblad, B. 1925 ApJ, 62, 191

Liu X.-W., Barlow M.J., Zhang Y., Bastin R.J., Storey P.J., 2006, MNRAS, 368, 1959

López-Sánchez, A. R. & Esteban, C. 2010, A&A, 517, A85

López-Sánchez, A. R., Dopita, M. A., Kewley, L. J. et al. 2012, MNRAS, 426, 2630

Maciel, W., Costa, R. & Uchida, M. 2003, A&A, 397, 667

Makarov, D., Prugniel, P, Terekhova, N. et al. 2014, A&A, 570, 13

Marino, R. A., Gil de Paz, A., Castillo-Morales, A. et al. 2012, ApJ, 754, 61

Marino, R. A., Rosales-Ortega, F. F., Sánchez, S. F. et al. 2013, A&A, 559, 114

Marino, R. A., Gil de Paz, A., Sánchez, S. F. et al. 2015, submitted

Mármol-Queraltó, E., Sánchez, S. F., Marino, R. A. et al. 2011, A&A, 534, A8

Martín-Navarro, I., Bakos, J., Trujillo, I., et al. 2012, MNRAS, 427, 1102

Martínez-Serrano, F. J., Serna, A., Doménech-Moral, M., & Domínguez-Tenreiro, R. 2009, ApJ, 705, L133

Maschberger T. 2013, MNRAS, 429, 1725

Mast, D., Rosales-Ortega, F. F., Sánchez, S. F. et al. 2014, A&A, 561, A129

Matsuura M., Dwek E., Meixner M., et al. 2011, Science, 333,1258

Matteucci, F., & François, P. 1989, MNRAS, 239, 885

Mazzei, P. & de Zotti, G. 1994, ApJ, 426, 97

McGaugh, S. S. 1991, ApJ, 380, 140

Meurer, G., Heckman, T., Leitherer, C.; Kinney, A. et al. 1995, AJ, 110, 2665

Meurer, G., Heckman, T. & Calzetti, D. 1999, ApJ, 521, 64

Miller G. E. & Scalo J. M. 1979, ApJS, 41, 513

Minchev, I., Famaey, B., Quillen, A. C., et al. 2012, A&A, 548, A126

Misiriotis, A., Popescu, C. , Tus, R. & Kylas, N. D. 2001, A&A, 372, 775

Mo, H. J., Mao, S., & White, S. D. M. 1998, MNRAS, 295, 319

Mollá, M, Cavichia, O., Gavilán, M. & Gibson, B. 2015, arXiv150503341M

Möller, P. & Fynbo, J. U. 2001, A&A, 372, 57

Mueller, M. W. & Arnett, W. D. 1976, ApJ, 210, 670

Muñoz-Mateos, J. C., Sheth, K., Gil de Paz, A., et al. 2013, ApJ, 771, 59

Nagao, T., Maiolino, R., & Marconi, A. 2006, A&A, 459, 85

Navarro, J. F., Frenk, C. S., White, S. D. M. 1997, ApJ, 493, 508.

Noll, S., Burgarella, D., Giovannoli, E. et al. 2009, A&A, 507, 1793

Oke, J. B. 1974, ApJS, 27, 21

Osterbrock, D. E. 1989, S&T, 78, 491

Osterbrock, D. E. & Ferland, G. J. 2006, *Astrophysics of gaseous nebulae and active galactic nuclei*, University Science Books

Pagel, B. E. J., Edmunds, M. G., Blackwell, D. E., Chun, M. S. & Smith, G. 1979, MNRAS, 189, 95

Pagel, B.E.J., Edmunds, M.G., & Smith, G. 1980, MNRAS, 193, 219

Papaderos, P., Gomes, J. M., Vílchez, J. M. et al. 2013, A&A, 555, L1

Patterson, F. S. 1940, Harvard College Observatory Bulletin, 913, 13

Peebles, P. J. E, 1982, ApJ, 263, 1

Peimbert M. 1978, IAU Symp. 76, Planetary Nebulae, 215

Peimbert, M., Storey, P. J., & Torres-Peimbert, S. 1993, ApJ, 414, 626

Peimbert, M., Peimbert, A., Ruiz, M. 2000, ApJ, 541, 688

Peñarrubia, J., McConnachie, A. & Babul, A. 2006, ApJ, 650, 33

Pérez, E., Cid Fernandes, R., González Delgado, R. M. et al. 2013, ApJ, 764, L1

Pérez-Montero, E., & Díaz, A. I. 2005, MNRAS, 361, 1063

Pérez-Montero, E., & Contini, T. 2009, MNRAS, 398, 949

Pérez-Montero, E. 2014, MNRAS, 441, 2663

Pettini, M.,& Pagel, B. E. J. 2004, MNRAS, 348, L59

Pilbratt, G. L., Riedinger, J. R., Passvogel, T., 2010, A&A 518L, 1P

Pilyugin, L. S. 2000, A&A, 362, 325

Pilyugin, L. S. 2001a, A&A, 369, 594

Pilyugin, L. S. 2001b, A&A, 374, 412

Pilyugin, L. S., & Thuan, T. X. 2005, ApJ, 631, 231

Pilyugin, L. S., Grebel, E. K., Zinchenko, I. A., & Kniazev, A. Y. 2014, AJ, 148,134

Pilkington, K., Gibson, B. K., Brook, C. B., 2012, MNRAS, 425, 969

Planck Collaboration & Ade, P. A. R. et al. 2015, arXiv150201589P

Poglitsch, A., Waelkens, C., Geis, N., 2010, A&A, 518L, 2P

Pohlen, M., & Trujillo, I. 2006, A&A, 454, 759

Popescu, C., Misiriotis, A., Kylas, N et al. 2000, A&A, 362, 138

Popescu, C., Tus, R. J., Madore, B. F., et al. 2005, ApJ, 619, L75

Popescu, C. Tus, R. J., Volk, H. et al. 2002, ApJ, 567, 221

Pottasch, S. R. & Bernard-Salas, J. 2006, A&A, 457, 189

Prantzos, N., & Boissier, S. 2000, MNRAS, 313, 338

Rolleston, W., Smartt, S., Dufton, P. & Ryans, R. 2000, A&A, 363, 537

Rosales-Ortega, F. F., Kennicutt, R. C., Sánchez, S. F. et al. 2010, MNRAS, 405, 735

Rosales-Ortega, F. F., Díaz, A., Kennicutt, R. C. & Sánchez, S. F. 2011, MNRAS, 415, L2439

Rosales-Ortega, F. F., Sánchez, S. F., Iglesias-Páramo, J. et al. 2012, ApJ, 756, L31

Roškar, R., Debattista, V. P., Stinson, G. S., et al. 2008, ApJ, 675, L65

Roth, M. M., Becker, T., Kelz, A., Schmoll, J., 2004, ApJ, 603, 531

Roth, M.M., Kelz, A., Fechner, T. et al. 2005, PASP, 117, 620

Rudolph, A. L., Fich, M., Bell, G. R. et al. 2006, ApJS, 162, 346

Saito, T., Matsuda, Y., Lacey, C. G. et al. 2015, MNRAS, 447, 3069

Sánchez, S. F. 2004, Astron. Nachr., 325, 167

Sánchez, S. F. 2006, Astron. Nachr., 327, 580

Sánchez, S. F., Aceituno, J., Thiele, U., Pérez-Ramírez, D. & Alves, J. 2007a, PASP, 119, 1186

Sánchez, S. F., Cardiel, N., Verheijen, M. A.W., Pedraz, S., & Covone, G. 2007b, MNRAS, 376, 125

Sánchez, S. F., Kennicutt, R. C., Gil de Paz, A. et al. 2012a, A&A, 538, A8

Sánchez, S. F., Rosales-Ortega, F. F., Kennicutt, R. C. et al. 2011, MNRAS, 410, 313

Sánchez, S. F., Rosales-Ortega, F. F., Marino, R. A. et al. 2012b, A&A, 546, A2

Sánchez, S. F., Rosales-Ortega, F. F., Iglesias-Páramo, J. et al. 2014, A&A, 563, A49

Sánchez, S.F., Pérez, E., Rosales-Ortega, F. F. et al. 2015, A&A, 574, 47

Sánchez-Blázquez, P., Courty, S., Gibson, B. K. & Brook, C. B. 2009, MNRAS, 398, 591

Sánchez-Blázquez, P., Rosales-Ortega, F. F., Méndez-Abreu, J. et al. 2014, A&A, 570, A6

Sandin, C., Becker, T., Roth, M. M., et al. 2010, A&A, 515A, 35

Salpeter, E. E. 1955, ApJ, 121, 161

Sauvage, M., Vigroux, L., & Thuan, T. X. 1990, A&A, 237, 296

Sauvage, M. & Thuan, T. X. 1994, ApJ, 429, 153

Schaye, J. 2004, ApJ, 609, 667

Schlegel, D. J., Finkbeiner, D. P., & Davis, M. 1998, ApJ, 500, 525

Searle, L. 1971, ApJ, 168, 327

Searle, L. & Zinn, R. 1978, ApJ, 225, 357

Sellwood, J. A., & Wilkinson, A. 1993, RPPh, 56, 173

Sérsic, J. L., 1968, *Atlas de Galaxias Australes* (Córdoba, Argentina: Observatorio Astronómico)

Shaver, P., McGee, R., Newton, L., Danks, A. & Pottasch, S. 1983, MNRAS, 204, 53

Shields, G. A. 1990, ARA&A, 28, 525

Shepard, D. 1968 ACM Nat. Confi, 517, 524

Singh, R., van de Ven, G., Jahnke, K. et al. 2013, A&A, 558, A43

Springel, V. et al. 2005, Nature, 435, 629

Stanghellini, L., & Haywood, M. 2010, ApJ, 714, 1096

Statler, T. & Smecker-Hane, T. 1999, AJ, 117, 839S

Storchi-Bergmann, T., Calzetti, D., & Kinney, A. L. 1994, ApJ, 429, 572

Strömgren, B. 1939, ApJ, 89, 526

Tabatabaei, F., Beck, R., Krause, M., et al. 2007, A&A, 466, 509

Thilker et al. 2005, A&A, ApJ, 619, L79

Tremonti, C. A., Heckman, T. M., Kauffmann, G. et al. 2004, ApJ, 613, 898

Toomre, A. 1964, ApJ, 139, 1217

Tsamis, Y., Péquignot, D. 2005, MNRAS, 364, 687

Tsamis, Y., Walsh, J., Vílchez, J., Péquignot, D. 2011, MNRAS, 412, 1367

Twarog, B. A., Ashman, K. M., & Anthony-Twarog, B. J. 1997, AJ, 114, 2556

van der Kruit, P. C. 1979, A&AS, 38, 15

Vanderriest, C., 1980, PASP, 92, 858

Venemans, B. P., Röttgering, H. J. A.,Miley, G. K. et al. 2005, A&A, 431, 793

Verheijen, M. et al. 2004, Astron. Nachr., 325, 151

Viironen, K., Sánchez, S. F., Marmol-Queraltó, E. et al. 2012, A&A, 538, A144

V'ilchez, J. M. & Esteban, C. 1996, MNRAS, 280, 720

Vlajić, M., Bland-Hawthorn, J., & Freeman, K. C. 2009, ApJ, 697, 361

Walcher, C. J., Wisotzki, L., Bekeraité, S. et al. 2014, A&A, 569, A1

Wells, D.C., Greisen, E.W., Harten, R.H., 1981, A&AS, 44, 363

Wild, V., Rosales-Ortega, F., Falcón-Barroso, J. et al. 2014, A&A, 567, A132

Willett, Kyle W., Lintott, Chris J., Bamford, Steven P. et al. 2013, MNRAS, 435, 2835

Wisotzki, L., Becker, T., Christensen, L. et al. 2003, A&A, 408, 455

White, S. D. M., & Frenk, C. S. 1991, ApJ, 379, 52

White, S. D. M., & Rees, C. S. 1978, MNRAS, 341, 358

Wolfire, M. G., Hollenbach, D., McKee, C., Tielens, A., & Bakes, E. 1995, ApJ, 443, 152

Woodgate, B. E., Kimble, R. A., Bowers, C. W., Kraemer, S., 1998, PASP, 110, 1183

Wu, H., Zhu, Y., Cao, C., & Qin, B. 2007, ApJ, 668, 87

Xu, C. 1990, ApJ, 365, L47

Xu, C., Buat, V. 1995, A&A, 293, 65

Xu, C. & Helou, G. 1996, ApJ, 456, 163

Yoachim, P., Roskar, R., Debattista, V. 2010, ApJ, 716, L4

Yong, D., Carney, B. W., Friel, E. D. 2012, AJ, 144, 95

Younger, J. & Bryan, G. 2007, ApJ, 666, 647

Zaritsky, D., Kennicutt, Jr., R. C., & Huchra, J. P. 1994, ApJ, 420, 87

Zaritsky, D., Christlein, D. 2007, AJ, 134, 135

Zheng, Z., Thilker, D. A., Heckman, T. M., et al. 2015, ApJ, 800, 120

Zwicky, F. 1933, Helvetica Physica Acta, 6, 110

Zwicky, F. 1957, *Morphological astronomy*